rijksuniversiteit
groningen

UNIVERSITY OF OULU

Evolution of dwarf galaxies in the Fornax cluster

PhD thesis

to obtain the degree of PhD of the
University of Groningen
on the authority of the
Rector Magnificus, Prof. E. Sterken,
and in accordance with
the decision by the College of Deans,

and

to obtain the degree of PhD of the
University of Oulu
on the authority of the
dean of the Graduate School, Prof. Harri Oinas-Kukkonen
and in assent of
the University of Oulu Graduate School.

Double PhD degree

This thesis will be defended in public on

Friday 29th of March 2019 at 11.00 hours

by

Aku Petrus Venhola
born on 22 May 1990
in Joensuu, Finland

Supervisors
Prof. R.F. Peletier
Prof. H. Salo
Dos. E. Laurikainen

Assessment Committee
Prof. C. Conselice
Prof. C. Mihos
Prof. M.A.W. Verheijen
Prof. D. Zaritsky

ISBN: 978-94-034-1581-9 (printed version)
ISBN: 978-94-034-1580-2 (electronic version)
Cover: An image showing the surroundings of NGC 1399 in the center of the Fornax cluster. The image is generated using the images of the Fornax Deep Survey.

Contents

1. Introduction

Abstract

In this chapter, I make an overview of the current knowledge about dwarf galaxies and their evolution in the cluster environment, and describe some of the open questions of the field. I start by defining dwarf galaxies and their morphological types and shortly introduce the observational framework of the field. I then describe the main environmental effects taking place in galaxy clusters and how they shape the dwarf galaxy populations in them. In addition, I give an introduction to the Fornax Deep Survey and shortly review the previous studies addressing the Fornax cluster, which plays a major role in the scientific chapters of this thesis. Finally, I summarize the contents of this thesis and how it tries to answer the open questions in the dwarf galaxy evolution.

1.1 GALAXIES AS THE BUILDING BLOCKS OF THE UNIVERSE

Galaxies are gravitationally bound systems of dark matter, stars and interstellar matter. They are the basic building blocks of the Universe appearing in a range of galactic environments from highly isolated galaxies to dense galaxy clusters (see Fig. 1.1a). Galaxies have been transforming gas into stars and are co-evolving with the larger scale structures of the Universe through the cosmic time, interacting at the same time with their surroundings. This process has led to an astonishing diversity of galaxies with different sizes and appearances that we observe in the local Universe. Obtaining a detailed understanding of this process of galaxy evolution has been one of the major endeavours of astronomical research during the last century.

The current theory of galaxy formation based on the cosmological constant (Λ) and Cold Dark Matter (CDM), i.e. ΛCDM-cosmology, states that the seeds of the first galaxies were born from small fluctuations in the density field of the hot young universe (White & Rees 1978, White & Frenk 1991). These density anomalies on various scales caused dark matter (DM) to collapse onto dark halos of different sizes. After cosmic inflation and subsequent cooling of the baryonic matter, the cold gas started to concentrate in the centers of these DM haloes and began to transform into stars, thus becoming the luminous part of the first galaxies. The radiation caused by these first stars started to heat and reionize the surrounding gas again, thus began a complex cycle of gas within the galaxies. This cosmic era, called as the "epoch of reionization", took place approximately between redshifts z=6–30 (for a review see Dayal & Ferrara 2018), corresponding to the times when the age of the Universe was between 0.1–0.9 Gyrs.

The galaxy population that we observe in the nearby Universe is the end product of the environmental and internal evolution of the early galaxies. The cosmological simulations based on ΛCDM-cosmology like Millenium II (Boylan-Kolchin et al. 2009) or Illustris (Pillepich et al. 2018) suggest that the structures in the Universe grow hierarchically from smaller to larger scales by merging of the systems, so that the first galaxies in the Universe were systematically smaller than the present day galaxies. However, not all small galaxies end up merging into larger ones, and as a result the stellar luminosity-scale of the observed galaxies in the local Universe span over the excessive range from 100 $L_\odot$ to 10^{12} $L_\odot$ (Brodie et al. 2011), corresponding to stellar masses of $M_* \approx 10^{2-12}$ $M_\odot$ (using transformations from Taylor et al. 2011).

There is also another important theory of galaxy formation in which the larger structures form first and then fragment into smaller ones during interactions of those massive systems. However, the main difference is that it contains no DM. In this theory, called MOdified Newtonian Dynamics (MOND, for a review see Famaey & McGaugh 2012), the Newtonian law of gravity is modified with an interpolating function, $\mu(x)$, which satisfies $\mu(x << 1) = x$ and $\mu(x >> 1) = 1$ (Milgrom 1989).

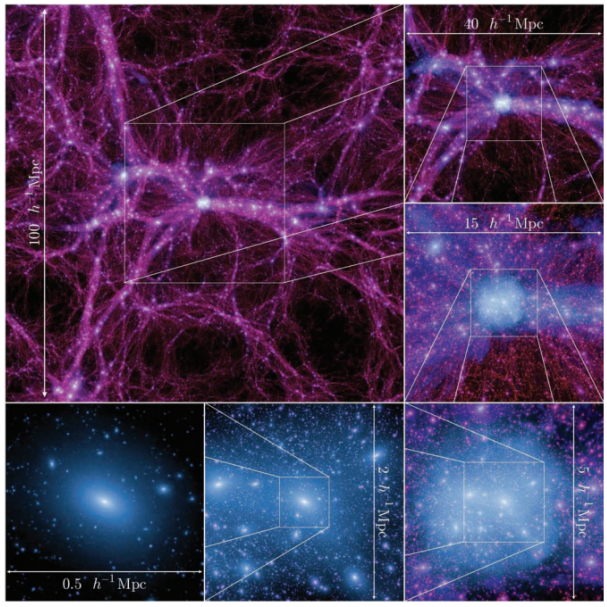

(a)

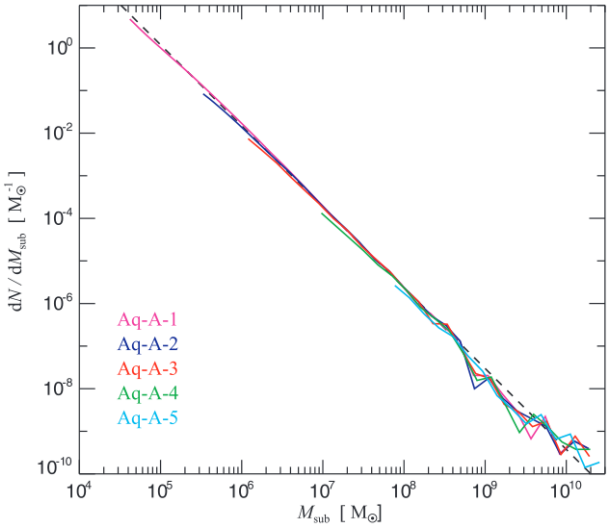

(b)

Figure 1.1: **(a):** A zoom-in into the Millenium II simulation showing the hierarchical DM structure of the Universe. The different panels show structures in different spatial scales, with the corresponding scales shown in each panel. Each bright clump corresponds to a DM halo of a galaxy. The image is from Boylan-Kolchin et al. (2009) (their Figure 1). **(b):** The predicted differential subhalo abundance by mass (i.e. the number of subhalos per unit mass interval) in a halo of Milky Way-size galaxy within 433.5 kpc from the galactic center. The plot is from Springel et al. (2008) (their Figure 6), where they present high resolution cosmological simulations of the halo merging processes ending correspond to different resolutions in the simulations.

In this formalism, the Poisson equation,

$$\nabla \cdot \mathbf{g} = -4\pi G\rho \tag{1.1}$$

which relates the gravitation acceleration, $\mathbf{g}$, caused by a density distribution, ρ , can be written in form

$$\nabla \cdot (\mu(g/a_0)\mathbf{g}) = -4\pi G\rho, \tag{1.2}$$

where a_0 is some characteristic acceleration (Milgrom 1989). MOND has been capable of explaining many discrepancies that have been noticed between the observations and the early theoretical predictions based on the ΛCDM (e.g. Kroupa et al. 2005, Kroupa et al. 2012, Famaey & McGaugh 2012). However, as the ΛCDM-based simulations have become more accurate by improving resolution and taking into account more baryonic physics, these discrepancies have proven to be mostly artificial (see e.g. Verbeke et al. 2017, Navarro et al. 2017). As the previous work of galaxy evolution has been mostly done based on the ΛCDM paradigm, and it is thus better tested and studied, this thesis is based on the ΛCDM paradigm.

In this thesis, I concentrate on the evolution of low-mass galaxies. Regardless of their low mass, they constitute an important part of the luminous Universe by being the most abundant type of the galaxies (Ferguson & Binggeli 1994). To illustrate this, in Fig. 1.1b, I show the sub-halo abundance of a present day Milky Way-sized galaxy, as found by Springel et al. (2008) as an end product of a cosmological simulation. The number density of dark matter sub-halos increases towards the low-mass end of the mass spectrum. Thus, understanding the evolution of the dwarf galaxies living in those low-mass DM haloes is an essential part in building our knowledge of the whole Universe.

1.2 CLASSIFICATION OF DWARF GALAXIES

Dwarf galaxy is a common name for a galaxy that has total absolute B-band magnitude $M_B >$ -18 mag (e.g. Boselli et al. 2008). This limit is a historical convention rather than a physical limit and some other conventions also exist, e.g. Ferguson & Binggeli (1994) use $M_B >$ -16 mag. There are many stellar systems such as small star clusters that also pass this condition, but they are not generally considered as galaxies (see Fig. 1.2) since they do not posses dark matter haloes. Despite their low total luminosity, dwarf galaxies show a broad scale of different shapes and appearances, and thus describing them accurately requires a classification system.

There are several ways of classifying dwarf galaxies depending on the research interest: they can be classified based on their appearance (morphology), or by some parameter describing their structure or constitution, e.g. the surface brightness. Like larger galaxies, dwarfs can also be divided into quiescent, i.e. gas-poor early-type dwarfs, and star-forming, gas-rich late-type dwarfs (see Fig. 1.3). Some galaxies that have properties between these two classes are called transitional types. Since verifying the existence of gas in a galaxy requires specific observations, which are not always available, the division between the early- and

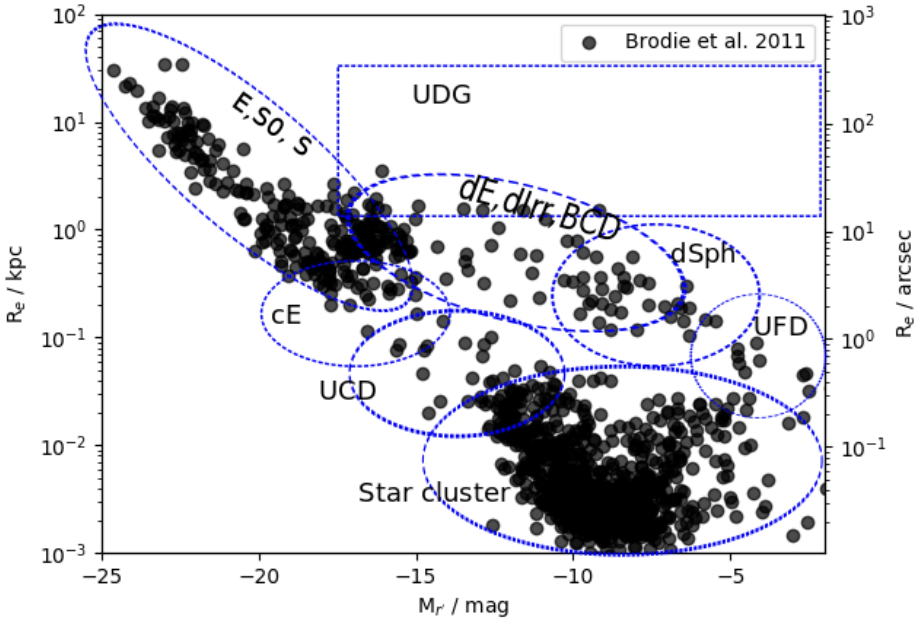

Figure 1.2: Galaxy classification scheme based on their effective radius R_e and absolute r'-band magnitude $M_{r'}$. The galaxy compilation of Brodie et al. (2011) is plotted with black points. The left y-axis shows the sizes in kilo parsecs and the right axis the angular sizes when shifted to the distance of the Fornax cluster. The labels correspond to the morphological galaxy classes that appear within the ellipses. The definitions and explanations of the morphological classes are given in the Section 1.2.

late-type systems is often made using the galaxy colors and graininess (internal clumpiness) of the stellar component. The dwarfs can further be divided into several sub-classes within the late- and early-types based on their morphology, size and luminosity (see Fig. 1.2). Most of these groups are also physically motivated due to the different formation mechanisms of these galaxies (see Section 1.3.5).

A classification system based on the luminosity and the Hubble type (late-type vs. early-type, Hubble 1926) of the galaxies is made by Sandage & Binggeli (1984) (see Fig. 1.4a), who classified early-type dwarfs as dEs based on their low luminosity and smooth spherical appearance, and as dS0s that differ from dEs by consisting of two components, a disk and a smooth spheroidal component. Additional sub-groups have been added afterwards. For example, Lisker et al. (2007) use dE(di) to refer to dwarf ellipticals that have faint spiral arms in their disks and dE(bc) for dwarfs with a blue center, i.e. a positive color gradient.

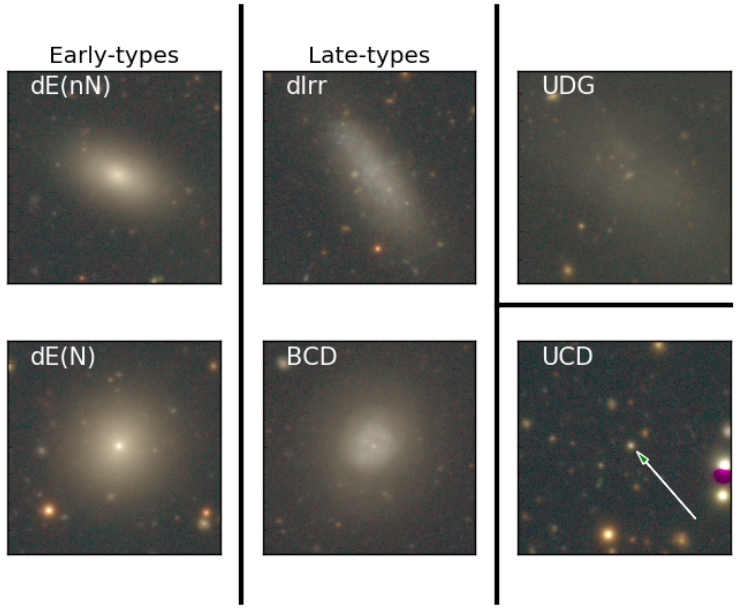

Figure 1.3: Prototypes of different morphological types of dwarf galaxies in the Fornax cluster. The different morphological types are explained in Section 1.2. The size (80"×80") and contrast is the same in all images, and the color images are combined from the i', r', and g'-band images of the Fornax Deep Survey.

dE(N) and dE(nN) are used to refer to dwarf ellipticals that have, or do not have a nuclear star cluster in their center, respectively.

Correspondingly, the late-type dwarfs can be divided into sub-groups based on their morphology. In the de Vaucouleurs' (de Vaucouleurs 1959) extension to Hubble's classification system, that also Sandage & Binggeli (1984) adopted, Sm and Im are the most late-type and low luminosity disk galaxies (see Fig. 1.4a). They show no bulge and have clumpy irregular appearance. These two types are often called together as dIrrs. Blue compact dwarfs (BCD) have also low luminosities, but the star formation is concentrated to the very central area of the galaxy (Sandage & Binggeli 1984), contrary to dIrrs where stars are forming in a more extended area. When BCDs are investigated with deep observations they typically appear as dEs in their outer parts, i.e. having smooth non star-forming outskirts, and as dIrrs in their inner parts (Noeske et al. 2003, Micheva et al. 2013, Janowiecki & Salzer 2014).

Another way to arrange the morphological classes is the revised parallel-sequence morphological classification (van den Bergh 1976, see Fig. 1.4b). This naming convention comes from an idea to revise the classical Hubble's naming scheme (Hubble 1926) and arrange it to a more physically motivated form. The difference to the Hubble tuning fork is, that in the revised parallel-sequence, the

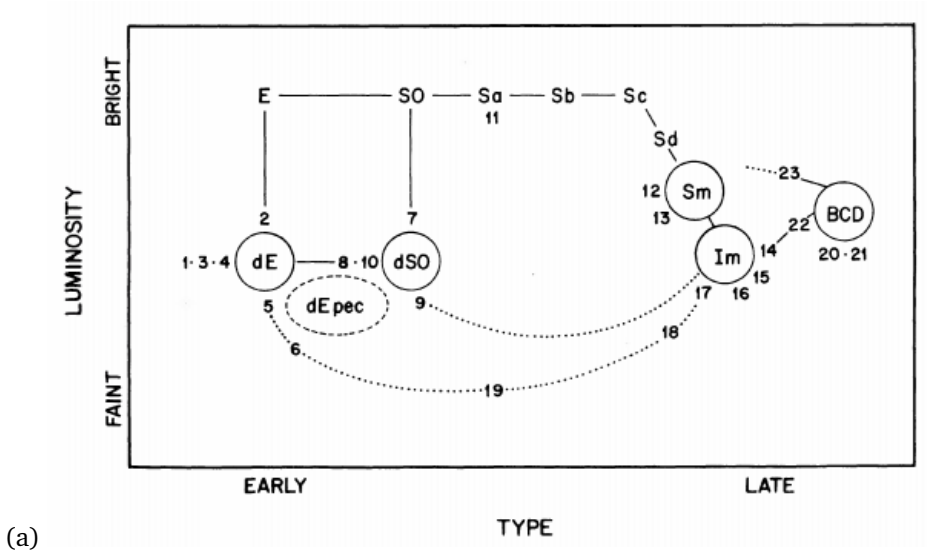

(a)

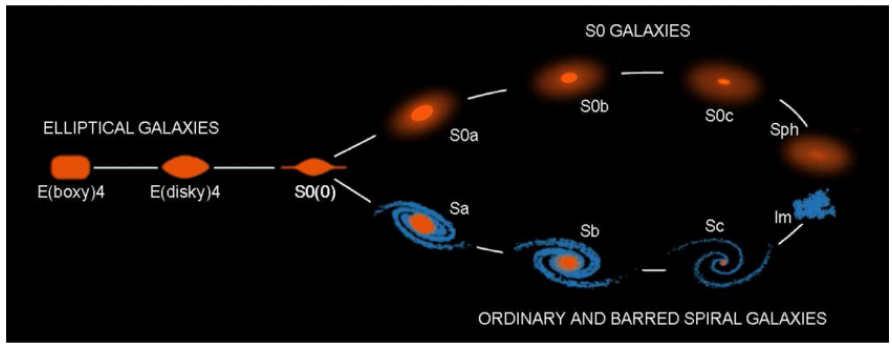

(b)

Figure 1.4: **a)** The classification system of Sandage & Binggeli (1984) (their Figure 1) showing the different morphological types in the luminosity-morphological type plane. **b)** The revised parallel sequence morphological classification scheme. The image is taken from Kormendy & Bender (2012) (their Figure 1).

disk galaxies are divided into two parallel sequences based on their star formation, i.e. the gas-rich spirals and the gas-poor S0s. van den Bergh (1976) suggested that the left-to-right axis of the fork represents the sequence of increasing angular momentum of the galaxies, and the two sequences for the disk galaxies divide the galaxies based on their gas richness, the idea being that a gas-rich spiral can transform into a S0 if it loses its gas. Kinematic evidence for this classification was later provided by Cappellari et al. (2011), and based on structural decompositions by Laurikainen et al. (2010). They showed that, indeed both S0s and spirals can be arranged into similar sequences based on their bulge-to-total flux ratios.

This parallel sequence was extended with dwarf galaxies by Kormendy & Bender (2012). They added the bulgeless gas-poor dwarfs called as spheroidals (Sph), and the bulgeless late-types, called as irregulars (Im, see Fig. 1.4b). In this system, Ims are positioned into the very end of the star-forming sequence, Sa-Sb-Sc-Sd-Im, arranged by decreasing bulge-to-total flux fraction. Correspondingly, Sphs are positioned into the end of the S0-sequence, S0a-S0b-S0c-S0d-Sph. This idea is also supported by the structural scaling relations where the elliptical galaxies and the disk galaxy central bulges form one sequence, and the galaxy disks form another, in which also Sphs and Irrs are located (Kormendy & Bender 2012). According to Kormendy & Bender (2012) most dEs and dSOs particularly in the Virgo cluster are Sphs, although some "true dwarf ellipticals" also exist. The "true dEs", like M 32 extend the fundamental plane correlations of the bright galaxies.

Dwarf galaxies are also named by their structural parameters. The dwarf galaxy groups that are usually defined by their sizes and surface brightness, are the most extended and the most compact dwarfs. Low surface brightness (LSB) dwarfs are generally considered as dwarfs that have B-band central surface brightness $\mu_{0,B}$ > 23 mag arcssec^{-2} (Impey & Bothun 1997), whereas a sub-group of LSBs called as Ultra Diffuse Galaxies (UDG, van Dokkum et al. 2016) are limited to galaxies which in addition have effective radii $R_e > 1.5$ kpc. The LSB dwarfs are typically early-type galaxies (Koda et al. 2015), but there is a growing evidence showing that this tendency is only resulting from a bias of LSB surveys concentrating to galaxy clusters (see e.g. Leisman et al. 2017). The most compact dwarf galaxies, named as Ultra Compact Dwarfs (UCD, Hilker et al. 1999, Drinkwater et al. 2000) are dwarf galaxies with R_e=10-50 pc, with sizes similar to star clusters. There is some evidence of these galaxies being a mixed group of massive star clusters and stripped dE nuclei (Mieske et al. 2002, Hilker 2017, Goodman & Bekki 2018).

Finally, the Tidal Dwarf Galaxies (TDGs) are a group of dwarfs that form from the tidal debris detached from larger galaxies during tidal interactions (Mirabel et al. 1992, van der Hulst 1979, Elmegreen et al. 1993). These galaxies are typically identified as large mass concentrations in the tidal tails of large galaxies (Duc et al. 2007,), and can be difficult to distinguish from other types of dwarfs after they get detached from their parent galaxies. After detaching, TDGs should differ from other dwarfs only by having a very low mass dark matter halo. So far, there are no known dwarfs identified with certainty as detached and virialized TDG.

Throughout this thesis we use the subdivisions defined in Fig. 1.2, with an additional division of dwarf ellipticals into nucleated, dE(N), and non-nucleated, dE(nN), ones. By this naming, we are not suggesting that dEs are miniature version of Es, but rather use dE as a synonym of early-type dwarf, thus just referring to their red and smooth appearance.

1.3 OBSERVATIONAL FRAMEWORK OF DWARFS

1.3.1 Local Group

A natural start for the investigations of the dwarf galaxies was the Local Group (LG), where the largest nearby dwarfs, the Large Magellanic Cloud (LMC) and the Small Magellanic Cloud (SMC), can be seen even with the naked eye from the ground. Several other LG dwarfs were identified very early on, and by 1971 there were 14 known local group dwarf galaxies (see the review of Hodge 1971). It was noticed that these smaller galaxies were significantly more abundant than the large galaxies, and that they appear both as star-forming and quiescent analogues to the giant galaxies (see Fig. 1.5a). Also, it was clear that their surface brightness is lower than that of the giant galaxies, which suggested that many more of them were yet to be found.

Nowadays, more than 130 dwarf galaxies have been identified in the LG (see McConnachie 2012 and the updated Table 1 in Nearby Dwarf Database[1]). Most of these galaxies are quiescent low-luminosity and low-surface brightness dwarf spheroidal galaxies, but also some star-forming dwarfs exist, mostly in the outer parts of the LG. There are also a few nucleated dwarfs in the LG, e.g. NGC 205 and M32. The LG dwarfs span a large range in the luminosity, from the LMC with M_V = -18 mag to the faintest dwarfs in the LG, called Ultra Faint Dwarfs (UFD), that have absolute magnitudes M_V = -1 – -5 mag (McConnachie 2012). UFDs are very similar to star clusters by their stellar masses and also by their effective radii, which makes the interpretation of the nature of these objects difficult. Galaxies as faint as these can nowadays be detected only within few Mpc from the Milky Way (MW), where the galaxies can be resolved to individual stars. When moving outwards from the LG, apparent luminosities of the stars of the galaxies become fainter, and also their surface brightness becomes too low to be detected. Analyses of the resolved stellar populations of the LG dwarf galaxies show that these galaxies have a large range of different star formation histories (Weisz et al. 2014, Salaris et al. 2013, Savino et al. 2015) and that they become extremely dark matter dominated towards lower stellar masses (Wolf et al. 2010).

1.3.2 Galaxy clusters

In the 1980's, systematic studies of the bright dwarf galaxies extended also to nearby clusters like the Virgo (Binggeli et al. 1984), Fornax (Ferguson 1989), and Coma (Godwin et al. 1983) clusters. The works concentrating on galaxies of these

[1] www.astro.uvic.ca/~alan/Nearby_Dwarf_Database_files/table1_SEPT2015.pdf

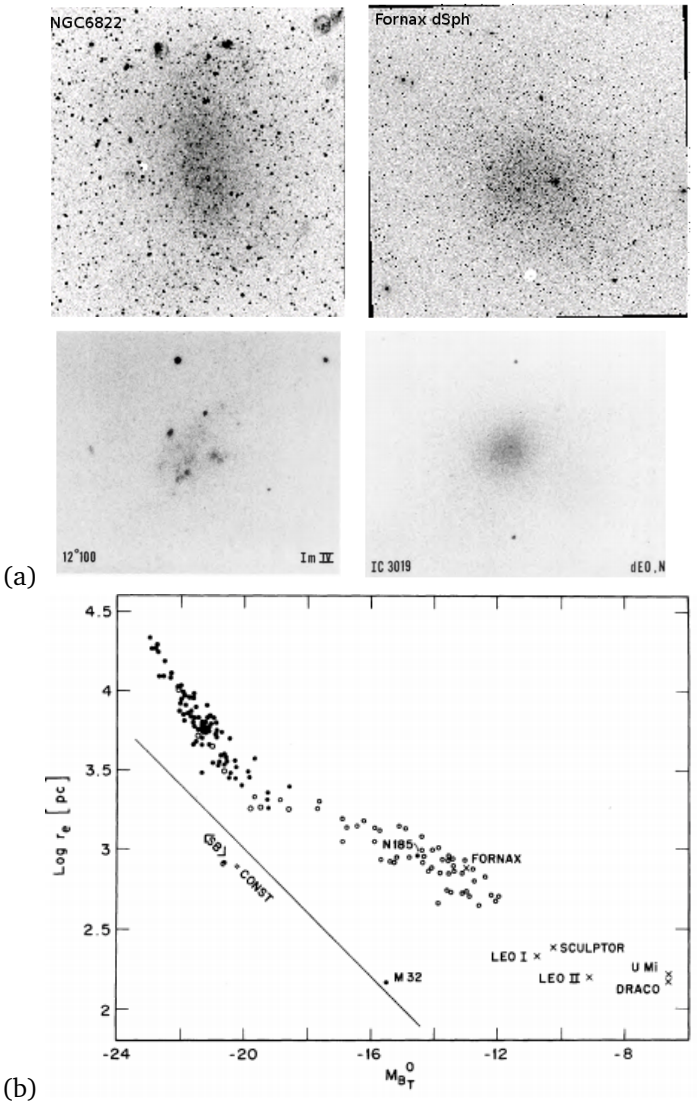

Figure 1.5: a) Examples of the early observations of the dwarf galaxies. The left panels show examples of late-type dwarfs and the right panels show early-type dwarfs. The upper panels show images of resolved LG dwarfs from the Digitized Sky Survey (DSS, *left panel:* image from DSS1 using red filter, *right panel:* image from DSS2 using blue filter), and the lower panels show Virgo cluster dwarfs from Sandage & Binggeli (1984) (their Figure 2). **b)** The size-magnitude diagram from Binggeli et al. (1984) (their Figure 7). The solid black symbols show a compilation of elliptical galaxies as a reference, the open circles show dEs from the Virgo cluster, and the crosses show the LG dwarfs.

more massive and distant clusters increased significantly the number of known dwarf galaxies. For example, the Virgo Cluster Catalog (Binggeli et al. 1984) and the Fornax Cluster Catalog (Ferguson 1989) include 1,842 and 313 dwarf galaxies, respectively, with the absolute total magnitudes $M_B <$ -12 mag. Due to the large distances to these clusters[2], the observations of the dwarfs in them are typically not resolved into stars (see Fig. 1.5a), which makes their analysis different from their nearby counterparts. The large distances of the clusters also limited the early studies of the cluster dwarfs to brighter luminosities than in the LG (see the magnitude gap between the Virgo and LG dwarfs in Fig. 1.5b). However, nowadays the new imaging surveys like the Next Generation Virgo Survey (NGVS, Ferrarese et al. 2012) are pushing down those luminosity limits. The advantage of studying the cluster dwarfs is that the sample sizes are much larger than in the LG, and thus these samples (Binggeli et al. 1984, Venhola et al. 2018, Hoyos et al. 2011) allows us to make statistical analysis of the morphological and structural differences of the dwarfs in different environments.

For the cluster dwarfs it is difficult to obtain their distances with spectroscopic observations, and therefore the cluster-memberships are often deduced using the fact that the density of the galaxies is much larger than in the field, so that most galaxies are more or less at the same distance. This allows to use the known relations between the galaxy luminosity, colors and structure, for identifying the galaxies belonging to the cluster. As in galaxy cluster, there are hundreds of galaxies at a similar distance, they form continuous locii in the relations between their photometric parameters, whereas the background galaxies appear as outliers. Especially the color-magnitude and surface-brightness luminosity functions are useful: follow-ups of such studies have showed that it is possible to obtain ≈90% purity for the sample memberships (Mieske et al. 2007). However, in order to be sure about the membership spectroscopic redshifts or surface brightness fluctuation analysis is required. Obtaining the spectroscopic memberships is not only important for removing the background objects, but also for finding galaxies that are outliers from typical scaling relations. For example, UCDs were discovered in the Fornax cluster on the basis of a blind spectroscopic survey (Drinkwater et al. 2000). However, due to their very compact morphology and high surface brightness, they would not have been considered as cluster objects if the cluster-memberships were deduced from the photometric scaling relations.

The dwarf galaxy populations in clusters have appeared to be mostly dominated by reddish and featureless dEs. However, also dIrrs and BCDs are found in the outer parts of clusters, although they become increasingly rare towards the dense inner regions of the clusters (Venhola et al., 2019). In spite of the fact that the cluster galaxies are dominated by early-types, the dwarf population is far from being homogeneous. Within dEs there are dE(N) that are rounder and on average located in denser environment in the cluster than dE(nN)s (Lisker et al. 2007). Even less centrally concentrated are dE(bc) and dE(di). The relative fractions of these different dE sub-classes seem to depend on the type of cluster. For example, in the very sparse Ursa Major cluster, 16 out of the 23 dEs (16/23=70%) have

[2]The Virgo and Fornax clusters are at the distances of 16.5 Mpc and 20.0 Mpc, respectively (Blakeslee et al. 2009).

blue centers (Pak et al. 2014), whereas in the Virgo cluster the corresponding fraction is only 23/476=5% (Lisker et al. 2006). UCDs are located at very short cluster-centric distances, and they tend to be even deeper in the potential well of the cluster than dE(N)s (Gregg et al. 2009). The differences between the morphologies of the dwarf galaxy populations inside the clusters and in less massive groups, and the different distributions of the various types of dwarfs within the clusters, seem to suggest that the galaxy environment is an important factor in the evolution of the galaxy.

1.3.3 Low density environments

The dwarf population outside dense clusters has been also studied extensively during the last 60 years. dIrrs that mostly exist outside clusters, are long known to be the most numerous types of star-forming galaxies (Zwicky 1957, de Vaucouleurs 1959, van den Bergh 1959). Hodge (1971) compared the properties of the early- and late-type dwarfs and showed that unlike dEs in the LG, dIrrs are gas-rich, contain interstellar dust and show a lot of ongoing star formation in blue star-forming clumps. As dIrrs are typically located in low -density environments, deducing their distances using scaling relations is difficult. However, dwarf galaxies in the field are mostly gas-rich which means that the gas velocity can be used to deduce their distances. Like larger late-type galaxies, also dwarf galaxies have most of their gas in the form of neutral hydrogen (H_I), which emits radiation at the wavelength of 21 cm. Large H_I-surveys like the Arecibo Legacy Fast ALFA survey (ALFALFA, Haynes et al. 2011) have provided thousands of redshifts and H_I line widths for gas-rich dwarf galaxies. The analysis done using resolved H_I rotation curves of the late-type dwarfs have shown that they are increasingly dark matter dominated towards the low-mass end (Navia 2018). They also follow the baryonic Tully-Fisher relation (Tully & Fisher 1977, Verheijen 2001, Ponomareva et al. 2017) down to 10^8 $M_\odot$ (Lelli et al. 2016), thus being in the same kinematic family as the rotationally supported late-type disks. Below that mass limit the maximum rotation velocity of late-type dwarfs starts to deviate from the linear Tully-Fisher relation (Navia 2018).

Morphologically the field dwarfs are typically dIrrs, or BCDs. They can also have bars and other substructures in their disks (Buta et al. 2015, Herrera-Endoqui et al. 2015, Díaz-García et al. 2016). The lower mass late-type dwarfs become increasingly irregular and do not typically have distinguishable structures. Some early-type dwarfs also exist in the field, but they only exist among the highest mass dwarfs ($M_* > 10^9$ $M_\odot$ (Geha et al. 2012).

1.3.4 Low surface brightness dwarfs

As the observational instruments become increasingly more sensitive for detecting the Low Surface Brightness (LSB) galaxies, new galaxies are expected to be found (Mihos et al. 2018, Torrealba et al. 2018). Yet we do not know what is the lowest surface brightness that the galaxies can have. Binggeli et al. (1985) found that there exists large (R_e = several kpc) low surface brightness galaxies in the Virgo

cluster that are dwarfs by their luminosity but have large effective radii of the order of a few kpcs. Later, Lauberts & Valentijn (1989) pointed out how many large surveys miss a significant amount of these LSB galaxies. The LSB galaxies were later studied systematically in the Fornax cluster by Bothun et al. (1991) and Davies et al. (1990). They were able to show that these galaxies indeed are numerous in galaxy clusters and that they are mostly early-type systems. Large late-type LSBs were also found from the field (Romanishin et al. 1983, Impey & Bothun 1989, Bothun et al. 1985), but they were mostly of larger total luminosity than those found in the clusters. Later the interest to the most extended dwarf LSB galaxies were reignited by Conselice et al. (2003), and van Dokkum et al. (2015) who named these galaxies as Ultra Diffuse Galaxies (UDGs). UDGs have now been extensively searched for in nearby clusters (van der Burg et al. 2016,Mancera Piña et al. 2018), galaxy groups (van der Burg et al. 2017, Román & Trujillo 2017) and in the field (Leisman et al. 2017, Greco et al. 2018). The observations suggest that they are abundant in all these environments. The UDGs have been shown to share many properties with the less extended dwarfs of the same mass. For example, UDGs exist both as late- and early-types, the early-types being the dominant population in high-density environments (Greco et al. 2018). They also have similar colors, cluster-centric spatial and axis-ratio distributions as the less extended dwarf galaxies of the same luminosity (Koda et al. 2015, Mancera Pina et al., *private communication*). It is not yet clear whether UDG is simply a superfluous name for the most extended normal dwarf galaxies, or whether if they actually form differently (see Conselice 2018). Some individual UDGs that have been studied more extensively suggest that UDGs might have a different origin compared to the smaller dwarfs (van Dokkum et al. 2018). For example, one UDG, DF2, may have a very low mass-to-light ratio for its stellar mass and very bright globular cluster population (van Dokkum et al. 2018, but see Trujillo et al. 2018), and DF17 has a large number of globular clusters for its stellar mass (Peng & Lim 2016).

1.3.5 Spectroscopic approach

Kinematics of dwarf galaxies has been studied using slit spectroscopy, H_I rotation curves, and Integral Field Unit (IFU)-spectroscopy. Recently also GAIA has opened an unprecedented kinematic view of the MW satellite dwarfs by providing proper motions and distances of individual stars in these systems (Gaia Collaboration et al. 2018). As mentioned above, late-type dwarfs are mostly rotationally supported systems with extended H_I-gas disks. dSphs in the LG have shown to be either rotationally or pressure supported systems (see Kormendy & Freeman 2016, Wolf et al. 2010). dEs in the nearby clusters have a range of kinematics from rotationally supported systems to mostly pressure supported ones (see e.g. Toloba et al. 2011, Toloba et al. 2015). Toloba et al. (2015) showed that the fast rotator dEs are mostly located in the outer parts, and the slow rotators in the inner parts of the Virgo cluster. They showed also that the fast rotators are typically morphologically of dE(di) type, and that the fraction of the fast rotators increases with decreasing

galaxy surface brightness. Some of the dEs also show kinematically decoupled cores.

The stellar populations of the LG dwarf galaxies can be studied by fitting the stellar color-magnitude diagram with weighted stellar population isochrones (Salaris et al. 2013; Weisz et al. 2014). For the more distant unresolved dwarfs, their stellar populations need to be obtained via spectral energy distribution (SED) fitting (Mentz et al. 2016). Both methods give qualitatively similar results: late-type dwarfs and early-type dwarfs can both have a range of different star-formation histories, involving initial star-burst when the first stars of these galaxies were formed and either bursty or more stable star-formation afterwards (Weisz et al. 2014, Koleva et al. 2009). A significant difference between the early- and late-type dwarfs is their recent star-formation history (Weisz et al. 2014): E.g. NGC 205 that appears morphologically as dE stopped forming stars only 10^8 yrs ago (Butler & Martínez-Delgado 2005), indicating that the morphological transformation can happen in a short time-scale.

1.4 EVOLUTION OF DWARF GALAXIES IN DENSE ENVIRONMENTS

The evolution of dwarf galaxies is driven both by internal and external processes. After a galaxy forms its first stars its fate will highly depend on the environment where it is located. If it is located in an isolated part of the Universe it may spend its entire history slowly forming stars and growing in stellar mass. On the other hand, if the galaxy is located in a more crowded environment like in a galaxy group or cluster, its star formation will likely be affected by tidal and gas interactions, as well as interactions with the cluster potential well. The galaxy may eventually end up merging with a larger or similar sized galaxy, or to change morphologically via various stripping processes, in which gas, dark metter, and stars are stripped.

One of the first systematic evidence of the environmental processes acting on galaxies was obtained by Dressler (1980), who studied the morphology of galaxies in galaxy clusters. He found that the fraction of early-type galaxies from the total galaxy population is increased in dense galaxy environments, which trend is called as morphology-density relation. Later this relation was shown to be even stronger among the dwarf galaxies (Binggeli et al. 1990). Also within the dense environments, where the majority of the dwarfs are dEs, the morphology of those dwarfs is dependent of the local galaxy density (Lisker et al. 2007). These observations clearly showed the importance of the environment on galaxy evolution. Nowadays, many steps have been taken in building of our understanding of the different environmental processes, but the details of the dwarf galaxy evolution are still not fully understood. In the following sections I summarize the most important environmental effects related to dwarf galaxies and the corresponding observations.

1.4.1 Tidal interactions and harassment

Galaxies interact with each other gravitationally, which increases their internal kinetic energy, leading to stripping of material from the galaxy outskirts, to transform the galaxy morphology from late to early-type, or ultimately leading even to disruption or merging of the colliding galaxies. These interactions can also cause instabilities in the gas and/or stellar disks of the dwarfs (Fujita 1998), which then lead to star-bursts and can induce bars and spiral arms. The gravitational interactions can be divided into galaxy-galaxy tidal interactions, when the relative velocities of the encountering galaxies are small, harassment, which is a term used for the high-speed interactions[3] between galaxies, and the interaction with the cluster potential.

Galaxy-galaxy tidal interactions have been studied extensively since Toomre & Toomre (1972), who showed how these interactions may induce tidal arms and bridges into the interacting galaxies and strip material from them. As the strength of the tidal interactions is approximately $\propto M/(vP)$ (Aguilar & White 1985), where M is mass of the perturber, v is the relative velocity and P is the impact parameter, galaxy-galaxy interactions are mostly important in cases where the relative distances and velocities of the encountering galaxies are small. In galaxy clusters the relative velocities of the galaxies are of the order of hundreds of km s^{-1}, which makes individual galaxy-galaxy interactions weaker than in less dense environments, where the relative velocities are typically an order of tens of km s^{-1}.

The most dramatic interactions for dwarfs are the ones with larger galaxies. In fact, interactions between dwarf galaxies are not yet much studied. However, the catalog of interacting dwarf galaxies by Paudel et al. (2018) is an example of such catalogs. More than 98% of the galaxies in this catalog are star forming field galaxies, supporting the above mentioned idea that galaxy-galaxy interactions are more important in the field and in galaxy groups.

Interactions between massive galaxies can also be important in forming dwarf galaxies: In interactions of grand spirals, huge tidal tails can be formed, which may become gravitationally unbound from the parent galaxies. These detached tails, or some clumpy parts of them, may then contract into new separate galaxies. Such TDGs have been proposed to form from the tidal debris in galaxy simulations (Barnes & Hernquist 1992), and have also been observed in nearby galaxies (see Mirabel et al. 1992, van der Hulst 1979, Hunsberger et al. 1996, Lelli et al. 2015). The importance of the tidal dwarfs in the total dwarf galaxy population is not yet known, but it is likely to be more important in low density environments where the grand tidal tails form.

In galaxy clusters, harassment may transform late-type disks into rounder early-type galaxies (Moore et al. 1996, Mastropietro et al. 2005). A high-velocity encounter between two galaxies transforms some orbital energy of the galaxies into their internal energy, which heats the galaxies. If this heating is strong enough it may also strip material from the outer parts of the galaxies (Smith et al. 2015)

[3]Encounters in which the relative velocities of the galaxies are larger than the internal stellar velocities of the galaxies are considered as high-speed interactions.

and during the subsequent relaxation after the stripping, the galaxy becomes more dense in its central parts (Binney & Tremaine 2008). This contraction of the effective radii due to harassment is demonstrated in Fig. 1.6a that shows the amount of contraction for simulated galaxies with different orbits in the cluster. Using N-body simulations Mastropietro et al. (2005) showed how harassment can transform dynamically cold disk galaxies into dynamically hot and dense spheroids in the cluster environment. Naively, one could think that this process could straightforwardly explain the different galaxy populations in the field and cluster environments. However, later Smith et al. (2015) showed, using an extensive set of orbital parameters, that harassment is only efficient in stripping material in orbits whose pericenters are very close to the cluster center. Figure 1.6b shows the stripped mass fractions for the different galaxy components for a set of simulated galaxy orbits from Smith et al. (2015). However, there are many observations that support the importance of harassment. For example, Janz et al. (2016) showed that the sizes of the field late-type dwarfs are two times larger than the dwarf galaxies of the same mass located in the Virgo cluster, which suggests stripping of the outer disks in the cluster. Also kinematic evidence for harassment has been observed both in the Virgo (Toloba et al. 2015) and Fornax clusters (PhD thesis of J. Mentz, Univ. of Groningen), as the ratio v/σ of the dwarf galaxies decreases towards the centers of the clusters. The current theory of the formation of UCDs is also consistent with the idea that harassment might be significant in galaxy clusters.

Another, even more drastic consequence of harassment/galaxy-galaxy tidal interactions is the disruption of the dwarf galaxies, which might happen in the centers of galaxy clusters (Koch et al. 2012, McGlynn 1990). These disrupted galaxies then end up into the intra-cluster medium, piling up into the central parts, and leaving an underdense core to the galaxy number density profile of the cluster. Several studies support the idea that this disruption of galaxies takes place in the centers of the galaxy clusters, observed in cored galaxy number density distributions (e.g., Ferguson 1989) and as remnant nuclei of stripped dwarf galaxies (Drinkwater et al. 2003, Voggel et al. 2016, Wittmann et al. 2016)observed in the nearby galaxy clusters.

1.4.2 Gas stripping

Stripping of gas happens when the gas of a galaxy interacts with the hot intra-cluster gas, observed in X-ray. If the ram pressure of hot gas is larger than the anchoring force of the host galaxy, the gas from the galaxy gets stripped. The pressure experienced by the cold gas can be estimated by the formula: $P_{ram} = \rho_{ICM}\Delta v_{cl}^2$, where ρ_{ICM} (Gunn & Gott 1972) is the density of the intra-cluster matter and Δv_{cl} is the relative velocity of the galaxy with respect to the hot gas. This force thus increases towards the central parts of the cluster, where the density of the hot gas is high and where the velocities of the galaxies are the highest. The process where this pressure strips part or all the gas of a galaxy from its potential well is called ram pressure stripping (Boselli et al. 2008).

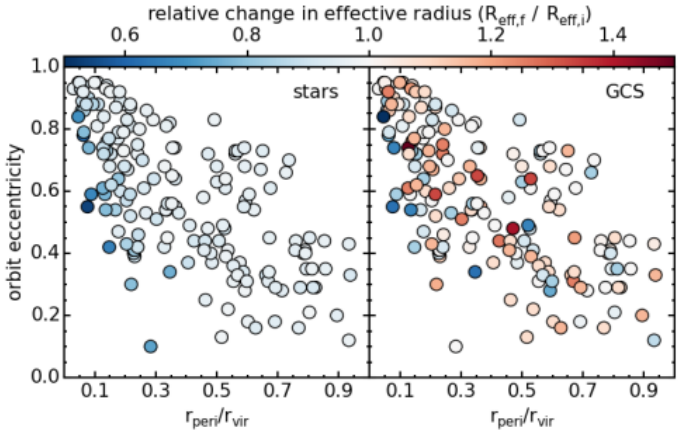

(a)

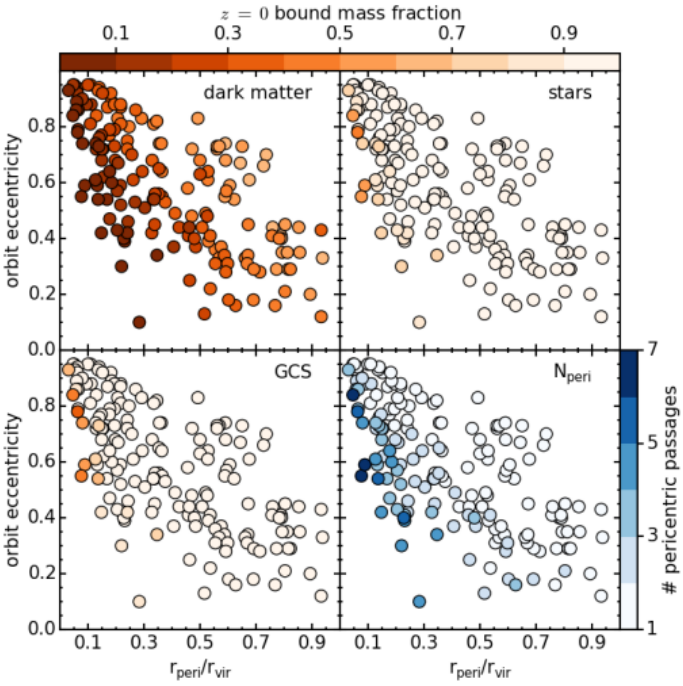

(b)

Figure 1.6: **(a):** The relative change in the effective radii of the stellar (*the left panel*) and globular cluster (*the right panel*) components of the galaxies on different orbits by Smith et al. (2015) (their Figure 6). The x-axis shows the pericenter distance normalized by the virial radius (r_{peri}/r_{vir}) and y-axis shows the eccentricity of the orbit. The galaxies were followed over 7 Gyr in the cluster. **(b):** Bound mass fraction in different components of the galaxy at z=0, after the galaxy has spent 7 Gyr in the cluster on the given orbit. The upper left and right panels show the bound mass-fractions for DM and stars, relatively, and the lower left for the globular clusters. The lower right panel shows the number of peri-center passages. The image is from Smith et al. (2015) (their Figure 2)

Both ram pressure stripping, that acts on the gas component of the galaxy, and harassment, that acts on its stars, are effective especially in the orbits going near the center of the cluster, but clear signs of ram pressure stripping have been also observed in much larger cluster-centric distances than where harassment is efficient (Jaffé et al. 2018). Fig. 1.7 shows a compilation of galaxies (Jaffé et al. 2018) that are experiencing ram-pressure stripping, using the cluster-centric radius normalized by the virial radius as x-axis (r_{cl}/R_{200}) and the line-of-sight velocity normalized with the velocity dispersion of the cluster as y-axis ($\Delta v_{cl}/\sigma_{cl}$). The figure shows that galaxies experiencing ram-pressure stripping are detected in the whole parameter space occupied by the cluster galaxies, indicating that this process it is not only limited to the short cluster-centric distances. In the orbits with close pericenters, all the gas of the galaxy may be depleted in a single crossing corresponding to a time scale less than half a Gyr (Lotz et al. 2018). There is strong observational evidence about the removal of gas from the galaxies when they enter the cluster environment. Namely the relative fraction of gas-poor galaxies of the total galaxy population have been shown to be higher in the clusters than in the field (Solanes et al. 2001, Serra et al. 2012). Ram pressure stripping is also observed in action in infalling galaxies using Hα- and UV-imaging (Poggianti et al. 2017, Jaffé et al. 2018, Boselli et al. 2018).

In spite of the fact that ram-pressure stripping does not directly affect the stars, it may still have some indirect effects on the stellar component of a galaxy. If a gas-rich galaxy suddenly loses all of its gas, this changes the gravitational potential of a galaxy in its central regions, which must lead to subsequent relaxation process. Also, if ram-pressure stripping is not efficient enough to strip the gas from the inner parts of a galaxy, where the anchoring force is strong, it may continue forming stars in the galaxy center. A direct consequence of this is that galaxies will increase their surface brightness in the center, and the center appears blue due to the new young stars. On the other hand, the outer parts of the galaxy will start to fade and become redder due to ageing of the stellar populations. This effect leaves an age and metallicity gradient to the stellar populations of the galaxy, which appears as a positive color gradient. Such blue cored dEs have been detected in the LG (Peletier 1993), in the Virgo cluster (Lisker et al. 2006, Urich et al. 2017), and in the Ursa Major system (Pak et al. 2014).

1.4.3 Evidence of quenching from the high-z cluster galaxy populations

First seeds of the Galaxy clusters form as large scale overdensities in the primordial Universe. During the cosmic time, they concentrate and grow in mass and size by accretion of individual galaxies and small groups of galaxies, or by merging with other galaxy clusters, thus forming a complex system of galaxies, star clusters and intra-cluster medium (Evrard 1990, Klypin & Shandarin 1983). The first proto-clusters have been identified at z=4–6 (Franck & McGaugh 2016, Lemaux et al. 2018), and they evolve at the same time as the galaxies within them, leading into a range of different cluster morphologies in the nearby Universe (Abell et al. 1989).

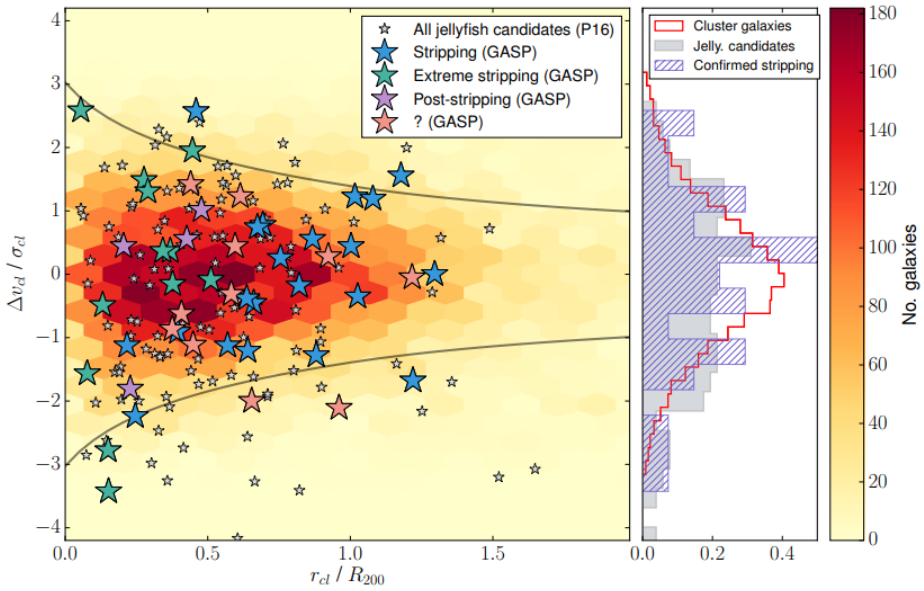

Figure 1.7: Distribution of the galaxies that have been observed being influenced by ongoing ram pressure stripping (star symbols) compared to the distribution of other cluster galaxies (density histogram). The x-axis shows the cluster-centric radius normalized with the virial radius (r_{cl}/R_{200}) and y-axis the line of sight velocity normalized by the velocity dispersion of the cluster ($\Delta v_{cl}/\sigma_{cl}$, Jaffé et al. 2018). The black lines show the caustics of the possibly virialized area within the cluster for the normalized distribution. The intensity of the stripping events increases from blue to green stars, respectively, and the purple stars correspond to objects that morphologically appear as post-stripping galaxies. The small yellow and large orange stars are galaxies with possible stripping events. Notable is that the tripping event happen even outside the virial radius of the cluster. The image is from Jaffé et al. (2018) (their Figure 7).

In galaxy clusters in the local Universe, early-type galaxies are more abundant than late-type galaxies (Dressler 1980). Therefore in the galaxy color-magnitude diagram we observe a prominent red locus called the red sequence (RS, see Fig. 1.8). The shape and location of the RS is defined by the stellar population ages and metallicities of the galaxies forming the sequence (Roediger et al. 2017, Janz & Lisker 2009, Janz et al. 2016). Clearly, these early-type galaxies must have been star-forming at some point of their life in order to grow in stellar mass, which implies that the RS must have been formed in clusters during a certain cosmic epoch. Indeed, Muzzin et al. (2013) showed that the contribution of the early-type galaxies to the stellar mass budget of the Universe grows much faster than the one of late-types during the redshifts z<3, indicating a transformation of

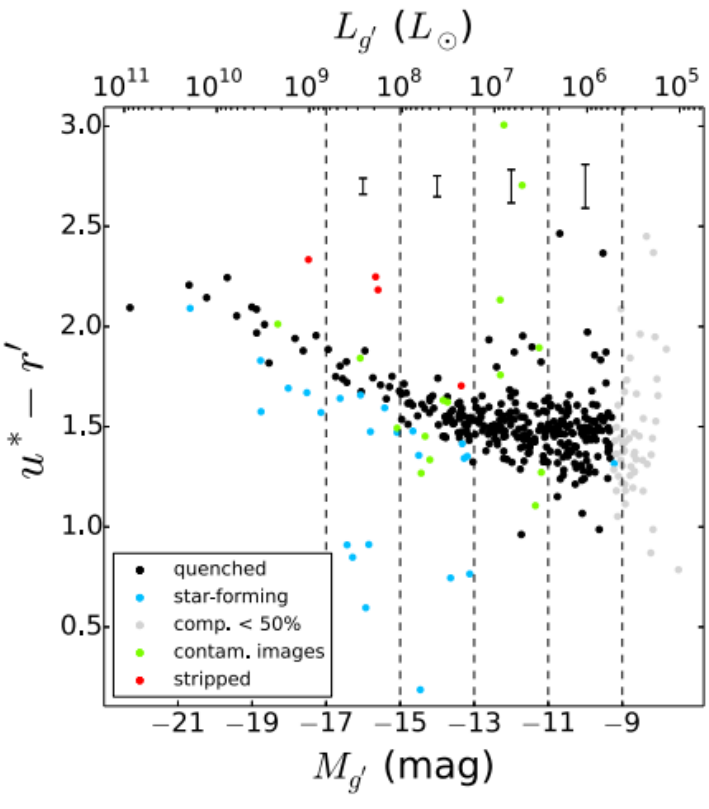

Figure 1.8: Color-magnitude diagram in the center of the Virgo cluster from Roediger et al. (2017) (their Figrue 1). Black and turquoise symbols, show the early- and late-type galaxies, respectively, and the red symbols show the galaxies that are likely gone through strong tidal stripping. The green and grey symbols indicate the galaxies whose measurements may be biased by their close companions, and the faint galaxies for which the detections are not complete, respectively. Notable in the diagram is the prominent locus consisting of the early-type dwarfs, which flattens at low luminosities.

late-types to early-types by quenching of star-formation. At z=3, the majority of the most massive cluster galaxies are still dusty star-forming systems with masses of $\approx 10^{11}$ $M_\odot$ (Marchesini et al. 2014, Marsan & Marchesini 2014, Martis et al. 2016). These massive galaxies get quenched between z=2.75–1.25 (Marchesini et al. 2014), and accumulate half of their present day mass by minor mergers after z<1. Other observations have also confirmed the increasing fraction of massive early-type galaxies in the clusters since z=1–2 up to present (Bell et al. 2004, Cassata et al. 2008, Mei et al. 2009).

Several works that have studied the RS in high-redshift clusters have found that the ratio of bright-to-faint galaxies is elevated up to z=0.8 compared to the values in the local Universe (e.g. Rudnick et al. 2009 and summary of Roediger et al. 2017). These observations suggest that the emergence of the faint end of the RS is a relatively recent phenomenon. In their review Boselli & Gavazzi (2014) summarize the growing observational evidence supporting the idea that most of the low-mass galaxies that enter into the cluster environment get quenched during their first 1 Gyr in the cluster via ram-pressure stripping. This idea has also support from galaxy simulations (Lotz et al. 2018, Jiang et al. 2018). In spite of the fact that the galaxy populations seem to be mostly consistent with the suggested ram-pressure stripping scenario, we need also to discuss the different morphological types of dwarf galaxies, and to evaluate whether also their properties can be explained by this scenario.

It has been known long that dEs and dIrrs have qualitatively similar structures in terms of luminosity and surface brightness (e.g. Binggeli 1994), which does not cause any tension with the proposed quenching scenario. However, it is also known that in the magnitude range of $M_r < -16$ mag early-type dwarfs start to be more centrally peaked compared to the late-type dwarfs of similar luminosity (Misgeld et al. 2009), which is incompatible with a straightforward transformation by gas-depletion. The fact that there are some dwarfs with blue centers in clusters (Lisker et al. 2006, Urich et al. 2017) indicates that star-formation in the galaxy centers has been quenched later than in the galaxy outskirts. This may solve the discrepancy between the stellar distribution profiles between the early- and late-type systems, since more stellar mass is accumulated to the center due to extended star-formation. However, the details of this process still need to be studied, in order to conclude whether the extended central star-formation alone is enough to explain the difference. It is obvious that cEs and UCDs cannot be explained only by gas-stripping, since their effective radii are an order of magnitude smaller and surface brightnesses an order of magnitude brighter than for the dIrrs. Also, an increasing fraction of slow-to-fast rotators towards denser galaxy environment (Toloba et al. 2015) suggests that also the stellar kinematics of the dwarfs have to be affected during their infall into the cluster. However, Koleva et al. (2014) shows that there might be some problems in that interpretation, as some BCDs show similar pressure supported kinematics as the dEs, which suggests that they do not necessary need to be heated by external processes.

To summarize, the high-redshift observations show that galaxy clusters start to form at z=4–6, and the quenching of the massive galaxies in them takes place between z=1–3. After z=1 the low-mass end of the RS starts to form. Most probably it is mainly happening via quenching by ram-pressure stripping, although there is clear evidence showing that also tidal interactions have affected the evolution of dwarf galaxies. As these studies are done for high- and mid-redshift clusters, where resolution and other issues may affect the photometry, it is interesting to compare whether the low mass galaxies in the nearby clusters have properties that are consistent with the above mentioned quenching mechanisms. Especially, it is interesting to study the properties of the lowest mass dwarfs that can only be now studied in the nearest galaxy clusters.

1.5 THE FORNAX CLUSTER

This thesis concentrates on the analysis of dwarf galaxies in the Fornax cluster. In the following I describe the Fornax cluster as an environment and summarize some of the important surveys and studies concentrating to this environment.

The Fornax cluster appears in the southern sky centered around the elliptical galaxy NGC 1399 with coordinates R.A. = 54.6209 deg and Dec. = -35.4507 deg (Watson et al. 2009). Its mean recession velocity is 1493$\pm$36 kms^{-1} (Drinkwater et al. 2001), and the mean distance calculated from surface brightness fluctuations of early-type galaxies is d= 20.0$\pm$0.3$\pm$1.4 Mpc (Blakeslee et al. 2009). The main cluster is very compact and consists of 22 galaxies brighter than M_B < -18 mag, and around 300 fainter galaxies (Ferguson 1989). The Fornax Cluster is part of the larger Fornax-Eridanus structure (see Nasonova et al. 2011) located in the Fornax-filament of the cosmic web. Fornax, having a virial mass of M = 7×10^{13} $M_\odot$ (Drinkwater et al. 2001), is the most massive mass concentration (see Fig. 3.1) in the filament. Other significant mass concentrations near the Fornax cluster are the groups around NGC 1316 (Fornax A), NGC 1407 and the Dorado group (see Fig. 3.1). The NGC 1316 group is currently falling into the main group (Drinkwater et al. 2001), whereas the other spectroscopically confirmed significant groups are located at least 15 deg ($\approx$ 5 Mpc) away from the Fornax cluster.

The Fornax cluster is an interesting environment to study, since it bridges the mass range of evolved groups to more massive clusters. For instance Trentham & Tully (2009) study dwarf galaxies in the group environments of which for example NGC 5846 group, with a mass of M = 8.4$\pm$2.0$\times10^{13}$ $M_\odot$, is more massive than the Fornax cluster. However, regardless of its low mass, many properties of the Fornax cluster, like its concentration, X-ray intensity and evolved galaxy population, makes it appropriate to call Fornax a cluster.

Due to its southern location the Fornax cluster is not covered by the Sloan Digital Sky Survey (SDSS, Alam et al. 2015). The most recent galaxy catalog covering the whole cluster is the Fornax Cluster Catalog (FCC) by Ferguson (1989). The catalog covers 40 deg^2 area centered onto the cluster, and it contains 2678 galaxies. Its given completeness limit in apparent B-magnitude is $m_B \approx 19$ mag, but it may vary due to visual identification of the galaxies. Ferguson classified galaxies into likely cluster galaxies and likely background galaxies, based on their morphology and surface brightness.

Another major effort for mapping the Fornax cluster galaxies, but with higher resolution was done by Jordán et al. (2007) using the Hubble Space Telescope. In their "Advanced Camera for Surveys Fornax Cluster Survey" (ACSFCS, Jordán et al. 2007), they targeted the brightest 43 galaxies using two different filters. Their spatial coverage is much smaller than the one of FCC, but the spatial resolution of the observations is superior. The core region of the cluster was also covered with deep observations by Hilker et al. (2003) and Mieske et al. (2007), who used the "Inamori-Magellan Areal Camera and Spectrograph" - instrument (IMACS, Dressler et al. 2011) attached to the 100-inch du Pont telescope, located at Las Campanas Observatory (Chile). Both observational surveys were performed in

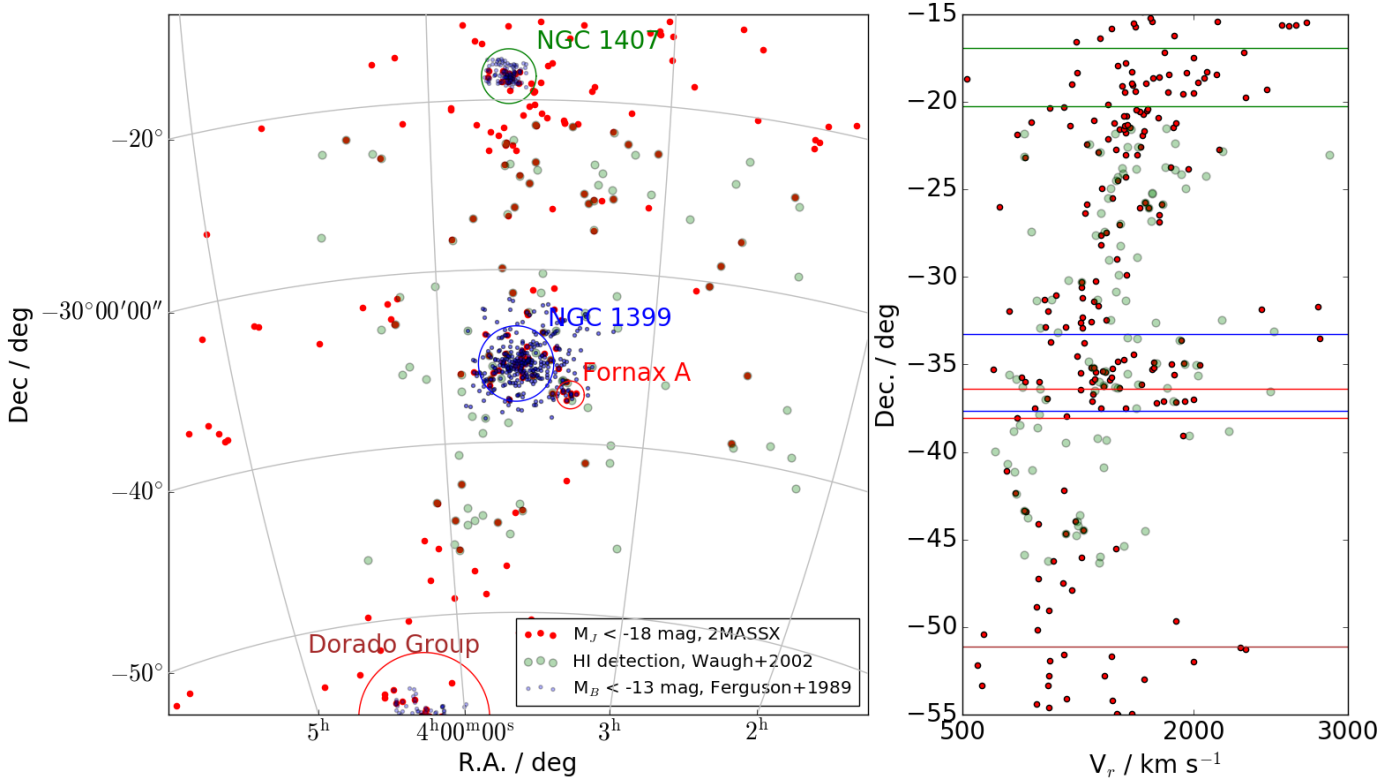

Figure 1.9: The large scale structure surrounding the Fornax cluster. The left panel shows galaxy right ascension and declination in International Celestial Reference System (ICRS) coordinates and the right panel shows the recession velocities of the galaxies as a function of declination. At the distance of the Fornax cluster 1 deg corresponds to 0.3 Mpc, whereas 1000 km/s velocity difference due to Hubble flow corresponds to 14 Mpc (to first order independent of the distance). The galaxies with recession velocities $V_r < 4000$ km s^{-1} in the 2 Micron All Sky Survey catalog (2MASSX, Huchra et al. 2012), are plotted with the red dots, and the galaxies with velocities $V_r < 4000$ km s^{-1} from Waugh et al. (2002) with the green circles. The FCC galaxies are shown with the blue dots. We also mark the virial radii of the most significant groups in the surroundings of the Fornax cluster with the large circles, and show their names with the corresponding colors. The locations of the circles of the left panel are indicated with the horizontal lines in the right panel using the corresponding colors. The figure is from Venhola et al. (2018)

V and I bands and they were able to obtain colors and structural parameters of the cluster dwarfs down to M_V = -9 mag. Another ongoing effort to image the Fornax cluster with modern instruments is the Next Generation Fornax Survey (NGFS, Muñoz et al. 2015, Eigenthaler et al. 2018) collaboration. The NGFS aims to cover 30 deg^2 area of the Fornax cluster, with similar observations as Fornax Deep Survey (FDS, see the next section for details), using the DECam instrument attached to 4-m telescope Blanco at Cerro Tololo Inter-American Observatory (CTIO) for the optical u', g', and i', bands, and using VISTA/VIRCAM (Sutherland et al. 2015) for the Ks-band.

A major effort for obtaining spectroscopic redshifts for the Fornax cluster galaxies was made by Drinkwater et al. (1999), who obtained spectroscopy for several hundreds of galaxies located in a $\approx$ 6 deg^2 area in the main cluster using the Two-degree Field (2dF) spectrograph attached to Anglo-Australian Telescope (AAT). However, only a few percent of the observed objects were cluster galaxies, since there was no morphological selection for the targets. Recently, the 2dF spectroscopic observations were extended by additional 8 deg^2 (private communication with Natasha Maddox), which more than doubles the available spectroscopic data. The spectroscopic data are limited to relatively high surface brightness objects (B-band central surface brightness $\mu_{0,B} < 23$ mag arcsec^{-2}), which unfortunately excludes most of the dwarf galaxies. Spectroscopic redshifts are also available for several tens of bright galaxies ($m_J < 14$ mag) in the Fornax cluster and in its surroundings, from the 2 Micron All-Sky Survey (2MASS) spectroscopic survey (Huchra et al. 2012). Several spectroscopic redshifts from H_I-data were obtained by Waugh et al. (2002), but most of those galaxies are in the surroundings of the main cluster outside its virial radius.

Previous work on the Fornax cluster suggests that the center of the cluster is dynamically evolved, which means that most of the galaxies have travelled at least once through the cluster center, but there is still ongoing in-fall of subgroups and galaxies in the outskirts. The X-ray analysis of the hot intra-cluster gas by Paolillo et al. (2002) shows that there is a concentration of X-ray gas in the center of the cluster that has a mass of 10^{11} $M_\odot$ within the inner 100 kpc. However, this X-ray gas shows a lopsided distribution towards North-West, which is a sign of it not being fully virialized. The high concentration of galaxies in the center of the Fornax cluster (Ferguson 1989), and the observed mass segregation of the galaxies (Drinkwater et al. 2001) are both signs that the galaxies in the center have spent several Gyrs in the cluster environment corresponding to a few crossing times[4]. This longstanding interaction of galaxies with the cluster potential is possibly the main reason that has produced a significant intracluster population of stars in the halo of NGC 1399 (Iodice et al. 2016), which is also traced by Globular Clusters (Pota et al. 2018) and Planetary Nebulae (Spiniello et al. 2018). The GC population shows a velocity dispersion which is consistent with the one of the galaxy population in the same area, hence supporting the picture that the cluster core is dynamically evolved. Drinkwater et al. (2001) analyzed the substructure

[4]If we consider a galaxy located at half a virial radius from the cluster center (R=0.35 Mpc) with a velocity similar to the velocity dispersion of the cluster galaxies, (V =370 km s^{-1}), the crossing time is t_{cross} $\approx$1 Gyr.

of the Fornax cluster using the Fornax spectroscopic survey. They discussed that, although showing signs of a relaxed system, the Fornax cluster still has two groups of galaxies with common systematic velocities, clearly different from the one of the main cluster. Additionally, the high early-type galaxy fraction in the Fornax cluster (E+S0+dE+dS0)/all = 0.87 (Ferguson 1989) is a sign that the galaxies have spent a long time in the cluster without forming many new stars.

1.6 THE FORNAX DEEP SURVEY

This thesis is mostly based on the data of the recently finished Fornax Deep Survey. In this section I summarize the aims and the data of the survey and how it compares with the previous Fornax cluster observations.

The Fornax Deep Survey (FDS) is a collaboration of two guaranteed observing time surveys, Fornax Cluster Ultra-deep Survey (FoCUS, PI: R. Peletier) and the VST Early-type GAlaxy Survey (VEGAS, PI: E. Iodice, see also Capaccioli et al. 2015), which cover the area of the Fornax cluster and Fornax A sub-group, with deep multi-band imaging. The FDS is performed using the OmegaCAM (Kuijken et al. 2002) instrument attached to the VLT Survey Telescope (VST, Schipani et al. 2012), which is a 2.6 m telescope located at Cerro Paranal, Chile. The camera consists of 32 CCD-chips, has a 0.21 arcsec pixel^{-1} resolution, and a field of view of $\approx$1 deg $\times$ 1 deg. Our observations of the FDS were performed between November 2013 and November 2017, and they are listed in Table 3.1. All the observations were performed in clear (photometric variations $<$ 10 %) or photometric conditions. The u' and g'-band observations were performed in dark time, and the other bands in grey or dark time.

Since the images of the previous whole Fornax cluster survey are from the 1980's, the improvements that can be obtained with the present day's instruments are significant. After the Virgo cluster, Fornax is the second nearby cluster that is investigated with the new wide field instruments. The current FDS aims to study the galaxies in the Fornax cluster from the largest ones down to the resolution limit of the images. As the scientific interests of the FDS collaboration are diverse, the imaging strategy is planned so that the dynamical range of the images allows studying everything from the central parts of the brightest objects to the low surface brightness envelopes and streams around the galaxies.

The observations were performed using short 3 min exposure times and large $\approx$ 1 deg dithers between the consecutive exposures. The large dithers and offsets ensure that the same objects do not appear twice in the same pixel, and makes it possible to stack consecutive observations as a background model. The observations cover a 21 deg^2 area in the main cluster in u', g', r', and i', and additional 5 deg^2 in the Fornax A South-West sub-group in g', r', and i'.

The FDS aims to obtain a detailed overview of the Fornax cluster in photometric point of view. Furthermore it will work as a base for further follow-up studies investigating Fornax in other than optical wavelengths and from the spectroscopic perspective. Many of these follow-up studies have already started like the Atacama Large Millimeter Array (ALMA) Fornax Cluster Survey (AlFoCS, Zabel et al. 2018),

Table 1.1: Fornax Deep Survey observations used in this work. The columns correspond to the date, ESO observing period, and total exposure times per filter in hours.

		Total exposure time [h]			
Date	Period	u'	g'	r'	i'
Nov, 2013	P92	9.2	6.0	7.0	0.4
Nov, 2014	P94	16.0	15.9	11.2	12.3
Oct, Nov, 2015	P96	6.2	20.7	21.0	2.7
Oct, Nov, 2016	P98	-	15.5	15.1	7.9
Oct, Nov, 2017	P100	31.8	-	-	17.2

that observes CO in the Fornax galaxies. Also integral field unit (IFU) observations of Fornax dwarfs have been performed for several tens of Fornax dwarfs using the SAMI instrument at the Anglo-Australian Telescope (AAT). The Fornax H_I-survey (Serra et al. 2016) that uses the extended Karoo Array Telescope, MeerKAT, is also soon starting.

During the preparation of this thesis, I have observed a part of the FDS observations. More specifically, I have observed altogether 18 nights at Paranal during 2015 and 2016. I have also reduced and calibrated all the FDS data in Groningen during my PhD work.

1.7 Open questions in the dwarf galaxy evolution

In the last section, I introduced the observational and theoretical framework of the dwarf galaxy science. Some of the open questions that remain in the dwarf galaxy evolution, and that we try to investigate in this thesis are the following:

- *How does the cluster early-type galaxy population form? Do they transform from galaxies similar to the field late-types, and what is the relative importance of the environmental processes that quench the galaxies?* It has been shown that harassment and ram pressure stripping are both taking place in galaxy clusters, but their details and relative importance are yet not well known. With the FDS observations and accurate photometric measurements of the Fornax dwarfs, we can compare the late-type and early-type dwarfs in the cluster in detail, which will give us more constraints for the transformation mechanisms. It is also not clear how easily the small galaxies can be dissolved by the tidal field in the cluster center. With the FDS data we can test whether we see differences in the luminosity functions of the inner and outer parts of the Fornax cluster.
- *How does the low surface brightness galaxy population in the Fornax look like?* The low surface brightness galaxies have been studied in small areas in the Fornax cluster, but extended homogeneous studies do not yet exist. Especially the number and properties of very small and large LSB galaxies in the Fornax cluster are not well studied.

- *What is the nature of the ultra diffuse galaxies?* The existence of these galaxies has been shown in many clusters, but it is yet unclear what is the abundance of these galaxies in the Fornax cluster, and how it compares with that in other clusters. Also, it is not yet clear whether these galaxies form a homogeneous group with common formation mechanism, or are they rather a mixed bag of objects with different formation mechanisms.
- *How the galaxy population in Fornax compares with the populations in other galaxy environments?* Fornax cluster is an interesting environment since its mass of 7×10^{13} $M_{\odot}$ is similar to that in large groups, but still it has many properties that make it reasonable to call it as a cluster. How does structure and colors of the dwarf galaxy population in the Fornax look compared to those of the dwarf populations in other galaxy groups or clusters?
- *How do the properties of the galaxies change towards lower luminosities in the Fornax cluster?* Properties of the low luminosity dwarfs ($M_{r'} > -14$ mag) have been studied with high resolution in the LG and Virgo cluster. With the FDS we reveal similar dwarf galaxies in a new cluster, which extends our observational knowledge of such galaxies.

1.8 THIS THESIS

In this Ph.D. thesis I investigate the open questions of the dwarf galaxy evolution using the new optical images of the Fornax Deep Survey. This data allows us to see the dwarf galaxy populations of the Fornax cluster with unprecedented depth, and thus to study the structures and colors of the faintest dwarf galaxies in the Fornax cluster. In particular, I use this data to understand the abundance and structure of the low-luminosity and low surface brightness galaxies in the area of the Fornax cluster. Additionally, I test the importance of the different environmental processes acting on the dwarf galaxies by studying their properties at different cluster-centric radii.

In practice, first, I needed to reduce the newly obtained FDS data and assess its quality with various tests (Chapter 2 & 3). I first identified new galaxies, measured their photometric properties, and classified them into cluster and background galaxies (Chapter 2 & 3). After that I used this dwarf galaxy sample to study how the structure, abundance, and colors of the different types of dwarf galaxies compare in the inner and outer parts of the cluster and with other galactic environments (Chapter 4).

This thesis aims to improve our observational knowledge about the abundances and structures of the faintest dwarfs, and to draw conclusions about the likely evolutionary mechanisms taking place in the cluster.

1.8.1 OUTLINE OF THE THESIS

This thesis consists of four scientific chapters (Chapters 2-5) that, with the exception of the last one, are published in scientific journals. The fifth chapter is

based on ongoing work that will be published later. The contents of the chapters are the following:

- **Chapter 2:** I investigate the abundance and properties of the Ultra Diffuse Galaxies (UDGs) in the central area of the Fornax cluster by identifying them visually from the images. I show that the abundance of UDGs in the center of the Fornax cluster is typical for its total mass. We find that UDGs do not appear to be a distinct group of objects, but rather consist of a continuous distribution with the dwarf ellipticals. The elongated shapes of the largest UDGs suggests that they might be tidally distorted but due to the small number of galaxies in our sample, understanding the significance of such galaxies in the UDG population is only premature.

- **Chapter 3:** I describe the steps required for producing the new Fornax Deep Survey dwarf catalog. I use SExtractor to detect extended galaxies from the FDS data, and make Sérsic fits using GALFIT for all the galaxies. I then use colors, different structural parameters and morphology of the galaxies to identify the Fornax cluster dwarf galaxies from the background objects. I then assess the quality of the catalog by comparing it with the other works about the Fornax cluster, given in the literature. The final catalog consists of 564 Fornax cluster dwarf galaxies.

- **Chapter 4:** I investigate how the abundance, structure and colors of the dwarf galaxies change from the outkirts to the core of the Fornax cluster. I find that the galaxies become redder and smoother when going towards the inner parts of the cluster, showing that the objects are more evolved. We also find that the most luminous dwarfs become redder with increasing surface brightness, whereas the lower luminosity dwarfs behave in the opposite way. This behaviour suggests that the transformation of galaxies from star-forming to quiescent galaxies happens mostly via harassment in the high-luminosity end, whereas in the low-luminosity end that happens via gas-removal and subsequent fading of the stellar populations.

- **Chapter 5:** I test a new automatic segmentation algorithm called Max-Tree Objects (MTO) for identifying low surface brightness galaxies. I first assess the detection efficiency and output parameter estimation of MTO by using artificial galaxies and the sample described in Chapter 2. I find that MTO is superior compared to the previous state of art algorithm, SExtractor, and is capable of finding almost all the structures from the images that a human eye can see. I then apply MTO to FDS data in order to identify new LSB galaxy candidates in the whole Fornax cluster area.

- **Chapter 6:** I draw my conclusions based on the previous chapters and discuss the prospects of the future research.

1.9 References

Abell, G. O., Corwin, Jr., H. G., & Olowin, R. P. 1989, ApJS, 70, 1

Aguilar, L. A. & White, S. D. M. 1985, ApJ, 295, 374

Alam, S., Albareti, F. D., Allende Prieto, C., et al. 2015, ApJS, 219, 12

Barnes, J. E. & Hernquist, L. 1992, ARA&A, 30, 705

Bell, E. F., Wolf, C., Meisenheimer, K., et al. 2004, ApJ, 608, 752

Binggeli, B. 1994, Vol. 49, European Southern Observatory Conference and Workshop Proceedings, ed. G. Meylan & P. Prugniel, 13

Binggeli, B., Sandage, A., & Tammann, G. A. 1985, AJ, 90, 1681

Binggeli, B., Sandage, A., & Tarenghi, M. 1984, AJ, 89, 64

Binggeli, B., Tarenghi, M., & Sandage, A. 1990, A&A, 228, 42

Binney, J. & Tremaine, S. 2008, Galactic Dynamics: Second Edition (Princeton University Press)

Blakeslee, J. P., Jordán, A., Mei, S., et al. 2009, ApJ, 694, 556

Boselli, A., Boissier, S., Cortese, L., & Gavazzi, G. 2008, ApJ, 674, 742

Boselli, A., Fossati, M., Ferrarese, L., et al. 2018, A&A, 614, A56

Boselli, A. & Gavazzi, G. 2014, A&A Rev., 22, 74

Bothun, G. D., Beers, T. C., Mould, J. R., & Huchra, J. P. 1985, AJ, 90, 2487

Bothun, G. D., Impey, C. D., & Malin, D. F. 1991, ApJ, 376, 404

Boylan-Kolchin, M., Springel, V., White, S. D. M., Jenkins, A., & Lemson, G. 2009, MNRAS, 398, 1150

Brodie, J. P., Romanowsky, A. J., Strader, J., & Forbes, D. A. 2011, AJ, 142, 199

Buta, R. J., Sheth, K., Athanassoula, E., et al. 2015, ApJS, 217, 32

Butler, D. J. & Martínez-Delgado, D. 2005, AJ, 129, 2217

Capaccioli, M., Spavone, M., Grado, A., et al. 2015, A&A, 581, A10

Cappellari, M., Emsellem, E., Krajnović, D., et al. 2011, MNRAS, 416, 1680

Cassata, P., Cimatti, A., Kurk, J., et al. 2008, A&A, 483, L39

Conselice, C. J. 2018, Research Notes of the American Astronomical Society, 2, 43

Conselice, C. J., Gallagher, III, J. S., & Wyse, R. F. G. 2003, AJ, 125, 66

Davies, J. I., Phillipps, S., & Disney, M. J. 1990, MNRAS, 244, 385

Dayal, P. & Ferrara, A. 2018, ArXiv e-prints [arXiv:1809.09136]

de Vaucouleurs, G. 1959, Handbuch der Physik, 53, 275

Díaz-García, S., Salo, H., Laurikainen, E., & Herrera-Endoqui, M. 2016, A&A, 587, A160

Dressler, A. 1980, ApJ, 236, 351

Dressler, A., Bigelow, B., Hare, T., et al. 2011, PASP, 123, 288

Drinkwater, M. J., Gregg, M. D., & Colless, M. 2001, ApJ, 548, L139

Drinkwater, M. J., Gregg, M. D., Hilker, M., et al. 2003, Nature, 423, 519

Drinkwater, M. J., Phillipps, S., & Jones, J. B. 1999, in Astronomical Society of the Pacific Conference Series, Vol. 170, The Low Surface Brightness Universe, ed. J. I. Davies, C. Impey, & S. Phillips, 120

Drinkwater, M. J., Phillipps, S., Jones, J. B., et al. 2000, A&A, 355, 900

Duc, P.-A., Braine, J., Lisenfeld, U., Brinks, E., & Boquien, M. 2007, A&A, 475, 187

Eigenthaler, P., Puzia, T. H., Taylor, M. A., et al. 2018, ApJ, 855, 142

Elmegreen, B. G., Kaufman, M., & Thomasson, M. 1993, ApJ, 412, 90

Evrard, A. E. 1990, ApJ, 363, 349

Famaey, B. & McGaugh, S. S. 2012, Living Reviews in Relativity, 15, 10

Ferguson, H. C. 1989, AJ, 98, 367

Ferguson, H. C. & Binggeli, B. 1994, A&A Rev., 6, 67

Ferrarese, L., Côté, P., Cuillandre, J.-C., et al. 2012, ApJS, 200, 4

Franck, J. R. & McGaugh, S. S. 2016, ApJ, 833, 15

Fujita, Y. 1998, ApJ, 509, 587

Gaia Collaboration, Brown, A. G. A., Vallenari, A., et al. 2018, A&A, 616, A1

Geha, M., Blanton, M. R., Yan, R., & Tinker, J. L. 2012, ApJ, 757, 85

Godwin, J. G., Metcalfe, N., & Peach, J. V. 1983, MNRAS, 202, 113

Goodman, M. & Bekki, K. 2018, MNRAS, 478, 3564

Greco, J. P., Greene, J. E., Strauss, M. A., et al. 2018, ApJ, 857, 104

Gregg, M. D., Drinkwater, M. J., Evstigneeva, E., et al. 2009, AJ, 137, 498

Gunn, J. E. & Gott, III, J. R. 1972, ApJ, 176, 1

Haynes, M. P., Giovanelli, R., Martin, A. M., et al. 2011, AJ, 142, 170

Herrera-Endoqui, M., Díaz-García, S., Laurikainen, E., & Salo, H. 2015, A&A, 582, A86

Hilker, M. 2017, in IAU Symposium, Vol. 316, Formation, Evolution, and Survival of Massive Star Clusters, ed. C. Charbonnel & A. Nota, 99–104

Hilker, M., Kissler-Patig, M., Richtler, T., Infante, L., & Quintana, H. 1999, A&AS, 134, 59

Hilker, M., Mieske, S., & Infante, L. 2003, A&A, 397, L9

Hodge, P. W. 1971, ARA&A, 9, 35

Hoyos, C., den Brok, M., Verdoes Kleijn, G., et al. 2011, MNRAS, 411, 2439

Hubble, E. P. 1926, ApJ, 64, 321

Huchra, J. P., Macri, L. M., Masters, K. L., et al. 2012, ApJS, 199, 26

Hunsberger, S. D., Charlton, J. C., & Zaritsky, D. 1996, ApJ, 462, 50

Impey, C. & Bothun, G. 1989, ApJ, 341, 89

Impey, C. & Bothun, G. 1997, ARA&A, 35, 267

Iodice, E., Capaccioli, M., Grado, A., et al. 2016, ApJ, 820, 42

Iodice, E., Spavone, M., Cantiello, M., et al. 2017, ApJ, 851, 75

Jaffé, Y. L., Poggianti, B. M., Moretti, A., et al. 2018, MNRAS[arXiv:1802.07297]

Janowiecki, S. & Salzer, J. J. 2014, ApJ, 793, 109

Janz, J., Laurikainen, E., Laine, J., Salo, H., & Lisker, T. 2016, MNRAS, 461, L82

Janz, J. & Lisker, T. 2009, ApJ, 696, L102

Jiang, F., Dekel, A., Freundlich, J., et al. 2018, ArXiv e-prints [arXiv:1811.10607]

Jordán, A., Blakeslee, J. P., Côté, P., et al. 2007, ApJS, 169, 213

Klypin, A. A. & Shandarin, S. F. 1983, MNRAS, 204, 891

Koch, A., Burkert, A., Rich, R. M., et al. 2012, ApJ, 755, L13

Koda, J., Yagi, M., Yamanoi, H., & Komiyama, Y. 2015, ApJ, 807, L2

Koleva, M., de Rijcke, S., Prugniel, P., Zeilinger, W. W., & Michielsen, D. 2009, MNRAS, 396, 2133

Koleva, M., De Rijcke, S., Zeilinger, W. W., et al. 2014, MNRAS, 441, 452

Kormendy, J. & Bender, R. 2012, ApJS, 198, 2

Kormendy, J. & Freeman, K. C. 2016, ApJ, 817, 84

Kroupa, P., Pawlowski, M., & Milgrom, M. 2012, International Journal of Modern Physics D, 21, 1230003

Kroupa, P., Theis, C., & Boily, C. M. 2005, A&A, 431, 517

Kuijken, K., Bender, R., Cappellaro, E., et al. 2002, The Messenger, 110, 15

Lauberts, A. & Valentijn, E. A. 1989, The surface photometry catalogue of the ESO-Uppsala galaxies (European Southern Observatory)

Laurikainen, E., Salo, H., Buta, R., Knapen, J. H., & Comerón, S. 2010, MNRAS, 405, 1089

Leisman, L., Haynes, M. P., Janowiecki, S., et al. 2017, ApJ, 842, 133

Lelli, F., Duc, P.-A., Brinks, E., et al. 2015, A&A, 584, A113

Lelli, F., McGaugh, S. S., & Schombert, J. M. 2016, ApJ, 816, L14

Lemaux, B. C., Le Fèvre, O., Cucciati, O., et al. 2018, A&A, 615, A77

Lisker, T., Glatt, K., Westera, P., & Grebel, E. K. 2006, AJ, 132, 2432

Lisker, T., Grebel, E. K., Binggeli, B., & Glatt, K. 2007, ApJ, 660, 1186

Lotz, M., Remus, R.-S., Dolag, K., Biviano, A., & Burkert, A. 2018, ArXiv e-prints [arXiv:1810.02382]

Mancera Piña, P. E., Peletier, R. F., Aguerri, J. A. L., et al. 2018, MNRAS, 481, 4381

Marchesini, D., Muzzin, A., Stefanon, M., et al. 2014, ApJ, 794, 65

Marsan, Z. C. & Marchesini, D. 2014, in American Astronomical Society Meeting Abstracts, Vol. 224, American Astronomical Society Meeting Abstracts #224, 222.15

Martis, N. S., Marchesini, D., Brammer, G. B., et al. 2016, ApJ, 827, L25

Mastropietro, C., Moore, B., Mayer, L., et al. 2005, MNRAS, 364, 607

McConnachie, A. W. 2012, AJ, 144, 4

McGlynn, T. A. 1990, ApJ, 348, 515

Mei, S., Holden, B. P., Blakeslee, J. P., et al. 2009, ApJ, 690, 42

Mentz, J. J., La Barbera, F., Peletier, R. F., et al. 2016, MNRAS, 463, 2819

Micheva, G., Östlin, G., Bergvall, N., et al. 2013, MNRAS, 431, 102

Mieske, S., Hilker, M., & Infante, L. 2002, A&A, 383, 823

Mieske, S., Hilker, M., Infante, L., & Mendes de Oliveira, C. 2007, A&A, 463, 503

Mihos, J. C., Carr, C. T., Watkins, A. E., Oosterloo, T., & Harding, P. 2018, ApJ, 863, L7

Milgrom, M. 1989, Comments on Astrophysics, 13, 215

Mirabel, I. F., Dottori, H., & Lutz, D. 1992, A&A, 256, L19

Misgeld, I., Hilker, M., & Mieske, S. 2009, A&A, 496, 683

Moore, B., Katz, N., Lake, G., Dressler, A., & Oemler, A. 1996, Nature, 379, 613

Muñoz, R. P., Eigenthaler, P., Puzia, T. H., et al. 2015, ApJ, 813, L15

Muzzin, A., Marchesini, D., Stefanon, M., et al. 2013, ApJ, 777, 18

Nasonova, O. G., de Freitas Pacheco, J. A., & Karachentsev, I. D. 2011, A&A, 532, A104

Navarro, J. F., Benítez-Llambay, A., Fattahi, A., et al. 2017, MNRAS, 471, 1841

Navia, C. E. 2018, ArXiv e-prints [arXiv:1811.12384]

Noeske, K. G., Papaderos, P., Cairós, L. M., & Fricke, K. J. 2003, A&A, 410, 481

Pak, M., Rey, S.-C., Lisker, T., et al. 2014, MNRAS, 445, 630

Paolillo, M., Fabbiano, G., Peres, G., & Kim, D.-W. 2002, ApJ, 565, 883

Paudel, S., Smith, R., Yoo, S. J., Calderón-Castillo, P., & Duc, P.-A. 2018, ArXiv e-prints [arXiv:1807.07195]

Peletier, R. F. 1993, A&A, 271, 51

Peng, E. W. & Lim, S. 2016, ApJ, 822, L31

Pillepich, A., Springel, V., Nelson, D., et al. 2018, MNRAS, 473, 4077

Poggianti, B. M., Moretti, A., Gullieuszik, M., et al. 2017, ApJ, 844, 48

Ponomareva, A. A., Verheijen, M. A. W., Peletier, R. F., & Bosma, A. 2017, MNRAS, 469, 2387

Pota, V., Napolitano, N. R., Hilker, M., et al. 2018, MNRAS, 481, 1744

Roediger, J. C., Ferrarese, L., Côté, P., et al. 2017, ApJ, 836, 120

Román, J. & Trujillo, I. 2017, MNRAS, 468, 4039

Romanishin, W., Strom, K. M., & Strom, S. E. 1983, ApJS, 53, 105

Rudnick, G., von der Linden, A., Pelló, R., et al. 2009, ApJ, 700, 1559

Salaris, M., de Boer, T., Tolstoy, E., Fiorentino, G., & Cassisi, S. 2013, A&A, 559, A57

Sandage, A. & Binggeli, B. 1984, AJ, 89, 919

Savino, A., Salaris, M., & Tolstoy, E. 2015, A&A, 583, A126

Schipani, P., Capaccioli, M., Arcidiacono, C., et al. 2012, in Proc. SPIE, Vol. 8444, Ground-based and Airborne Telescopes IV, 84441C

Serra, P., de Blok, W. J. G., Bryan, G. L., et al. 2016, in Proceedings of MeerKAT Science: On the Pathway to the SKA. 25-27 May, 2016 Stellenbosch, South Africa (MeerKAT2016)., 8

Serra, P., Oosterloo, T., Morganti, R., et al. 2012, MNRAS, 422, 1835

Smith, R., Sánchez-Janssen, R., Beasley, M. A., et al. 2015, MNRAS, 454, 2502

Solanes, J. M., Manrique, A., García-Gómez, C., et al. 2001, ApJ, 548, 97

Spiniello, C., Napolitano, N. R., Arnaboldi, M., et al. 2018, MNRAS, 477, 1880

Springel, V., Wang, J., Vogelsberger, M., et al. 2008, MNRAS, 391, 1685

Sutherland, W., Emerson, J., Dalton, G., et al. 2015, A&A, 575, A25

Taylor, E. N., Hopkins, A. M., Baldry, I. K., et al. 2011, MNRAS, 418, 1587

Toloba, E., Boselli, A., Cenarro, A. J., et al. 2011, A&A, 526, A114

Toloba, E., Guhathakurta, P., Boselli, A., et al. 2015, ApJ, 799, 172

Toomre, A. & Toomre, J. 1972, ApJ, 178, 623

Torrealba, G., Belokurov, V., Koposov, S. E., et al. 2018, arXiv e-prints [arXiv:1811.04082]

Trentham, N. & Tully, R. B. 2009, MNRAS, 398, 722

Trujillo, I., Beasley, M. A., Borlaff, A., et al. 2018, arXiv e-prints [arXiv:1806.10141]

Tully, R. B. & Fisher, J. R. 1977, A&A, 54, 661

Urich, L., Lisker, T., Janz, J., et al. 2017, A&A, 606, A135

van den Bergh, S. 1959, Publications of the David Dunlap Observatory, 2, 147

van den Bergh, S. 1976, ApJ, 206, 883

van der Burg, R. F. J., Hoekstra, H., Muzzin, A., et al. 2017, A&A, 607, A79

van der Burg, R. F. J., Muzzin, A., & Hoekstra, H. 2016, A&A, 590, A20

van der Hulst, J. M. 1979, A&A, 71, 131

van Dokkum, P., Abraham, R., Brodie, J., et al. 2016, ApJ, 828, L6

van Dokkum, P., Cohen, Y., Danieli, S., et al. 2018, ApJ, 856, L30

van Dokkum, P. G., Abraham, R., Merritt, A., et al. 2015, ApJ, 798, L45

Venhola, A., Peletier, R., Laurikainen, E., et al. 2018, A&A, 620, A165

Verbeke, R., Papastergis, E., Ponomareva, A. A., Rathi, S., & De Rijcke, S. 2017, A&A, 607, A13

Verheijen, M. A. W. 2001, ApJ, 563, 694

Voggel, K., Hilker, M., & Richtler, T. 2016, A&A, 586, A102

Watson, M. G., Schröder, A. C., Fyfe, D., et al. 2009, A&A, 493, 339

Waugh, M., Drinkwater, M. J., Webster, R. L., et al. 2002, MNRAS, 337, 641

Weisz, D. R., Dolphin, A. E., Skillman, E. D., et al. 2014, ApJ, 789, 147

White, S. D. M. & Frenk, C. S. 1991, ApJ, 379, 52

White, S. D. M. & Rees, M. J. 1978, MNRAS, 183, 341

Wittmann, C., Lisker, T., Pasquali, A., Hilker, M., & Grebel, E. K. 2016, MNRAS, 459, 4450

Wolf, J., Martinez, G. D., Bullock, J. S., et al. 2010, MNRAS, 406, 1220

Zabel, N., Davis, T. A., Smith, M. W. L., et al. 2018, MNRAS

Zwicky, F. 1957, Morphological astronomy (Berlin/Heidelberg, Springer-Verlag)

2. The Fornax Deep Survey (FDS) with the VST: III. Low Surface Brightness (LSB) dwarfs and Ultra Diffuse Galaxies (UDGs) in the center of the Fornax cluster

—— *A. Venhola, R. Peletier, E. Laurikainen, H. Salo, T. Lisker, E. Iodice, M. Capaccioli, G. Verdoes Kleijn, E. Valentijn, S. Mieske, M. Hilker, C. Wittmann, G. van de Ven, A. Grado , M. Spavone, M. Cantiello, N. Napolitano, M. Paolillo, J. Falcón-Barroso* ——

Published in Astronomy & Astrophysics, 608, id.A142, 32pp. (2017)

Abstract

Context: Studies of low surface brightness (LSB) galaxies in nearby clusters have revealed a sub-population of extremely diffuse galaxies with central surface brightness of $\mu_{0,g'} > 24$ mag arcsec^{-2}, total luminosity $M_{g'}$ fainter than -16 mag and effective radius between 1.5 kpc $< R_e <$ 10 kpc. The origin of these Ultra Diffuse Galaxies (UDGs) is still unclear, although several theories have been suggested. As the UDGs overlap with the dwarf-sized galaxies in their luminosities, it is important to compare their properties in the same environment. If a continuum is found between the properties of UDGs and the rest of the LSB population, it would be consistent with the idea that they have a common origin.

Aim: Our aim is to exploit the deep g', r' and i'-band images of the Fornax Deep Survey (FDS), in order to identify LSB galaxies in an area of 4 deg^2 in the center of the Fornax cluster. The identified galaxies are divided into UDGs and dwarf-sized LSB galaxies, and their properties are compared.

Methods: We identified visually all extended structures having r'-band central surface brightness of $\mu_{0,r'} > 23$ mag arcsec^{-2}. We classified the objects based on their appearance into galaxies and tidal structures, and perform 2D Sérsic

model fitting with GALFIT to measure the properties of those classified as galaxies. We analyzed their radial distribution and orientations with respect of the cluster center, and with respect to the other galaxies in our sample. We also studied their colors and compare the LSB galaxies in Fornax with those in other environments.

Results: Our final sample complete in the parameter space of the previously known UDGs, consists of 205 galaxies of which 196 are LSB dwarfs (with $R_e <$ 1.5kpc) and nine are UDGs ($R_e >$ 1.5 kpc). We show that the UDGs have (1) g'-r' colors similar to those of LSB dwarfs of the same luminosity. (2) The largest UDGs ($R_e >$ 3kpc) in our sample appear different from the other LSB galaxies, in that they are significantly more elongated and extended, whereas (3) the smaller UDGs differ from the LSB dwarfs only by having slightly larger effective radii. (4) We do not find clear differences between the structural parameters of the UDGs in our sample and those of UDGs in other galaxy environments. (5) We find that the dwarf LSB galaxies in our sample are less concentrated in the cluster center than the galaxies with higher surface brightness, and that their number density drops within 180 kpc from the cluster center. We also compare the LSB dwarfs in Fornax with the LSB dwarfs in the Centaurus group, where data of similar quality to ours is available. (6) We find the smallest LSB dwarfs to have similar colors, sizes and Sérsic profiles regardless of their environment. However, in the Centaurus group the colors become bluer with increasing galaxy magnitudes, an effect which is probably due to smaller mass and hence weaker environmental influence of the Centaurus group.

Conclusions: Our findings are consistent with the small UDGs forming the tail of a continuous distribution of less extended LSB galaxies. However, the elongated and distorted shapes of the large UDGs could imply that they are tidally disturbed galaxies. Due to limitations of the automatic detection methods and uncertainty in the classification the objects, it is yet unclear what is the total contribution of the tidally disrupted galaxies in the UDG population.

2.1 INTRODUCTION

For several decades it has been known that some galaxies have much lower surface brightnesses than others. Davies et al. (1994) demonstrated, using the ESO-Uppsala galaxy catalog (Lauberts & Valentijn 1989), how galaxy samples with fixed magnitude and size limits are biased by missing the low surface brightness galaxies due to limits in depth and sensitivity, resulting in a lower data quality. Historically, all galaxies with B-band central surface brightness of $\mu_{0,B} > 23$ mag arcsec^{-2} are considered as Low Surface Brightness (LSB) galaxies (Impey & Bothun 1997). However, this definition is relatively broad and includes galaxies ranging from almost Milky Way sized galaxies to the smallest Milky Way satellite dwarf spheroidals (dSph). Early studies of LSB galaxies with detailed photometric measurements (Romanishin et al. 1983, Bothun et al. 1985, Sprayberry et al. 1995, Impey & Bothun 1989 and Bothun et al. 1990) concentrated mostly on relatively massive galaxies. These giant LSB galaxies, like Malin 1 (Impey & Bothun 1989), for which they measured a disk scale length of 55 kpc and a V-band central surface brightness of $\mu_{0,V} = 25.5$ mag arcsec^{-2}, form an interesting class of objects in terms of galaxy evolution processes, as it is not well understood how they have managed to grow so massive without increasing their surface brightness. The appearance of such giant LSB galaxies has been proposed to be a result of their high angular momentum, and low star formation rate (Jimenez et al. 1998). These galaxies are predicted to be relatively rare and only appear in low density environments. In dense environments like the Fornax cluster, galaxies experience frequent tidal interactions with other galaxies and are affected by the cluster potential. This process, called harassment (Moore et al. 1998), tends to rip off material from the galaxies that enter deep into the cluster core, and eventually makes them denser (Smith et al. 2015).

In the end of 1980's, large galaxy catalogs of the Virgo (Binggeli et al. 1985) and Fornax clusters (Ferguson 1989b) included also many dwarf sized (B-band absolute magnitude $M_B >$ -18 mag[1]) LSB galaxies, which greatly increased the number of known LSB galaxies. The automated photometry of Davies et al. (1988) allowed the detailed analysis of dwarf galaxies in these samples. Later studies, like the ones of Davies et al. (1990) or Sabatini et al. (2005), showed that dwarf LSB galaxies actually form the bulk of the population at the low luminosity end of the luminosity function. Most of these galaxies were found in clusters. In fact, galaxies with central V-band surface brightness of $\mu_{0,V} = 22$ - 25 mag arcsec^{-2} have been estimated to contribute significant amount (even 50%) of the light emitted by galaxies (Impey & Bothun 1997).

It is only recently that new instruments, such as OmegaCAM (Kuijken et al. 2002), Suprime-Cam (Miyazaki et al. 2002), DECam (Flaugher et al. 2015), and MegaCAM (Boulade et al. 1998), have made it possible to perform multi-band surveys with limiting V-band surface brightness down to $\mu_V \sim$28 mag arcsec^{-2}, over large areas in the sky. These new observations allow us to study also the distribution and properties of the dwarf LSB galaxies in statistically significant samples. Indeed, new imaging surveys like the Next Generation Virgo Survey

[1] $M_B >$ -18 corresponds to $M_{r'} \sim$-19 mag. See Appendix 2.11.3 for details.

(Ferrarese et al. 2012), have revealed a large number of low surface brightness galaxies. Although the wide-field instruments attached to large telescopes have shown their efficiency performing deep surveys, other approaches have proven effective as well. One of them used the Dragonfly instrument (Abraham & van Dokkum 2014), which consists of a set of small 143 mm cameras, and was used when van Dokkum et al. (2015) discovered a large number of extended LSB galaxies in the Coma cluster, which they named Ultra Diffuse Galaxies (UDG).

The UDGs discovered by van Dokkum et al. (2015) are defined to be extended (effective radius $R_e > 1.5$ kpc) and faint (V-band absolute magnitude -16 mag $< M_V <$ -13 mag), and have similar central surface brightnesses ($\mu_{0,g} > 24$ mag arcsec^{-2}) as the faintest dwarf galaxies. However, their effective radius can be even ten times larger. What makes these galaxies particularly interesting is that UDGs reside in the cluster environment where they appear in large numbers (Yagi et al. 2016, van der Burg et al. 2016,Wittmann et al. 2017, van der Burg et al. 2017). UDGs have now been found in all clusters where they have been searched for. For example, van der Burg et al. (2016) used an automated algorithm to find UDGs in clusters in the redshift range $0.044 < z < 0.063$. They found that their abundance increases with increasing cluster halo mass, reaching ~ 200 UDGs in typical halo masses of $M_{200} \approx 10^{15}$ $M_\odot$. Recently UDGs have been reported also in some nearby galaxy groups (Merritt et al. 2016, Toloba et al. 2016, Crnojević et al. 2016, Román & Trujillo 2017) and low density environments (Martínez-Delgado et al. 2016 and Leisman et al. 2017) showing that these galaxies appear in all kind of galaxy environments.

In our study, we hereafter define all the galaxies with $\mu_{0,r'} > 23$ mag arcsec^{-2} as LSB galaxies, and the ones additionally having absolute r'-band magnitude $M_{r'} >$ -19 mag as dwarf LSB galaxies. LSB galaxies that have an effective radius $R_e >$ 1.5 kpc are called UDGs[2].

The formation mechanism of UDGs is still unclear. They have been suggested to form from medium mass (halo mass of $10^{10-11} M_\odot$) galaxies as a result of strong gas outflows due to star formation feedback (Di Cintio et al. 2017), whereas Baushev (2018) suggested that UDGs can form via head-on collisions of gas-rich systems in the centers of galaxy clusters. UDGs have also been suggested to be the high spin tail of the typical dwarf elliptical (dE) galaxy population (Amorisco & Loeb 2016). Indeed, it is important to study the photometric properties of UDGs and LSB dwarf galaxies in different environments to see if there is a continuum between their properties.

The Fornax cluster, with a virial mass of 7×10^{13} $M_\odot$ (Drinkwater et al. 2001a), is less massive than the Coma (1.4×10^{15} $M_\odot$, Łokas & Mamon 2003) and Virgo clusters ($1\text{-}3\times10^{14}$ $M_\odot$, McLaughlin 1999). However, in spite of its fairly low mass the Fornax cluster has a high fraction of early-type galaxies (E+S0+dE+dS0)/all = 0.87 (Ferguson 1989a), and a central galaxy density similar to that of the more massive Virgo cluster. The core of the Fornax is also filled with hot X-ray emitting gas (Paolillo et al. 2002 and references therein), which makes the galaxies vulnerable to ram pressure stripping, which removes the cold gas from

[2]For typical LSB galaxies g'-r' ~ 0.6, so our limits correspond to $\mu_{g',0} = 23.6$ mag arcsec^{-2} and $M_{g'} = -18.4$ mag.

the galaxies. This implies that any galaxy which has spent a long time in the core of the Fornax cluster, should consist only of fairly old stellar populations.

So far only a few studies have mapped the LSB galaxy population in the Fornax cluster. Bothun et al. (1991) studied the properties of the LSB galaxies with central B-band surface brightnesses of $\mu_{0,B} > 23$ mag arcsec^{-2}, and showed that there are tens of relatively metal-poor galaxies, which make a significant contribution to the faint end of the luminosity function. Due to their low surface brightnesses it is problematic to spectroscopically confirm their distances, and therefore often the cluster membership has been deduced from the clustering of these galaxies. However, the cluster membership of several LSB galaxies were spectroscopically confirmed in the sample of Drinkwater et al. (1999), which included galaxies with B-band total apparent magnitudes brighter than $m_B < 19.7$ mag ($M_B <$ -11.7) and central surface brightnesses between 20 and 24 mag arcsec^{-2}. Also the study of Mieske et al. (2007), which used surface brightness fluctuation analysis to define galaxy distances, confirmed the cluster membership of several Fornax LSB galaxies. These studies support the idea that at least two thirds of the LSB galaxies in the area of Fornax are real cluster members. A recent study of Muñoz et al. (2015), performed with the DECam instrument, searched for new faint galaxies in the central parts of the Fornax cluster. Their observations reaching g'-band point sources down to 26.6 mag with S/N > 5, reveal more than hundred previously non-detected dwarf sized LSB galaxies. The faintest LSB dwarf galaxies in their sample have $R_e \approx 100$ pc, which means that they have similar sizes as the Local Group dSph's (McConnachie 2012 and the references therein).

In this paper, we perform a systematic search for LSB galaxies in the images of the Fornax Deep Survey (FDS), which is an ongoing survey using the VLT Survey Telescope (VST) at ESO / Cerro Paranal. It covers a larger field-of-view than any of the previous Fornax surveys with deep multi-band observations, and has similar depth as the Next Generation Virgo Survey (Ferrarese et al. 2012). The survey has already obtained several results, such as the discovery of an extended globular cluster population (D'Abrusco et al. 2016), the characterization of the extended stellar halo of NGC 1399 (Iodice et al. 2016), and the analysis of the merger system around NGC 1316 (Iodice et al. 2017). Since we have deep data in g', r' and i'-bands, we can determine also the colors of the galaxies.

We present a sample of LSB galaxies in the Fornax cluster, based on our analysis, and combined with those obtained in the previous studies. In Sections 2 and 3 we describe the data used in this work, and briefly describe the reduction steps. In Sections 4 and 5 we present the sample selection and the photometric measurements performed to obtain the structural parameters. We show the cluster-centric radial distributions (Section 6.1), orientations (Section 6.2) and colors (Section 7) of the galaxies. In Section 8 we discuss the results in the context of different formation theories of UDGs, and in Section 9 give the conclusions of this paper. For the Fornax cluster we use the distance of 19.95 Mpc (Tonry et al. 2001) corresponding to the distance modulus of 31.43 and scale of 0.0967 kpc arcsec^{-2}.

2.2 DATA

We use the ongoing Fornax Deep Survey (FDS), which consists of the combined data of the Guaranteed Time Observation Surveys FOCUS (P.I. R. Peletier) and VEGAS (P.I. E. Iodice), dedicated to the Fornax cluster. Both surveys are performed with the ESO VLT Survey Telescope (VST), which is a 2.6-meter diameter optical telescope located at Cerro Paranal, Chile (Schipani et al. 2012). The imaging is done with the OmegaCAM instrument (Kuijken et al. 2002), using the u', g', r' and i'-bands, and $1^\circ \times 1^\circ$ field of view. OmegaCAM consists of an array of 8×4 CCDs, each with 2144×4200 pixels. The pixel size is 0.21 arcsec and the average FWHM of the observations is ≈ 1 arcsec, so that the *PSF* is well sampled. For further information about the data see Iodice et al. (2016) and Peletier et al. (*in prep.*).

The observations used in this work were gathered in visitor mode runs during November 2013, 2014 and 2015 (ESO P92, P94 and P96, respectively). All the observations were performed in clear (photometric variations < 10 %) or photometric conditions. The observations in u' and g'-bands were obtained in dark time, and those of the other bands in gray or dark time.

The observation area of FDS is divided into $1^\circ \times 1^\circ$ fields (see Fig. 3.2) with some overlaps between the fields. The observations of each field were performed using offsets larger than 1 deg between consecutive exposures, always covering an adjacent field. During the sequence of multiple exposures, additional dithers of $\lesssim$10 arcmin width have been added to the 1 deg offsets with a fixed pattern for all fields. This ensures that the whole area has a uniform depth, meaning that whenever an exposure is dithered from the field center, and thus only partially covers the original field, there will be exposures in the adjacent fields with identical dithers providing a full coverage over all fields. This offset and dither strategy makes it possible to perform accurate sky subtraction without spending time for separate sky exposures (see Section 3.2 for details). The total exposure times in all fields are 11000, 8000, 8000, and 5000 sec in u', g', r' and i'-bands, respectively. The total exposure times are divided into 150 s exposures meaning that each field is covered with a minimum of 75, 55, 55 and 35 exposures in u', g', r' and i', respectively.

The data used in this work cover an 4 deg^2 area centered on NGC 1399 (see Fig. 2.2). All the fields are imaged using the four bands. The limiting 5σ magnitudes (in AB system) for 1 arcsec^2 area are 27.6, 28.5, 28.5 and 27.1 mag in u', g', r' and i', respectively. In this work only g', r' and i' bands are used, due to their deeper surface brightness limit and higher sensitivity for the relatively red galaxies in the Fornax cluster. The sources studied in this work have a central r'-band surface brightness of $\mu_{0,r'} \geq 23$ mag arcsec^{-2}, so that most of them are not bright enough in the u'-band to detect them. In this work we analyze the fields 10, 11, 12 and 16 (see Fig. 3.2).

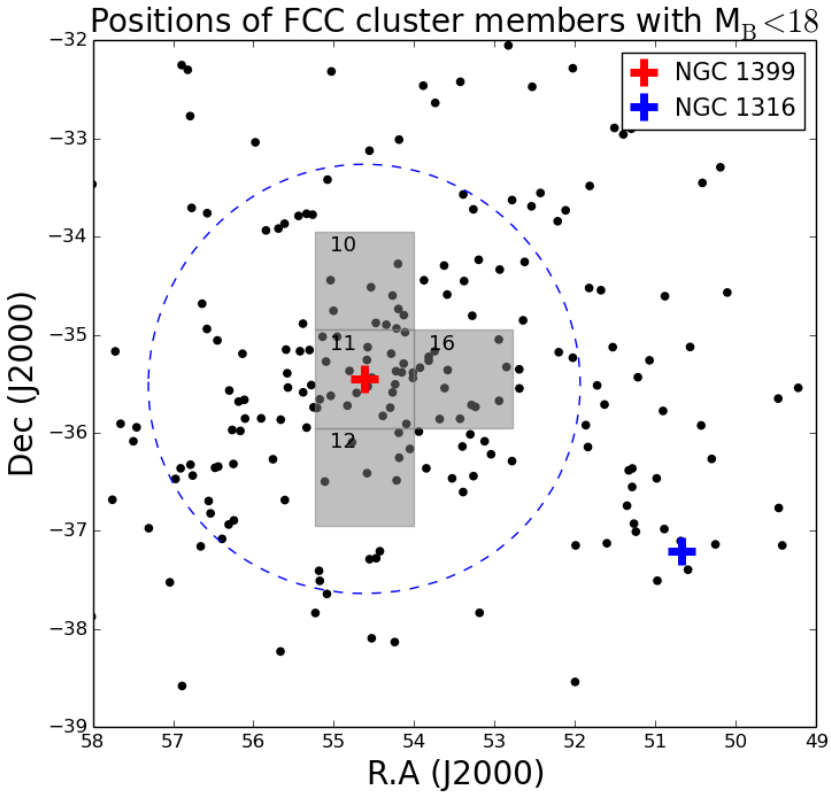

Figure 2.1: Locations of the analyzed 1° x 1° Fornax fields (highlighted with gray), plotted over the FCC galaxies (the black points, Ferguson 1989b) with $m_B < 18$ mag and the member classification 1 or 2 (confirmed or likely member, respectively, in Ferguson 1989b). The blue dashed circle is the virial radius 2.2° (or 0.7 Mpc at the distance of Fornax cluster) adopted from Drinkwater et al. (2001a). The red cross shows the cD galaxy NGC 1399 (see Iodice et al. 2016) in the core of the Fornax cluster, and the blue cross shows the elliptical shell galaxy NGC 1316 (see Iodice et al. 2017) , which is the central galaxy of the Fornax-SW subcluster.

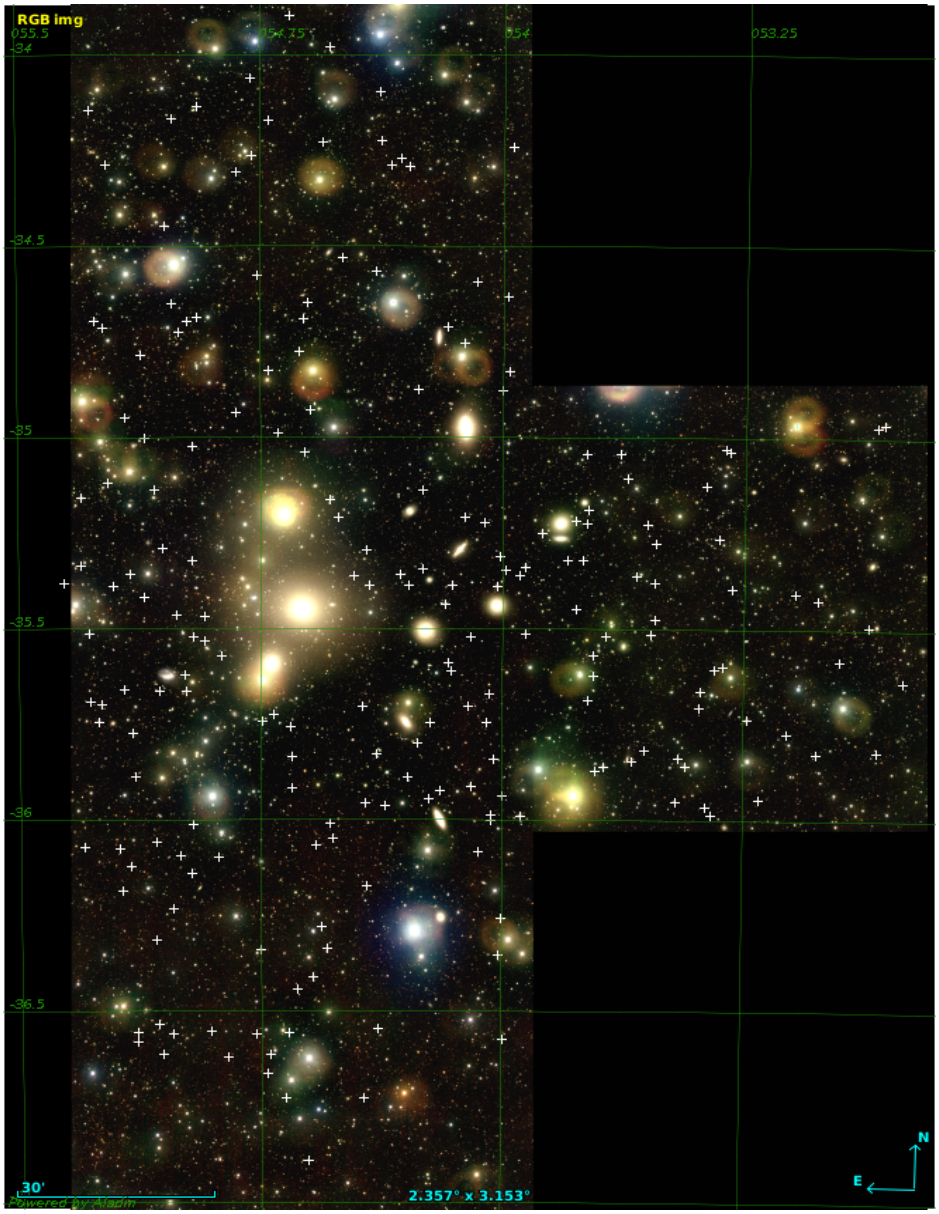

Figure 2.2: Locations of the galaxies identified by us (marked with crosses). The background image shows the fields 10, 11, 12 and 16 using the combined i', r' and g' bands. Aladin (Boch et al. 2011) is used to generate the graphics.

2.3 DATA REDUCTION

We have developed a pipeline to reduce FDS OmegaCAM data adapting the general OmegaCAM pipeline within the AstroWISE environment (McFarland et al. 2013). The pipeline used in this work is different from the one described in Iodice et al. (2016). However, the results of these two pipelines are consistent with each other (details will be given in Peletier et al. *in prep.*). The main reduction steps are provided in the next paragraphs.

2.3.1 INSTRUMENTAL CORRECTIONS

The instrumental corrections include removal of bias and correcting the sensitivity variations over the field of view (flat-field and illumination correction).

Bias was first defined from the overscan regions of the images, and the row-wise median values were subtracted from each science image. For not to add too much noise in the bias subtraction, we used the overscan corrected master bias image, obtained by median combining ten bias images taken each night.

After removing bias from the science images, they were corrected for the sensitivity variations over the focal plane by dividing the images by a master flat-field image. We adopted the flat-fielding method that was used by the Kilo Degree Survey (KiDS, de Jong et al. 2015): the master flat-field was achieved by first median-combining and normalizing eight dome flat-fields and eight twilight flat-fields, and then multiplying the averaged flat-fields with each other. High-frequency spatial Fourier modes are corrected using the dome flats and low frequencies using the twilight flats. This is based on the pre-assumption that the large-scale illumination of the twilight flat-field matches better the observational situation than that obtained from the dome. On the other hand, in the dome flats the *S/N* is high, which can be used to capture the pixel-by-pixel variations in the pixel sensitivity.

However, even after applying the flat-field correction small systematic flux variations remain across the instrument. These variations can be corrected by applying an illumination correction. We used the correction models made for the KiDS (see Verdoes Kleijn et al. 2013 for details). The models were made by mapping the photometric residuals across the CCD array using a set of dithered Landolt Selected Area (SA) field (Landolt 1992) observations, and fitting a linear model to the residuals. The images were multiplied with this illumination correction. The correction was applied after sky subtraction (see the next sub-section), to avoid the sky residuals being amplified by the illumination correction procedure.

2.3.2 BACKGROUND SUBTRACTION AND DE-FRINGING

The images contain sky background flux composed of direct and scattered atmospheric emission, and scattered light of bright celestial sources. A careful removal of the atmospheric background light is essential when studying LSB objects such as UDGs. When considering a single image at low luminosity levels,

we cannot directly tell which part of the light is diffuse light coming from the sources and which is background light. To bypass the problem, we can make an assumption that the pattern of background light stays constant if the telescope pointing direction is not changed by more than a few degrees. Due to the large dithers between the consecutive integrations the objects are not likely to appear twice in the same pixel, which allows us to produce background models by averaging a stack of images. The intensity of the sky changes thorough the night (1–10% between exposures), especially at the beginning and at the end of the night, which forces to scale the images used for the background model before combining them. The pattern of the scattered light changes also as a function of telescope pointing direction and the positions of the Sun and the Moon, so that any accurate model of those variations is not available.

A unique background model was made for each CCD of each exposure by scaling and stacking 12 consecutive dithered exposures (six before and six after the frame, whose background is modeled). First, SExtractor (Bertin & Arnouts 1996) was used to mask all stars and galaxies from all individual images (12 consecutive pointings). Specifically, we masked the objects with 5 pixels above the 5σ threshold, using a 50×50 pixel grid to estimate the background in the masking process. We ensured that we are not masking systematically any shapes (like vignetted edges) of the background by comparing a set of masks of background models. After the masking, the images were scaled with each other assuming that the shape of the background scales linearly with the total level of the background. The scaling factor s can be found by:

$$s = \mathrm{Median}\left(\frac{m_{1,i}}{m_{2,i}}\right),\ i = 1, ..., 96, \tag{2.1}$$

where $m_{1,i}$ is a set of medians measured within 96 90 $\times$ 90-pixel areas in image 1, used as a reference image (i.e., the image for which we are making the background model). Correspondingly, $m_{2,i}$ is a set medians measured at the same locations in image 2, which we are scaling. Before combining the frames we exclude the images that are not suitable for obtaining the background model. We excluded frames, where more than 1/3 of the area was masked. Excluded were also frames which have a large scatter in $\frac{m_{1,i}}{m_{2,i}}$, since they have either large unmasked objects or have otherwise peculiar background. If only six or less frames were found to be useful for the background model (e.g., if an extended source fills the whole CCD being modeled, it is excluded), the scaling was done by using the median values of all 32 CCDs (instead of just one) and then using the equation 2.1. After masking and multiplying the images with s, the selected frames were combined by taking the median of the stacks. This background model was then subtracted from the final image.

OmegaCAM has interference patterns (fringes) in i'-band images due to the internal reflections in the CCDs. Intensity of the fringe patterns is proportional to the total light coming to the CCD. As long as the background and the filter does not vary, the fringes have always the same shape since they are related to the properties of the CCD. Luckily, the fringes appear also in the background model

and are subtracted with it. No other fringe correction was applied. The intensity of the fringe patterns in our images was lower than the masking threshold, which leaves them unmasked.

2.3.3 ASTROMETRIC AND PHOTOMETRIC CALIBRATIONS

The first-order astrometric calibration was done by first matching the pixel coordinates to RA and DEC using the World Coordinate System (WCS) information from the fits header. Point source coordinates were then extracted using SExtractor and associated with the 2 Micron All Sky Survey Point Source Catalog (2MASS PSC, Skrutskie et al. 2006). The transformation was then extended by a second-order two-dimensional polynomial across the focal plane. SCAMP (Bertin 2006) was used for this purpose. The polynomial was fit iteratively five times, each time clipping the 2σ-outliers. The astrometric solution gives typically RMS errors of 0.3 arcsec (compared to 2MASS PSC) for a single exposure, and 0.1 arcsec for the stacked final mosaic.

The absolute photometric calibration was performed by observing standard star fields each night and comparing their OmegaCAM magnitudes with the Sloan Digital Sky Survey Data Release 11 (SDSS DR11, Alam et al. 2015) catalog values. The OmegaCAM point source magnitudes were first corrected for the atmospheric extinction by subtracting a term kX, where X is airmass and k is the atmospheric extinction coefficient with the values of 0.182, 0.102 and 0.046 for g', r' and i', respectively. The zero-point for a given CCD is the difference between the object's corrected magnitude measured from a standard star field exposure and the catalog value. The zero-point for each CCD was kept constant for the whole night, only correcting for the varying airmass.

Fornax is poorly covered with stellar catalogs (in the optical) which could be used to check the accuracy of the photometric calibration. The American Association of Variable Star Observers Photometric All-Sky Survey catalog (APASS, Henden et al. 2012) is the only catalog with a large coverage over our observed Fornax fields. However, as the photometric errors of stars in this catalog with $M_{r'} > 16$ mag are as high as 0.05 mag, and because the photometric accuracy of our data is expected to be better than that, we did not use APASS for comparison. We made principal color analysis in a similar manner as was done for the Sloan Digital Sky Survey (SDSS) data by Ivezić et al. (2004). We did this test for the stacked $1^\circ \times 1^\circ$ mosaics. We measured standard deviations of 0.035, 0.029, and 0.046 mag for the widths of the stellar locus principal colors s, w and x. The corresponding values for SDSS are 0.031, 0.025, and 0.042 mag. The offsets of stellar locii are -0.009, 0.003, and 0.009 mag for s, w and x, respectively. The typical rms scatter of the same offsets for SDSS are 0.007, 0.005, and 0.009 mag for s, w and x showing that our photometric accuracy is comparable to that of the SDSS. Zeropoint errors for SDSS are 0.01, 0.01, and 0.02 mag for g', r' and i' (Ivezić et al. 2004). As the scatter in the stellar locii measured from our data is $\approx$ 10 % larger than in SDSS, we estimate that our photometric errors are 0.02, 0.02, and 0.03 mag in g', r' and i'-bands, respectively.

2.3.4 CREATING MOSAICS

After the astrometric and photometric calibrations, the images were sampled to 0.20 arcsec pixel size and combined using the SWarp software (Bertin 2010). Before combining the images cosmic rays and bad pixels were removed using the weight maps. Regardless of this removal of contaminated pixels, the resulting pixel distribution in the final mosaic were often non-Gaussian. To obtain better stability against outlier pixels, we decided to use median instead of mean when combining the mosaics. In order to achieve maximal depths in the images, the mosaics were combined from all the overlapping exposures. As a result the pipeline produces $1^\circ \times 1^\circ$ mosaics with a 0.2 arcsec pixel resolution, and the corresponding weight images. The pixel values $W_{x,y}$ for the final weight mosaic are obtained as (Kendall & Stuart 1977):

$$W_{x,y} = \begin{cases} \frac{2}{\pi}\left(\frac{\sum_k \sqrt{w_k}}{n_{\neq 0}}\right)^2 \left(n_{\neq 0} + \frac{\pi}{2} - 1\right), \text{ if } n_{\neq 0} \text{ is even} \\ \frac{2}{\pi}\left(\frac{\sum_k \sqrt{w_k}}{n_{\neq 0}}\right)^2 \left(n_{\neq 0} + \pi - 2\right), \text{ otherwise.} \end{cases} \tag{2.2}$$

where $W_{x,y}$ is the weight of the median in a re-sampled mosaic pixel,$\sum_k$ is a sum over all the images that overlap with the pixel, w_k is the weight value in the image k, and $n_{\neq 0}$ is the number of non-zero pixels.

2.4 CATALOG OF LOW SURFACE BRIGHTNESS OBJECTS

2.4.1 QUANTITATIVE SELECTION CRITERIA

We aim to identify and classify the LSB galaxies in the selected Fornax fields, in particular the extended UDGs. According to our experience (see also Muñoz et al. 2015 and Müller et al. 2015), automatic detection using for instance SExtractor at low surface brightness levels is at present not as reliable as the eye, so that the catalog was created by visually inspecting the images (done by AV). In future this catalog can be used as a control sample to test the completeness of any automatic detection method. Our sample includes diffuse sources fulfilling the criteria listed below, in other words we are deliberately excluding compact galaxies with the r'-band central surface brightness of $\mu_{0,r'} < 23$ mag arcsec^{-2}. Most of the galaxies with surface brightnesses brighter than that are already identified in the Fornax Cluster Catalog (FCC; Ferguson 1989b) or can be easily found with automatic detection algorithms.

The selection criteria for the sources are:

1. **Low surface brightness**: the object has a central r'-band surface brightness of $\mu_{0,r'} \gtrsim 23$ mag arcsec^{-2}.
2. **Extended:** the object has a diameter of $d_{27} \gtrsim 10$ arcsec (corresponding to 0.9 kpc) in the r'-band, at the surface brightness level of 27 mag arcsec^{-2}. So, we excluded small dwarf galaxies, and sources too faint for any reliable fitting of the surface brightness profiles. The Point Spread Function (PSF) for a source with a central surface brightness of $\mu_{0,r'} = 23$ mag arcsec^{-2} has $d_{27} < 4$ arcsec, so that there is no danger to mix faint stars with objects.

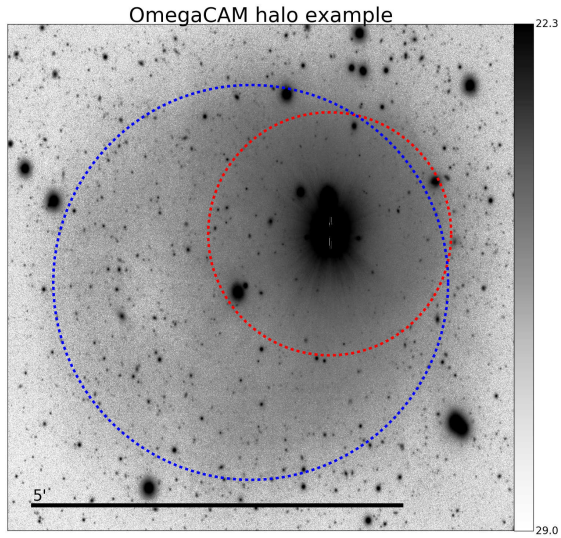

Figure 2.3: Example of the reflection halo of OmegaCAM in an r'-band mosaic image. The position of the reflection halo (marked with the blue dashed line) depends on the location of its parent star (red dashed line) on the instrument's focal plane. Objects residing within the red and blue dashed circles are excluded from the sample due to the halo contamination. The surface brightness of the area highlighted with the blue circle is ∼15 magnitudes fainter than the peak surface brightness of the source star (Capaccioli et al. 2015). In typical seeing conditions, the stars brighter than $\mathrm{m}_{r'} = 8.3$ mag have central surface brightness of $\mu_{0,r'} = 9$ mag arcsec^{-2}, which will cause a halo with the surface brightness of 24 mag arcsec^{-2}. In the studied 4 deg^2 area, there were ∼40 stars bright enough to cause halos which had to be excluded. The colorbar corresponds to the surface brightness in the image in units of mag arcsec^{-2}.

3. **Multi-band detection:** the object can be recognized visually, and it has similar shapes in g', r' and i'-bands.
4. **No contamination from bright sources:** we excluded all the areas which have severe contamination from stellar halos (see Fig. 2.3) meaning that the overlapping halo is brighter than 24 mag arcsec^{-2}. This is to make sure that possible halo patterns are not confused with sources or cause biases to the photometry. In the vicinity of bright and extended galaxies like NGC 1399, we included only objects, which are located outside the 24 mag arcsec^{-2} isophotes of the bright galaxy.

The identification criterion 1 was set to guarantee that also faint sources possibly omitted in the previous studies, are systematically identified. The objects

with the lowest surface brightness in FCC have $\mu_{0,B} \approx 24$ mag arcsec^{-2}, which corresponds to $\mu_{0,r'} \approx 23$ mag arcsec^{-2}. The galaxies fainter than this limit have been only rarely mapped before (Muñoz et al. 2015, Hilker et al. 2003, Bothun et al. 1991, Mieske et al. 2007 and Kambas et al. 2000).

2.4.2 ACCOUNTING FOR IMAGING ARTEFACTS

Due to their low surface brightness true objects can easily be confused with imaging artifacts, such as residuals from the background subtraction, or faint reflections from the instrument's optics. The criterion 3 was set to filter out such false detections.

OmegaCAM, like many other wide-field instruments such as MegaCAM, is known to have strong halos (see Fig. 2.3) around bright stars, caused by reflections from the secondary mirror. These halos appear on the extension of the line connecting the bright source and the focal point of the CCD array. They are easy to identify as they are always associated with a bright star, and their brightness scales with that of the source. The criterion 4 ensures that these reflections will not bias our photometric analysis.

OmegaCAM is also known to have cross-talk between the CCDs 93-96 (see OmegaCAM user manual[3] provided by ESO), which can lead a bright source (a star or a galactic nucleus) to appear as a faint ghost image in an adjacent CCD. The cross-talk can manifest either as positive or negative patterns, which have the same shape as the object causing that pattern. The negative crosstalk cannot be confused with the sources, but the positive crosstalk, ending up to 4 % of the surface brightness of the source causing it, is more problematic. A crosstalk pattern may therefore have the same appearance as a faint diffuse source. However, as the crosstalk appears always in the same pixels in both CCDs, it is possible to identify that pattern by looking for a bright source with a similar shape within a distance of 7.5 arcmin. Even if a faint source appears in all three bands with a similar shape, it does not automatically exclude the possibility of being a crosstalk ghost. Indeed, in the vicinity of bright point sources the shapes and locations of the LSB sources always need to be compared with possible crosstalk sources.

Earlier works, such as that by Duc et al. (2015) have shown that Milky Way's dust (cirrus) can be easily confused with LSB galaxies or streams. However, Iodice et al. (2016) showed that neither cirrus nor zodiacal light can cause contamination to the images in the Fornax cluster.

2.4.3 PRODUCING THE OBJECT CATALOG

The four fields used in this study were inspected visually to detect the sources (see Fig. 2.4). They were first identified from the 4×4 re-binned images and then from the unbinned r'-band images. Using both re-binned and unbinned images helped detecting LSB galaxies and structures in different intensity scales. As the objects were identified and selected visually, some of the smallest objects in our

[3]https://www.eso.org/sci/facilitiess/parnal/instruments/omegacam/doc.html

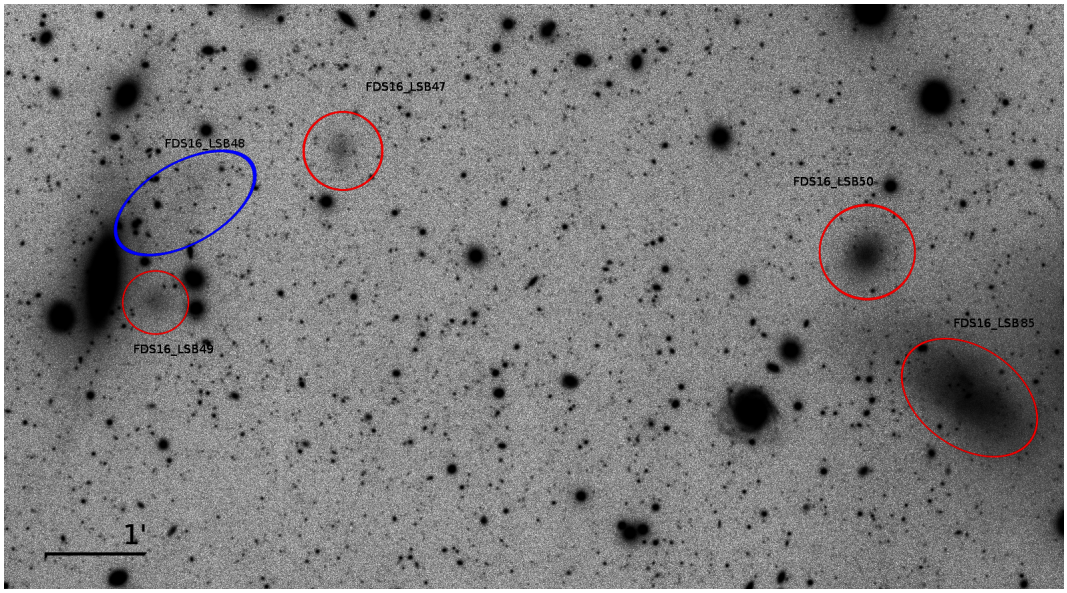

Figure 2.4: r'-band cut from the field 16. In the image north is up and east is left. The red ellipses mark the objects which were classified as galaxies. The blue ellipse shows an object which was identified as a tidal feature. In the case of FDS16_LSB48, the object is not classified as a galaxy as it is asymmetric, has no clear center, and is connected to the nearby galaxy at its South-East side. The galaxies FDS16_LSB50 and FDS16_LSB85 appearing on the right are already identified in Bothun et al. (1991) as F2L7 and F2L8. Also several brighter galaxies appear in the image, but they do not match the surface brightness criteria of our sample. The image is shown in the same logarithmic scale used for the identification with lower and upper limits of -1×10^{-12} ADU pix^{-1} (or "-26.5" mag arcsec^{-2}) and 4×10^{-11} ADU pix^{-1} (or 22.5 mag arcsec^{-2}), respectively.

sample do not fulfil the criterion 2 after taking into account the effects of the *PSF*. However, as they are yet LSB galaxies, they are included in the analysis. We used the field definitions and running numbers to name the objects: for example, the sources found within the field 11 are called as FDS11_LSBn, where n is replaced with a running number.

After detection, the coordinates of the object were stored and postage stamp images (see Fig. 2.5 for an example) were cut in all three bands. The size of the image was adjusted manually to be at least eight times the isophotal (d_{27}) diameter of the object so that a sufficient number of background pixels are included, but as little as possible light is coming from the other sources. The maximum size was limited to 500 $\times$ 500 pixels (corresponding to 1.7 arcmin $\times$ 1.7 arcmin) to make the data easily editable. The postage stamps which were larger than the maximum size were rebinned to fit the limits.

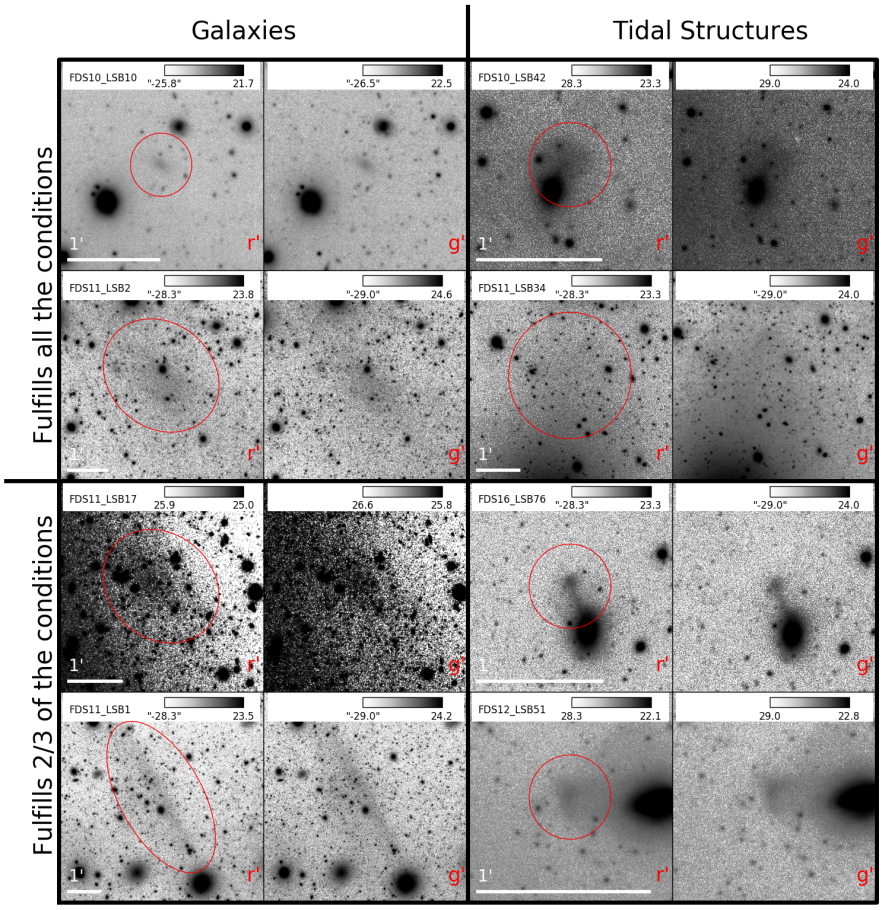

Figure 2.5: Left two columns show g'- and r'-band cut-outs of objects (highlighted with the red ellipses) classified as galaxies. Correspondingly the two rightmost panels show examples of tidal structures. The two top rows show typical examples of both classes, which fulfill all three classification criteria of their classes. The two lower rows show examples of objects which only fulfill two of the three criteria of their classes. Specifically: FDS11_LSB17 has a center with excess light and symmetrical shape, but overlaps with the outskirts of NGC1399. FDS11_LSB1 has a very elongated shape, but still has radially fading light profile away from its center, and it is not connected to any nearby galaxies. FDS12_LSB51 has an area with excess light which could be called a center, but its irregular shape and strong connection to the larger galaxy next to it makes it a tidal structure. The criteria for classifying FDS16_LSB76 as a tidal structure are the same as for FDS12_LSB51.

After checking the original mosaic for possible crosstalk or false detections, masks were generated using SExtractor (Bertin 2010). All the sources were

masked, and a 2D-plane with three degrees of freedom (intensity level and gradients along the x- and y-axes) was least square fit to the masked image and subtracted. This gives the first order approximation for the background level, and helps in judging whether a faint structure is real or not. We emphasize here that this model is not the final background model used for photometry, but only for editing the masks and identifying the object. If necessary, the masks were then modified, as in some cases the SExtractor masks were partly masking also the galaxy, or were not masking the *PSF* wings properly.

A total of 251 diffuse sources were initially identified from the four inspected fields. From this sample 17 objects are considered as imaging artifacts or they are too faint to be analyzed properly, leaving a sample of 234 objects. As discussed in the next section, 205 of these appeared to be galaxies.

2.4.4 DISTINGUISHING GALAXIES FROM TIDAL STRUCTURES

In this work we are particularly interested in the effects of the environment on the properties of LSB galaxies, and therefore want to exclude structures which most probably are tidal debris of an ongoing interaction. Therefore, the objects are classified either as galaxies or tidal structures based on their appearance. At this stage this distinction is qualitative and has an intrinsic uncertainty that is impossible to remove without spectroscopic data. We are aware of the possibility that some of the galaxies might have been born as a result of stripped tidal debris (Bournaud 2010), a possibility which is not ruled out in our approach.

In our classification galaxies can be identified as separate objects from their surroundings. They are structures that have distinguishable centers with excess light, and/or have apparent symmetry. Nevertheless, an irregular structure which is not connected to any other nearby sources will still be classified as a galaxy. Tidal structures have elongated or irregular shapes. They are typically connected to a pair or a group of galaxies that have disturbed appearance. They do not have a center with excess light. A structure that has a connecting bridge with another object is a galaxy if it has a clear center, but is otherwise classified as a tidal structure.

The classification criteria for both classes are listed in Table 2.1. As the objects appear in a variety of shapes it is not always immediately clear in which group an object should be classified. Therefore, a peculiar object is classified to the class where it fulfills at least two of the criteria. Examples of objects belonging to the two classes are shown in Fig. 2.5. From the total sample of 234 objects 205 are classified as galaxies and 29 as tidal structures. We compared these galaxies with the catalogs of Muñoz et al. (2015), Mieske et al. (2007), Bothun et al. (1991), and Ferguson (1989b). 59 of our galaxies are not included in any of those catalogs and are therefore new identifications.

Table 2.1: Definitions of the two classification classes used. The objects that fulfill at least two of the criteria in a class, are classified as a members of that class.

	"Galaxy"	"Tidal structure"
Center with excess light	yes	no
Connected to other objects	no	yes
Symmetric	yes	no

2.5 STRUCTURAL PARAMETERS AND PHOTOMETRY

We used the calibrated r'-band postage stamp images to measure the effective radius (R_e), the apparent magnitude ($m_{r'}$), and the minor-to-major axis ratio (b/a), for all identified galaxies. Two different methods were used. In the first method we produced the radial light profile for each galaxy using azimuthally averaged bins, and then fit the 1D-profile with a single Sérsic function. In the second method, we used GALFIT 3.0 (Peng et al. 2010, 2002) for fitting the 2D flux distribution of the galaxy, again using a single Sérsic function, and if needed an additional *PSF* component was fit to the nucleus.

2.5.1 AZIMUTHALLY AVERAGED SURFACE BRIGHTNESS PROFILES

Radial profiles can be defined by fitting the isophotes with a series of ellipses leaving the center, axis ratio, and position angle as free parameters. However, since the S/N of the galaxies in our sample is low, the shape of the ellipses in this approach becomes unreliable in the galaxy outskirts. To prevent this from affecting the measured profiles, we decided to use fixed ellipticity for the elliptical annuli based on pixel value distribution moments. Also, as the galaxies we study typically do not have well defined central peaks, a special approach was needed for defining the centers.

The center of the galaxy and its shape were defined using pixel distribution moments. A detailed description of the method can be found in Appendix 2.11.1. In the measurement of the profiles, we used a radial bin width of 4 pixels, or 0.8 arcsec (for comparison the *FWHM* of the *PSF* is $\approx$ 1.1 arcsec, see Fig. 2.6 below). The adopted bin width ensures that the bins are small enough to be able to capture the changes in the radial shape of the profile. The radial bins extend to the distance where the intensity level within the bin drops to 1/3 of the pixel-to-pixel background *RMS*, which typically corresponds to $\mu_{r'} \sim 28$ mag arcsec^{-2}. All the masked pixels are rejected, and three times σ-clipped averages are used as the bin values. For the error of the bin we adopted the standard deviation of the non masked pixels within the bin, divided by the square root of number of the pixels.

At this point the images may still include some positive or negative residual sky, since the initial sky fit was done using SExtractor masks which often fail to cover the faint outskirts of the sources. For the final sky level we used the value measured at the radius of 4 R_e. The value of R_e was obtained from the cumulative

light profile, and the sky level was measured from an 8 pixel wide galactocentric annulus, placed at r = 4 R_e. The annulus was divided into 20 azimuthal sectors, and a median of each sector was taken. Finally we used four times σ-clipped average of the medians as the residual sky value, which was then subtracted from each bin.

The sky corrected azimuthally averaged radial profiles were fit with a single Sérsic function using intensity units:

$$\mathrm{I(r)} = \mathrm{I}_e \exp\left[-\mathrm{b}_n \left(\frac{\mathrm{r}}{\mathrm{R}_e}\right)^{\frac{1}{\mathrm{n}}} - 1\right], \tag{2.3}$$

where R_e is the effective radius, I_e is the surface brightness at R_e, and n defines how peaked the Sérsic profile is. The parameter b_n depends on n as $\Gamma(2\mathrm{n}) = 2\gamma(2\mathrm{n}, \mathrm{b}_n)$, where Γ and γ are the complete and incomplete gamma functions, respectively (Sersic 1968, Ciotti 1991). While least-square fitting the Sérsic function, the radial bins were weighted with their inverse variances. The values for R_e, n and the total apparent magnitude $\mathrm{m}_{r'}$ were obtained from the 1D-Sérsic fit. Those values were also used as the initial values of the Sérsic profile in the GALFIT models.

2.5.2 GALFIT MODELS

GALFIT has been successfully used in several works to model the 2D light-distributions of bright galaxies (see e.g., Peng et al. 2010, Salo et al. 2015 and Hoyos et al. 2011) and also those of faint galaxies (Janz et al. 2012, 2014). However, Muñoz et al. 2015 claim that for the low surface brightness galaxies not all of their fits using GALFIT converged. Nevertheless, in this study we have successfully fit all our sample galaxies with GALFIT, to obtain R_e, m'_r, n and b/a. Most likely our success stems from using good initial parameters in GALFIT obtained from the 1D fits.

GALFIT is capable of fitting several components simultaneously, taking into account the effects of the *PSF* and proper weighting of the data. The weights created during the data reduction were used for obtaining the σ-images needed for the GALFIT fits. The pixel value $\sigma_{i,j}$ for the σ- image is calculated as follows:

$$\sigma^2_{i,j} = \frac{1}{W_{i,j}}, \tag{2.4}$$

where $W_{i,j}$ corresponds to the value of the weight image in pixel coordinate i, j.

While fitting with GALFIT it is possible to convolve the models with a given *PSF*-image. In order to take into account the variations of the *PSF*, we made a separate model for each field. We used SExtractor to detect and select the stars to be used for the model. SExtractor has a parameter *CLASS_STAR*, which indicates the probability of an object to be a star (see Bertin & Arnouts 1996 for details). We selected the objects with *CLASS_STAR* > 0.8. We also excluded saturated and faint stars from the stack by using SExtractor's automatic aperture photometry

MAG_AUTO. As the stars brighter than 15 mag are typically saturated, we included only the stars with 16 mag $<$ *MAG_AUTO* $<$ 19 mag. A pixel area 101 $\times$ 101 pixels was cut around each star, and normalized by the total flux within it. All the cut images were then median combined to get an average *PSF* model. As the background has been subtracted in the images already in the reduction, we do not apply further background subtraction at this point. Any possible contamination from the nearby objects in the *PSF* - stack is averaged out when the stack is median combined. Fig. 2.6 shows an example of the stacked model (for field 11) as well the best fit Gaussian and Moffat (Moffat 1969) models. We decided to use the stacked model, as particularly the Gaussian function fail to fit the faint outermost parts of the *PSF*. We did not take into account the *PSF FWHM* variations within the $1^\circ \times 1^\circ$ fields, as we found them to be less than 10% (consistent with de Jong et al. 2015).

Initially, we fit all the images using a single Sérsic function as a model for the galaxy, and a plane with three degrees of freedom (intensity level and gradients along the x- and y- axes) as the sky component. The parameters for R_e, $\mathrm{m}_{r'}$, n, b/a and the center coordinates obtained with the 1D fitting method (explained in Section 5.1), were used as input parameters in GALFIT. All the parameters except for the galaxy center, were fit as free parameters.

In some of the fits the center of the galaxy was initially defined incorrectly. This can be seen as asymmetric residuals, so that part of the galaxy has positive residual values and the other part has negative values. In such cases we fixed all the other fit parameters except for the galaxy center, and let GALFIT to refit the center of the Sérsic profile. After this the center was fixed again and the other Sérsic parameters were fit again. This procedure reduced the fit residuals significantly.

Some of the galaxies show also a peaked nucleus (see the 4th row in Fig. 2.7) which is clearly a separate component in the galaxy center. In such cases, we manually place an additional *PSF*-component to fit the nucleus. The *PSF*-component is added to improve the overall fit of the galaxy rather than aiming for the detailed analysis of the nuclear star clusters. We fit the *PSF*-component using a fixed center position, and leave the total magnitude of the nucleus as a free parameter to fit.

Using the steps described before, our fits converged for all the galaxies in our sample. In the end, we examined the fits for systematics in the residuals, and corrected the ones where the center of the galaxy was wrong or the nucleus was missed. To ensure that the sky components are fit correctly, the radial surface brightness profiles and the cumulative radial profiles were inspected. Specifically we checked that GALFIT does not mix the sky component with the Sérsic profile, which would give unrealistically large effective radii and total magnitudes to the galaxies. The opposite (absorbing galaxy light to sky) is unlikely, since all our images had large areas of background sky not covered by the galaxy.

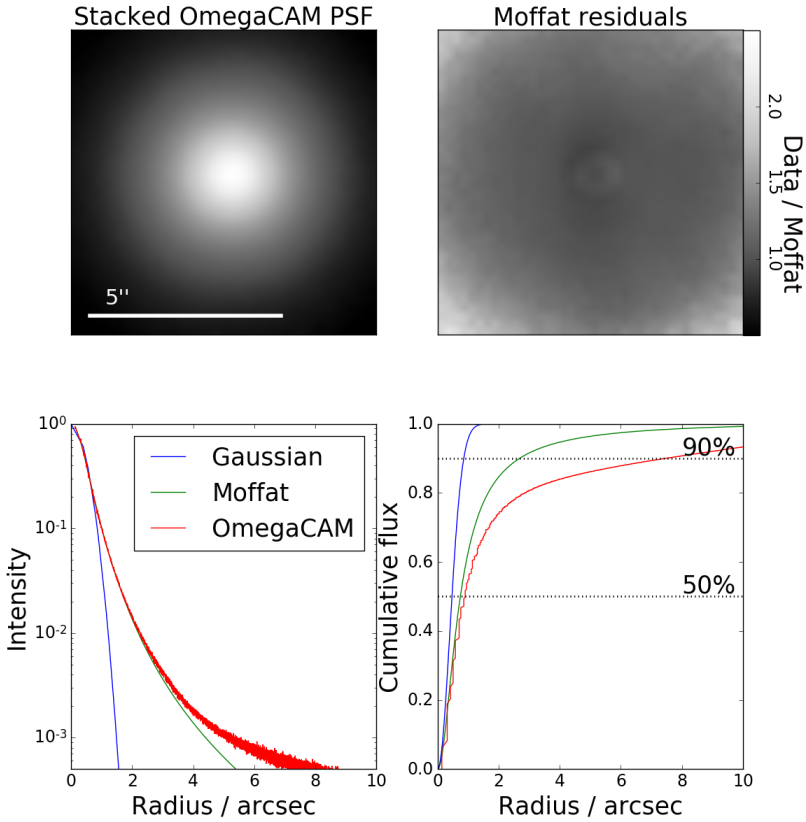

Figure 2.6: Upper panels show the *PSF* images, averaged from the field 11 in the r'-band observations (*upper left*) and the stack model divided with the best fit Moffat model (*upper right*). *Lower left:* the stacked radial intensity profile of the averaged *PSF* (OmegaCAM) is compared with Gaussian and Moffat fits to that profile. All the models are normalized by their central intensity. *Lower right:* cumulative profiles of the average observed *PSF*, and the Gaussian and Moffat fits. The horizontal dotted lines show the levels where 90% and 50% of the light are included.

2.5.3 COMPARISON OF THE 1D AND 2D METHODS

Fig. 2.8 shows a comparison of the Sérsic n-values, axis ratios (b/a), total r'-band magnitudes ($m_{r'}$), and effective radii (R_e) obtained with the two methods. Both methods give similar distributions for the Sérsic n values, although the scatter is significant with RMS = 0.47. The effective radii and magnitudes are well in

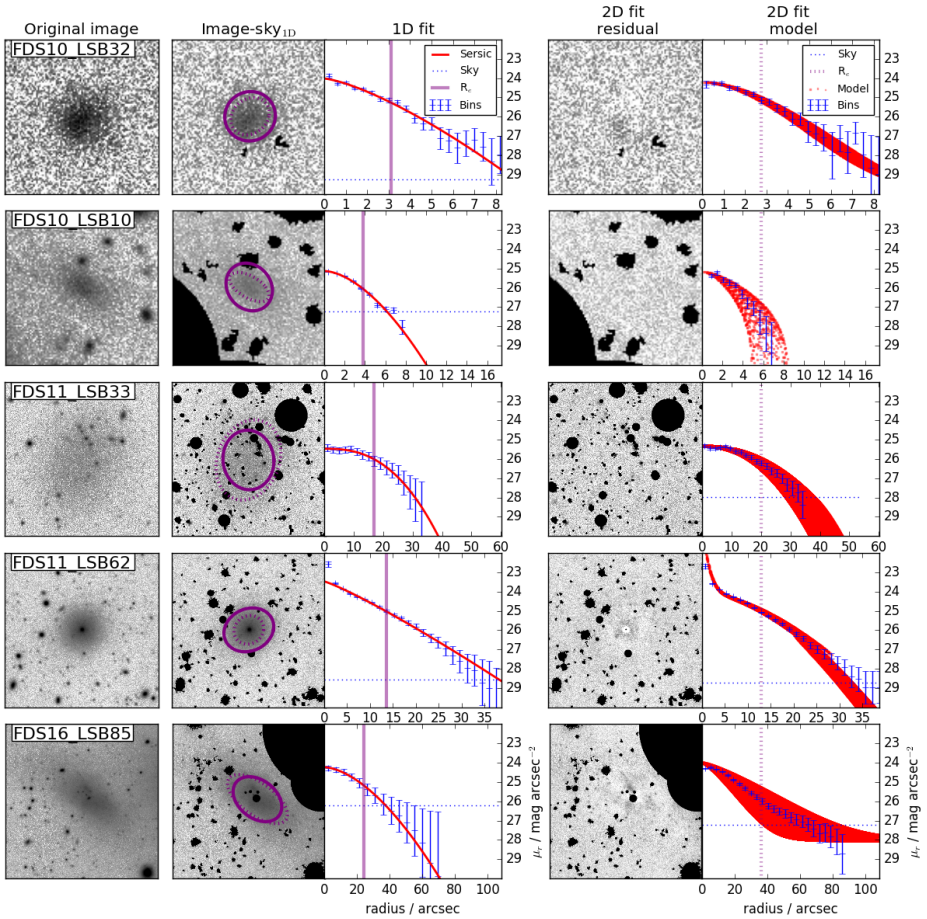

Figure 2.7: Comparison of the two photometric methods for individual galaxies. Explanations for the columns from left to right: The *first frame* shows the r'-band postage image of the galaxy. The *second frame* shows the sky subtracted and masked image, with the elliptical bin shapes at R_e over-plotted using purple color (solid line: shape using pixel distribution moments, dotted line: shape using GALFIT). The *third frame* shows the sky-subtracted 1D radial profile derived using the azimuthally averaged bins, with the Sérsic fit, effective radius (R_e) from 1D fit, and the measured sky level over-plotted. The blue dashed line marks the level of the residual sky measured using the sectors at 4 R_e. The *fourth frame* shows the residual image after subtracting the 2D GALFIT model. The *last frame* shows the azimuthally averaged radial profile measured using the elliptical shape from GALFIT. The red dots correspond to each pixel of the (2D) GALFIT model (pixel value as a function of the distance from the center), the purple dotted line shows the corresponding effective radius, and the blue dotted line shows the sky level from the GALFIT decomposition. The distribution moments fail to measure the actual isophotal shape of the second galaxy from the top. This can be seen as a misalignment between the purple solid ellipse and the actual galaxy shape in the second column image. The fourth galaxy from the top possesses a nucleus, which can be seen as a peak in the radial bins (the 3rd and 5th panels from the left). Only the GALFIT model contrives to fit the nucleus.

agreement in the two measurements (the lower panels of 2.8), except for the four outliers. The outliers are explained due to the different fitting of their background levels in the 1D and 2D methods. Only for the axis ratios b/a a systematic shift appears between the two methods (see upper right panel), so that the values defined using the distribution moments are systematically closer to unity than the ones obtained using GALFIT. By inspecting the residual images, we concluded that the axis ratios obtained by GALFIT resemble more the actual shapes of the galaxies (see e.g., the second row of Fig. 2.7).

As expected, the position angles are similar when both methods show small b/a values. The galaxies which show a large difference between the elliptical shape measured with GALFIT and the distribution moments, are often located near to other sources. GALFIT seems to be more stable in the presence of such disturbances. Therefore, for the analysis we decided to use the values measured with GALFIT. The histogram for R_e values used in the analysis is shown in Fig. 2.9, and the histograms for magnitudes ($m_{r'}$), mean effective surface brightness[4] ($\bar{\mu}_{e,r'}$), axis ratios (b/a), and Sérsic n-values are shown in Fig. 2.10.

We conclude that both of these methods can be used for studying LSB galaxies. However, GALFIT is more accurate in obtaining the axis ratios. Also, as it is capable of correcting for the effect of the *PSF*, it should be used when the intrinsic shapes of these galaxies are analyzed. When comparing the background estimation of these methods, GALFIT has slight advantage as it uses all the non-masked pixels and allows the background to have gradients. However, our observation that the background level of GALFIT can be somewhat degenerated with the outer parts of the Sérsic-profile is clearly an issue that should be acknowledged when this method is used.

2.5.4 ACCURACY OF THE PHOTOMETRIC MEASUREMENTS AND COMPLETENESS OF THE UDG DETECTIONS

2.5.4.1 COMPARISON TO MUÑOZ ET AL. (2015)

We checked how the completeness of the galaxy sample obtained by us compares with that of Muñoz et al. (2015). Since the two samples have a different spatial coverage, we limited the comparison to field 11 (see Fig. 3.2) which is covered by both studies. There are 96 and 62 galaxies located in that field in the samples of Munoz et al. and this study, respectively. 52 of those galaxies are common to both studies. The sample of Munoz et al. has 44 objects that are not included in our sample, which is explained by our selection criteria given in Section 4.1. When these criteria are taken into account, 43 of the 44 galaxies appearing only in the sample of Munoz et al. are excluded[5] from our sample. The remaining object was classified as a tidal structure by us. In that same field, there are ten objects that are not in the sample of Munoz et al., but appear in our sample.

[4]Mean effective surface brightness ($\bar{\mu}_e$) depends on central surface brightness (μ_0) and Sérsic n as $\mu_0 = \bar{\mu}_e + 2.5 \times \log_{10}\left(n/b^{2n} \times \Gamma(2n)\right)$, where b is defined as in equation 2.4. For n=0.5 / 1 / 1.5, central surface brightness is $\mu_0 - \bar{\mu}_e$ = 0.3, -1.1, -2.0 mag arcsec^{-2} respectively.

[5]21 objects are excluded by the criterion 1., 25 objects are excluded by the criterion 2., and 9 by the criterion 4.

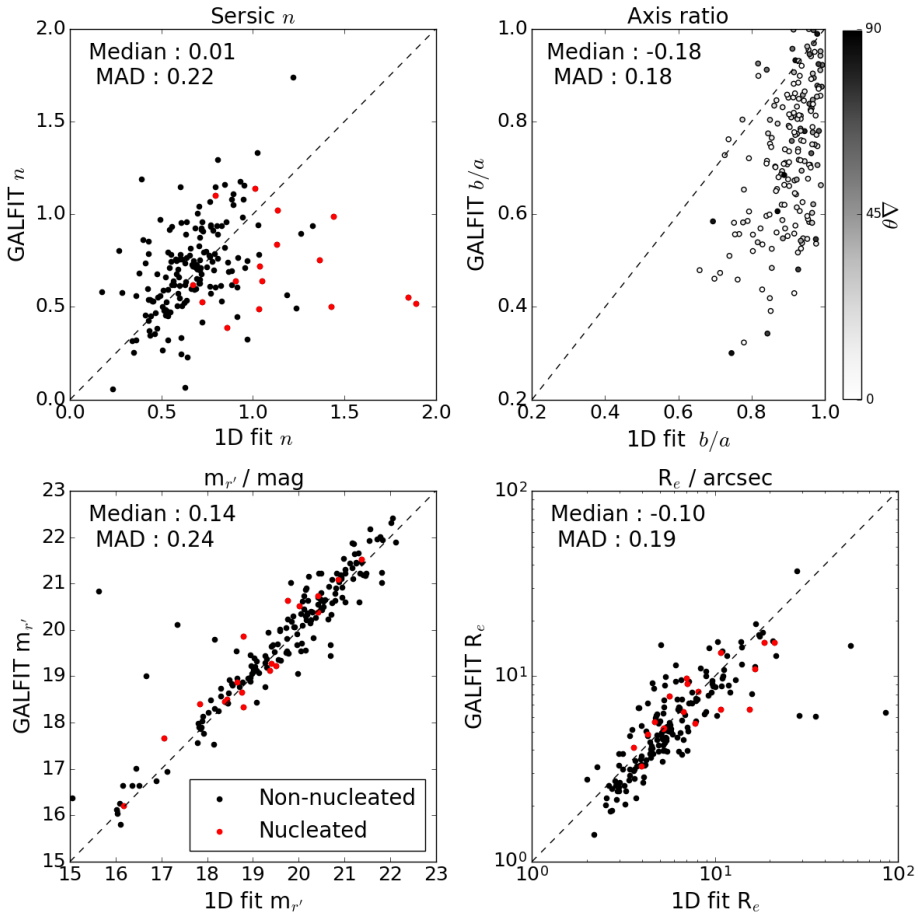

Figure 2.8: Different panels show a comparison of the parameters obtained using the different photometric methods explained in Section 5: the x-axes correspond to the 1D fit and y-axes to the 2D GALFIT model. The upper panels compare the Sérsic n-values (*upper left*) and axis ratios b/a (*upper right*), whereas the lower panels compare the r'-band magnitudes $m_{r'}$ (*lower left*) and the effective radii R_e(*lower right*). The differences in the position angles obtained by the two methods are indicated with gray scale colors in the upper right panel; dark colors correspond to a large difference, and light colors to a small difference. The most obvious difference appears between the b/a-values, which are systematically closer to unity when calculated using the 1D method. The galaxies which have a nucleus are marked in red. The median differences ($n_{2d}-n_{1d}$, $b/a_{2d}-b/a_{1d}$, $m_{r',2d}-m_{r',1d}$, $2\times$($R_{e,2d}$-$R_{e,1d}$)/($R_{e,2d}$+$R_{e,1d}$)), and the corresponding median absolute differences (MAD=$\mathrm{Median}\,(|\mathrm{Median}(x_i) - x_i|)$), where x_i is the difference between 2D- and 1D- measurements) are reported in the upper left corner of the plots.

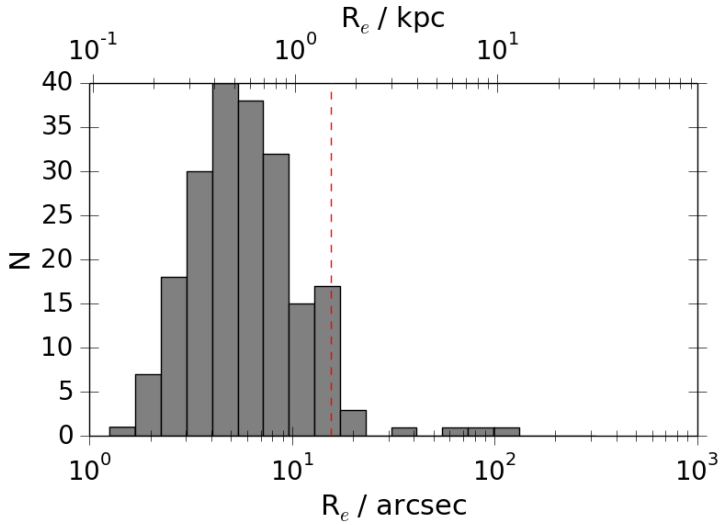

Figure 2.9: Distribution of effective radii (R_e) obtained from the GALFIT fits. The red dashed line shows the 1.5 kpc limit, which divides the galaxies into UDGs and LSB dwarfs.

We also checked how the parameters obtained by us compare with those given in Muñoz et al. (2015), for the 126 sources identified in both studies. In both studies the parameters are obtained using GALFIT. Fig. 2.11 (*right panels*) shows the differences for the galaxies as a function of the surface brightness, and Fig. 2.12 shows a comparison of Sérsic n, R_e and $m_{i'}$ between the two measurements. In order to convert the i'-band magnitudes of Muñoz et al. (2015) to r'-band, we used the median r'-i' aperture color[6] of $\langle$r'-i'$\rangle$ = 0.3 mag from the FDS data, measured within R_e. The measured offsets and their standard deviations are $\Delta m_{i'}$ = 0.3 with σ = 0.3 mag, $\Delta R_e/R_e$ = 0.0 with σ = 0.2, and Δn = 0.0 with σ = 0.2. We find that our R_e and n values are well in agreement with those of Muñoz et al. (2015). However, there is a small offset in the total magnitudes, so that the values measured by us are 0.3 magnitudes brighter.

2.5.4.2 TESTS WITH MOCK GALAXIES

In order to test the completeness of our faint galaxy detections, and the reliability of the parameters obtained for them, we added mock-galaxies to our images. The detection efficiency is tested for UDGs by embedding mock UDGs with their parameters adopted from Mihos et al. (2015) and van Dokkum et al. (2015) to the science images (see Appendix 2.11.2 for details). Additionally, we tested the photometric accuracy of our measurements for the UDGs and LSB dwarfs using

[6] r'-i' = 0.3 is consistent with the Virgo red sequence between -13 mag > $M_{g'}$ > -16 mag (Roediger et al. 2017), where the values are between 0.2 mag and 0.3 mag.

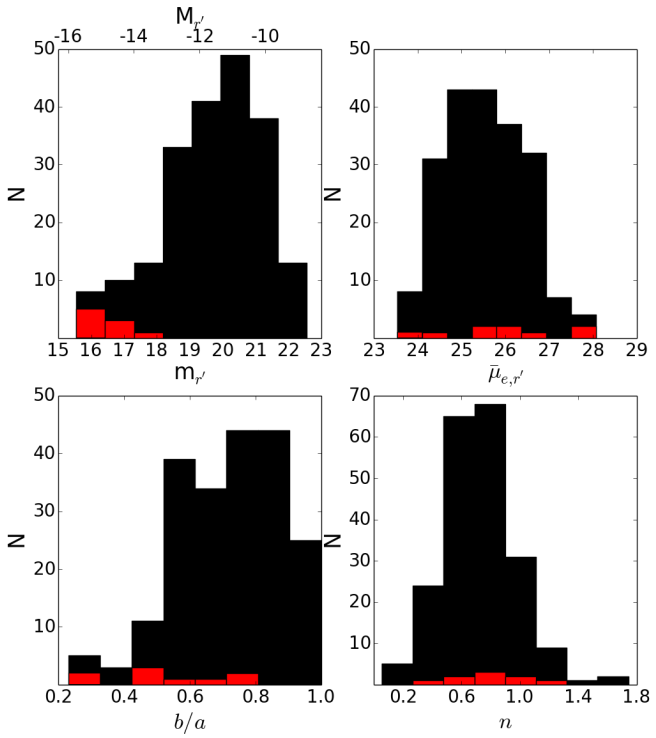

Figure 2.10: Histograms of the apparent magnitudes $m_{r'}$ (*upper left panel*), mean effective surface brightnesses $\bar{\mu}_{e,r'}$ (*upper right panel*), axis ratios b/a (*lower left panel*), and the Sérsic n-values (*lower right panel*) obtained with GALFIT. The black histograms show the distributions for the total sample, and the red histograms those for the UDGs.

Table 2.2: Fit parameters of equation 2.5, which is used to estimate the 1σ-deviations of the photometric parameters as a function of the mean effective surface brightness.

Fit parameters:	α	β
$\sigma_{\rm m}$	0.1829	-5.3650
$\log_{10}(\sigma_{\rm R_e})$	0.0945	-3.2528
$\log_{10}(\sigma_{b/a})$	0.1494	-5.1128
$\log_{10}(\sigma_n)$	0.0307	-1.5330

additional $\sim$150 mock galaxies with parameters typical for the galaxies in the sample of Muñoz et al. (2015). The parameter ranges of the used mock galaxies are shown in Appendix 2.11.2.

The detection efficiency for UDGs is tested by embedding mock UDGs with parameters adopted from 16 representative UDGs from Mihos et al. (2015) and van Dokkum et al. (2015), to the r'-band science images of all the studied fields one by one. They were distributed randomly across the image and their coordinates were stored. After embedding the mock galaxies, the image was inspected and the sources were identified (see Section 4). In this test, we failed to find only one UDG, which should have been detected according to our selection criteria. This UDG was not detected as it was overshadowed by the diffuse light of a nearby star and the outskirts of a galaxy. The results of this test for different fields are listed in Appendix 2.11.2. The test shows that our data and the visual detection is efficient ($\approx$92% efficiency) in detecting UDGs such as those presented in van Dokkum et al. (2015) and Mihos et al. (2015).

We made GALFIT fits for all the mock galaxies described in Appendix 2.11.2. The photometry was performed as described in Section 5.2 Fig. 2.11 collects the differences in $\rm m_{r'}$, $\rm R_e$, b/a, and Sérsic n, between the original and measured values (red and black dots), for all identified mock galaxies. Any possible systematic shifts are negligible in all studied parameters. The measured offsets are $\Delta \rm m_{r'}$ = 0.00 mag, $\Delta \rm R_e/R_e$ = 0.01, Δ (b/a) = 0.00, and Δ n = -0.01.

To characterize the typical uncertainties of the fit parameters, we tabulate the 1σ-deviations in Fig. 2.11 as a function of the mean effective surface brightness. Similarly as Hoyos et al. (2011), we fit these intrinsic standard deviations (σ) , which we assume to follow a Gaussian distribution, with a simple linear function:

$$\log_{10}(\sigma) = \alpha \times \bar{\mu}_{e,r'} + \beta, \tag{2.5}$$

where α and β are free parameters. The fit results are listed in Table 2.2, and the error estimates for the individual galaxies are given with their other photometric parameters in the Appendix 2.11.4.

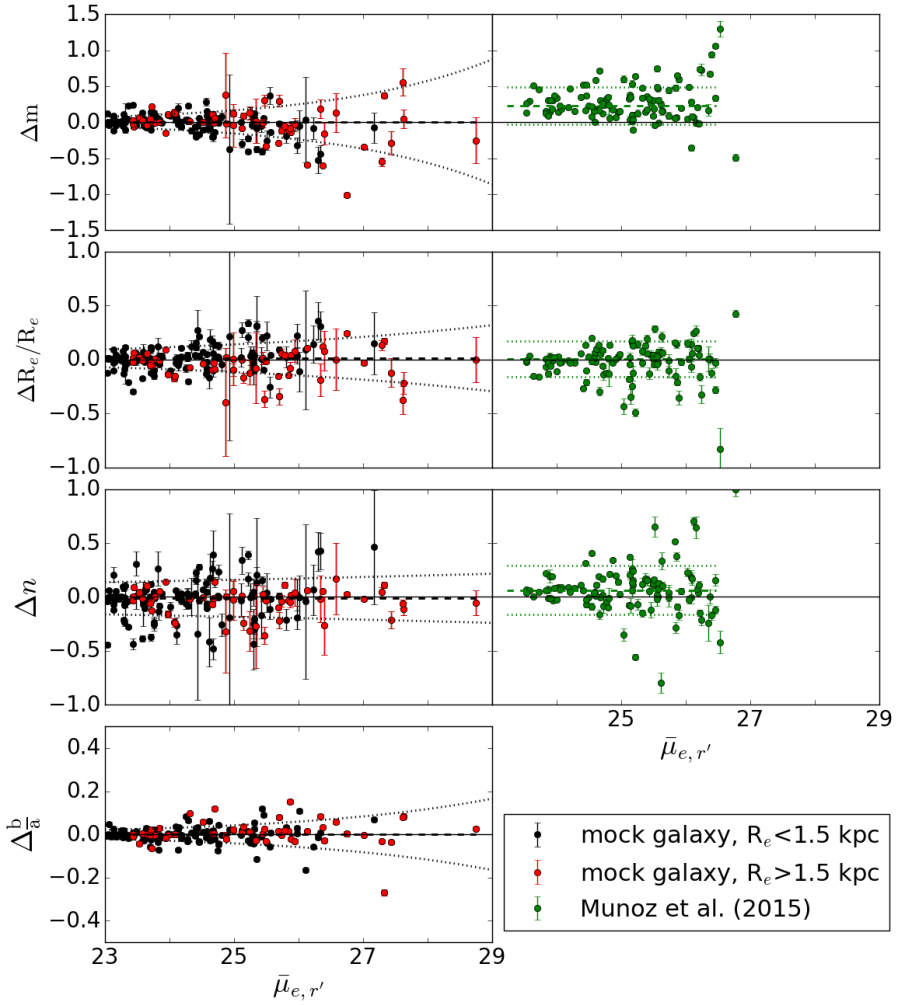

Figure 2.11: Left panels show the difference between the input and output parameters for the mock galaxies. The mock galaxies with effective radii $R_e > 1.5$ kpc, and those smaller than that are plotted with red and black dots, respectively. From top to bottom they show the differences (input - output) of apparent magnitudes (Δm), effective radii ($\Delta R_e/R_e$), and values of the Sérsic n (Δn), as a function of the mean effective surface brightness $\bar{\mu}_e$. The right panels compare our measurements with the values measured by Muñoz et al. (2015) for the galaxies common in the two studies. The differences in axis ratios ($\Delta \frac{b}{a}$) are only shown for the mock galaxies, since these values are not available for the galaxies of Munoz et al.. Since the magnitudes in Muñoz et al. (2015) are in i'-band, we have added the median r'-i' color of 0.3 mag to their values before the comparison. The errorbars represent the formal errors from our GALFIT fits. The dotted lines in the left panels show the 1σ-deviations given by the equation 2.5. In the right panels, the dotted lines show the standard deviations of the differences of the compared measurements. The dashed lines show the mean differences between the compared values.

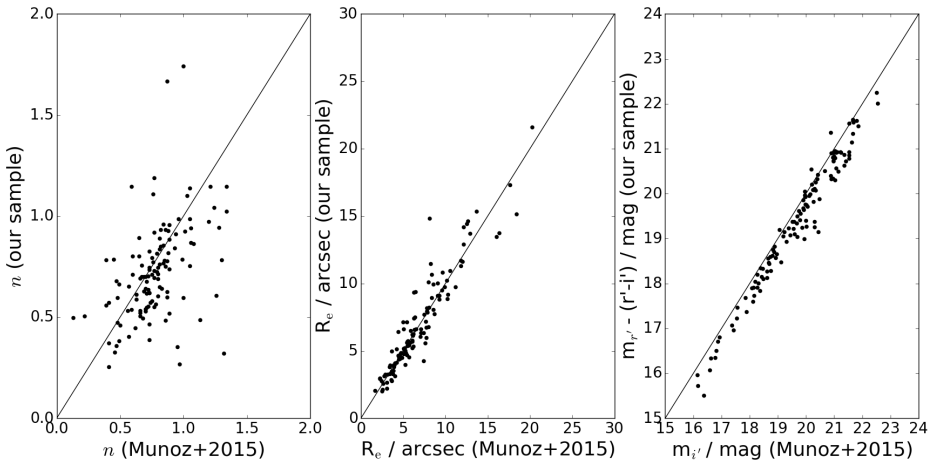

Figure 2.12: Comparison of the effective radii R_e, apparent i'-band magnitudes m'_i, and the values of Sérsic n of the LSB galaxies, as obtained by Muñoz et al. (2015) and by us for the same galaxies. The median r'-i' color of the objects was used to transform our r'-band magnitudes to i'-band magnitudes. The black diagonal line shows the 1/1 ratio. The plots show that even though the scatter in n (standard deviation: 0.24) is fairly large, R_e and $m_{i'}$ still match very well with each other. In both works, GALFIT fits were used.

2.6 LOCATIONS AND ORIENTATIONS OF LSBS WITHIN THE FORNAX CLUSTER

2.6.1 RADIAL NUMBER DENSITY PROFILE

The locations of the galaxies identified by us in the four Fornax cluster fields are plotted over the combined i', r', and g'-band image in Fig. 2.2. As explained in Section 4.1, we masked all the areas covered by stellar halos or bright extended galaxies. Then a cluster-centric radial surface density profile was made by counting the number of objects in radial bins and dividing those numbers by the non-masked area within each bin. The number density profile and the corresponding cumulative profile are shown in Fig. 2.13. We used NGC 1399 as the center of the cluster, since the hot intra-cluster x-ray gas is centered to it (Paolillo et al. 2002). Also, the smoothed FCC galaxy number density distribution peaks on top of NGC 1399 (Drinkwater et al. 2001a).

We make a comparison between the radial distribution in the cluster of the LSB dwarf galaxies identified by us, and that of the FCC galaxies (see Fig. 13). For the FCC galaxies we used those classified as "confirmed" or "probable cluster members" in Ferguson (1989b). It appears that the LSB galaxies of this study are less centrally concentrated than the more luminous FCC galaxies. The Kolmogorov-Smirnov (K-S) test gives a p-value of 0.032 for the assumption that the two distributions are from the same underlying distribution, indicating that the difference is statistically

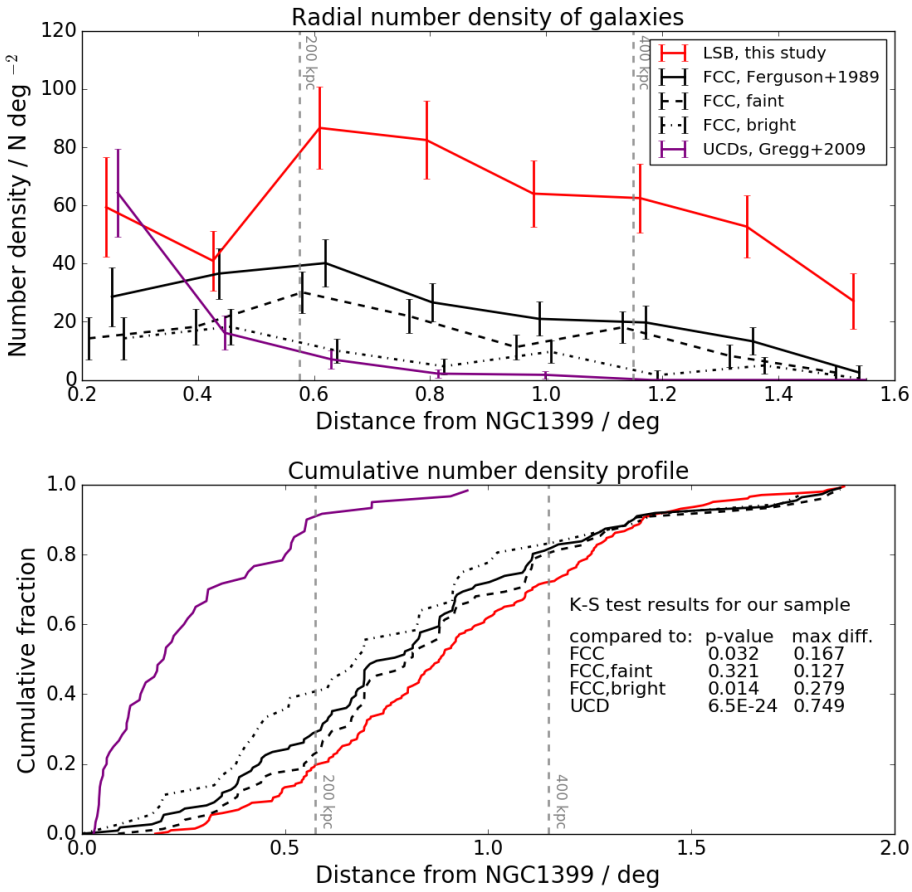

Figure 2.13: Radial number density profile of the LSB dwarfs in our sample (red line) is compared with that of all galaxies in FCC (black line). We plot also the Ultra Compact Dwarfs from Gregg et al. (2009; purple line). Plotted separately are also the high surface brightness (with $\bar{\mu}_{e,r'} < 23$ mag arcsec^{-2}) and low surface brightness ($\bar{\mu}_{e,r'} > 23$ mag arcsec^{-2}) galaxies from FCC, indicated by semi-dotted and the dashed lines, respectively. The results of the K-S tests comparing our sample distribution with those of the other surveys are listed in the lower right corner of the lower panel.

significant (p<0.05). In principle there can be a bias in this comparison, because the FCC galaxies are identified also on top of the halos of bright stars and galaxies, which areas were excluded in our study. However, such bias would affect our result only if the galaxies in the central parts of the cluster were more concentrated to the halos of bright galaxies than to the surrounding fields.

We further divided the FCC into bright galaxies with mean effective surface brightness $\bar{\mu}_{e,r'} < 23$ mag arcsec^{-2}, and to faint galaxies with $\bar{\mu}_{e,r'} > 23$ mag

arcsec^{-2}. By comparing the radial distributions of the galaxies in these two bins shows that the bright FCC galaxies are more centrally concentrated than the galaxies in our sample (K-S test p-value = 0.014). When comparing the radial distributions of the faint FCC galaxies with our sample galaxies, the K-S test gives a p-value of 0.32. This p-value means that these two distributions are not statistically different, which is expected as these two samples have several galaxies in common.

2.6.2 ORIENTATIONS

The orientations for the individual galaxies in our sample are shown in Fig. 2.14, where over-plotted are also the locations of the FCC galaxies in the same field. The relative orientations with respect to the cluster center and the closest FCC galaxy with $\mathrm{M_{r'}} <$ -18 mag[7] are plotted in Fig. 2.15. However, as the galaxies with $b/a \sim 1$ may cause additional noise to the orientation plots, thus blurring possible underlying dependencies, only galaxies with $b/a < 0.9$ are considered. It appears that when including all the galaxies up to $b/a = 0.9$, there is no statistically significant preferred alignment, neither toward the closest bright galaxies (p-value = 0.657, for retaining the hypothesis that the alignments are random), nor toward NGC 1399 (p-value = 0.060). However, the galaxies with $b/a < 0.7$ show a weak preferred alignment toward their bright nearby galaxies, for which a K-S test gives a p-value of 0.031.

2.7 COLORS OF THE SAMPLE GALAXIES

We measured the aperture magnitudes in the g', r' and i'-bands for the galaxies in our sample, using the background (GALFIT) subtracted and masked images. However, in this paper we only analyze the g'-r' color, since in these bands the data are the deepest, and give accurate colors for most objects. We used elliptical apertures defined by the parameters obtained from our r'-band GALFIT fits (center coordinates, and $\mathrm{R}_{e,r'}$ used as the major axis of the aperture). Instead of using total magnitudes aperture colors were obtained. This is to minimize systematic errors from the sky background determination. As in Capaccioli et al. (2015), we estimate the errors $\sigma_{g'-r'}$ for g'-r' colors as:

$$\sigma^2_{g'-r'} = \sigma^2_{ZP,g'} + \sigma^2_{ZP,r'} + \left(\frac{2.5}{I_{g'}\ln 10}\right)^2 (\sigma_{I,g'} + \sigma_{sky,g'})^2 + \left(\frac{2.5}{I_{r'}\ln 10}\right)^2 (\sigma_{I,r'} + \sigma_{sky,r'})^2, \quad (2.6)$$

where $I_{g'}$ is g'-band mean intensity within the aperture, and $\sigma_{I,g'}$, $\sigma_{sky,g'}$ and $\sigma_{ZP,g'}$ are the errors for the surface brightness, the sky, and the photometric zero point in g'-band, respectively. $I_{r'}$, $\sigma_{I,r'}$, $\sigma_{sky,r'}$ and $\sigma_{ZP,r'}$, are the corresponding quantities in r'-band. For the mean intensity we assumed simple Poissonian

[7]Transformed from B-band, see Appendix 2.11.3 for details.

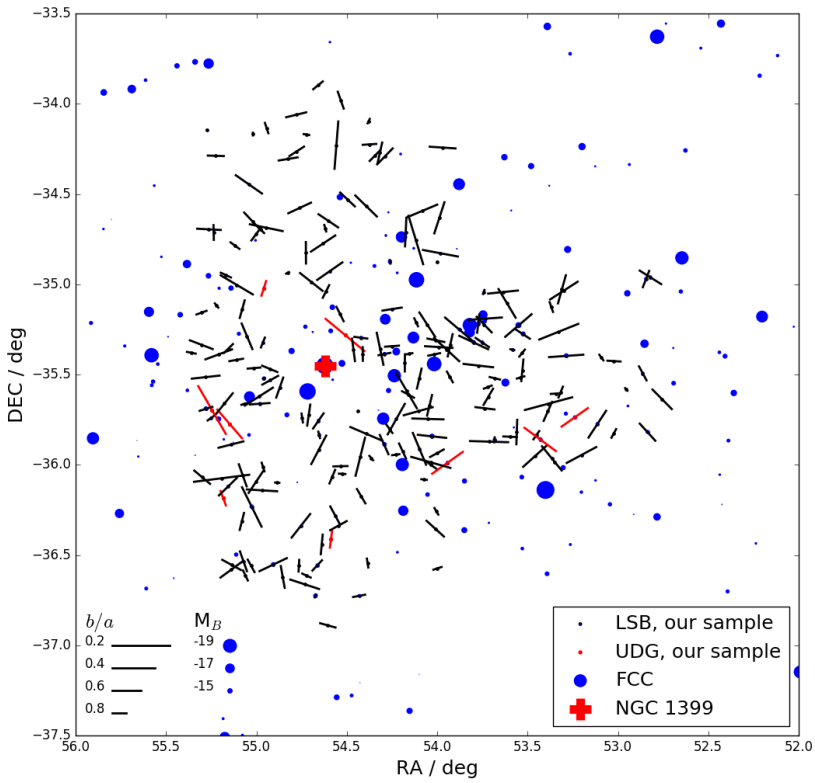

Figure 2.14: Orientations of the LSB dwarf galaxies in our sample are shown with the black sticks, and the UDGs with the red sticks. The lengths of the sticks correspond to the actual ellipticities so that the ellipticity increases with increasing length of the stick. The galaxies appearing in FCC (Ferguson 1989b) are plotted with the blue circles. The size of the circle corresponds to the brightness of the galaxies; the larger the circle is the brighter the galaxy is. The position of the NGC 1399 is marked with the orange cross.

behavior, so that $\sigma_{I,r'/g'} = \sqrt{I_{g'/r'}/(GAIN \times n)} \times GAIN$, where n is the number of pixels within the aperture. I, σ_I and σ_{sky} are given in flux units, whereas σ_{ZP} are in magnitudes.

The g'-r' colors of the galaxies as a function of their total absolute r'-band magnitudes $M_{r'}$ are shown in the upper panel of Fig. 2.16, with the typical

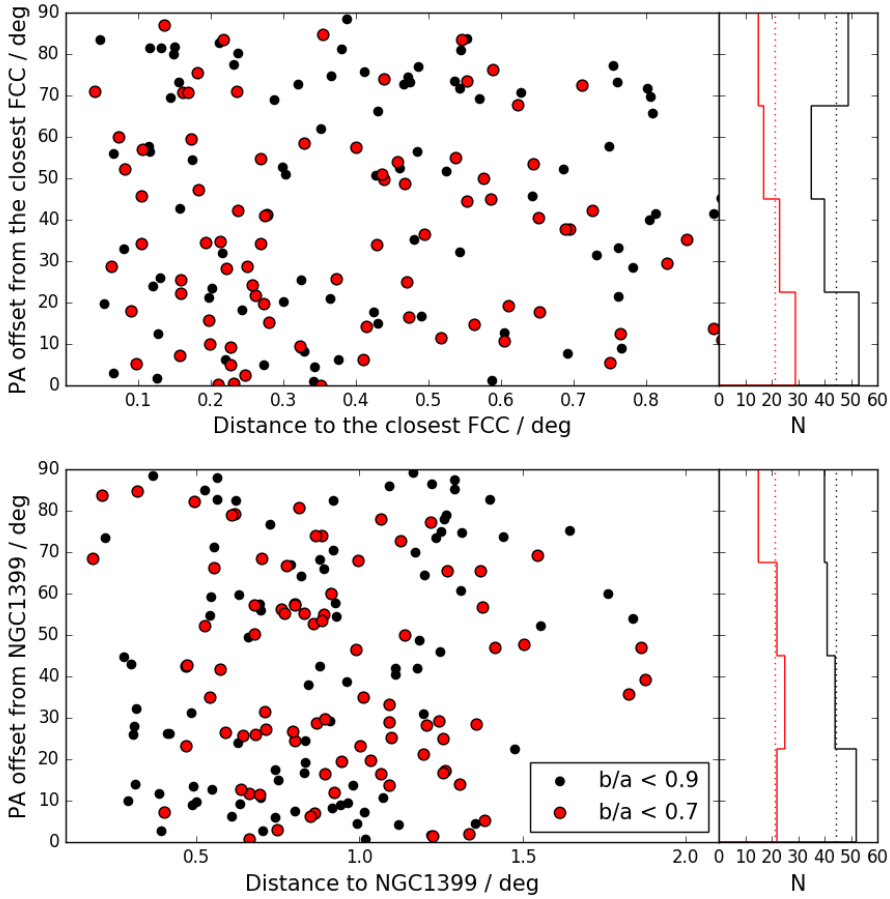

Figure 2.15: In the upper plot we show the difference between the position angle of our sample galaxy, and the position angle of the line drawn from the galaxy to the closest FCC galaxy with $M_{r'}$ <-18 mag. In the bottom plot we show the difference between the position angle of our sample galaxies and the position angle of the line drawn from that galaxy to NGC 1399. The red and the black dots correspond to the galaxies with $b/a < 0.7$ and < 0.9, respectively. The vertical histograms show the number distributions of the points in the scatter plots. The red and black histograms correspond to the red and black points, respectively.

errorbars of the colors shown below the points. Plotted separately are the nucleated and non-nucleated LSB dwarfs (with $R_e < 1.5$ kpc), and the UDGs (with $R_e > 1.5$ kpc). Pearson's correlation coefficient for the points shows a negative correlation ρ = -0.33 $\pm$ 0.04, and a linear fit gives the relation $g' - r' = -0.04(\pm 0.01) \times (M_{r'} + 12) - 0.48(\pm 0.09)$. In the color-magnitude relation the UDGs are among the brightest galaxies, but follow the same relation

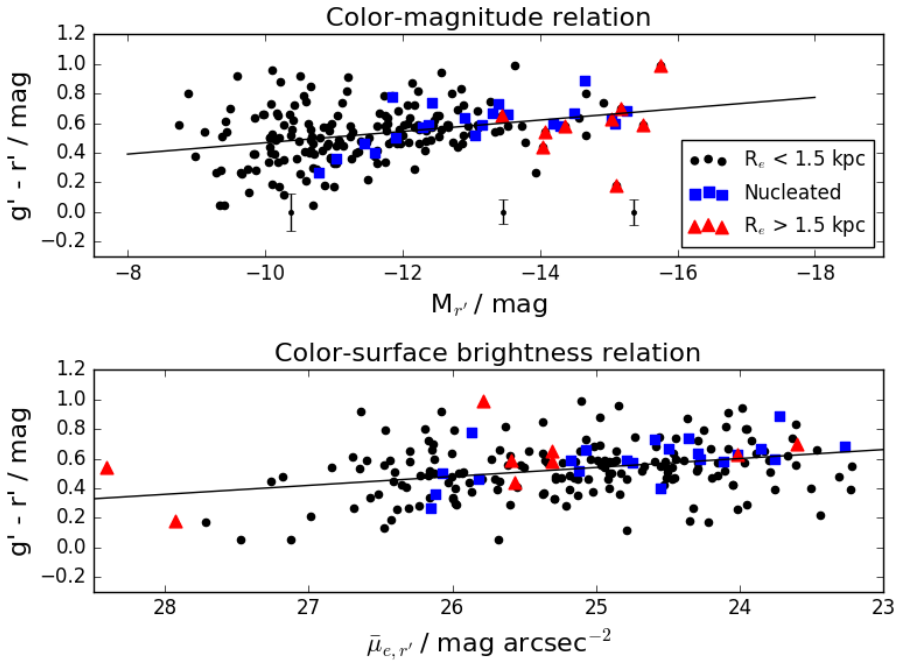

Figure 2.16: Upper panel: The color-magnitude relation shown for the galaxies with effective radius $R_e < 1.5$ kpc for nucleated (blue squares) and non-nucleated galaxies (black points), and for the UDGs with R($_e > 1.5$ kpc, (red triangles) in our sample. The black line shows the linear least squares fit to the data points. The g'-r' colors are measured with an elliptical aperture with semi major axis of R_e taken from GALFIT. The errorbars below the points show the size of the errors (Eq. 2.6) along the color-magnitude relation. Lower panel: The color-surface brightness relation of the galaxies in our sample. The symbols are the same as in the upper plot.

with the dwarf LSB galaxies in our sample. The measured slope of the color-magnitude relation of our sample is the same as that measured for the Virgo dwarf ellipticals by Kim et al. (2010) $d(g'-r')/d\mathrm{M}_{r'}$=-0.04± 0.01, and for the Virgo red sequence by Roediger et al. (2017) $d(g'-r')/d\mathrm{M}_{r'}$=0.3–0.4.

The g'-r' colors of the galaxies as a function of the mean effective surface brightness in the r'-band are shown in the lower panel of Fig. 2.16. We find that the colors correlate also with the surface brightness becoming redder with increasing surface brightness. Pearson's correlation coefficient for the points is ρ = -0.26 ± 0.05, and a linear fit gives the relation $g'-r' = -0.06(\pm0.01) \times (\bar{\mu}_{e,r'} - 24) + 0.7(\pm0.3)$. A more thorough discussion of the colors of galaxies in the FDS catalog will follow in a future paper.

2.8 DISCUSSION

The motivation of this work is to study the properties of the LSB galaxies in the Fornax cluster, and how they compare with those observed in other clusters or galaxy groups. We are particularly interested in the Ultra Diffuse Galaxies (UDGs), using a threshold surface brightness and size typical for the previously identified UDGs in clusters.

2.8.1 CONCEPT OF AN UDG IN THE LITERATURE

To conduct a meaningful comparison between the UDGs in the Fornax cluster and in other galaxy environments, it is important to make sure that the objects we are comparing are selected similarly. The definition of UDGs, adapted from van Dokkum et al. (2015) for the Coma cluster, was that they are galaxies with $R_e >$ 1.5 kpc, and stellar mass of $M_{*,L} \approx 10^7 M_\odot$, or -16.2 mag $< M_{r'} <$ -13.2 mag [8]. Works published earlier than that might contain a few similar galaxies (see e.g., Sandage & Binggeli 1984,Bothun et al. 1991, Conselice et al. 2002), in which case they were typically called as LSB galaxies. Since the largest UDGs found so far have $R_e \approx$ 10 kpc (Mihos et al. 2015), and the smallest ones overlap with the typical dE galaxies, it is possible that some of the UDGs form the low mass tail of the dEs with atypically large effective radii, and some of them form a genuinely distinct population. To study this, in the following we analyze separately the properties of the small UDGs with 1.5 kpc $< R_e <$ 3.0 kpc (i.e., with typical sizes of UDGs in Coma), and large UDGs with $R_e >$ 3 kpc.

A comprehensive collection of UDG studies in the literature has been presented by Yagi et al. (2016). However, not all of these works have sufficient image depth and the same measurements given as in this study. Also, most of these works contain very few UDGs. Here we discuss only those works to which we can make comparisons easily, without any auxiliary assumptions about the shapes or colors of these galaxies. The most complete available UDG samples have been made for the Coma cluster by Koda et al. (2015) (included in Yagi's collection), and for galaxy clusters at larger distances by van der Burg et al. (2016). Both of these studies used SExtractor to generate object lists, and GALFIT to fit Sérsic profiles to the galaxies.

2.8.2 COMPARISON OF UDGS IN FORNAX AND IN OTHER ENVIRONMENTS

We found nine UDG candidates in Fornax within the 4 deg^2 search area, of which five have $R_e <$ 3 kpc, and four have $R_e >$ 3 kpc. Three of these galaxies appear also in the sample of Muñoz et al. (2015), two of them are detected in Mieske et al. (2007), five appear in the FCC, and four are detected by Bothun et al. (1991). Additionally, two of the UDGs appear in Lisker et al. (*submitted*), but in that work FDS11_LSB1 is not considered as a galaxy. We identified all the UDGs

[8] Transformed (see Appendix 2.11.3) from g'-band measurements of van Dokkum et al (2015).

Table 2.3: Properties of the UDGs in the Fornax (N = 9, our sample) and Coma clusters (N = 288, the galaxies with $R_e > 1.5$ kpc from the sample of Yagi et al. 2016). The columns show the median, standard deviation (σ), minimum (Min.), and maximum (Max.) values of a given quantity, repectively.

Fornax	Median	σ	Min.	Max.
$M_{r'}$ / mag	-15.1	0.7	-15.8	-13.5
R_e / kpc	2.09	3.22	1.59	11.25
b/a	0.48	0.18	0.24	0.79
g'-r' / mag	0.59	0.20	0.18	0.99
Sérsic n	0.80	0.22	0.40	1.18
Coma (Yagi et al. 2016)	**Median**	σ	**Min.**	**Max.**
$M_{r'}$ / mag	-14.8	0.9	-16.8	-11.8
R_e / kpc	1.86	0.57	1.51	6.12
b/a	0.73	0.16	0.25	0.99
g'-r' / mag	0.68	0.13	0.25	1.03
Sérsic n	0.89	0.33	0.17	2.71

in Muñoz et al. (2015) that were located within the area of our study. We also identified "FDS11_LSB30", classified as UDG in Muñoz et al. (2015), but because of its small size ($R_e < 1.5$ kpc) it was not classified as UDG. Two of our UDGs are new detections. Fig. 2.17 shows the r'-band stamp images of the detected UDGs, with their structural parameters and cluster centric distances listed in the upper right corner. The structural parameters of these UDGs are given in Table 2.3.

2.8.2.1 Sizes

The sample of Yagi et al. (2016) includes 288 UDGs (the total number of galaxies is 854 galaxies) residing in the Coma cluster, of which 267 have $R_e < 3$ kpc, and 21 are larger than 3 kpc. Most of these UDGs have $R_e \sim 1.5$ kpc, and the number of UDGs drops rapidly with increasing effective radius. The largest UDG in Coma has $R_e = 6.1$ kpc, whereas in Fornax the largest one has $R_e \sim 10$ kpc, which is considerably larger. The Coma UDGs have r'-band magnitudes[9] between -16.8 mag $< M_{r'} <$ -11.8 mag, whereas in our sample for Fornax the magnitude range is -15.8 mag $< M_{r'} <$ -13.5 mag. The narrower magnitude range in Fornax is explained by the smaller sample size, as these two samples have similar medians and standard deviations (see Table 2.3).

The size-magnitude relations of the UDGs in the Fornax and Coma clusters (van Dokkum et al. 2015, Yagi et al. 2016) are shown in the upper and lower left panels of Fig. 2.18, respectively. It appears that in the Coma cluster the division between UDGs and LSB dwarfs at 1.5 kpc is artificial meaning that they form a continuous distribution in the size-magnitude parameter space. The same is not

[9] transformed from Suprime-Cam R-band, see appendix 2.11.3

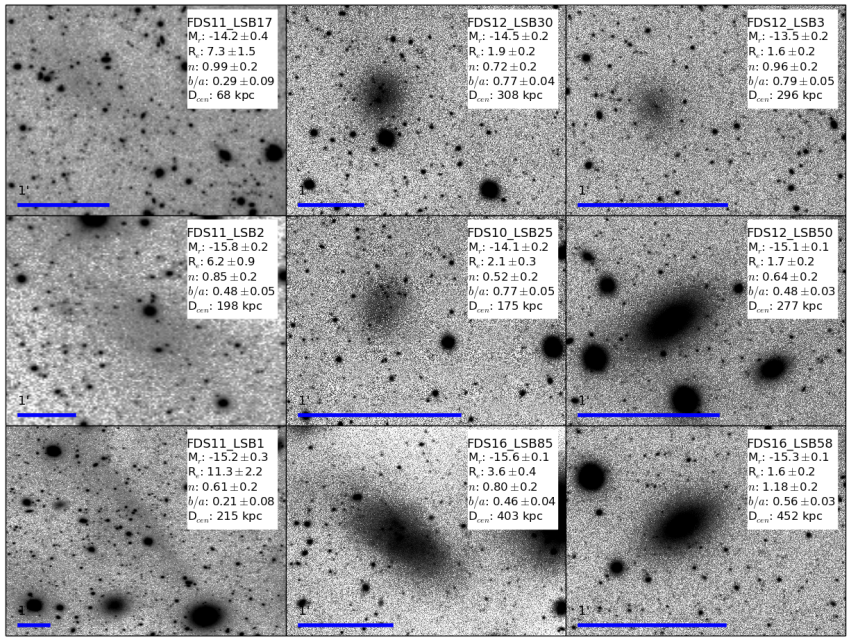

Figure 2.17: Postage stamp images of the UDGs of our sample in r'-band, all shown in the same brightness scale (logarithmic scale between "-27.8" mag arcsec^{-2} and 24 mag arcsec^{-2}). In the right corner shown are the name, the absolute r'-band magnitude M$_{r'}$, the effective radius R$_e$ in kilo parsecs, Sérsic n, axis ratio b/a and the projected cluster-centric distance D$_{cen}$. The postage stamps have different sizes on the sky, and therefore 1 arcmin scale bars are shown in the lower left corner of the images. FDS11_LSB1, FDS11_LSB2 and FDS12_LSB3 do not appear in any previously published works. However, FDS11_LSB1 and FDS11_LSB2 have also been identified in Lisker et al. (*submitted*), although there only FDS11_LSB2 is considered as a galaxy.

that apparent from the size-magnitude relation of the Fornax galaxies, where at least the two largest UDGs are clearly outliers.

UDGs appear also in the Virgo cluster, although no systematic search of them has been done. Gavazzi et al. (2005) measured structural parameters of a sample of early-type galaxies in the Virgo cluster, and found 14 galaxies with 1.5 kpc $<$ R$_e$ $<$ 3.0 kpc and $\bar{\mu}_{e,r'} > 24$ mag arcsec^{-2}, which according to our criteria would be classified as UDGs. However, their study does not reach similar image depths as the deepest images obtained for the Coma and Fornax clusters, which probably explains why they do not find many UDGs larger than 3 kpc. Particularly the large UDGs in our study have low effective surface brightnesses being fainter than $\bar{\mu}_{e,r'}$ $>$ 26 mag arcsec^{-2}. However, Mihos et al. (2015) find three large UDGs (R$_e$ $\sim$ 3kpc – 10 kpc) in the central parts of the Virgo cluster. Although these findings do

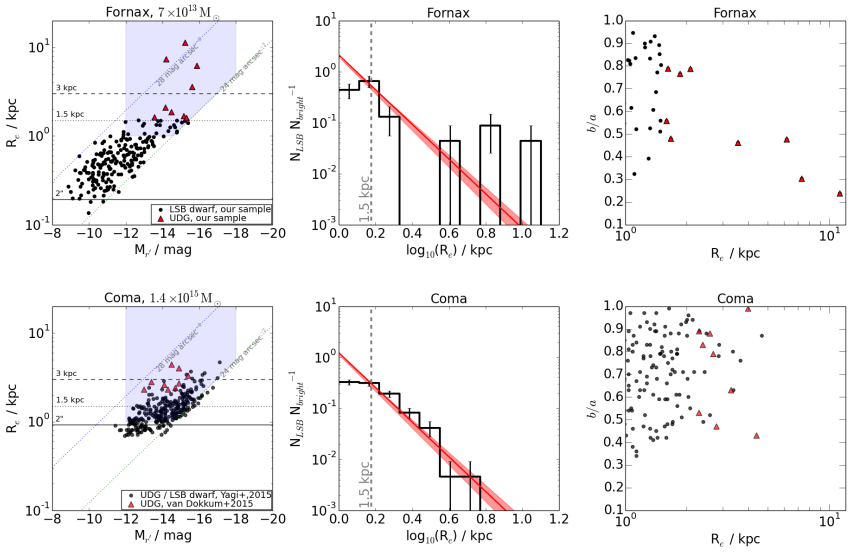

Figure 2.18: *Left panels* show the luminosity-size relation of the known UDGs, and of the LSB dwarf galaxies within two cluster core radii in the Fornax (upper) and Coma (lower) clusters. The two horizontal lines represent the effective radii of 1.5 kpc and 3 kpc. The black points and the red triangles in the upper left panel show the LSB dwarfs and UDGs in our sample, respectively, and the black points, and the red triangles in the lower left plot correspond to the LSB dwarfs and UDGs from Yagi et al. (2016) and van Dokkum et al. (2015), respectively. The blue areas show the selection limits of the middle and right panels. *The middle panels* show the number distribution of effective radii normalized by the number of bright galaxies in the studied area. The dashed lines show the scaled n[dex^{-1}] $\propto$ r$_e^{-3.4}$ relation found (van der Burg et al. 2016) between the number of UDGs with a given effective radius in logarithmic bins. The solid vertical lines in the middle of the bins show the Poisson noise uncertainties in the bins. *The right panels* show axis ratios of the selected galaxies in Fornax (upper right panel) and Coma (lower right panel) against their effective radii.

not comprise a complete sample, they already demonstrate that UDGs in Virgo can be as large as the largest UDGs in the Fornax cluster.

The observation that the largest UDGs in Coma are smaller than in Fornax or Virgo clusters, most likely is a detection bias related to the fact that the UDG identifications both in Yagi et al. (2016) and van Dokkum et al. (2015) are made using SExtractor. van der Burg et al. (2016) tested the detection efficiency of SExtractor using artificial LSB galaxies: they found that the detection efficiency is less than 0.5 for the UDGs with R$_e$ $\sim$ 3 kpc and $\bar{\mu}_{e,r'} \sim$ 26 mag arcsec^{-2}, and further drops toward lower surface brightnesses and larger effective radii. Thus, if large UDGs like the ones detected in this study exist in Coma, most of them would not have been detected using automatic methods.

In the middle panels of Fig. 2.18 we show the normalized number distributions of the effective radii (of a magnitude- and size-limited sample) of the LSB galaxies in Coma and Fornax clusters. The galaxies are chosen so that neither sample is limited by its selection criteria: we selected the galaxies within two cluster core radii from the cluster centers corresponding to 450 kpc and 700 kpc in the Fornax (Ferguson 1989a) and Coma clusters (Kent & Gunn 1982), respectively. Additionally, we required these galaxies to have $R_e > 1$ kpc, $\bar{\mu}_{e,r'} > 24$ mag arcsec^{-2} and -18 mag $< M_{r'}$ -12 mag (shown with the blue area in the left panels). The histograms are normalized by the number of bright galaxies[10] (N_{bright}) with $M_{r'} <$ -17 mag in the selected area. These histograms highlight the difference between Fornax and Coma, the large UDGs in the former being clearly detached from the rest of the LSB population. We also plot the relation observed by van der Burg et al. (2016), which tells that the number of UDGs with given R_e decreases as $n[dex^{-1}] \propto R_e^{-3.4\pm0.2}$, where $n[dex^{-1}]$ is the number of UDGs within a logarithmic bin. In the Fornax cluster, this relation clearly underestimates the number of large UDGs. This is not surprising as the sample of van der Burg et al. (2016) is known to miss many such galaxies, since they are using SExtractor. Using Monte Carlo modeling and assuming the sizes of the UDGs in Fornax to follow the van der Burg (2016) size distribution, we find that the probability of four or more UDGs out of nine having $R_e > 3$ kpc is p = 0.01. However, the number statistics alone is not sufficient to tell if the distribution of our sample is different from the one found by Van der Burg et al. A sample that is not limited by the number statistics (as is our sample) nor missing the large UDGs (like the ones using SExtractor are) is clearly needed to understand the total contribution of large UDGs to the total galaxy populations in clusters.

2.8.2.2 NUMBER OF UDGS

Taking into account the homogeneity of the data and our tests made with the mock galaxies, we should be able to detect all the galaxies down to $\bar{\mu}_{e,g'} = 28.5$ mag arcsec^{-2}. Given the fact that we are excluding 20 % of the area to avoid possible source confusion, we are probably missing 1-3 UDGs, which would be bright enough to be detected in case that they were not overlapping with other sources. Adding these missed galaxies to the nine identified UDGs we get surface number density of $\nu_{UDG} = 25\pm8$ UDGs Mpc^{-2}, which compares to $\nu_{UDG} \approx 64$ UDGs Mpc^{-2} in the Coma cluster (N(UDGs) = 98 within the innermost 700 kpc in Yagi et al. 2016). While normalizing these numbers with the surface densities of the bright galaxies[11] in the studied areas, we get $\frac{\nu_{UDG}}{\nu_{bright}} = 0.7\pm0.2$ and 0.45 ± 0.05 for Fornax and Coma clusters, respectively. This shows that the normalized surface number density of UDGs in the Fornax cluster is larger than that in the Coma cluster.

[10] We selected the galaxies in FCC that have $M'_r <$ -17 mag (corresponding in $M_B \sim$ -16 mag, see appendix 2.11.3 for details), and a membership status "confirmed" or "likely member". The galaxies in the Coma cluster were selected using the SDSS (DR10), at a redshift range of $0.0164 < z < 0.0232$, and having r'-band magnitude $M_{r'} <$ -17 mag. This results to 23 galaxies in Fornax and 218 in Coma.

[11] The same sample of bright galaxies was used as in Section 8.2.1. Giving surface densities of $\nu_{bright} = 36$ galaxies Mpc^{-2} in Fornax and $\nu_{bright} = 140$ galaxies Mpc^{-2} in Coma.

Table 2.4: Fractions of UDGs in the Fornax and Coma clusters. The first column gives the UDG identifications in this study (within two core radii from the center $\sim$ 450 kpc), the second column gives the upper limits when those numbers are extrapolated to the virial radius of 0.7 Mpc (Drinkwater et al. 2001a), being corrected also for the expected number of UDGs that are missed as parts of the area is excluded due to bright sources. The third column gives the number of UDGs in the Coma cluster within two core radii ($\sim$700 kpc) from the center. The fourth column gives the number of UDGs in the whole sample of Yagi et al. (2016), which reaches up to 2.5 Mpc from the center of the Coma cluster. The Poisson uncertainties are based on the actual number of objects.

	Fornax (r=450kpc)	Fornax (r=0.7Mpc)	Coma (r=700kpc)	Coma (r=2.5Mpc)
UDGs	9±3	42±12	98	288
1.5 kpc $<$ R_e $<$ 3 kpc	5	22±8	91	267
R_e $>$ 3 kpc	4	19±7	7	21
UDGs / Mpc^{-2}	25±8	-	64	-
Normalized frequency, $\frac{\nu_{UDG}}{\nu_{bright}}$	0.7±0.2	-	0.45±0.05	-

There exists a correlation between the virial mass (M_{200}) of the cluster and the number of UDGs within the virial radius (r_{200}) (van der Burg et al. 2016, see Fig. 2.19). For a cluster halo mass of 7×10^{13} $M_\odot$, corresponding to that of the Fornax cluster (Drinkwater et al. 2001a), the expected number of UDGs within r_{200} is 10–20. If we assume uniform density of UDGs and extrapolate it up to the virial radius of Fornax r_{200} (0.7 Mpc, or 2.2°, Drinkwater et al. 2001a), we get an upper limit of N = 42±12 UDGs. However, the sample of van der Burg et al. (2016) excludes galaxies that have $\bar{\mu}_{r',e} > 26.5$ mag arcsec^{-2}, or $R_e > 7$ kpc. Therefore, in order to make a fair comparison to their study we need to drop two out of the nine identified UDGs in our sample. Taking this into account leads to the upper limit of N = 33±9 UDGs inside r_{200}, which brings the Fornax cluster to the relation by van der Burg et al. (see Fig. 2.19). For comparison, the Coma cluster has a mass of M = 1.4 $\times10^{15}$ $M_\odot$ (Łokas & Mamon 2003), and has 288 identified UDGs, which also matches well with the relation by van der Burg et al. (2016).

2.8.2.3 SHAPES AND ORIENTATIONS

The stamp images in Fig. 2.17 show that the large UDGs in our sample are less symmetric and more elongated than the smaller ones (see also the upper right panel of Fig. 2.18). Their shapes can be caused by tidal interactions, but in principle they can also be inclined disks or prolate spheroidals as suggested by Burkert (2017). Some UDGs have earlier been identified as disrupted early-type dwarfs, like HCC-087 in the Hydra I cluster (with M_V = -11.6 mag and R_e = 3.1 kpc) studied by Koch et al. (2012). Koch et al. were able to reproduce the observed s-shaped morphology of this galaxy by modeling its gravitational interaction with the cluster center. Also several other studies have identified signs of tidal disruption in UDGs (Mihos et al. 2015, Merritt et al. 2016, Toloba

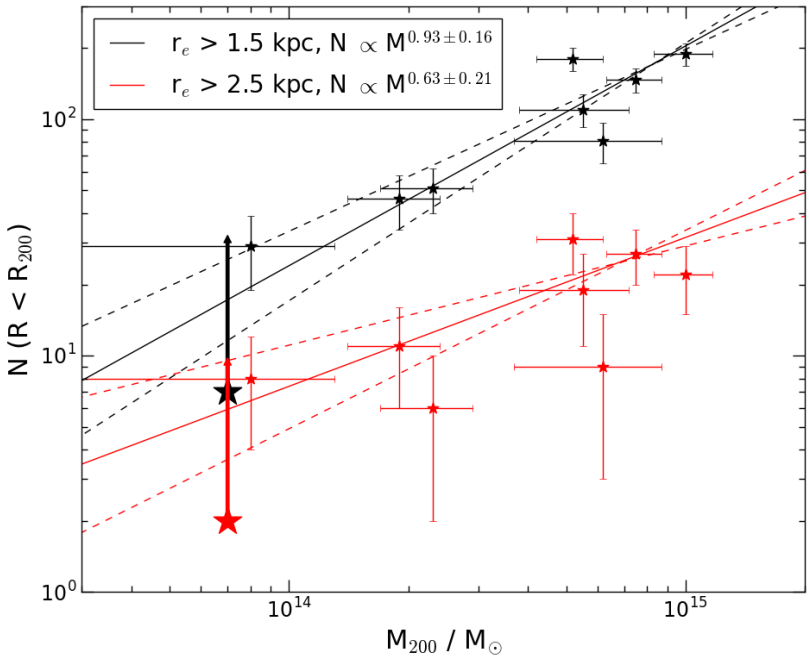

Figure 2.19: Relation between the cluster mass (M_{200}) and the number of UDGs within the virial radius (R_{200}) in galaxy clusters at $0.044 < z < 0.063$ is shown with black points (van der Burg et al. 2016). The red symbols show the same relation for the UDGs with $R_e > 2.5$ kpc. The observed values from our sample are marked with the large symbols, with the extrapolated upper limits shown with the arrows.

et al. 2016, Wittmann et al. 2017). Obviously, at some level tidal interactions are shaping the morphology of the LSB galaxies in clusters.

In the Coma cluster the UDGs are preferably elongated toward the cluster center (Yagi et al. 2016), which is not the case for the nine UDGs in the Fornax cluster (see Fig. 14). The number statistics are not good enough to conduct a conclusive analysis, but we found that some of the UDGs in Fornax are elongated toward their nearby dwarf galaxies ($M_{r'}$ >-19 mag). In this sense an interesting pair is FDS11_LSB1 and FDS11_LSB2 (see Fig. 2.20), which galaxies are located at a projected distance of 15 kpc from each other. Both galaxies point toward a spectroscopically confirmed Fornax dE, FCC252 (Drinkwater et al. 2001b), which has a B-band total magnitude of M_B= -15.2 mag (Ferguson 1989b). FCC252 itself does not show any signs of tidal interaction. Another UDG showing signs of galaxy interaction is FDS16_LSB85 (see Fig. 2.4), which has a tidal tail pointing toward the nearby LSB dwarf, FCC 125 (Ferguson 1989b, or FDS 16_LSB50 in our sample). FCC 125 has $M_{r'}$ = -13.3 mag assuming that it resides at the distance of

Fornax, although it has no spectral confirmation of the cluster membership. On the other hand, the four smallest UDGs with round and symmetric appearance do not show any signs of tidal interactions. In order to test if the elongated shapes of the large UDGs are resulting from tidal interactions, a larger sample is needed.

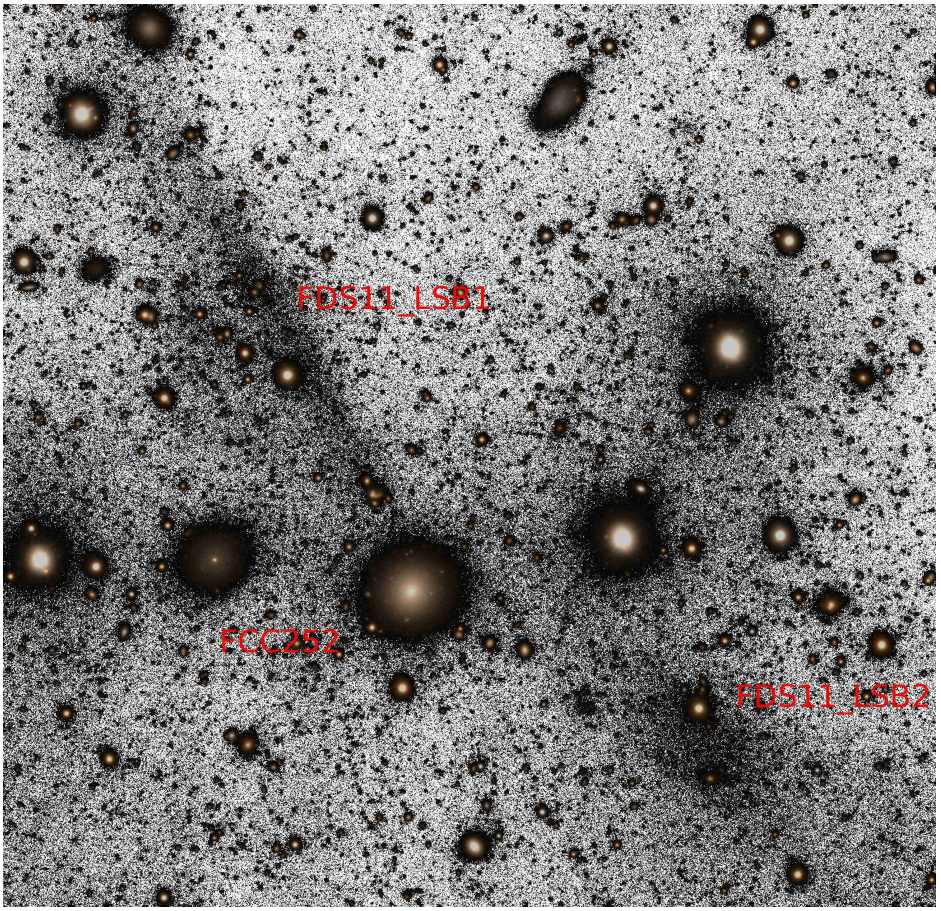

Figure 2.20: g'+r' color image showing FDS11_LSB1, FDS11_LSB2 and FCC252. Colors are displayed for the areas brighter than $\mu_{r'} > 26$ mag arcsec^{-2}. Only r'-band image is shown for the levels fainter than that. FDS11_LSB1 and FDS11_LSB2 are separated by projected distance of 15 kpc from each other and $\sim$ 7 kpc from FCC252, which is a dwarf elliptical galaxy spectroscopically confirmed to be in Fornax (radial velocity = 1415 km s^{-1}, Drinkwater et al. 2001b). The morphology of these large UDGs is very elongated and may be due to tidal interactions.

The properties of UDGs in our Fornax sample, and of those in the Coma cluster given by Yagi et al. (2016), are compared in Table 2.3. The mean axis ratio in Coma is $\langle b/a \rangle = 0.73 \pm 0.16$, the small ($R_e < 3$ kpc, $\langle b/a \rangle = 0.75$), and large ($R_e > 3$ kpc, $\langle b/a \rangle = 0.69$) UDGs having similar axis ratios. However, in our sample

in Fornax the large UDGs are more elongated ($\langle b/a \rangle$ = 0.69 and $\langle b/a \rangle$ = 0.38, for small and large UDGs, respectively).

While comparing the b/a-values between the small UDGs and the dwarf LSB galaxies ($R_e < 1.5$ kpc), we don't find any significant differences, neither in the Fornax nor in the Coma clusters. However, the large UDGs in Fornax have a significantly different b/a-distribution compared to the one of LSB dwarfs (K-S test p-value = 0.0005, for the b/a distributions being the same). The same comparison between the two types of galaxies in Coma shows no significant difference (p-value = 0.24, see also the right panels in Fig. 2.18). We conclude that in the Fornax cluster the large UDGs are significantly more elongated than the dwarf LSB galaxies, but the same is not obvious in Coma. We find no difference between the axis ratio distributions of the LSB dwarfs and small UDGs.

As expected for the dwarf LSB galaxies (e.g., Bothun et al. 1991), the values of the Sérsic index are below unity for the UDGs, both in the Coma and the Fornax clusters. In fact, the n-values are similar in the Fornax ($\langle n \rangle$ = 0.8±0.2, n = 0.4-1.2) and in the Coma ($\langle n \rangle$=0.9±0.2, n=0.4-2.0) clusters. The galaxies in both samples are fit using GALFIT, the only difference in the fitting approach being that Yagi et al. allowed the central *PSF* component of the galaxies to be off-centered from the Sérsic component.

2.8.2.4 COLORS

The colors of UDGs set constraints for their formation mechanisms. The UDGs in Coma (Koda et al. 2015) have been shown to have similar colors as the normal red sequence dEs of the same luminosity. Also, the measured slope of the color-magnitude relation of our LSB sample matches well with the one of dE:s in Virgo cluster, which supports also them being mostly quiescent red-sequence galaxies. The mean color of the Coma UDGs is $\langle$g'–r'$\rangle$[12] = 0.67 mag, which color is the same for the large and small UDGs. This is comparable to $\langle$g'–r'$\rangle$ = 0.59 mag (with the range of 0.2 – 1.0) that we obtain for the UDGs in Fornax (see red triangles in Fig. 16). The only exception is FDS11_LSB1, which has g'-r' = 0.18 mag, being a clear outlier toward blue colors. The observation that the UDGs do not clearly deviate from the colors of the LSB dwarf galaxies within the same luminosity range is consistent with them having similar origin.

2.8.3 HOW TO EXPLAIN THE ORIGIN OF UDGS?

2.8.3.1 EXPLANATIONS IN THE LITERATURE

Van Dokkum et al. (2015) first pointed out that UDGs form a population that is continuous with the dwarf galaxies in the size-magnitude relation, and therefore can simply be a diffuse end tail in that relation. However, they do not think that UDGs originate from the same progenitors as the typical dwarf galaxies in clusters, since processes like harassment (Moore et al. 1998, Smith et al. 2015) and tidal stirring, rather make the galaxies more compact than diffuse. Their suggestion

[12]Transformed from the Suprime-Cam $\langle$B–R$\rangle$ color. See Appendix C for details.

was that UDGs could be failed Milky Way mass (halo mass of $\sim 10^{12}$ $M_{\odot}$) galaxies which lost their gas during their in-fall into the cluster environment, and therefore were not able to form a large amount of luminous matter, otherwise typical for their observed size. This means that compared to their sizes, these galaxies might have massive dark matter halos. However, the number of globular clusters (GC) around these galaxies (Amorisco et al. 2018, Beasley & Trujillo 2016) rather suggest that they are Large Magellanic Could (LMC) type galaxies with halo mass of $\sim 10^{10}$ $M_{\odot}$). Also, the similar cluster-centric distributions of dwarf galaxies and UDGs found by Roman & Trujillo (2016) and by van der Burg et al. (2016), is problematic in the interpretation of van Dokkum et al.. This is because due to the large dark matter halos dynamical friction should have made these originally Milky Way sized galaxies to sink deeper into the cluster potential well, which is not observed.

Amorisco & Loeb (2016) suggested that UDGs are dwarf galaxies with especially high original angular momentum. In this scenario, the high angular momentum makes the UDGs more flattened and extended than the typical dEs are. Otherwise the formed galaxies are expected to be similar, and to appear in similar environments as the other dwarf galaxies. Their model predicts that the sizes of the UDGs increase with increasing angular momentum, which makes the largest UDGs more disk-like (elongated when inclined) than the smaller ones. This prediction is well in agreement with our observation that the largest UDGs are more elongated. However, the analysis of Burkert (2017) shows that the b/a-distribution of UDGs is more compatible with them being prolate spheroidals than disks. In Amorisco & Loeb (2016) the baryonic physics is not modeled, but they were able to model the relation between the cluster halo mass and the total number of UDGs as seen by van der Burg et al. (2016).

On the other hand, Di Cintio et al. (2017) suggested that UDGs are dwarf sized galaxies, which are extended due to their feedback driven gas outflows which give rise to an expanded stellar component. They modeled baryon physics of isolated galaxies, and for comparison with observations selected objects which fulfil the criteria of typical UDGs. Their models predict average B-R colors of 0.77 $\pm$ 0.12 mag (or g'-r' = 0.5 mag) for these galaxies. The predicted color is 0.13 mag bluer than the mean observed value for the Coma UDGs, and 0.07 mag bluer than that the UDGs in the Fornax cluster in our sample. This discrepancy between the models and observations might be reduced if the galaxies were simulated in the cluster environment, where also external quenching takes place. An important prediction from their model is that the UDGs should mostly form outside the clusters, and also contain gas if it is not externally removed. This is well consistent with the observations of the ALFALFA survey (Leisman et al. 2017), where 115 HI rich isolated UDGs were studies. Additionally, Román & Trujillo (2017) find that the colors of the UDGs located in the periphery of group environments have bluer colors (g-i$\sim$0.45) than the UDGs in the clusters (g-i$\sim$0.76), which is also consistent with this formation scenario. One discrepancy between the models of Di Cintio et al. (2017) and the observations is that the effective radii in the simulated galaxies vary between 1 kpc $< R_e <$ 3 kpc, whereas the observed R_e

can be as large as $\sim$ 10 kpc. This discrepancy can simply be a sampling issue of the simulations, or alternatively the largest UDGs have a different origin.

Baushev (2018) suggested that UDGs can form via straight-on collisions of two massive galaxies, which penetrate each other with large relative velocities. This collision has little effect on the stellar content, but will rip out the cold gas in these galaxies. The collision rate strongly depends on the number density of galaxies, and high relative velocities are needed to prevent merging of the colliding systems. Therefore, this model is not good for explaining UDGs in galaxy groups nor in the field, where the relative velocities of galaxies are smaller. However, such collisions can hardly be prevented in galaxy clusters, where besides major mergers, also dwarf-sized galaxy collisions are expected. Since the strength of galaxy-galaxy interactions is stronger in low velocity encounters, the dwarf galaxies in groups are more likely to experience strong tidal forces than the ones in clusters, which could explain the large sizes of UDGs in the lower mass environments (e.g., Merritt et al. 2016). As these dwarf-dwarf interactions in clusters and groups are not well studied in simulations, further simulations of the importance of these tidal encounters are needed.

It seems that both the high angular momentum origin, and feedback induced gas outflows, can reproduce most of the observed properties of UDGs at present. However, at this moment, we also should seriously consider the contribution of the tidal interactions, which could be the explanation of the most extended UDGs.

2.8.3.2 IS THE ENVIRONMENT IMPORTANT FOR THE FORMATION OF UDGS?

The Coma and Fornax clusters are clearly different environments, which should affect the observed properties of UDGs, if their evolution is driven by their environment. The virial mass of Coma is 1.4×10^{15} $M_\odot$, and the virial radius is 2.9 Mpc (Łokas & Mamon 2003), while the corresponding values for the Fornax cluster are 7×10^{13} $M_\odot$ and 0.7 Mpc (Drinkwater et al. 2001a). This means that although Coma is 20 times more massive than Fornax, it is less dense. The velocity dispersion of the Coma main group galaxies is σ = 1082 km s^{-1} (Colless & Dunn 1996), which is nearly three times larger than the one of the Fornax cluster galaxies with σ = 374 km s^{-1} (Drinkwater et al. 2001a). Therefore galaxy-galaxy interactions are expected to be stronger in the Fornax than in the Coma cluster.

As discussed above, the average magnitudes, g'-r' colors and Sérsic n-values of the UDGs are similar in the Coma and Fornax clusters. The preferred alignment toward the cluster center that appears among the Coma UDGs, but not among those in the Fornax cluster, might suggest that the galaxy - cluster potential interaction might be more important in Coma.

On the other hand, UDGs have been found also in lower density environments outside the clusters. Four tidally disturbed UDGs have been found in the NGC 5485 group (Merritt et al. 2016), one UDG in a filament of the Pisces-Perseus supercluster (Martínez-Delgado et al. 2016), one UDG in the NGC 253 group (Toloba et al. 2016), and one as a satellite of Centaurus A (Crnojević et al. 2016). All these galaxies are large having effective radii R_e = 2.5 – 5 kpc. The size distribution of the low density environment UDGs seems to be different from the

one in clusters, but again this can be a bias of cluster samples missing the large UDGs. However, recently Wittmann et al. (2017) visually inspected the UDG population in the core of the Perseus cluster (M_{vir} = 8.5×10^{14} $M_{\odot}$, Mathews et al. 2006), but did not find any UDGs larger than $R_e > 4.1$ kpc. This observation might indicate that the difference in the effective radii distributions is not only an observational bias. Otherwise, there seems to be no structural difference between the UDGs in the group environments and the ones in clusters.

Recently, the observations of the isolated UDGs showed that they contain HI gas (Trujillo et al. 2017; Leisman et al. 2017), and posses bluer colors than the ones in clusters (Román & Trujillo 2017; Leisman et al. 2017). Additionally, Leisman et al. (2017) observed that these HI rich UDGs may exist in high angular momentum halos. These observations are consistent with the scenario where UDGs are formed in dwarf-sized dark matter halos outside the clusters.

To conclude, from the observational (photometric) point of view we do not find systematic differences in the structure of the bulk of the UDGs in different galaxy environments. However, in Fornax, Virgo and group environments there are elongated large UDGs, which have not been found in higher mass clusters like Coma or Perseus. The UDGs in the isolation and outskirts of groups possess bluer colors than the ones in groups and clusters, which might be an indication of environmental effects.

2.8.4 LSB DWARFS IN FDS

Most of the galaxies in our sample are not UDGs but rather dwarf-sized LSB galaxies. The effective radii of these galaxies range from 120 pc to 1.5 kpc (an upper limit by definition), and the total r'-band magnitude between -8.9 mag $>$ $M_{e,r'}$ $>$ -15.2 mag, which means that we are reaching the sizes of the largest Milky Way satellite dSph galaxies. For comparison, Ursa Minor has R_e = 181 pc and M_V = -8.8 mag, and the Fornax dSph has R_e = 710 pc and M_V = -13.4 mag (McConnachie 2012). Having in mind that the dividing line between the LSB dwarfs and the other dwarf galaxies is physically not very clear, it is interesting to compare their radial distributions in the Fornax cluster. As the LSB dwarfs appear also in galaxy groups, we can compare the Fornax LSB dwarfs with those appearing in the Centaurus group, where a sample comparable to ours exists.

2.8.4.1 RADIAL DISTRIBUTION

Dynamical friction (Chandrasekhar 1943) transfers kinetic energy from massive galaxies to smaller galaxies, making the massive galaxies to sink deeper into the cluster potential well. This mass segregation takes place in time scales shorter than Hubble time (White 1977). Thus, assuming that all galaxies spend a similar amount of time in the cluster, the distribution of massive galaxies should be more centrally concentrated. Harassment should also make the galaxies themselves more centrally concentrated near the cluster center. For a dynamically relaxed cluster we would then expect that also among the dwarf galaxies the more massive and higher surface brightness galaxies preferentially appear in the

central regions of the cluster. However, according to the cosmological simulations like the Millennium simulations by Boylan-Kolchin et al. (2009), clusters grow hierarchically by accreting galaxy groups, which in reality makes the situation more complicated than that.

To study if the above mentioned processes are relevant in the Fornax cluster we studied the radial number density profiles of the galaxies. We found that the bright FCC galaxies indeed are more centrally clustered than the fainter galaxies in our sample (see Fig. 2.13). In the same figure plotted are also Ultra Compact Dwarf galaxies (UCDs) from the sample of Gregg et al. (2009), which is complete up to 0.9° of the Fornax cluster. UCDs are compact dwarf galaxies, with sizes similar to GCs or nuclei of dwarf galaxies. It appears that the dwarf galaxy concentration in the central regions of the Fornax cluster increases with increasing compactness of the object, so that the most concentrated are the UCDs, and the least concentrated the LSB dwarfs.

It seems that LSB dwarfs are the most numerous type of galaxies in Fornax, everywhere except in the area within 0.3° from NGC 1399 (only the area within 5 arcmin from NGC 1399 was masked). A similar phenomenon has been observed also in several other clusters (van der Burg et al. 2016, Wittmann et al. 2017). In principle this could be a bias due to difficulties in detecting the LSB galaxies in the central regions of the clusters, but it is also possible that the galaxies entering too close to the cluster center get tidally disturbed and finally accreted to the central cD galaxy. Most probably we can exclude the first possibility, because bright stars, which are the main reason for possible overlapping with the LSB galaxies, are not clustered into the cluster center. We see a drop also in the number of bright FCC galaxies which should be easily visible throughout the Fornax cluster.

2.8.4.2 COMPARISON WITH THE CENTAURUS GROUP

In the following we compare the properties of the Fornax LSB dwarfs with those in the Centaurus group, located at the distance of 4 Mpc (Jerjen et al. 2000). The main body of the Centaurus group consists of four bright galaxies (brighter than $M_{r'} <$ -17 mag). The photometric measurements for the dwarf galaxies in this group in the g'- and r'-bands are provided by Müller et al. (2017). The images reach the V-band surface brightness of 28 mag arcsec^{-2}. With that limiting surface brightness they should be able to find all similar LSB dwarfs as detected by us in the Fornax cluster. The Centaurus group is located at suitable distance so that the analysis can be done in a similar manner as in this paper.

The size-magnitude, color-magnitude and Sérsic n-magnitude relations of the LSB dwarf galaxies in the Fornax cluster, and in the Centaurus group are shown in Fig. 2.21. The Centaurus group sample is complete for the sources which have diameters larger than 28 arcsec (0.6 kpc at 4 Mpc distance) at a surface brightness of 28 mag arcsec^{-2}. The effective radii of these galaxies range between 0.10 kpc $< R_e <$ 1.82 kpc, and the r'-band absolute magnitudes between -7.9 mag $> M_{r'} >$ -17.2 mag. To eliminate selection effects from the comparison, we removed from the Centaurus sample the galaxies with $\bar{\mu}_{e,r'} < 24$ mag arcsec^{-2}, as these galaxies would not be included in our sample.

The g'-r' colors and the values of Sérsic n of the Fornax and Centaurus LSB dwarf galaxies, are plotted as a function of the total r'-band magnitude in Fig. 2.21. The number histograms of the two parameters are shown in the small right panels of both figures. It appears that the LSB dwarf galaxy colors in both environments are fairly similar. Only difference is that the average colors of galaxies in the Centaurus group become bluer and the effective radii smaller than in Fornax with increasing magnitude. Also, the scatter in the colors of the Centaurus group LSB dwarfs is clearly higher. Notable is that there is no difference in the colors , sizes or Sérsic indices of the faintest LSB galaxies ($M_{r'} \gtrsim$ -12 mag).

The values of Séric n parameters of these galaxies are also similar. In both environments the Sérsic n value drops from $n \sim$1 to 0.5 with decreasing galaxy magnitude. A similar trend is found also by de Rijcke et al. (2009) for Perseus, and by Misgeld et al. (2009) for the Hydra I cluster, which has a virial mass of $4.4^{+1.1}_{-1.0} \times 10^{14}$ $M_{\odot}$, thus being ≈6 times more massive than the Fornax cluster.

Indeed, there are no differences in the properties of the smallest LSB dwarf galaxies ($M_{r'} \gtrsim$ -12 mag) in the Fornax cluster and the Centaurus group, regardless of the very different type of environments that they represent. This is consistent with the simulations (Zolotov et al. 2012, Oñorbe et al. 2015), which predict that strong background UV - radiation and star formation feedback in the early epoch of the universe suppresses the accretion of the cold gas into the smallest dwarf galaxies. Due to their low mass, these galaxies are inefficient in accreting more cold gas later in their evolution, whereas the more massive ones can continue accreting gas (if available) and forming stars.

2.9 SUMMARY AND CONCLUSIONS

New deep g', r' and i'-band images have been obtained for the central region of the Fornax cluster using the OmegaCAM instrument attached to the VST telescope at ESO. Four 1° x 1° fields of the data, covering the innermost 4 deg^2 of the cluster, have been analyzed in this work. The images, reaching a surface brightness of ∼28 mag $arcsec^{-2}$ (for *S/N* = 5 over 1 $arcsec^2$) in the r'-band, are used to compile a catalog of 205 LSB galaxies ($\mu_{0,r'} > 23$ mag $arcsec^{-2}$), of which galaxies 59 are new detections . These detections complement the previous catalogs of dwarfs in the Fornax cluster, namely the Fornax Cluster Catalog by Ferguson (1989b), the Next Generation Fornax Survey catalog by Muñoz et al. (2015), and the list of extended LSB structures in the Fornax cluster by Lisker et al. (*submitted*). Galaxies are separated from tidal structures, and for these galaxies the photometric parameters are derived, by fitting Sérsic functions to the azimuthally averaged light profiles, and by fitting the full 2D flux distributions of the galaxies using GALFIT. The reliability of the two methods is tested, and the completeness of the UDGs is evaluated by adding artificial mock galaxies to the images. Also, g'-r' aperture colors within the effective radii of the sample galaxies have been obtained.

The following conclusions are obtained:

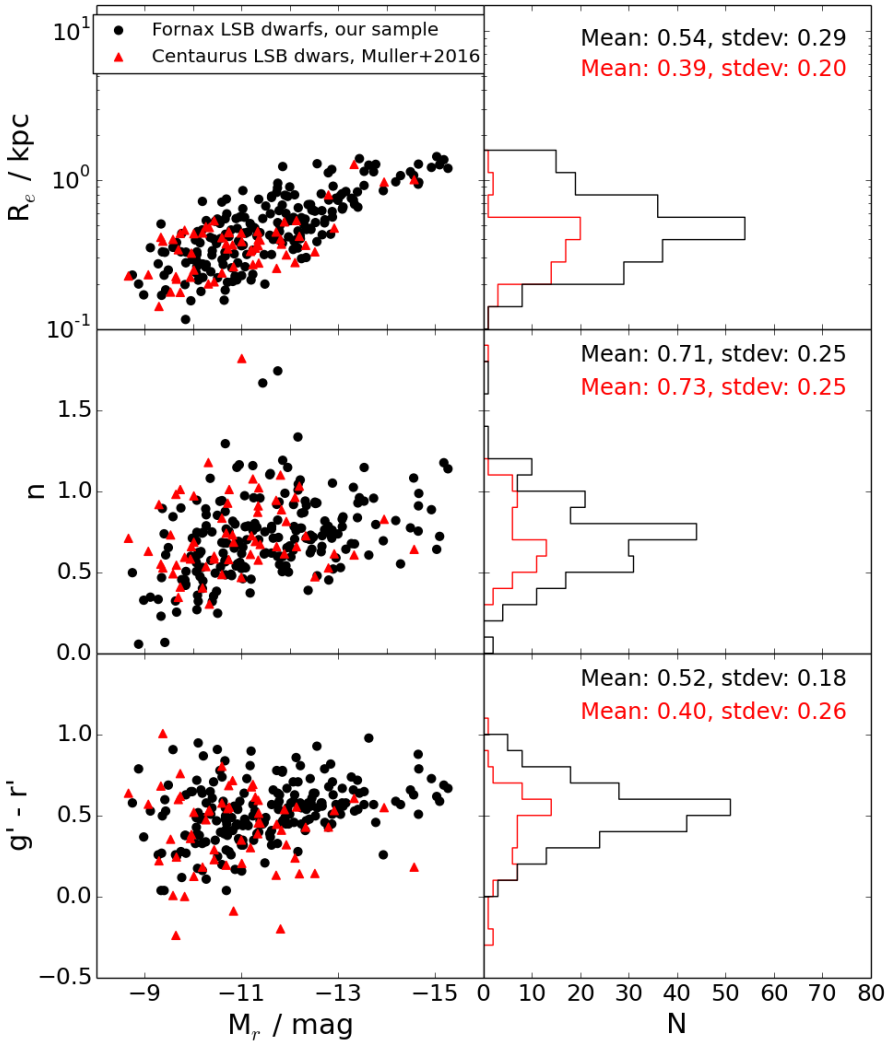

Figure 2.21: *Left panels* show the effective radii (R_e), Sérsic n-values and g'-r' colors as a function of absolute r'-band magnitude $M_{r'}$, for the LSB dwarfs of our sample (black points), and for the Centaurus group dwarfs from Müller et al. (2017) (red triangles). *The histograms on the right* show the distributions of these parameters for both samples with the corresponding colors.

1. Based on visual inspection we identify nine galaxies fulfilling the definition for Ultra Diffuse Galaxies (UDGs) by van Dokkum et al. (2015). Three of these galaxies are new detections. The number density of UDGs normalized with the number of bright galaxies, is found to be higher in Fornax than in the Coma cluster (i.e 0.7$\pm$0.2 and 0.45$\pm$0.05, respectively). However, this can be a detection bias of the Coma sample in a sense that not all UDGs are detected in Coma.

2. We made photometric measurements using GALFIT models and azimuthally averaged luminosity profiles. These two methods give consistent results in terms of effective radii (R_e), total r'-band magnitudes ($m_{r'}$), and Sérsic n-values. We find that the GALFIT models are more reliable for obtaining the ellipticities (b/a), and are therefore used in the analysis of this paper.

3. Assuming that the UDGs in our sample are located at the distance of Fornax they have -15.8 mag $< M_{r'} <$ -13.5 mag and 1.6 kpc $< R_e <$ 11 kpc, which are typical sizes of UDGs found in other environments. However, we find a larger fraction of large UDGs ($R_e >$ 3 kpc) than was found in the Coma cluster (Yagi et al. 2016), and in the distant clusters (van der Burg et al. 2016). As those studies, both using SExtractor, are not as effective as our visual inspection in detecting large UDGs, we can not exclude the possibility of the difference being a selection bias.

4. The five small UDGs with $R_e <$ 3 kpc detected in the Fornax cluster by us, are similar to the typical LSB dwarfs in terms of their magnitude, color and shape, being consistent with them having common origin. The four largest UDGs (with $R_e >$ 3 kpc) appear as outliers having ten times larger effective radii than the typical LSB dwarfs of the same galaxy luminosities. Additionally, the large UDGs in our sample are significantly more elongated (0.2 $< b/a <$ 0.4) than the typical LSB dwarfs, in our sample and in Coma, and they also show signs of tidal interactions.

5. Contrary to the UDG orientations in Coma, we find that the LSB dwarfs in the Fornax cluster are randomly oriented, without any preferences neither toward the cluster center, nor toward their nearby bright galaxies. However, the most elongated galaxies show a preferred alignment toward their nearest bright galaxies.

6. We find that the LSB galaxies in the center of the Fornax cluster follow a color-magnitude relation with a slope, which is same as the one of the red sequence in the Virgo cluster (Kim et al. 2010, Roediger et al. 2017). The UDGs follow the same relation as the smaller LSB dwarfs, although there is one clear outlier toward blue.

7. Our observations are in agreement with both the high-spin and the strong feedback models of UDG formation, where they are seen as an extension of the dwarf galaxy population. However, the large and elongated UDGs in our

sample are likely indications that the tidal forces can also produce some of these UDGs, at least their largest, most elongated representatives.

8. The LSB dwarf galaxies in our sample have magnitudes in the range of -15.4 mag $<$ $m_{r'}$ $<$ -8.9 mag (with the mean of -11.4 mag) and effective radii between 0.14 kpc $<$ R_e $<$ 1.5 kpc (with the mean values of 0.5 kpc). Their colors and profile shapes were compared with the ones of the LSB dwarf galaxies in the Centaurus group (Müller et al. 2017): they were found to be similar for the faintest LSB galaxies ($M_{r'} \gtrsim$ -12 mag). However, the LSB galaxies in the Centaurus become bluer and smaller with increasing magnitude, when compared to the ones in the Fornax cluster.

9. We find that the distribution of LSB dwarf galaxies in the Fornax cluster is less centrally concentrated than the one of the bright galaxies with $M_{r'} <$ -17 mag. Also, the number density of LSB galaxies drops at a cluster-centric distance of r = 0.6° (180 kpc) inward, which can be an indication of tidal disruption of galaxies that enter close to the cluster center. The observed drop in the number of the LSB galaxies in the center of the Fornax cluster is consistent with the findings in other clusters, showing that it is a common phenomenon in galaxy clusters (Wittmann et al. (2017),van der Burg et al. (2016)).

Acknowledgements: A. V. acknowledge the support from grant from the Vilho, Yrjö and Kalle Väisälä Foundation. J. F-B. and R. P. acknowledge support from grant AYA2016-77237-C3-1-P from the Spanish Ministry of Economy and Competitiveness (MINECO). A. V., E. L. and H. S. acknowledge the support from the academy of Finland (grant n:o 297738). This paper has benefited strongly from discussions within the SUNDIAL ITN network, a EU Horizon 2020 research and innovation program under the Marie Skłodowska-Curie grant agreement No 721463. We would also like to thank the anonymous referee, whose detailed comments and suggestions helped to significantly improve this paper.

2.10 References

Abraham, R. G. & van Dokkum, P. G. 2014, PASP, 126, 55

Alam, S., Albareti, F. D., Allende Prieto, C., et al. 2015, ApJS, 219, 12

Amorisco, N. C. & Loeb, A. 2016, MNRAS, 459, L51

Amorisco, N. C., Monachesi, A., Agnello, A., & White, S. D. M. 2018, MNRAS, 475, 4235

Baushev, A. N. 2018, New A, 60, 69

Beasley, M. A. & Trujillo, I. 2016, ApJ, 830, 23

Bertin, E. 2006, in Astronomical Society of the Pacific Conference Series, Vol. 351, Astronomical Data Analysis Software and Systems XV, ed. C. Gabriel, C. Arviset, D. Ponz, & S. Enrique, 112

Bertin, E. 2010, SWarp: Resampling and Co-adding FITS Images Together, Astrophysics Source Code Library

Bertin, E. & Arnouts, S. 1996, A&AS, 117, 393

Binggeli, B., Sandage, A., & Tammann, G. A. 1985, AJ, 90, 1681

Boch, T., Oberto, A., Fernique, P., & Bonnarel, F. 2011, in Astronomical Society of the Pacific Conference Series, Vol. 442, Astronomical Data Analysis Software and Systems XX, ed. I. N. Evans, A. Accomazzi, D. J. Mink, & A. H. Rots, 683

Bothun, G. D., Beers, T. C., Mould, J. R., & Huchra, J. P. 1985, AJ, 90, 2487

Bothun, G. D., Impey, C. D., & Malin, D. F. 1991, ApJ, 376, 404

Bothun, G. D., Schombert, J. M., Impey, C. D., & Schneider, S. E. 1990, ApJ, 360, 427

Boulade, O., Vigroux, L. G., Charlot, X., et al. 1998, in Proc. SPIE, Vol. 3355, Optical Astronomical Instrumentation, ed. S. D'Odorico, 614–625

Bournaud, F. 2010, in Astronomical Society of the Pacific Conference Series, Vol. 423, Galaxy Wars: Stellar Populations and Star Formation in Interacting Galaxies, ed. B. Smith, J. Higdon, S. Higdon, & N. Bastian, 177

Boylan-Kolchin, M., Springel, V., White, S. D. M., Jenkins, A., & Lemson, G. 2009, MNRAS, 398, 1150

Burkert, A. 2017, ApJ, 838, 93

Capaccioli, M., Spavone, M., Grado, A., et al. 2015, A&A, 581, A10

Chandrasekhar, S. 1943, ApJ, 97, 255

Ciotti, L. 1991, A&A, 249, 99

Colless, M. & Dunn, A. M. 1996, ApJ, 458, 435

Conselice, C. J., Gallagher, III, J. S., & Wyse, R. F. G. 2002, AJ, 123, 2246

Crnojević, D., Sand, D. J., Spekkens, K., et al. 2016, ApJ, 823, 19

D'Abrusco, R., Cantiello, M., Paolillo, M., et al. 2016, ApJ, 819, L31

Davies, J., Phillipps, S., Disney, M., Boyce, P., & Evans, R. 1994, MNRAS, 268, 984

Davies, J. I., Phillipps, S., Cawson, M. G. M., Disney, M. J., & Kibblewhite, E. J. 1988, MNRAS, 232, 239

Davies, J. I., Phillipps, S., & Disney, M. J. 1990, MNRAS, 244, 385

de Jong, J. T. A., Verdoes Kleijn, G. A., Boxhoorn, D. R., et al. 2015, A&A, 582, A62

de Rijcke, S., Penny, S. J., Conselice, C. J., Valcke, S., & Held, E. V. 2009, MNRAS, 393, 798

Di Cintio, A., Brook, C. B., Dutton, A. A., et al. 2017, MNRAS, 466, L1

Drinkwater, M. J., Gregg, M. D., & Colless, M. 2001a, ApJ, 548, L139

Drinkwater, M. J., Gregg, M. D., Holman, B. A., & Brown, M. J. I. 2001b, MNRAS, 326, 1076

Drinkwater, M. J., Phillipps, S., & Jones, J. B. 1999, in Astronomical Society of the Pacific Conference Series, Vol. 170, The Low Surface Brightness Universe, ed. J. I. Davies, C. Impey, & S. Phillips, 120

Duc, P.-A., Cuillandre, J.-C., Karabal, E., et al. 2015, MNRAS, 446, 120

Ferguson, H. C. 1989a, Ap&SS, 157, 227

Ferguson, H. C. 1989b, AJ, 98, 367

Ferrarese, L., Côté, P., Cuillandre, J.-C., et al. 2012, ApJS, 200, 4

Flaugher, B., Diehl, H. T., Honscheid, K., et al. 2015, AJ, 150, 150

Gavazzi, G., Donati, A., Cucciati, O., et al. 2005, VizieR Online Data Catalog, 343

Gregg, M. D., Drinkwater, M. J., Evstigneeva, E., et al. 2009, AJ, 137, 498

Henden, A. A., Levine, S. E., Terrell, D., Smith, T. C., & Welch, D. 2012, Journal of the American Association of Variable Star Observers (JAAVSO), 40, 430

Hilker, M., Mieske, S., & Infante, L. 2003, A&A, 397, L9

Hoyos, C., den Brok, M., Verdoes Kleijn, G., et al. 2011, MNRAS, 411, 2439

Impey, C. & Bothun, G. 1989, ApJ, 341, 89

Impey, C. & Bothun, G. 1997, ARA&A, 35, 267

Iodice, E., Capaccioli, M., Grado, A., et al. 2016, ApJ, 820, 42

Iodice, E., Spavone, M., Capaccioli, M., et al. 2017, ApJ, 839, 21

Ivezić, Ž., Lupton, R. H., Schlegel, D., et al. 2004, Astronomische Nachrichten, 325, 583

Janz, J., Laurikainen, E., Lisker, T., et al. 2012, ApJ, 745, L24

Janz, J., Laurikainen, E., Lisker, T., et al. 2014, ApJ, 786, 105

Jerjen, H., Freeman, K. C., & Binggeli, B. 2000, AJ, 119, 166

Jimenez, R., Padoan, P., Matteucci, F., & Heavens, A. F. 1998, MNRAS, 299, 123

Kambas, A., Davies, J. I., Smith, R. M., Bianchi, S., & Haynes, J. A. 2000, AJ, 120, 1316

Kendall, M. & Stuart, A. 1977, The advanced theory of statistics. Vol.1: Distribution theory

Kent, S. M. & Gunn, J. E. 1982, AJ, 87, 945

Kim, S., Rey, S.-C., Lisker, T., & Sohn, S. T. 2010, ApJ, 721, L72

Koch, A., Burkert, A., Rich, R. M., et al. 2012, ApJ, 755, L13

Koda, J., Yagi, M., Yamanoi, H., & Komiyama, Y. 2015, ApJ, 807, L2

Kuijken, K., Bender, R., Cappellaro, E., et al. 2002, The Messenger, 110, 15

Landolt, A. U. 1992, AJ, 104, 340

Lauberts, A. & Valentijn, E. A. 1989, The surface photometry catalogue of the ESO-Uppsala galaxies

Leisman, L., Haynes, M. P., Janowiecki, S., et al. 2017, ApJ, 842, 133

Łokas, E. L. & Mamon, G. A. 2003, MNRAS, 343, 401

Martínez-Delgado, D., Läsker, R., Sharina, M., et al. 2016, AJ, 151, 96

Mathews, W. G., Faltenbacher, A., & Brighenti, F. 2006, ApJ, 638, 659

McConnachie, A. W. 2012, AJ, 144, 4

McFarland, J. P., Verdoes-Kleijn, G., Sikkema, G., et al. 2013, Experimental Astronomy, 35, 45

McLaughlin, D. E. 1999, ApJ, 512, L9

Merritt, A., van Dokkum, P., Danieli, S., et al. 2016, ApJ, 833, 168

Mieske, S., Hilker, M., Infante, L., & Mendes de Oliveira, C. 2007, A&A, 463, 503

Mihos, J. C., Durrell, P. R., Ferrarese, L., et al. 2015, ApJ, 809, L21

Misgeld, I., Hilker, M., & Mieske, S. 2009, A&A, 496, 683

Miyazaki, S., Komiyama, Y., Sekiguchi, M., et al. 2002, PASJ, 54, 833

Moffat, A. F. J. 1969, A&A, 3, 455

Moore, B., Lake, G., & Katz, N. 1998, ApJ, 495, 139

Muñoz, R. P., Eigenthaler, P., Puzia, T. H., et al. 2015, ApJ, 813, L15

Müller, O., Jerjen, H., & Binggeli, B. 2015, A&A, 583, A79

Müller, O., Jerjen, H., & Binggeli, B. 2017, A&A, 597, A7

Oñorbe, J., Boylan-Kolchin, M., Bullock, J. S., et al. 2015, MNRAS, 454, 2092

Paolillo, M., Fabbiano, G., Peres, G., & Kim, D.-W. 2002, ApJ, 565, 883

Peng, C. Y., Ho, L. C., Impey, C. D., & Rix, H.-W. 2002, AJ, 124, 266

Peng, C. Y., Ho, L. C., Impey, C. D., & Rix, H.-W. 2010, AJ, 139, 2097

Roediger, J. C., Ferrarese, L., Côté, P., et al. 2017, ApJ, 836, 120

Roman, J. & Trujillo, I. 2016, ArXiv e-prints [arXiv:1603.03494]

Román, J. & Trujillo, I. 2017, MNRAS, 468, 4039

Romanishin, W., Strom, K. M., & Strom, S. E. 1983, ApJS, 53, 105

Sabatini, S., Davies, J., van Driel, W., et al. 2005, MNRAS, 357, 819

Salo, H., Laurikainen, E., Laine, J., et al. 2015, ApJS, 219, 4

Sandage, A. & Binggeli, B. 1984, AJ, 89, 919

Schipani, P., Capaccioli, M., Arcidiacono, C., et al. 2012, in Proc. SPIE, Vol. 8444, Ground-based and Airborne Telescopes IV, 84441C

Sersic, J. L. 1968, Atlas de galaxias australes

Skrutskie, M. F., Cutri, R. M., Stiening, R., et al. 2006, AJ, 131, 1163

Smith, R., Sánchez-Janssen, R., Beasley, M. A., et al. 2015, MNRAS, 454, 2502

Sprayberry, D., Impey, C. D., Bothun, G. D., & Irwin, M. J. 1995, AJ, 109, 558

Toloba, E., Sand, D. J., Spekkens, K., et al. 2016, ApJ, 816, L5

Tonry, J. L., Dressler, A., Blakeslee, J. P., et al. 2001, ApJ, 546, 681

Trujillo, I., Roman, J., Filho, M., & Sánchez Almeida, J. 2017, ApJ, 836, 191

van der Burg, R. F. J., Hoekstra, H., Muzzin, A., et al. 2017, A&A, 607, A79

van der Burg, R. F. J., Muzzin, A., & Hoekstra, H. 2016, A&A, 590, A20

van Dokkum, P. G., Abraham, R., Merritt, A., et al. 2015, ApJ, 798, L45

Verdoes Kleijn, G. A., Kuijken, K. H., Valentijn, E. A., et al. 2013, Experimental Astronomy, 35, 103

White, S. D. M. 1977, MNRAS, 179, 33

Wittmann, C., Lisker, T., Ambachew Tilahun, L., et al. 2017, MNRAS, 470, 1512

Yagi, M., Koda, J., Komiyama, Y., & Yamanoi, H. 2016, ApJS, 225, 11

Yagi, M., Yoshida, M., Komiyama, Y., et al. 2010, AJ, 140, 1814

Zolotov, A., Brooks, A. M., Willman, B., et al. 2012, ApJ, 761, 71

2.11 APPENDIX

2.11.1 PIXEL VALUE DISTRIBUTION MOMENTS.

The center and initial shape parameters of a galaxy are measured by calculating the first and second moments of the galaxy's pixel value distribution. The pixels from which the moments are calculated are selected by manually placing an elliptical aperture over the galaxy that follows the apparent shape of the galaxy and covers the visible part of the galaxy. If we mark x- and y-coordinates and intensity of a pixel i as x_i, y_i and I_i,respectively, we can calculate the first moments of pixel value distribution as follows

$$\begin{aligned} \overline{x} &= \frac{\sum_i I_i x_i}{\sum_i I_i}, \\ \overline{y} &= \frac{\sum_i I_i y_i}{\sum_i I_i}. \end{aligned} \tag{2.7}$$

The first moments correspond to the weighted center of the pixel value distribution. The second order moments

$$\begin{aligned} \overline{x^2} &= \frac{\sum_i I_i x_i^2}{\sum_i I_i} - \overline{x}^2, \\ \overline{y^2} &= \frac{\sum_i I_i y_i^2}{\sum_i I_i} - \overline{y}^2, \\ \overline{xy} &= \frac{\sum_i I_i x_i y_i}{\sum_i I_i} - \overline{x}\,\overline{y}, \end{aligned} \tag{2.8}$$

describe the spread of the distribution along the axes. They can be transformed to semi-minor axis b and semi-major axis a as

$$\begin{aligned} a^2 &= \frac{\overline{x^2}+\overline{y^2}}{2} + \sqrt{\left(\frac{\overline{x^2}-\overline{y^2}}{2}\right)^2 + \overline{xy}^2}, \\ b^2 &= \frac{\overline{x^2}+\overline{y^2}}{2} - \sqrt{\left(\frac{\overline{x^2}-\overline{y^2}}{2}\right)^2 + \overline{xy}^2}, \end{aligned} \tag{2.9}$$

and the position angle θ

$$\tan(2\theta) = 2\frac{\overline{xy}}{\overline{x^2} - \overline{y^2}}. \tag{2.10}$$

2.11.2 MOCK GALAXY PARAMETERS

The mock galaxies are generated by using 2D Sérsic functions with the chosen structural parameters and random position angles. Also, the Poisson noise is added to the galaxies, and the models are then convolved with the OmegaCAM *PSF* (see Section 5.2 for details) before adding them to the science mosaics.

The parameters of the UDG mock galaxies used for testing the detection efficiency are given in Table 2.5. Also the indications of the detections in different fields are given in 2.5. The additional $\sim$ 150 mock galaxies used for testing the photometric accuracy have $m_{r'}$ = 15–24 mag, R_e = 5–20 arcsec, Sérsic n = 0.3–2 and b/a = 0.2–1. The differences between the input model and measured parameters for all the mock galaxies are shown in the Fig. 2.11.

2.11.3 TRANSFORMATIONS BETWEEN PHOTOMETRIC FILTERS

To transform the Subaru Suprime-Cam B and R magnitudes into the r'- and g'-band values we used the transformations from Yagi et al. (2010). The r' band magnitude $m_{r'}$ is

$$m_{r'} = m_R - 0.0188 + 0.1492 \times (g' - r') - 0.0128 \times (g' - r')^2, \tag{2.11}$$

where m_R is the apparent magnitude in Suprime-Cam R-band. Also, the Suprime-Cam B-R color can be transformed into g'-r' color as follows:

$$B - R = 0.00440 + 1.32386 \times (g' - r') + 0.0010734 \times (g' - r')^2 \tag{2.12}$$

For the transformations between the Johnson U,B,V,R and I and SDSS g',r' and i' colors we used the equations given in the SDSS website by Lupton (2005[13]):

$$m_V = m_{r'} + 0.4216 \times (g' - r') - 0.0038, \tag{2.13}$$

where m_V and $m_{r'}$ are the apparent magnitudes in V- and r'- filters, respectively, and $g' - r'$ is g'-r' color. Similarly:

$$m_B = m_{r'} + 1.33130 \times (g' - r') + 0.2271, \tag{2.14}$$

where m_B is the apparent magnitude in B-band.

2.11.4 LIST OF GALAXIES

We list the properties of the galaxies in our sample In Table D.1. .

[13]http://www.sdss3.org/dr8/algorithms/sdssUBVRITransform.php#Lupton2005

Table 2.5: Structural parameters of the mock UDGs adopted from van Dokkum et al. (2015) and Mihos et al. (2015). The four last columns indicate if the mock galaxy was detected in the given field (Y = yes, N = no, O = not detected due to the selection criteria).

Name	M_g	R_e [kpc]	n	b/a	D_{10}	D_{11}	D_{12}	D_{16}
VLSB-A[b]	-15.0	9.7	1.2	0.5	O	Y	Y	O
VLSB-B[b]	-13.5	2.9	0.8	0.83	Y	Y	Y	Y
VLSB-C[b]	-14.9	5.5	0.7	0.88	Y	N	Y	Y
DF6[a]	-14.3	4.4	1	0.47	Y	Y	O	Y
DF9[a]	-14.0	2.8	1	0.92	Y	Y	Y	Y
DF14[a]	-14.4	3.8	1	0.51	Y	Y	Y	Y
DF1[a]	-14.6	3.1	1	0.82	Y	Y	Y	Y
DF22[a]	-13.8	2.1	1	0.84	Y	Y	Y	Y
DF17[a]	-15.2	4.4	1	0.71	Y	Y	Y	Y
DF20[a]	-13.0	2.3	1	0.53	Y	Y	Y	Y
DF24[a]	-12.5	1.8	1	0.38	Y	Y	Y	Y
DF30[a]	-15.2	3.2	1	0.70	Y	O	Y	Y
DF34[a]	-13.6	3.4	1	0.66	Y	Y	Y	Y
DF38[a]	-14.3	1.8	1	0.84	Y	Y	Y	Y
DF7[a]	-16.0	4.3	1	0.76	Y	Y	Y	Y

(a)van Dokkum et al. (2015), (b)Mihos et al. (2015)

Table 2.6: The columns in the table correspond to the following properties: Name of the object (Name), right ascension (RA) and declination (DEC) of the object, axis ratio and error (b/a), position angle (θ, east of north), apparent magnitude ($m_{r'}$) and error in r'-band , effective radius ($R_{e,r'}$) in r'-band and error in arc seconds , Sérsic index (n) and error, g'-r' color within R_e (g'-r') and error, and the possible FCC number and identifications in earlier works (References). The references in the table are $^{(a)}$: Ferguson (1989b), $^{(b)}$:Bothun et al. (1991), $^{(c)}$: Muñoz et al. (2015), $^{(d)}$:Mieske et al. (2007). The error estimations for each parameter are adopted from the tests made with the mock galaxies in Section 5.4.2. The asterisks in the end of the object name indicates that it was fit using a additional *PSF* component for the nucleus.

Name	R.A. (J2000)	DEC (J2000)	b/a	θ [deg]	$m_{r'}$	$R_{e,r'}$ [arcsec]	n	g'-r'	Ref
FDS10_LSB2	55.021	-34.652	0.66± 0.04	43.23	20.30 ± 0.16	4.4 ± 0.6	0.52 ± 0.17	0.33 ± 0.09	$^{(c)}$
FDS10_LSB3	54.945	-34.687	0.54± 0.09	78.32	21.96 ± 0.41	6.1 ± 1.3	0.23 ± 0.20	0.05 ± 0.11	
FDS10_LSB4	54.977	-34.696	0.86± 0.03	44.55	19.68 ± 0.13	3.8 ± 0.4	0.62 ± 0.16	0.42 ± 0.09	$^{(c)}$
FDS10_LSB5	55.262	-34.696	0.68± 0.08	86.94	20.61 ± 0.37	9.0 ± 1.8	0.58 ± 0.20	0.05 ± 0.08	
FDS10_LSB6	55.236	-34.713	0.80± 0.04	1.20	20.93 ± 0.16	2.9 ± 0.4	0.57 ± 0.17	0.52 ± 0.10	$^{(c)}$
FDS10_LSB8 *	55.002	-34.723	0.79± 0.05	-36.59	19.86 ± 0.22	6.6 ± 1.0	1.67 ± 0.18	0.46 ± 0.08	$^{(c)}$
FDS10_LSB9	55.119	-34.786	0.85± 0.06	53.72	21.44 ± 0.27	4.0 ± 0.7	0.50 ± 0.19	0.28 ± 0.09	$^{(c)}$
FDS10_LSB10	55.109	-35.003	0.48± 0.04	59.29	20.05 ± 0.17	5.8 ± 0.8	0.96 ± 0.17	0.36 ± 0.11	$^{(c)}$
FDS10_LSB11	54.827	-34.937	0.96± 0.03	-61.65	21.45 ± 0.11	1.4 ± 0.1	0.42 ± 0.16	0.39 ± 0.15	
FDS10_LSB12	54.696	-34.987	0.60± 0.05	51.72	21.89 ± 0.20	2.8 ± 0.4	0.74 ± 0.18	0.05 ± 0.11	$^{(c)}$
FDS10_LSB13	54.594	-34.927	0.58± 0.05	-55.11	21.22 ± 0.21	4.0 ± 0.6	0.27 ± 0.18	0.40 ± 0.09	$^{(c)}$
FDS10_LSB14	54.393	-34.566	0.58± 0.05	45.72	20.55 ± 0.20	5.0 ± 0.7	0.75 ± 0.18	0.29 ± 0.08	$^{(c)}$
FDS10_LSB15	54.496	-34.530	0.72± 0.05	46.66	20.21 ± 0.20	5.3 ± 0.8	0.53 ± 0.18	0.47 ± 0.08	
FDS10_LSB16	54.602	-34.649	0.67± 0.04	56.08	20.63 ± 0.16	3.7 ± 0.5	1.29 ± 0.17	0.56 ± 0.09	
FDS10_LSB17	54.631	-34.774	0.60± 0.04	-56.43	21.03 ± 0.16	3.1 ± 0.4	0.89 ± 0.17	0.35 ± 0.10	$^{(c)}$
FDS10_LSB20	55.275	-34.145	1.00± 0.07	-68.53	22.42 ± 0.28	2.4 ± 0.4	0.06 ± 0.19	0.80 ± 0.10	
FDS10_LSB21	55.225	-34.288	0.78± 0.03	88.31	20.43 ± 0.12	2.7 ± 0.3	0.80 ± 0.16	0.18 ± 0.10	
FDS10_LSB23	55.169	-34.949	0.85± 0.05	65.07	18.89 ± 0.18	8.2 ± 1.1	0.70 ± 0.17	0.49 ± 0.08	$^{(c)}$
FDS10_LSB25	54.959	-35.023	0.69± 0.05	-28.43	17.26 ± 0.20	21.6 ± 3.1	0.40 ± 0.18	0.44 ± 0.09	FCC226$^{(a)\ (b)\ (c)}$
FDS10_LSB27	55.042	-34.447	0.56± 0.03	55.06	16.64 ± 0.10	15.4 ± 1.6	0.91 ± 0.16	0.52 ± 0.08	FCC234$^{(a)}$
FDS10_LSB29	55.019	-34.168	0.96± 0.03	2.73	17.89 ± 0.12	7.9 ± 0.9	0.93 ± 0.16	0.55 ± 0.08	FCC231$^{(a)}$
FDS10_LSB30	54.943	-34.135	0.85± 0.03	18.23	20.48 ± 0.12	2.5 ± 0.3	0.81 ± 0.16	0.42 ± 0.10	
FDS10_LSB32	54.659	-33.898	0.83± 0.03	-50.83	20.29 ± 0.12	2.8 ± 0.3	0.62 ± 0.16	0.17 ± 0.10	
FDS10_LSB33	54.780	-34.061	0.72± 0.04	-76.23	21.19 ± 0.15	2.6 ± 0.3	0.32 ± 0.17	0.96 ± 0.11	
FDS10_LSB34	54.723	-34.171	0.92± 0.04	80.84	21.34 ± 0.14	1.9 ± 0.2	0.60 ± 0.17	0.66 ± 0.12	
FDS10_LSB35	54.777	-34.264	0.76± 0.02	-57.05	18.96 ± 0.08	3.6 ± 0.3	0.71 ± 0.15	0.48 ± 0.09	
FDS10_LSB36	54.824	-34.306	0.74± 0.03	-80.59	20.63 ± 0.11	2.2 ± 0.2	0.87 ± 0.16	0.49 ± 0.12	
FDS10_LSB37	54.761	-34.577	0.65± 0.03	-64.92	20.10 ± 0.09	2.6 ± 0.2	0.46 ± 0.16	0.91 ± 0.11	

Table 2.6: Continued.

Name	R.A. (J2000)	DEC (J2000)	b/a	θ [deg]	$m_{r'}$	$R_{e,r'}$ [arcsec]	n	g'-r'	Ref
FDS10_LSB38	54.726	-34.826	0.70± 0.06	0.40	19.34 ± 0.23	9.3 ± 1.4	1.15 ± 0.18	0.56 ± 0.07	(c)
FDS10_LSB39	54.619	-34.690	0.91± 0.03	15.84	20.65 ± 0.10	1.9 ± 0.2	0.68 ± 0.16	0.40 ± 0.12	
FDS10_LSB40	54.557	-34.229	0.34± 0.06	-4.54	20.70 ± 0.27	8.6 ± 1.4	0.68 ± 0.19	0.21 ± 0.08	
FDS10_LSB41	54.533	-33.980	0.75± 0.04	19.24	18.98 ± 0.15	6.6 ± 0.8	0.94 ± 0.17	0.42 ± 0.08	
FDS10_LSB43	54.379	-34.096	0.93± 0.05	-26.15	20.34 ± 0.21	4.6 ± 0.7	1.16 ± 0.18	0.36 ± 0.08	
FDS10_LSB44	54.374	-34.225	0.81± 0.04	-86.34	20.22 ± 0.13	3.2 ± 0.4	0.78 ± 0.17	0.46 ± 0.09	
FDS10_LSB45	54.344	-34.287	0.79± 0.04	-44.37	19.32 ± 0.13	5.0 ± 0.6	0.50 ± 0.17	0.46 ± 0.08	
FDS10_LSB46	54.317	-34.271	0.71± 0.03	-12.62	20.59 ± 0.11	2.5 ± 0.3	0.76 ± 0.16	0.39 ± 0.11	
FDS10_LSB47	54.289	-34.291	0.69± 0.02	-44.16	19.81 ± 0.08	2.4 ± 0.2	0.75 ± 0.15	0.22 ± 0.11	
FDS10_LSB49	54.261	-34.876	0.95± 0.04	11.19	19.21 ± 0.13	4.7 ± 0.5	0.78 ± 0.17	0.47 ± 0.08	FCC185 (a)
FDS10_LSB51	54.001	-34.878	0.99± 0.05	-15.58	19.38 ± 0.21	7.2 ± 1.1	0.54 ± 0.18	0.46 ± 0.09	(c)
FDS10_LSB52	53.982	-34.828	0.51± 0.04	79.41	17.52 ± 0.14	15.4 ± 1.9	0.79 ± 0.17	0.47 ± 0.08	FCC159 (a) (c)
FDS10_LSB53	54.174	-34.711	0.61± 0.04	-2.59	19.98 ± 0.16	5.1 ± 0.6	0.78 ± 0.17	0.40 ± 0.08	(c)
FDS10_LSB54	54.118	-34.755	0.30± 0.04	16.81	21.31 ± 0.14	3.5 ± 0.4	0.71 ± 0.17	0.66 ± 0.11	
FDS10_LSB55	53.988	-34.632	0.55± 0.03	-18.01	18.77 ± 0.11	6.2 ± 0.7	0.92 ± 0.16	0.51 ± 0.08	(c)
FDS10_LSB56	54.083	-34.594	0.55± 0.07	-67.20	21.64 ± 0.28	4.6 ± 0.8	0.25 ± 0.19	0.26 ± 0.09	(c)
FDS10_LSB57	53.970	-34.243	0.64± 0.03	86.22	20.79 ± 0.13	2.7 ± 0.3	0.25 ± 0.16	0.26 ± 0.11	
FDS11_LSB1	55.246	-35.697	0.24± 0.08	29.92	16.19 ± 0.37	116.4 ± 22.9	0.55 ± 0.20	0.18 ± 0.07	
FDS11_LSB2	55.148	-35.774	0.48± 0.05	40.76	15.55 ± 0.22	63.9 ± 9.7	0.85 ± 0.18	0.99 ± 0.14	
FDS11_LSB4	55.066	-35.662	0.91± 0.05	-72.81	20.26 ± 0.19	4.4 ± 0.6	0.53 ± 0.18	0.33 ± 0.08	(c)
FDS11_LSB6	54.711	-35.725	0.71± 0.07	-8.23	21.19 ± 0.29	5.2 ± 0.9	0.62 ± 0.19	0.53 ± 0.08	
FDS11_LSB7	54.035	-36.000	0.77± 0.07	54.15	20.74 ± 0.29	6.2 ± 1.1	0.94 ± 0.19	0.79 ± 0.08	
FDS11_LSB8	54.001	-35.936	0.78± 0.07	-61.15	21.23 ± 0.30	5.0 ± 0.9	0.56 ± 0.19	0.44 ± 0.08	(c)
FDS11_LSB10	54.105	-35.703	0.58± 0.05	-74.41	19.52 ± 0.18	7.5 ± 1.0	0.93 ± 0.18	0.60 ± 0.08	(c)
FDS11_LSB11	54.161	-35.610	0.81± 0.06	61.68	20.63 ± 0.24	5.2 ± 0.8	0.48 ± 0.18	0.51 ± 0.08	(c)
FDS11_LSB12	55.360	-35.380	0.88± 0.04	78.68	21.09 ± 0.17	2.7 ± 0.3	0.45 ± 0.17	0.50 ± 0.10	(c)
FDS11_LSB13	55.112	-35.419	0.81± 0.05	-79.83	20.36 ± 0.20	4.7 ± 0.7	0.69 ± 0.18	0.37 ± 0.08	(c)
FDS11_LSB14	55.154	-35.356	0.83± 0.07	-45.11	19.55 ± 0.30	10.7 ± 1.9	0.60 ± 0.19	0.34 ± 0.08	(b) (c)
FDS11_LSB15	55.220	-35.118	0.93± 0.04	39.58	19.06 ± 0.17	6.7 ± 0.9	0.86 ± 0.17	0.46 ± 0.08	(c)
FDS11_LSB16	54.615	-35.040	0.80± 0.07	-26.87	18.73 ± 0.30	15.5 ± 2.7	0.48 ± 0.19	0.56 ± 0.09	
FDS11_LSB17	54.510	-35.281	0.30± 0.09	50.31	17.22 ± 0.43	75.7 ± 16.1	1.00 ± 0.20	0.54 ± 0.09	
FDS11_LSB18 *	54.249	-35.138	0.73± 0.06	-81.05	20.51 ± 0.24	5.6 ± 0.9	0.49 ± 0.18	0.27 ± 0.11	(c)
FDS11_LSB30 *	54.155	-35.385	0.91± 0.05	-78.25	17.76 ± 0.19	13.8 ± 1.9	1.15 ± 0.18	0.66 ± 0.13	FCC171 (a) (c)
FDS11_LSB32	54.179	-35.436	0.76± 0.03	-0.30	17.96 ± 0.12	8.3 ± 0.9	0.67 ± 0.16	0.54 ± 0.15	FCC175 (a)
FDS11_LSB35	54.537	-35.165	0.78± 0.05	26.45	20.12 ± 0.22	6.2 ± 0.9	0.37 ± 0.18	0.82 ± 0.10	(c)
FDS11_LSB36	55.078	-35.138	0.75± 0.07	-15.66	20.84 ± 0.31	6.4 ± 1.1	0.49 ± 0.19	0.36 ± 0.08	(b) (c) (d
FDS11_LSB38 *	55.304	-35.157	0.85± 0.03	-69.87	16.20 ± 0.10	15.2 ± 1.6	0.72 ± 0.16	0.60 ± 0.08	FCC260 (a) (b) (c)

Table 2.6: Continued.

Name	R.A. (J2000)	DEC (J2000)	b/a	θ [deg]	$m_{r'}$	$R_{e,r'}$ [arcsec]	n	g'-r'	Ref
FDS11_LSB39	55.305	-35.335	0.66± 0.07	68.99	21.88 ± 0.29	3.9 ± 0.7	0.07 ± 0.19	0.61 ± 0.09	
FDS11_LSB40	55.208	-35.389	0.61± 0.06	-69.42	22.02 ± 0.25	3.3 ± 0.5	0.33 ± 0.18	0.27 ± 0.10	$^{(c)}$
FDS11_LSB41	54.964	-35.323	0.85± 0.04	-21.88	18.30 ± 0.15	8.8 ± 1.1	0.74 ± 0.17	0.53 ± 0.08	$^{(b)}$ $^{(c)}$ $^{(d}$
FDS11_LSB42	55.013	-35.464	0.82± 0.06	-85.27	19.30 ± 0.27	10.8 ± 1.8	0.66 ± 0.19	0.52 ± 0.08	$^{(b)}$ $^{(c)}$ $^{(d}$
FDS11_LSB43	54.926	-35.469	0.77± 0.07	67.40	21.66 ± 0.31	4.3 ± 0.8	0.32 ± 0.19	0.27 ± 0.08	$^{(c)}$ $^{(d}$
FDS11_LSB44	54.463	-35.364	0.69± 0.06	7.39	21.15 ± 0.25	4.6 ± 0.7	0.47 ± 0.18	0.49 ± 0.08	$^{(c)}$ $^{(d}$
FDS11_LSB45	54.412	-35.386	0.81± 0.05	0.62	19.70 ± 0.22	7.2 ± 1.1	1.11 ± 0.18	0.38 ± 0.08	$^{(c)}$ $^{(d}$
FDS11_LSB46	54.316	-35.357	0.55± 0.06	11.75	20.60 ± 0.27	7.1 ± 1.2	0.68 ± 0.19	0.46 ± 0.08	$^{(c)}$ $^{(d}$
FDS11_LSB47 ∗	54.250	-35.343	0.81± 0.05	-85.59	18.40 ± 0.19	11.0 ± 1.5	0.52 ± 0.18	0.64 ± 0.08	$^{(c)}$ $^{(d}$
FDS11_LSB48	54.007	-35.310	0.76± 0.05	78.70	21.02 ± 0.18	3.3 ± 0.4	0.85 ± 0.18	0.12 ± 0.11	$^{(c)}$ $^{(d}$
FDS11_LSB49	53.930	-35.514	0.83± 0.04	28.68	17.57 ± 0.16	13.7 ± 1.8	0.96 ± 0.17	0.58 ± 0.08	FCC157$^{(a)}$ $^{(b)}$ $^{(c)}$
FDS11_LSB50	54.099	-35.523	0.72± 0.05	-12.94	22.32 ± 0.20	2.0 ± 0.3	0.33 ± 0.18	0.38 ± 0.13	$^{(c)}$
FDS11_LSB51	54.170	-35.589	0.43± 0.08	30.21	21.10 ± 0.35	8.7 ± 1.7	0.40 ± 0.20	0.17 ± 0.08	$^{(d}$
FDS11_LSB53	54.437	-35.704	1.00± 0.04	13.73	20.50 ± 0.16	3.1 ± 0.4	0.48 ± 0.17	0.50 ± 0.09	$^{(c)}$ $^{(d}$
FDS11_LSB55	54.871	-35.573	0.71± 0.07	-19.33	19.94 ± 0.28	8.9 ± 1.5	0.70 ± 0.19	0.41 ± 0.08	$^{(c)}$ $^{(d}$
FDS11_LSB56	54.923	-35.532	0.75± 0.05	-61.01	20.16 ± 0.20	5.4 ± 0.8	0.79 ± 0.18	0.45 ± 0.08	$^{(c)}$ $^{(d}$
FDS11_LSB57 ∗	54.958	-35.522	0.97± 0.04	-56.59	19.01 ± 0.15	6.1 ± 0.8	0.87 ± 0.17	0.57 ± 0.08	FCC227$^{(a)}$ $^{(c)}$
FDS11_LSB58 ∗	54.986	-35.622	0.54± 0.06	-57.40	20.27 ± 0.25	7.7 ± 1.2	0.46 ± 0.18	0.36 ± 0.08	$^{(c)}$ $^{(d}$
FDS11_LSB59	54.982	-35.662	0.73± 0.04	-85.93	18.34 ± 0.15	9.1 ± 1.1	0.59 ± 0.17	0.58 ± 0.08	FCC229$^{(a)}$ $^{(c)}$
FDS11_LSB60	55.280	-35.515	0.61± 0.03	-83.68	17.76 ± 0.13	11.1 ± 1.3	0.94 ± 0.17	0.58 ± 0.08	FCC259$^{(a)}$ $^{(b)}$
FDS11_LSB61	55.279	-35.690	0.82± 0.04	-72.47	19.50 ± 0.17	6.0 ± 0.8	0.60 ± 0.17	0.46 ± 0.08	FCC258$^{(a)}$ $^{(c)}$
FDS11_LSB62 ∗	55.253	-35.743	0.90± 0.03	-54.30	17.01 ± 0.13	12.9 ± 1.5	0.55 ± 0.16	0.58 ± 0.08	FCC254$^{(a)}$ $^{(c)}$
FDS11_LSB63	55.141	-35.888	0.65± 0.05	-75.69	20.38 ± 0.21	5.7 ± 0.9	0.55 ± 0.18	0.46 ± 0.08	$^{(c)}$
FDS11_LSB64	54.747	-35.741	0.88± 0.03	8.90	20.39 ± 0.12	2.6 ± 0.3	1.15 ± 0.16	0.57 ± 0.10	$^{(c)}$
FDS11_LSB65 ∗	54.657	-35.757	0.75± 0.04	-34.75	18.92 ± 0.17	8.2 ± 1.1	0.39 ± 0.17	0.59 ± 0.09	FCC215$^{(a)}$ $^{(c)}$
FDS11_LSB66	54.226	-35.747	0.52± 0.05	-29.25	20.73 ± 0.19	4.9 ± 0.7	0.53 ± 0.18	0.41 ± 0.09	$^{(c)}$ $^{(d}$
FDS11_LSB67 ∗	54.264	-35.801	0.86± 0.04	35.84	19.71 ± 0.17	5.1 ± 0.7	1.10 ± 0.17	0.40 ± 0.08	$^{(c)}$ $^{(d}$
FDS11_LSB68	54.293	-35.888	0.71± 0.05	24.16	19.12 ± 0.18	7.8 ± 1.1	1.04 ± 0.17	0.57 ± 0.08	FCC192$^{(a)}$ $^{(c)}$
FDS11_LSB69	54.029	-35.843	0.61± 0.05	83.86	18.43 ± 0.21	14.2 ± 2.1	0.71 ± 0.18	0.46 ± 0.08	FCC163$^{(a)}$ $^{(c)}$
FDS11_LSB70	54.229	-35.944	0.90± 0.05	-81.87	21.95 ± 0.19	2.0 ± 0.3	0.47 ± 0.18	0.28 ± 0.12	$^{(c)}$ $^{(d}$
FDS11_LSB71	54.365	-35.963	0.92± 0.05	40.42	19.91 ± 0.20	5.3 ± 0.8	0.96 ± 0.18	0.48 ± 0.09	$^{(c)}$ $^{(d}$
FDS11_LSB72	54.425	-35.956	0.46± 0.05	-13.90	19.67 ± 0.21	9.2 ± 1.4	0.77 ± 0.18	0.33 ± 0.09	$^{(c)}$ $^{(d}$
FDS11_LSB73	54.535	-36.008	0.81± 0.06	-88.59	21.22 ± 0.23	3.8 ± 0.6	0.75 ± 0.18	0.50 ± 0.09	$^{(c)}$ $^{(d}$
FDS11_LSB74	55.176	-35.661	0.64± 0.03	-38.83	17.37 ± 0.10	10.2 ± 1.0	0.69 ± 0.16	0.27 ± 0.07	FCC247$^{(a)}$ $^{(c)}$
FDS11_LSB76	55.052	-35.289	0.62± 0.07	22.78	21.20 ± 0.28	5.4 ± 0.9	0.36 ± 0.19	0.19 ± 0.08	$^{(c)}$

Table 2.6: Continued.

Name	R.A. (J2000)	DEC (J2000)	b/a	θ [deg]	$m_{r'}$	$R_{e,r'}$ [arcsec]	n	g'-r'	Ref
FDS11_LSB77	54.653	-35.834	0.91± 0.03	14.21	18.63 ± 0.11	5.2 ± 0.5	0.73 ± 0.16	0.57 ± 0.08	FCC214[a] [c]
FDS11_LSB78 *	54.392	-35.829	0.52± 0.03	66.83	17.11 ± 0.09	11.7 ± 1.1	0.82 ± 0.16	0.60 ± 0.07	FCC196[a] [c]
FDS11_LSB79	54.292	-35.387	0.83± 0.03	-78.41	18.86 ± 0.13	5.6 ± 0.6	0.70 ± 0.16	0.59 ± 0.08	FCC191[a] [c]
FDS11_LSB80	54.422	-35.296	0.82± 0.03	82.65	18.57 ± 0.13	6.5 ± 0.7	0.82 ± 0.16	0.47 ± 0.08	FCC197[a] [c]
FDS11_LSB81	54.116	-35.211	0.88± 0.04	25.14	18.20 ± 0.13	7.9 ± 0.9	0.84 ± 0.17	0.57 ± 0.07	FCC168[a] [c]
FDS12_LSB2	55.300	-36.069	0.71± 0.04	49.87	21.23 ± 0.17	2.9 ± 0.4	0.50 ± 0.17	0.50 ± 0.10	[c]
FDS12_LSB3	55.184	-36.185	0.79± 0.05	20.40	17.86 ± 0.22	16.8 ± 2.5	0.96 ± 0.18	0.65 ± 0.09	
FDS12_LSB4	55.157	-36.121	0.65± 0.04	-45.70	18.22 ± 0.14	9.8 ± 1.2	0.83 ± 0.17	0.59 ± 0.08	FCC246[a] [c]
FDS12_LSB5	55.138	-36.580	0.62± 0.07	-53.68	21.53 ± 0.32	5.3 ± 1.0	0.45 ± 0.19	0.13 ± 0.08	
FDS12_LSB6	55.137	-36.555	0.71± 0.08	61.44	22.18 ± 0.36	4.2 ± 0.8	0.35 ± 0.20	0.54 ± 0.09	
FDS12_LSB8	55.061	-36.613	0.85± 0.06	25.33	21.44 ± 0.23	3.4 ± 0.5	0.43 ± 0.18	0.64 ± 0.09	
FDS12_LSB9 *	55.029	-36.560	0.80± 0.04	28.65	18.25 ± 0.15	9.5 ± 1.2	0.53 ± 0.17	0.52 ± 0.08	
FDS12_LSB10 *	55.071	-36.535	0.71± 0.04	19.45	18.14 ± 0.15	10.1 ± 1.2	0.64 ± 0.17	0.59 ± 0.08	FCC238[a] [c]
FDS12_LSB11	54.907	-36.553	0.58± 0.04	-64.51	19.27 ± 0.14	6.4 ± 0.8	0.59 ± 0.17	0.59 ± 0.10	FCC225[a]
FDS12_LSB12 *	55.081	-36.314	0.76± 0.06	-14.31	19.40 ± 0.24	9.5 ± 1.5	0.99 ± 0.18	0.50 ± 0.07	[c]
FDS12_LSB13	55.025	-36.234	0.39± 0.04	26.28	18.50 ± 0.17	13.5 ± 1.8	0.78 ± 0.17	0.44 ± 0.08	FCC233[a] [c]
FDS12_LSB14	54.969	-36.142	0.58± 0.04	86.51	21.11 ± 0.17	3.3 ± 0.4	0.53 ± 0.17	0.65 ± 0.10	[c]
FDS12_LSB16	55.001	-36.094	0.63± 0.06	-33.54	20.23 ± 0.23	6.8 ± 1.1	0.97 ± 0.18	0.49 ± 0.08	[c]
FDS12_LSB17	54.885	-36.099	0.94± 0.05	85.27	20.02 ± 0.22	5.7 ± 0.9	0.80 ± 0.18	0.54 ± 0.08	[c]
FDS12_LSB18	55.076	-36.059	0.68± 0.07	19.50	21.93 ± 0.30	4.0 ± 0.7	0.89 ± 0.19	0.51 ± 0.09	[c]
FDS12_LSB19	54.963	-36.013	0.87± 0.05	18.17	21.23 ± 0.22	3.5 ± 0.5	0.69 ± 0.18	0.50 ± 0.09	[c]
FDS12_LSB20	54.655	-35.917	0.56± 0.03	-27.62	19.53 ± 0.12	4.8 ± 0.5	0.71 ± 0.16	0.55 ± 0.09	[c] [d
FDS12_LSB21	54.754	-36.338	0.59± 0.03	-38.17	18.96 ± 0.11	5.6 ± 0.6	0.91 ± 0.16	0.55 ± 0.08	[c]
FDS12_LSB22	54.664	-36.558	0.81± 0.04	-42.76	18.63 ± 0.15	7.5 ± 0.9	0.66 ± 0.17	0.59 ± 0.08	FCC216[a]
FDS12_LSB23	54.723	-36.614	0.87± 0.05	64.90	20.24 ± 0.22	5.3 ± 0.8	0.53 ± 0.18	0.65 ± 0.08	
FDS12_LSB24	54.854	-36.622	0.69± 0.07	10.07	21.11 ± 0.30	5.6 ± 1.0	0.74 ± 0.19	0.34 ± 0.08	
FDS12_LSB25	54.765	-36.560	0.84± 0.07	-3.23	21.55 ± 0.28	4.0 ± 0.7	0.90 ± 0.19	0.29 ± 0.09	
FDS12_LSB26	54.673	-36.727	0.96± 0.04	-27.40	19.08 ± 0.13	5.1 ± 0.6	1.07 ± 0.17	0.59 ± 0.08	FCC217[a]
FDS12_LSB27	54.733	-36.662	0.58± 0.04	71.91	21.46 ± 0.15	2.4 ± 0.3	0.45 ± 0.17	0.39 ± 0.12	
FDS12_LSB28	54.605	-36.890	0.78± 0.03	74.44	19.13 ± 0.10	4.2 ± 0.4	1.33 ± 0.16	0.29 ± 0.09	
FDS12_LSB29	54.432	-36.726	0.83± 0.04	-79.16	18.42 ± 0.13	7.4 ± 0.9	0.76 ± 0.17	0.52 ± 0.09	FCC199[a]
FDS12_LSB30	54.587	-36.412	0.76± 0.04	-7.53	16.94 ± 0.17	19.2 ± 2.5	0.72 ± 0.17	0.58 ± 0.08	FCC212[a]
FDS12_LSB31	54.638	-36.441	0.73± 0.07	-5.50	21.71 ± 0.30	4.3 ± 0.8	0.84 ± 0.19	0.92 ± 0.09	
FDS12_LSB32	54.546	-36.337	0.74± 0.05	-61.14	20.81 ± 0.22	4.5 ± 0.7	0.38 ± 0.18	0.48 ± 0.08	[c]
FDS12_LSB33	54.564	-36.281	0.72± 0.06	28.27	20.41 ± 0.26	6.6 ± 1.1	0.54 ± 0.19	0.45 ± 0.08	[c]
FDS12_LSB34	54.420	-36.174	0.77± 0.08	30.46	19.44 ± 0.38	14.8 ± 3.0	1.19 ± 0.20	0.48 ± 0.08	[c]

Table 2.6: Continued.

Name	R.A. (J2000)	DEC (J2000)	b/a	θ [deg]	$m_{r'}$	$R_{e,r'}$ [arcsec]	n	g'-r'	Ref
FDS12_LSB35	54.526	-36.050	0.91± 0.04	86.99	20.06 ± 0.16	4.1 ± 0.5	0.76 ± 0.17	0.58 ± 0.08	(c) (d
FDS12_LSB42	53.998	-36.574	0.88± 0.03	-71.62	16.74 ± 0.11	12.9 ± 1.4	1.08 ± 0.16	0.64 ± 0.08	
FDS12_LSB44	54.011	-36.354	0.68± 0.04	47.77	21.86 ± 0.17	2.2 ± 0.3	0.61 ± 0.17	0.54 ± 0.12	(c)
FDS12_LSB46	54.004	-36.258	0.89± 0.04	30.21	20.37 ± 0.15	3.4 ± 0.4	0.55 ± 0.17	0.55 ± 0.09	(c)
FDS12_LSB47	54.072	-36.082	0.92± 0.06	83.65	20.90 ± 0.23	4.0 ± 0.6	0.32 ± 0.18	0.62 ± 0.09	
FDS12_LSB50 *	53.943	-35.989	0.48± 0.03	-54.45	16.26 ± 0.09	17.3 ± 1.7	0.64 ± 0.16	0.63 ± 0.09	FCC158(a) (b) (c)
FDS12_LSB52	55.192	-36.075	0.23± 0.03	-82.74	19.51 ± 0.09	5.4 ± 0.5	0.55 ± 0.16	0.64 ± 0.10	
FDS12_LSB53	54.580	-36.066	0.80± 0.03	-22.64	18.21 ± 0.12	7.7 ± 0.9	0.78 ± 0.16	0.68 ± 0.08	FCC210(a) (c)
FDS12_LSB54	54.385	-36.545	0.88± 0.03	8.69	19.08 ± 0.12	4.9 ± 0.5	0.77 ± 0.16	0.82 ± 0.08	
FDS12_LSB55	54.191	-35.924	0.77± 0.06	24.90	21.81 ± 0.24	3.0 ± 0.5	0.65 ± 0.18	0.70 ± 0.24	(c) (d
FDS16_LSB6	54.055	-35.224	0.60± 0.02	32.85	19.06 ± 0.08	3.6 ± 0.3	0.77 ± 0.15	0.56 ± 0.09	
FDS16_LSB7	53.928	-35.338	0.68± 0.03	-12.23	16.37 ± 0.10	14.6 ± 1.4	0.89 ± 0.16	0.74 ± 0.08	FCC156(a) (c)
FDS16_LSB10	53.991	-35.348	0.62± 0.03	86.59	19.23 ± 0.10	4.1 ± 0.4	0.64 ± 0.16	0.72 ± 0.09	(c) (d
FDS16_LSB11	54.017	-35.389	0.83± 0.03	-77.94	16.63 ± 0.10	11.6 ± 1.1	0.99 ± 0.16	0.80 ± 0.08	FCC160(a) (c)
FDS16_LSB12	53.947	-35.362	0.53± 0.04	47.10	20.70 ± 0.14	3.5 ± 0.4	0.94 ± 0.17	0.75 ± 0.10	(c) (d
FDS16_LSB14	54.042	-35.671	0.71± 0.06	-13.55	21.25 ± 0.27	4.8 ± 0.8	0.58 ± 0.19	0.34 ± 0.08	(c)
FDS16_LSB16	54.051	-35.746	0.57± 0.04	88.31	21.17 ± 0.17	3.3 ± 0.4	0.61 ± 0.17	0.39 ± 0.10	(c)
FDS16_LSB20 *	54.098	-35.912	0.52± 0.03	22.59	16.81 ± 0.10	13.7 ± 1.4	0.77 ± 0.16	0.67 ± 0.07	FCC165(a) (c)
FDS16_LSB23	54.035	-35.987	0.44± 0.04	74.22	21.22 ± 0.15	3.2 ± 0.4	0.94 ± 0.17	0.73 ± 0.11	(c)
FDS16_LSB24	53.713	-35.872	0.47± 0.03	88.30	19.83 ± 0.10	3.8 ± 0.4	0.61 ± 0.16	0.47 ± 0.10	
FDS16_LSB25 *	53.683	-35.862	0.93± 0.03	-5.67	16.03 ± 0.10	14.4 ± 1.4	1.14 ± 0.16	0.68 ± 0.08	FCC137(a) (b) (c)
FDS16_LSB26	53.736	-35.687	0.74± 0.05	83.04	21.08 ± 0.18	3.3 ± 0.5	0.75 ± 0.18	0.88 ± 0.09	(c)
FDS16_LSB28	53.720	-35.570	0.88± 0.03	-68.40	19.17 ± 0.13	4.8 ± 0.5	0.76 ± 0.16	0.87 ± 0.08	
FDS16_LSB29	53.717	-35.623	0.74± 0.03	-30.43	20.06 ± 0.10	2.8 ± 0.3	1.16 ± 0.16	0.51 ± 0.10	
FDS16_LSB30	53.681	-35.521	0.85± 0.05	76.54	20.64 ± 0.19	3.9 ± 0.6	0.57 ± 0.18	0.85 ± 0.09	(c)
FDS16_LSB31	53.772	-35.451	0.59± 0.06	83.56	19.57 ± 0.24	10.0 ± 1.6	0.92 ± 0.18	0.79 ± 0.08	(c) (d
FDS16_LSB32	53.751	-35.322	0.78± 0.03	55.68	18.58 ± 0.12	6.2 ± 0.7	0.76 ± 0.16	0.80 ± 0.08	FCC144(a) (c)
FDS16_LSB33 *	53.798	-35.323	0.56± 0.03	65.01	18.88 ± 0.11	5.7 ± 0.6	0.62 ± 0.16	0.74 ± 0.08	FCC146(a) (c)
FDS16_LSB34	53.877	-35.252	0.48± 0.04	49.69	18.65 ± 0.15	9.7 ± 1.2	0.63 ± 0.17	0.59 ± 0.08	FCC154(a) (c)
FDS16_LSB35	53.740	-35.224	0.70± 0.03	44.00	19.45 ± 0.12	4.5 ± 0.5	0.60 ± 0.16	0.79 ± 0.08	(c) (d
FDS16_LSB36 *	53.735	-35.191	0.54± 0.03	-85.89	17.90 ± 0.12	10.0 ± 1.1	0.84 ± 0.16	0.73 ± 0.07	FCC140(a) (c)
FDS16_LSB37	53.773	-35.219	0.75± 0.03	-6.53	18.45 ± 0.09	5.2 ± 0.5	0.73 ± 0.16	0.83 ± 0.08	FCC145(a) (c)
FDS16_LSB38 *	53.742	-35.043	0.94± 0.04	-20.06	17.99 ± 0.14	8.9 ± 1.1	1.02 ± 0.17	0.67 ± 0.07	FCC142(a) (c)
FDS16_LSB39	53.636	-35.043	0.59± 0.06	-84.10	20.63 ± 0.26	6.6 ± 1.1	0.56 ± 0.19	0.42 ± 0.08	(c)
FDS16_LSB40	53.613	-35.106	0.54± 0.05	30.80	20.87 ± 0.21	4.9 ± 0.7	0.35 ± 0.18	0.72 ± 0.09	(c)
FDS16_LSB41	53.550	-35.229	0.52± 0.03	-49.41	19.64 ± 0.12	4.8 ± 0.5	0.71 ± 0.16	0.67 ± 0.09	FCC131(a) (c)

Table 2.6: Continued.

Name	R.A. (J2000)	DEC (J2000)	b/a	θ [deg]	$m_{r'}$	$R_{e,r'}$ [arcsec]	n	g'-r'	Ref
FDS16_LSB42	53.525	-35.277	0.77± 0.04	56.82	18.78 ± 0.15	7.4 ± 0.9	0.93 ± 0.17	0.65 ± 0.08	FCC127$^{(a)\ (c)}$
FDS16_LSB43 *	53.584	-35.362	0.95± 0.03	77.94	16.65 ± 0.10	11.3 ± 1.1	0.75 ± 0.16	0.89 ± 0.08	FCC133$^{(a)\ (c)}$
FDS16_LSB44	53.529	-35.477	0.70± 0.07	-5.49	20.79 ± 0.30	6.6 ± 1.2	0.85 ± 0.19	0.92 ± 0.10	$^{(c)}$
FDS16_LSB45	53.538	-35.516	0.89± 0.05	-73.46	17.67 ± 0.19	15.2 ± 2.1	0.61 ± 0.18	0.99 ± 0.13	FCC130$^{(a)\ (b)\ (c)}$
FDS16_LSB47	53.559	-35.819	0.66± 0.06	-2.03	19.67 ± 0.25	9.4 ± 1.5	0.78 ± 0.19	0.58 ± 0.07	$^{(c)}$
FDS16_LSB49	53.597	-35.845	0.81± 0.06	87.44	19.79 ± 0.26	8.1 ± 1.3	0.62 ± 0.19	0.50 ± 0.09	$^{(c)}$
FDS16_LSB50	53.451	-35.836	0.86± 0.04	-34.91	18.03 ± 0.14	9.1 ± 1.1	0.68 ± 0.17	0.75 ± 0.07	FCC125$^{(a)\ (b)\ (c)}$
FDS16_LSB52	53.458	-35.951	0.55± 0.07	-47.87	21.02 ± 0.29	6.4 ± 1.1	0.79 ± 0.19	0.59 ± 0.08	$^{(c)}$
FDS16_LSB54	53.350	-35.987	1.00± 0.07	-14.49	20.33 ± 0.30	6.8 ± 1.2	0.56 ± 0.19	0.60 ± 0.08	
FDS16_LSB55	53.202	-35.946	0.54± 0.04	-61.66	18.81 ± 0.13	7.6 ± 0.9	0.72 ± 0.17	0.65 ± 0.08	
FDS16_LSB56	53.366	-35.965	0.57± 0.04	39.07	20.67 ± 0.14	3.3 ± 0.4	0.62 ± 0.17	0.60 ± 0.10	
FDS16_LSB58	53.239	-35.737	0.56± 0.03	-54.81	16.12 ± 0.09	16.5 ± 1.6	1.18 ± 0.16	0.70 ± 0.09	FCC110$^{(a)\ (b)}$
FDS16_LSB59	53.388	-35.704	0.71± 0.04	-23.84	20.19 ± 0.14	3.8 ± 0.5	0.70 ± 0.17	0.74 ± 0.09	$^{(c)}$
FDS16_LSB60	53.384	-35.661	0.32± 0.05	-74.92	19.55 ± 0.21	11.5 ± 1.7	1.74 ± 0.18	0.65 ± 0.08	$^{(c)}$
FDS16_LSB62	53.317	-35.597	0.84± 0.04	-22.02	21.13 ± 0.14	2.2 ± 0.3	0.63 ± 0.17	0.67 ± 0.11	$^{(c)}$
FDS16_LSB63	53.286	-35.397	0.53± 0.04	-85.96	19.36 ± 0.14	6.3 ± 0.8	0.65 ± 0.17	0.68 ± 0.08	FCC114$^{(a)\ (c)}$
FDS16_LSB64	53.327	-35.263	0.42± 0.04	-68.11	19.20 ± 0.17	9.6 ± 1.3	0.70 ± 0.17	0.64 ± 0.08	
FDS16_LSB65	53.368	-35.126	0.86± 0.06	19.07	20.94 ± 0.27	5.0 ± 0.8	1.08 ± 0.19	0.66 ± 0.08	
FDS16_LSB66	53.299	-35.035	0.55± 0.07	-57.14	20.27 ± 0.32	10.2 ± 1.9	0.65 ± 0.19	0.45 ± 0.10	
FDS16_LSB67	53.310	-35.028	0.60± 0.05	-15.56	20.91 ± 0.18	3.8 ± 0.5	0.75 ± 0.17	0.56 ± 0.09	
FDS16_LSB70 *	53.092	-35.406	0.90± 0.06	35.90	19.45 ± 0.24	8.2 ± 1.3	0.50 ± 0.18	0.78 ± 0.07	
FDS16_LSB71	53.022	-35.426	0.82± 0.03	86.48	18.42 ± 0.12	6.8 ± 0.8	1.05 ± 0.16	0.72 ± 0.08	
FDS16_LSB72	52.954	-35.583	0.95± 0.04	41.89	19.13 ± 0.15	5.5 ± 0.7	1.01 ± 0.17	0.72 ± 0.08	
FDS16_LSB74	53.114	-35.775	0.56± 0.04	-33.29	18.87 ± 0.15	8.3 ± 1.0	0.73 ± 0.17	0.57 ± 0.09	FCC103$^{(a)\ (b)}$
FDS16_LSB75	53.023	-35.826	0.87± 0.06	-28.43	20.61 ± 0.24	5.0 ± 0.8	0.77 ± 0.18	0.30 ± 0.08	
FDS16_LSB77	52.836	-35.819	0.68± 0.04	42.24	19.22 ± 0.16	6.8 ± 0.9	0.92 ± 0.17	0.60 ± 0.08	FCC93$^{(a)}$
FDS16_LSB78	52.755	-35.638	0.62± 0.04	44.54	20.45 ± 0.15	3.8 ± 0.5	0.65 ± 0.17	0.57 ± 0.09	
FDS16_LSB79	52.863	-35.494	0.78± 0.04	28.26	18.49 ± 0.16	8.8 ± 1.1	0.45 ± 0.17	0.69 ± 0.08	FCC97$^{(a)}$
FDS16_LSB83	52.845	-34.971	0.76± 0.04	-21.21	18.84 ± 0.16	7.6 ± 1.0	0.64 ± 0.17	0.62 ± 0.08	FCC94$^{(a)}$
FDS16_LSB84	52.820	-34.962	0.65± 0.04	57.86	19.55 ± 0.16	6.2 ± 0.8	0.82 ± 0.17	0.58 ± 0.08	
FDS16_LSB85	53.430	-35.860	0.46± 0.04	53.43	15.81 ± 0.15	36.9 ± 4.5	0.80 ± 0.17	0.59 ± 0.07	$^{(b)\ (c)}$
FDS16_LSB86	53.530	-35.381	0.88± 0.07	-38.63	22.55 ± 0.32	2.8 ± 0.5	0.50 ± 0.19	0.59 ± 0.10	$^{(c)}$
FDS16_LSB87	53.343	-35.606	0.86± 0.03	-86.91	18.74 ± 0.10	4.6 ± 0.5	0.93 ± 0.16	0.94 ± 0.08	$^{(c)}$

3. The Fornax Deep Survey (FDS) with the VST. IV. A size and magnitude limited catalog of dwarf galaxies in the area of the Fornax cluster

—— *A. Venhola, R. Peletier, E. Laurikainen, H. Salo, E. Iodice, S. Mieske , M. Hilker, C. Wittmann, T. Lisker, M. Paolillo, M. Cantiello, J. Janz, M. Spavone, R. D'Abrusco, G. van de Ven, N. Napolitano, G. Verdoes Kleijn, N. Maddox, M. Capaccioli, A. Grado, E. Valentijn, J. Falcón-Barroso, L. Limatola* ——

Published in Astronomy & Astrophysics, Volume 620, id.A165, 31 pp. (2018)

Abstract

Context: The Fornax Deep Survey (FDS), an imaging survey in u', g', r', and i'-bands, has a supreme resolution and image depth compared to the previous spatially complete Fornax Cluster Catalog (FCC, Ferguson 1989). Our new data allows to study the galaxies down to r'-band magnitude $m_{r'} \approx 21$ mag ($M_{r'} \approx$ -10.5 mag), which opens a new parameter regime to investigate the evolution of dwarf galaxies in the cluster environment. After the Virgo cluster, Fornax is the second nearest galaxy cluster to us, and with its different mass and evolutionary state, it provides a comparison, which makes it possible to understand the various evolutionary effects on galaxies and galaxy clusters. These data provide an important legacy dataset to study the Fornax cluster.

Aim: We present the Fornax Deep Survey (FDS) dwarf galaxy catalog, focusing on explaining the data reduction and calibrations, assessing the quality of the data, and describing the methods used for defining the cluster memberships and first order morphological classifications for the catalog objects. We also describe the main scientific questions that will be addressed based on the catalogue. This catalog will also serve for future follow-up studies of the Fornax cluster dwarf galaxies.

Methods: As a first step we use SExtractor (Bertin & Arnouts 1996) fine tuned for dwarf galaxy detection, to find galaxies from the FDS data, covering a 26 deg^2 area of the main cluster up to its virial radius, and the area around the Fornax A sub-structure. We make 2D-decompositions of the identified galaxies using GALFIT, measure the aperture colors, and the basic morphological parameters like concentration and residual flux fraction. We use color-magnitude, luminosity-radius and luminosity-concentration relations to separate the cluster galaxies from the background galaxies. We then divide the cluster galaxies into early- and late-type galaxies according to their morphology and give first order morphological classifications using a combination of visual and parametric classifications.

Results: Our final catalog includes 14,095 galaxies. We classify 590 galaxies as likely Fornax cluster galaxies, of which 564 are dwarfs ($M_{r'} > -18.5$ mag) consisting our Fornax dwarf catalog. Of the cluster dwarfs we classify 470 as early-types, and 94 as late-type galaxies. Our final catalog reaches its 50% completeness limit at magnitude $M_{r'} = -10.5$ mag and surface brightness $\bar{\mu}_{e,r'} = 26$ mag arcsec^{-2}, which is $\sim$3 magnitudes deeper than the FCC. Based on previous works and comparison with a spectroscopically confirmed sub-sample, we estimate that our final Fornax dwarf galaxy catalog has $\lesssim$ 10% contamination from the background objects.

3.1 INTRODUCTION

Understanding galaxy evolution is one of the major problems of astronomy. During recent decades, our understanding of the basic processes involved in the evolution of galaxies in the context of the ΛCDM cosmology has taken great steps, but many details are not yet well understood. For example, the environmental dependence of the frequency of different galaxy morphologies was discovered by Dressler (1980). Despite this, the importance of the different mechanisms transforming star-forming late-type galaxies into quiescent and red early-type galaxies in the group and cluster environments (see e.g., Peng et al. 2012,Peng et al. 2014,Jaffé et al. 2018), is still unclear.

An important resource for studying galaxy evolution is the availability of homogeneous and complete samples of galaxy observations that can be used statistically to investigate how the properties of the galaxies change in different environments. The new deep surveys, such as the Next Generation Virgo Survey (NGVS, Ferrarese et al. 2012), the Next Generation Fornax Survey (NGFS, Muñoz et al. 2015), VST Early-type GAlaxy Survey (VEGAS, Capaccioli et al. 2015) and the Fornax Deep Survey (FDS, Peletier et al, in prep.) reveal a large number of previously unknown faint galaxies that are powerful probes to environmental processes. At the same time, large scale cosmological simulations such as IllustrisTNG (Pillepich et al. 2018), have reached such a high resolution that direct comparisons down to dwarf sized galaxies with stellar mass of $M_* = 10^{8-9}$ $M_\odot$ can be made.

The faint galaxies found in the new imaging surveys typically lack distance information, and many of these galaxies have such a low surface brightness that

obtaining their spectroscopic redshifts for a complete sample is not realistic with the currently available instruments. Thus, to be able to exploit these galaxies in a statistical way, one needs to assess cluster memberships using their photometric properties. Photometric redshifts (see e.g., Bilicki et al. 2018 and references therein) are often used to obtain distances for a large samples of galaxies. Another way to obtain distances of the galaxies is to use the known scaling relations for galaxies. In clusters, there are hundreds of galaxies located at a similar distance, and many of their parameters scale with each other. However, the background galaxies are located at a range of distances, so that their apparent properties do not follow these relations. Useful relations that are commonly used for identifying cluster members are the color-magnitude and luminosity-surface brightness relations (see e.g., Misgeld et al. 2009). Already Binggeli et al. (1985) and Ferguson (1989) have used colors, the magnitude-surface brightness relation and galaxy morphology for defining the membership status of their newly found galaxies in the Virgo and Fornax clusters, respectively. Follow-up studies of these surveys based on spectroscopy or surface brightness fluctuations (see e.g., Drinkwater et al. 2000, Mieske et al. 2007) have proven the photometric classifications to be very robust: more than 90% of the galaxies selected this manner are confirmed to be cluster members.

The Fornax cluster appears on the southern sky centered around the elliptical galaxy NGC 1399 with coordinates R.A. = 54.6209 deg and Dec. = -35.4507 deg (Watson et al. 2009). Its mean recession velocity is 1493 ± 36 kms^{-1} (Drinkwater et al. 2001), and the mean distance calculated from surface brightness fluctuations of early-type galaxies is $20.0\pm0.3\pm1.4$ Mpc (Blakeslee et al. 2009). The main cluster is very compact and consists of 22 galaxies brighter than $M_B <$ -18 mag and around 200 fainter galaxies (Ferguson 1989). The Fornax Cluster is part of the larger Fornax-Eridanus structure (see Nasonova et al. 2011) located in the Fornax-filament of the cosmic web. Fornax, having a virial mass of M = 7×10^{13} $M_\odot$, is the most massive mass concentration (see Fig. 3.1) in the filament. Other significant mass concentrations near the Fornax cluster are the groups around NGC 1316 (Fornax A), NGC 1407 and the Dorado group (see Fig. 3.1). The NGC 1316 group is currently falling into the main group (Drinkwater et al. 2001), whereas the other spectroscopically confirmed significant groups are located at least 15 deg ($\approx$ 5 Mpc) away from the Fornax cluster.

The Fornax cluster is an interesting environment to study, since it bridges the mass range of evolved groups to more massive clusters. For instance, Trentham & Tully (2009) study dwarf galaxies in the group environments of which the NGC5846 group, with a mass of M = $8.4\pm2.0\times10^{13}$ $M_\odot$, is more massive than the Fornax cluster. However, regardless of its low mass, the Fornax cluster has many properties that qualify it as a cluster, such as concentration, X-ray intensity, and evolved galaxy population. Due to its low mass it may also be an interesting test case for simulations: the high-resolution cosmological simulations like Millennium-II (Boylan-Kolchin et al. 2009), and the ongoing 50 Mpc box simulations of IllustrisTNG (Pillepich et al. 2018) have only a handful of Virgo-mass clusters, but many have a Fornax cluster mass, so they provide a great opportunity for

both dwarf resolution and good population statistics when using them to interpret observational data.

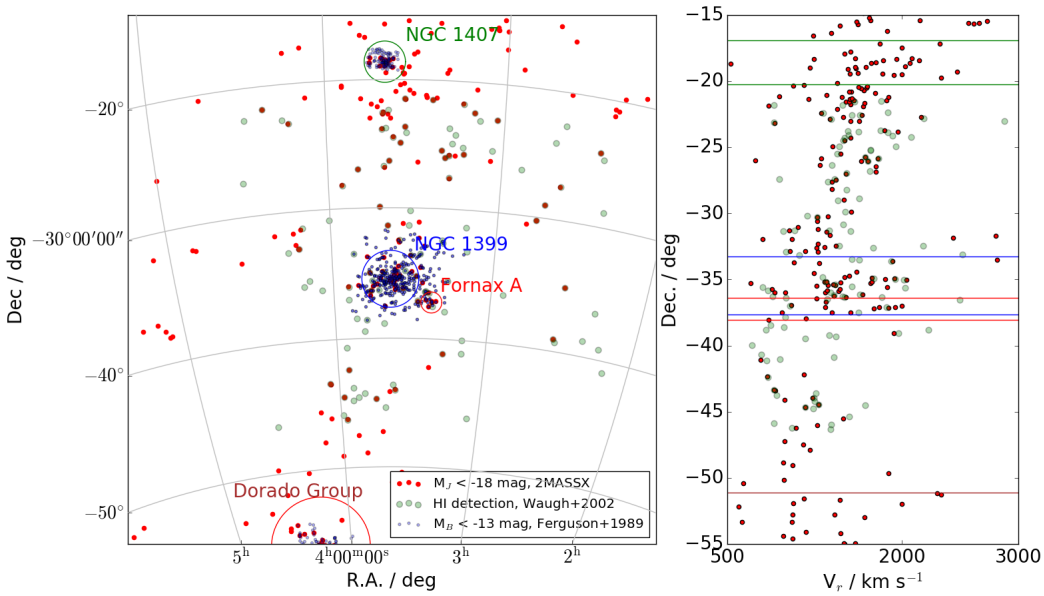

Figure 3.1: Large scale structure surrounding the Fornax cluster. The left panel shows galaxy right ascension and declination in International Celestial Reference System (ICRS) coordinates, and the right panel shows the recession velocities of the galaxies as a function of declination. At the distance of the Fornax cluster 1 deg corresponds to 0.3 Mpc, and 1000 km/s velocity difference due to Hubble flow corresponds to 14 Mpc (to first order independent of the distance). The galaxies with recession velocities $V_r < 4000$ km s^{-1} in the 2 Micron All Sky Survey catalog (2MASSX, Huchra et al. 2012), are plotted with the red dots, and the galaxies with velocities $V_r < 4000$ km s^{-1} from Waugh et al. (2002) with the green circles. The FCC galaxies are shown with blue dots. We also indicate the virial radii of the most significant groups in the surroundings of the Fornax cluster with the large circles, and show their names with the corresponding colors. The locations of the circles of the left panel are shown by the horizontal lines in the right panel using the corresponding colors.

Due to its southern location the Fornax cluster is not covered by the Sloan Digital Sky Survey (SDSS, Alam et al. 2015). The most recent galaxy catalog covering the whole cluster is the Fornax Cluster Catalog (FCC) by Ferguson (1989). The catalog covers 40 deg^2 area centered onto the Fornax cluster, and it contains 2678 galaxies in total. Its given completeness limit in apparent B-magnitude is $m_B \approx 19$ mag, but it may vary due to visual identification of the galaxies. In the catalog, Ferguson classified galaxies as being either likely cluster galaxies or likely

background galaxies using the morphology and surface brightness of the galaxies. The whole catalog contains 340 likely cluster members in the area of the Fornax cluster, and more than two thousand background galaxies.

Another major effort for mapping the Fornax cluster galaxies with higher resolution was done using the Hubble Space Telescope (Jordán et al. 2007). In their ACS Fornax Cluster Survey, the authors target the brightest 43 galaxies using two different filters. Their spatial coverage is much smaller than the one of FCC, but the spatial resolution of the observations is superior. The core region of the cluster was also covered with deep observations by Hilker et al. (2003) and Mieske et al. (2007), who used the 100-inch du Pont telescope and the Inamori-Magellan Areal Camera and Spectrograph - instrument (IMACS, Dressler et al. 2011) at Las Campanas Observatory (Chile), respectively. Both observational surveys were performed in V and I bands and they were able to obtain colors and structural parameters of the cluster dwarfs down to M_V = -9 mag. Another ongoing effort to image the Fornax cluster with modern instruments is the Next Generation Fornax Survey collaboration (NGFS, Muñoz et al. 2015, Eigenthaler et al. 2018). The NGFS aims to cover 30 deg^2 area in u', g', i', and Ks bands in the Fornax cluster with similar observations as FDS, using the DECam instrument attached to 4-m telescope Blanco at Cerro Tololo Inter-American Observatory (CTIO) for the optical u', g', and i' bands, and VISTA/VIRCAM (Sutherland et al. 2015) for the Ks-band. So far, the NGFS has published their galaxy catalog covering the area within the virial radius of the Fornax cluster (Eigenthaler et al. 2018, Ordenes-Briceño et al. 2018) with 643 dwarf galaxies altogether.

A major effort for obtaining spectroscopic redshifts for the Fornax cluster galaxies was the 2dF Fornax survey made by Drinkwater et al. (1999), who obtained spectroscopy for several hundreds of galaxies located in a $\approx$ 9 deg^2 area in the main cluster. However, only a few percent of the observed objects were cluster galaxies, since there was no morphological selection for the targets. Recently, the spectroscopic 2dF observations were extended by additional 12 deg^2 (Maddox et al., in prep.), which more than doubles the area with spectroscopic data. The spectroscopic data are limited to relatively high surface brightness objects (B-band central surface brightness $\mu_{0,B} < 23$ mag arcsc^{-2}), which unfortunately excludes most of the dwarf galaxies. Spectroscopic redshifts are available for several tens of bright galaxies ($m_J < 14$ mag) in the Fornax cluster and in its surroundings, made by the 2 Micron All-Sky Survey (2MASS) spectroscopic survey (Huchra et al. 2012). Several spectroscopic redshifts from HI-data were obtained by Waugh et al. (2002), but most of these galaxies are in the surroundings of the main cluster.

Previous work on the Fornax cluster suggests that the center of the cluster is dynamically evolved, which means that most of the galaxies have travelled at least once through the cluster center, but there is still ongoing in-fall of subgroups and individual galaxies in the outskirts. The X-ray analysis of the hot intra-cluster gas by Paolillo et al. (2002) shows that there is a concentration of X-ray gas in the center of the cluster that has a mass of M $\approx 10^{11}$ $M_\odot$ within the inner 100 kpc. However, this X-ray gas shows a lopsided distribution toward the northwest, which is a sign of it not being fully virialized. The high concentration of

galaxies in the center of the Fornax cluster (Ferguson 1989) and the observed mass segregation of the galaxies (Drinkwater et al. 2001) are both signs that the galaxies in the center have spent several Gyrs in the cluster environment corresponding to a few crossing times[1]. This long standing interaction of galaxies with the cluster potential is possibly the main mechanism that has produced a significant intracluster population of stars, as the one recently traced by globular clusters (Pota et al. 2018) and planetary nebulae (Spiniello et al. 2018) in the core of the Fornax cluster. This population shows a velocity dispersion which is consistent with the one of the galaxy population in the same area, hence supporting the picture of a cluster core being dynamically evolved. Drinkwater et al. (2001) analyzed the substructure of the Fornax cluster using the Fornax spectroscopic survey. They discussed that, although showing signs of a relaxed system, the Fornax cluster still has two groups of galaxies with common systematic velocities clearly different from the one of the main cluster. Additionally, the high early-type galaxy fraction in the Fornax cluster (E+S0+dE+dS0)/all = 0.87 (Ferguson 1989) is a sign that the galaxies have spent a long time in the cluster without forming many new stars.

The obtained multiband optical images of FDS extend the previous Fornax surveys with data that cover a large spatial area and are very deep[2]. At the same time their $\approx$ 1 arcsec (100 pc at the distance of the Fornax cluster) resolution allows detailed morphological analysis of dwarf galaxies. The survey has already led to publication of several papers, which have demonstrated the usefulness of this deep high resolution data in various different scientific cases (Iodice et al. 2016, D'Abrusco et al. 2016, Iodice et al. 2017a, Iodice et al. 2017b, Venhola et al. 2017, Cantiello et al. 2018).

In this paper we present the steps necessary to construct the FDS dwarf galaxy catalog containing all the cluster member galaxies with $M_{r'} > -18.5$ mag. Observations used in this work are described in Section 2. In Sections 3 and 4, we explain the data reduction and calibration, and assess the quality of the final data products, respectively. We then explain the preparation of the galaxy detection images (Section 5), our detection method (Section 6), and the photometric analysis done for the detected galaxies (Section 7). In section 8, we use the photometric parameters of the galaxies to separate the background objects from the cluster galaxies and finally classify the Fornax cluster galaxies into early- and late-type systems. In Section 9, we compare our catalog with the previous Fornax studies. Throughout the paper we assume a distance of 19.7 Mpc for the Fornax cluster, which corresponds to a distance modulus of 31.51 mag (Blakeslee et al. 2009). Due to the high Galactic latitude of the Fornax cluster (Galactic declination = -53.63 deg) the dust reddening is small[3] and therefore, if not stated explicitly, we use non-corrected values for magnitudes.

[1] If we consider a galaxy located at half a virial radius from the cluster center (R=0.35 Mpc) with a velocity similar to the velocity dispersion of the cluster galaxies, (V =370 km s^{-1}), the crossing time is $t_{cross} \approx$1 Gyr.

[2] Azimuthally averaged profiles can be determined down to $\mu_{r'}$=30 mag arcsec^{-2} (Iodice et al. 2016). See also Section 4.1.

[3] According to Schlafly & Finkbeiner (2011) the dust extinction coefficients in the area of the Fornax cluster are 0.05, 0.04, 0.03, and 0.02 mag for u', g', r', and i' filters.

Table 3.1: Fornax Deep Survey observations used in this work. The columns correspond to the date, ESO observing period, and total exposure times per filter in hours.

		Total exposure time [h]			
Date	Period	u'	g'	r'	i'
Nov, 2013	P92	9.2	6.0	7.0	0.4
Nov, 2014	P94	16.0	15.9	11.2	12.3
Oct, Nov, 2015	P96	6.2	20.7	21.0	2.7
Oct, Nov, 2016	P98	-	15.5	15.1	7.9
Oct, Nov, 2017	P100	31.8	-	-	17.2

3.2 OBSERVATIONS

The Fornax Deep Survey is a collaboration of the two guaranteed observing time surveys Focus (PI: R. Peletier) and VEGAS (PI: E. Iodice, see also Capaccioli et al. 2015) that covers the area of the Fornax cluster and Fornax A subgroup with deep multiband imaging. The FDS is executed using the OmegaCAM (Kuijken et al. 2002) instrument attached to the survey telescope of the Very Large Telescope (VST, Schipani et al. 2012), which is a 2.6 m telescope located at Cerro Paranal, Chile. The camera consists of 32 CCD-chips, has a 0.21 arcsec pixel^{-1} resolution, and a field of view of $\approx$1 deg $\times$ 1 deg. The observations of the FDS were performed between November 2013 and November 2017, and they are listed in Table 3.1. All the observations were performed in clear (photometric variations $<$ 10 %) or photometric conditions with a typical seeing FWHMs of 1.2, 1.1, 1.0, and 1.0 arcsec in u', g', r', and i'-bands. The u' and g'-band observations were performed in dark time, and the other bands in gray or dark time.

The observing strategy of the FDS is described in Venhola et al. (2017) and Iodice et al. (2016) and will be described more comprehensively in the survey paper by Peletier et al. (in preparation), but for completeness, a short description is given also here. The observations were performed using short 3 min exposure times and large $\approx$ 1 deg dithers between the consecutive exposures. The fields were observed in sets of two to three fields in such a way that after visiting all the fields once, an offset of 10 arcmin with respect to the previous observation of a given field was made. Directions of the small $\sim$10 arcmin offsets were randomly chosen around the centers of the fields. The large dithers and offsets ensure that the same objects do not appear twice in the same pixel, and makes it possible to stack consecutive observations as a background model (see Section 3.1). For reference, the halo of NGC 1399, located in Field 11, extends over an area of 1 deg^2 (Iodice et al. 2016), which would lead it covering the full field of view of the observations of that field if we did not use the adopted dithering and offset strategy. To obtain the necessary depth in the images each field was visited 75, 55, 55, and 35 times with the u', g', r', and i' filters, respectively. The locations of the observed fields are shown in Fig. 3.2. The observations cover a 20 deg^2 area in the main cluster in u', g', r', and i', and additional 6 deg^2 in the Fornax A

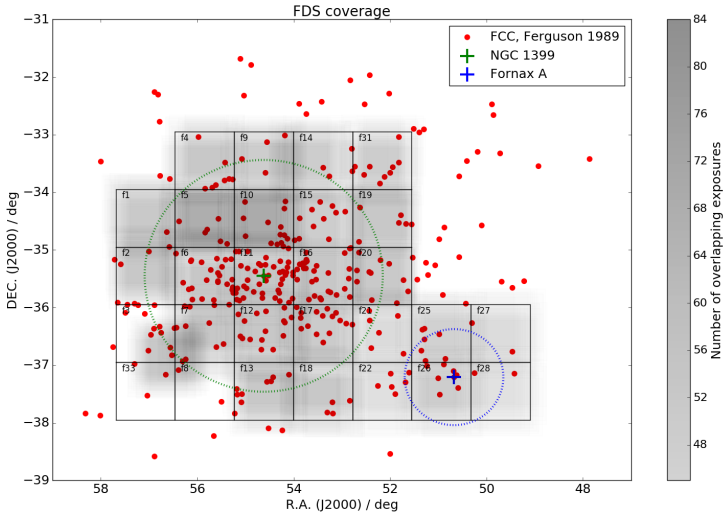

Figure 3.2: Locations of the observed 1° x 1° (corresponding to 325 kpc x 325 kpc at the distance of the Fornax cluster) sized FDS fields are plotted in black. The r'-band weight maps (see Section 3.1) are shown in the gray-scale colors, darker color corresponding to deeper observations. All the FCC galaxies (Ferguson 1989) classified as "likely members" or "definitive members" are shown with red points. We note that compared to FDS, FCC covers a slightly larger area of the cluster. The green dotted circle shows the virial radius of 2.2° ($\approx$ 0.7 Mpc, Drinkwater et al. 2001), and the green cross shows the central galaxy NGC 1399. The blue cross and the blue dotted line show the peculiar elliptical galaxy NGC 1316 in the center of the Fornax A subgroup, and the 2σ galaxy overdensity around it, respectively.

southwest subgroup in g', r', and i'. All observations follow a regular grid of target fields comprising continuous coverage, except in the area of Fields 3, 33, and 8 in which some gaps occur due to bright stars.

3.3 DATA REDUCTION

3.3.1 INSTRUMENTAL CORRECTIONS

The instrumental corrections applied for each frame include overscan correction, removal of bias, flatfielding, illumination correction, masking of the bad pixels, and subtraction of the background. The data is overscan corrected by subtracting from each pixel row the row-wise median values, read from the *CCD* overscan areas. The fine structure of the bias is then subtracted using a master bias frame stacked from ten overscan corrected bias frames.

Flatfielding is done after bias correction using a master flatfield which is combined from eight twilight flatfields and eight dome flatfields. Before combining the different flatfields, the high spatial frequencies are filtered out from the twilight flatfields, and the low frequency spatial Fourier frequencies from the dome flatfields. This approach is adopted, since the dome flatfields have better signal-to-noise ratios to correct for the pixel-to-pixel sensitivity variations, whereas the twilight flatfields have more similar overall illumination with the science observations.

During the instrumental reduction, weight maps are also created for each individual frame. Weight maps carry information about the defects or contaminated pixels in the images and also the expected noise associated with each pixel (see lower left panel of Fig. 3.3). The hot and cold pixels are detected from the bias and flatfield images, respectively. These pixels are then set to zero in the weight maps. The flatfielded and debiased images are also searched for satellite tracks and cosmic rays, and the values of the pixels in the weight maps corresponding to the contaminated pixels in the science images, are then set to zero. The Hough transformation method (Vandame 2001) is applied to the images to pick up the satellite tracks, which are eliminated by masking the lines consisting of more than 1000 pixels that have intensity above the 5-σ level relative to the background and are located on the same line. Cosmic rays are detected using SExtractor, and the corresponding pixels are masked from the weight maps. The pixels in the weight maps W have values

$$W = \frac{1}{\sigma^2} \times M_{bad}, \tag{3.1}$$

where σ is the standard deviation of the background noise and M_{bad} is the combined bad pixel map where the bad pixels have been set to zero and other pixels to one.

The observations contain an additional smooth light component resulting from scattered light. A careful removal of this component is essential for studying the outskirts of the galaxies and the low surface brightness objects. A background model is created first by scaling a set of 12 consecutive exposures of the targets, and then median averaging the stack. The scaling factor s between images A and B is defined by measuring median values within small boxes in image A (m_A), and in the same locations in image B (m_B), and then taking the median of their ratios:

$$s = \mathrm{median}\left(\frac{m_A}{m_B}\right). \tag{3.2}$$

For each image among those to be stacked, such a scaling factor is defined with respect to A, and the images are multiplied with these factors before stacking. If there is a large scatter between the ratios of s, the chip medians of the exposures are scaled with each other. The scaled images are then median stacked to the background model, and the model is subtracted from image A. This strategy allows us also to remove the fringe patterns appearing in the OmegaCAM i'-band images, and removes also all the possible residual patterns from the flatfielding.

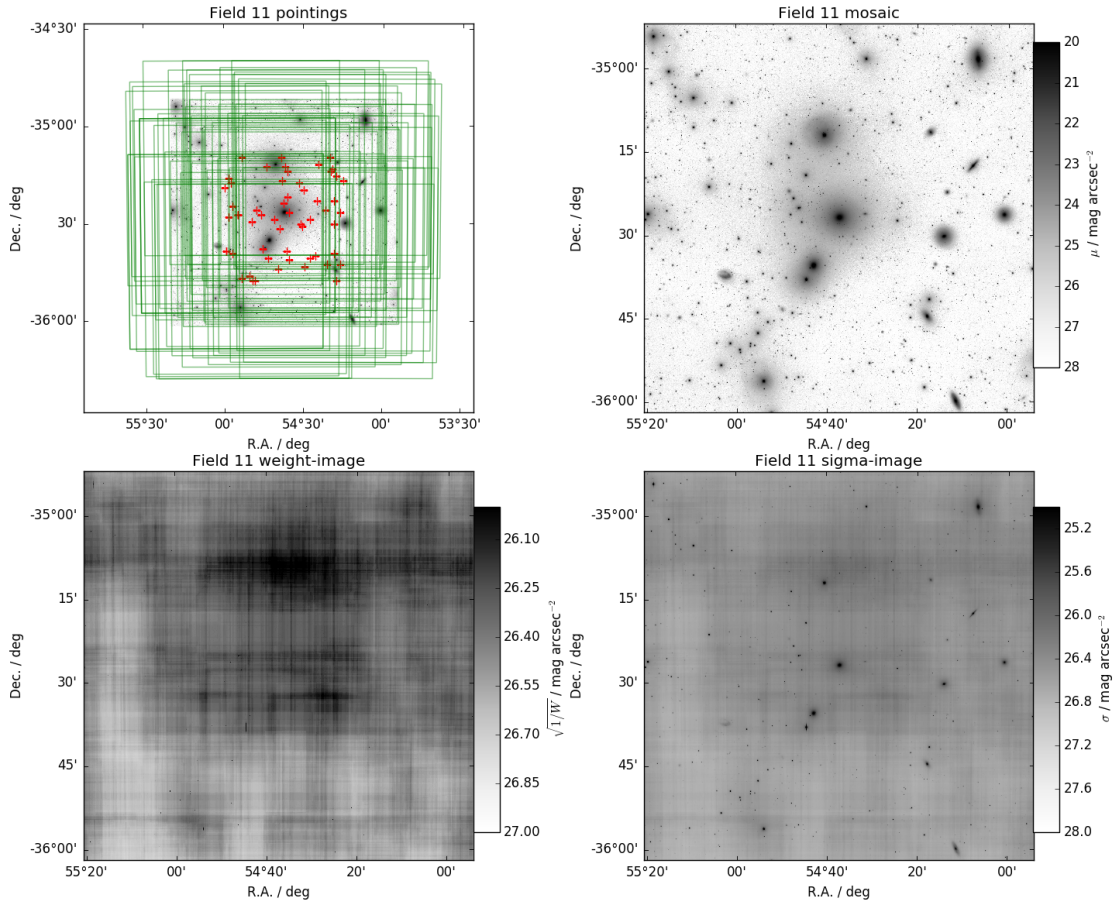

Figure 3.3: Coverage of the FDS field 11 observations in g'-band are shown with the green squares in the upper left panel, and the centers of the pointings with the red crosses. The median combined mosaic image is shown in the upper right corner, and the corresponding weight- and sigma-images are shown in the lower left and lower right panels, respectively. The color bars in the panels indicate the surface brightness and 1σ noise per pixel transformed into surface brightness, respectively.

Systematic photometric residual patterns still remain after flatfielding, which are corrected by applying an illumination correction to the data. We used the correction models made for the Kilo Degree Survey (KiDS, see Verdoes Kleijn et al. 2013 for details). The models were made by mapping the photometric residuals across the OmegaCAM's CCD array using a set of dithered observations of Landolt's Selected Area (SA) standard star fields (Landolt 1992), and fitting a linear model to the residuals. The images were multiplied with this illumination

correction. The illumination correction is applied after the background removal to avoid producing artificial patterns into the background of images.

3.3.2 ASTROMETRIC CALIBRATION

The reduced images are calibrated to world coordinates using SCAMP (Bertin 2006). We make the coordinate transformation by applying first the shifts and rotations according to the image headers. The fine tuning of the astrometric calibration is obtained by first associating the source lists extracted from the science images with the 2 Micron All-Sky Survey Point Source Catalog (2MASS PSC, Cutri et al. 2003) and fitting the residuals by a second order polynomial plane. This polynomial correction is then applied to the data coordinates, and the pixel size is sampled to 0.2 arcsec pixel^{-1}. After applying the astrometric calibration, the remaining differences between the 2MASS PSC objects and the corresponding objects in our data have root mean square of 0.1 arcsec.

3.3.3 FLUX CALIBRATION

The absolute zeropoint calibration is done by observing standard star fields each night and comparing their OmegaCAM magnitudes with the Sloan Digital Sky Survey Data Release 11 (SDSS DR11, Alam et al. 2015) catalog values. The OmegaCAM point source magnitudes are first corrected for the atmospheric extinction by subtracting a term kX, where X is airmass and k is the atmospheric extinction coefficient with the values of 0.515, 0.182, 0.102 and 0.046 for u', g', r' and i', respectively. The zero-point for a given CCD is the difference between the corrected magnitude of the object measured from a standard star field exposure and the catalog value. The zero-points are defined only once per night, so that for each science observation only the varying airmass was corrected. All magnitudes in the catalog are given in SDSS filters calibrated to AB-system.

3.3.4 MAKING THE MOSAIC IMAGES

The calibrated exposures are median stacked into mosaic images using SWarp (Bertin 2010), and the contaminated pixels are removed using the weight maps. SWarp produces also a mosaic weight map for each mosaic, where the pixel values are inverse of the variance associated to each pixel. We stack the images according to the FDS fields with an extra overlap of 5 arcmin on each side, so that we do not need to cut any large galaxies later in the analysis. As a final result we produce 1.17 deg $\times$ 1.17 deg mosaics and the corresponding weight images. Examples of a g'-band mosaic and the associated weight-images are shown in Fig. 3.3.

3.3.5 SIGMA-IMAGES

The weight images we produced include the information of the bad pixels and the inverse variance, but do not include the Poisson noise associated to the astronomical objects. For the right weighting of the pixels in the structure analysis

of the galaxies (see Section 7.2), we need also sigma-images that include the Poisson noise. We produced the sigma images from the weight images using the equation

$$\sigma = \sqrt{\sigma_{sky,i}^2 + \frac{f_i}{GAIN}}, \tag{3.3}$$

where $\sigma_{sky,i} = \frac{1}{\sqrt{W}}$, W being the pixel value in the weight image, f_i is the flux in the corresponding pixel in the science image, and $GAIN$ is the ratio of the calibrated flux units to observed electrons as calculated by SWarp during production of the mosaic-images. The lower right panel of Fig. 3.3 shows an example of a sigma-image of Field 11.

3.4 QUALITY OF THE MOSAICS

To understand the limits of our data and the uncertainties introduced by the calibrations, we made tests for the noise in the images, and the photometric and astrometric accuracy.

3.4.1 DEPTH

The image depth (or signal-to-noise ratio, S/N) can be calculated theoretically when the telescope size, efficiency of the detector and instrument, brightness of the sky, read-out noise of the instrument, number of exposures, along with the total exposure time, are known. However, in practice there will be also other sources of noise, from the scattered light, reflections between different parts of the images, imperfect background subtraction, and changing the observation conditions. To quantify these effects, we used the final mosaics to measure the actual obtained depth in the images.

To measure the background noise in the images, we defined 500 boxes with 200 $\times$ 200 pixels in size, randomly distributed in the images, and calculate the three times σ-clipped standard deviations of the pixel values within the boxes. As the final σ-value of each field we take the median of the calculated standard deviations. The measured σs for all fields in the different bands are listed in Table 3.5. We find that the obtained depth in the images for 1σ signal-to-noise per pixel corresponds to the surface brightness of 26.6, 26.7, 26.1, and 25.5 mag arcsec^{-2} in u', g', r', and i'-bands, respectively. When averaged over 1 arcsec^2 area, these values correspond to surface brightness of 28.3, 28.4, 27.8, 27.2 mag arcsec^{-2} in u', g', r', and i', respectively.

3.4.2 PHOTOMETRIC ACCURACY

As the Fornax cluster is poorly covered with standard star catalogs, a straightforward comparison of the obtained magnitudes with the standard stars to define the photometric accuracy is not possible. However, we can do an internal photometric consistency check by using the fact that the Milky-Way stars form locii in the

color-color space that have constant locations and small intrinsic scatters. Ivezić et al. (2004) have performed analysis for the zeropoint accuracy of the SDSS, using a test which can be used as a comparison.

In Fig. 3.4 we show non-saturated stars of the field 5 in u'-g' versus r'-i' color space. The stars appear in an inverse L-shaped distribution, where two loci are clearly apparent. The scatter in the vertical branch is relatively large in this projection, but reduces considerably when projected along the principal components defined from the full u', g', r', i'- distribution (see Fig. 3.5). The principal colors $P1$ and $P2$ as defined by Ivezić et al. (2004) are:

$$\begin{aligned}
P2s &= -0.249 \times u' + 0.794 \times g' - 0.555 \times r' + 0.234, \\
P2w &= -0.227 \times g' + 0.792 \times r' - 0.567 \times i' + 0.050, \\
P2x &= 0.707 \times g' - 0.707 \times r' - 0.988, \\
P1s &= 0.910 \times u' - 0.495 \times g' - 0.415 \times r' - 1.28, \\
P1w &= 0.928 \times g' - 0.556 \times r' - 0.372 \times i' - 0.425, \\
P1x &= 1.0 \times r' - 1.0 \times i',
\end{aligned} \tag{3.4}$$

where u', g', r' and i' are apparent magnitudes in the different bands. In our test, we projected stars in our data along these principal colors with the assumption that the stars intrinsically follow these equations with very small intrinsic scatter. To quantify the variations in the offsets of the loci and the scatter around them, we defined the scatter and offsets of the P2 colors with respect to zero projected along the P1 colors.

For the stellar locus test we wanted to use bright non-saturated stars. We used SExtractor for the identification of stars, and selected stars that have r'-band apparent magnitudes between 16 mag $<$ m$_{r'}$ $<$ 19 mag (we used MAG_AUTO[4] parameter in SExtractor), and have SExtractor parameter $CLASS\_STAR > 0.9$ ($CLASS\_STAR$ tells the probability of an object being a star). The stellar locus test is done for the stars that have $P1$ color components between -0.2 $< P1s <$ 0.8, -0.2 $< P1w <$ 0.6, and 0.8 $< P1x <$ 1.6. In Fig. 3.5 we show an example of a principal color diagram. The distributions of the measured offsets and scatters in each FDS field are shown in Fig. 3.6.

The standard deviations of the locus offsets in our data are 0.041, 0.020, 0.024 in s, w, and x, respectively. Within scatter, the deviations are consistent with zero offsets. The median scatters of the stars around the locus are 0.040, 0.025, 0.041 in s, w, and x, respectively. The corresponding values in SDSS are 0.011, 0.006, and 0.021 for the medians, and 0.031, 0.025, and 0.042 for the standard deviations. This test shows that the errors associated to our zero point definitions are roughly three time as large as for the SDSS images, corresponding to 0.03 mag in g', r', and i' -bands and 0.04 in u'-band.

[4] MAG_AUTO is the magnitude within 2.5 times the Kron-radius (Kron 1980) which is the luminosity weighted first order radial moment from the center of the star.

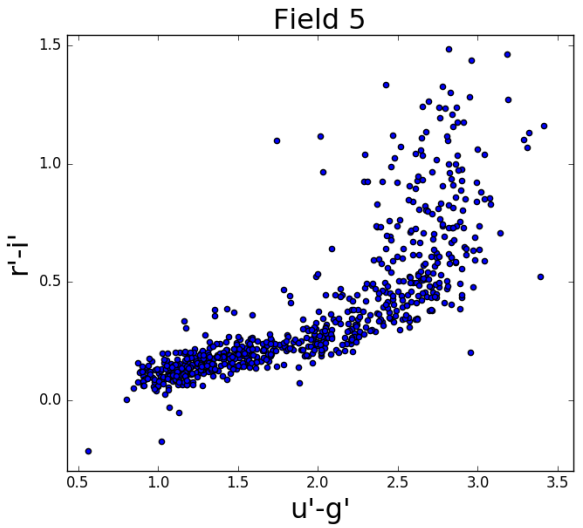

Figure 3.4: Colors of the stars in Field 5 are shown in the u'-g' vs. r'-i color-space. The positions of the stars form an inverse L-shaped figure whose two linear parts (*locii*) are known to have constant locations and small intrinsic scatter. The locations and scatter of the two apparent locii projected along the principal colors are used for the assessment of the FDS data quality.

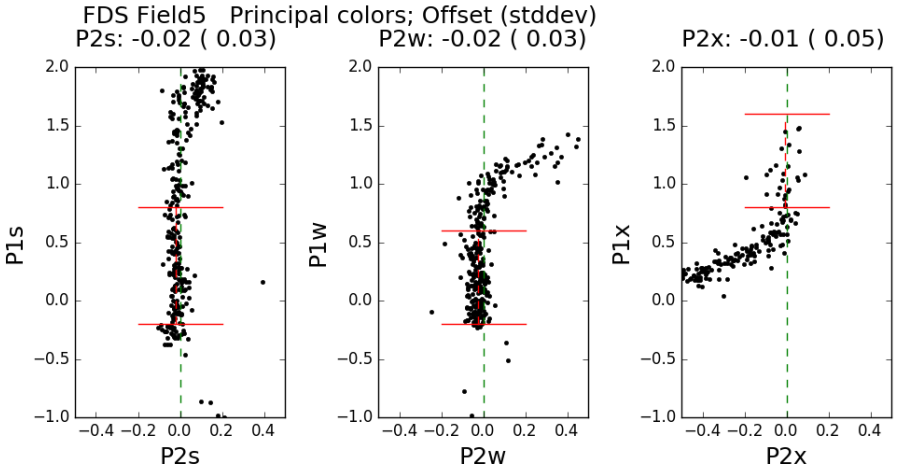

Figure 3.5: Stellar locii of the Milky Way stars shown along the three different principal color axes for the FDS Field 5. The dashed vertical lines show the zero offsets, and the horizontal red solid lines show the limits where the offsets and the standard deviations of the locii are measured.

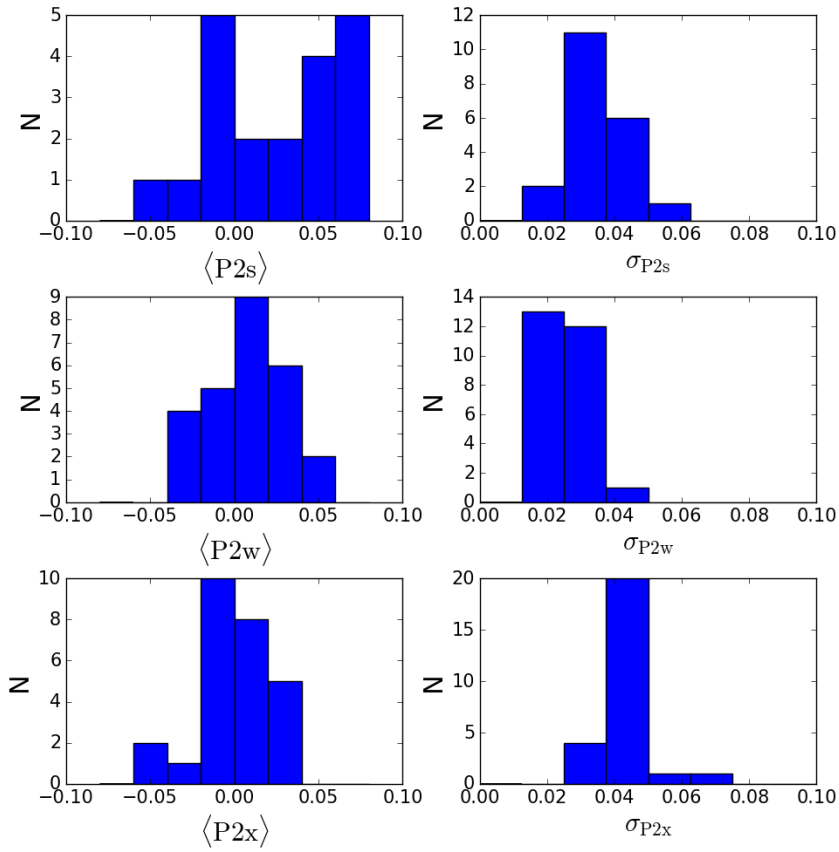

Figure 3.6: Left panels: Distributions of the clipped means of the principal colors in the different FDS fields. Right panels: Distributions of the standard deviations of the scatter of the stellar colors around the principal color axes in the different fields.

3.4.3 SEEING $FWHM$

As the images are taken during different epochs with different observing conditions, the point spread function (*PSF*) in the images varies. Additionally, when observations with different seeing conditions are stacked into the final mosaics, the radial profile of the *PSF* in the stacked images may be different from the original images. Below we describe how the full width at half maximum ($FWHM$) varies between the mosaics, and in Sections 5.1.1 and 5.1.2 we show how we model the *PSF* with analytic functions.

The $FWHM$ is straightforward to measure using SExtractor, so we ran it on all the fields to get object lists. From the object list we selected stars (CLASS_STAR[5]

[5]CLASS_STAR parameter requires an input FWHM estimation. We use the median FWHM of the objects in the image that are larger than FWHM>0.25 arcsec. This lower limit was adopted to

parameter > 0.95) that have the highest S/N, but are not yet saturated. In our images this corresponds to stars with r'-band aperture magnitudes between 15.5 mag $< m_{r'} <$ 18 mag. The measured median $FWHM$ and their standard deviations within the fields are listed in Table 3.5.

3.5 PREPARATION OF THE DETECTION IMAGES

In the following, we describe the steps for creating the images used for the identification of the galaxies. As a starting point the calibrated stacked mosaics are used (see Section 3.4). We first modelled and subtracted the bright stars ($m_{r'}$ < 15 mag) in the images in the different bands, and then stacked the different bands to make the final detection images.

3.5.1 POINT-SPREAD FUNCTION MODELS

For accurate modeling of the galaxies, it is necessary to take into account the effect of the *PSF*. The core of the *PSF* ($\lesssim 10$ arcsec from the center) is determined by the atmospheric turbulence and scattering which vary during the observations. The outer part ($\gtrsim 8$ arcsec) consists of light scattered from the optical surfaces of the camera that remain constant, apart from the amount of dust in the optics that can slightly alter the outer profile (see Sandin 2014).

We derived a *PSF* model for each of the fields separately. The model is derived in two parts: the inner *PSF* is modeled using the brightest non-saturated stars, and the outer *PSF* using the outer parts of the saturated stars. Since the number of saturated stars is limited, we use the same outer *PSF*-model for all fields, so that only the inner *PSF* is modeled in all fields. As shown in Table 3.5 the *PSF* varies also within one field on the order of few tenths of an arcseconds, which means that for a high accuracy modeling of the *PSF* one needs to do subfield modeling. This high accuracy is not needed for our Sérsic profile modeling of extended dwarf galaxies, but is important for compact objects such as ultra compact dwarfs (UCDs) or globular clusters (GCs).

3.5.1.1 INNER *PSF*

We followed Venhola et al. (2017) in the creation of the model for the inner 8 arcsec: first we selected stars with r'-band magnitudes between 15.5 mag $< m'_{r'} <$ 18 mag, and cut 80×80 pixel areas around the stars. We then more-accurately determined the peaks of the stars by fitting the innermost R < 1 arcsec areas around the centers with a 2D-parabola. We then resampled the images by dividing each pixel into 5×5 subpixels, and recentered the images using the accurate peak coordinates obtained via the parabola fitting. These cuts were then normalized with the flux within the innermost R < 1 arcsec from the center. These normalized

ensure that the median $FWHM$ is not biased by the false detections consisting of background noise fluctuations.

stamp images were then median averaged and resampled to the original pixel size to obtain the *PSF*-model.

Theoretically, a Moffat-profile should be sufficient to fit this inner part of the *PSF* (Moffat 1969, Trujillo et al. 2001), but as the mosaics typically consist of images with different seeings, the *PSF* of the mosaics is not well fit by a single Moffat-profile (see Venhola et al. 2017). We added a Gaussian to improve the fit in the peak, while leaving the Moffat-profile to dominate for radii R $>$ 2 arcsec. In the combined fitted function

$$I_{inner} = I_{0,Gaus} \exp\left[-\left(\frac{R}{\sqrt{2}\sigma}\right)^2\right] + I_{0,Mof}\left(1+\left(\frac{R}{\alpha}\right)^2\right)^{-\beta}, \quad (3.5)$$

the first part corresponds to the Gaussian profile, and the second one to the Moffat-profile. $I_{0,Gaus}$ and $I_{0,Mof}$ correspond to the central intensities of the Gaussian and the Moffat profiles, respectively, R corresponds to radius, σ is the standard deviation of the Gaussian, and α and β define the extent and the slope of the Moffat profiles, respectively.

The fitting was done so that first the innermost ten arcsec region of the profile was fitted with the Moffat function, and after that the profile within $<$1 arcsec from the center was fitted with the Gaussian function. These initial fits were then used as an input for the second fit where both components were fit simultaneously. The fit results for Field 11 are shown in Fig. 3.7, and the profiles of the individual non-saturated stars are shown in the left panels of the Fig. 3.8. Since the *PSF* profiles vary field by field, we list the fit parameters of all the *PSF*s in Table 3.6.

3.5.1.2 OUTER *PSF*

The previously described models of the inner *PSF* have low S/N in their outer parts, so that they cannot be used to trace the *PSF* down to I $< 10^{-4}$ of the central intensity. To follow the *PSF* to fainter levels we have to use the brightest saturated stars.

To model the outer parts of the *PSF*, we selected 15 saturated bright stars ($m_{r'}$ $<$ 10 mag) from different fields with no bright galaxies or stars nearby. To scale the flux of the stars we measured the central surface brightnesses of several hundreds of non-saturated stars from the FDS images, and compared the values with the magnitudes of American Association of Variable Star Observers' Photometric All Sky Survey catalog (APASS, Henden et al. 2012). These values have a linear relation, which we defined and used to scale the saturated stars (which are not saturated in the APASS-data). Azimuthally averaged radial profiles for the stars spanning up to 3 arcmin distance were made (see Fig. 3.8), which profiles were then combined making an average of them. The outer parts (from R = 40 to 160 arcsec) were fit with an exponential function,

$$I_{exp} = I_{0,exp} \exp\left(-\frac{R}{h}\right), \quad (3.6)$$

where $I_{0,exp}$ is the central intensity and h is the scale length. The exponential profile was selected empirically due to its good fit to the data. From the fits we

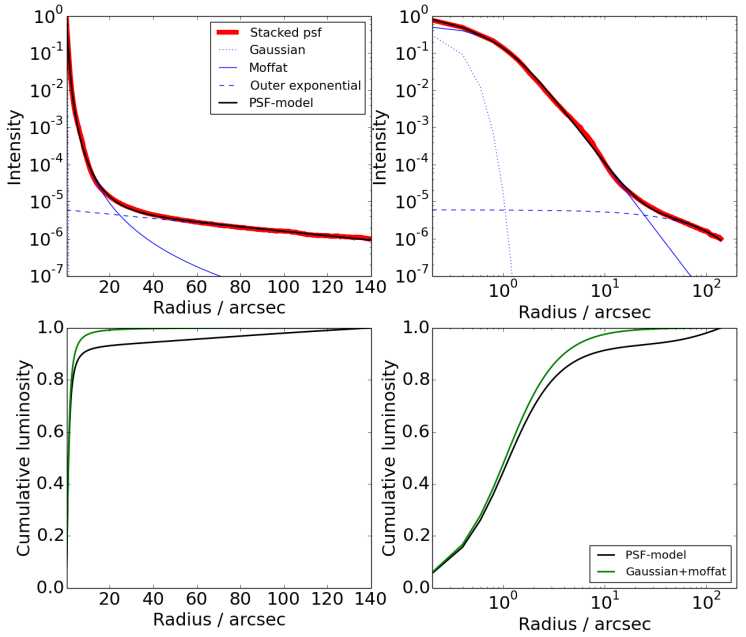

Figure 3.7: Upper left and right panels: Stacked intensity profiles (red lines) against linear and logarithmic radius scale, respectively. Shown also are the analytic *PSF* model (black lines), the model created from the inner Gaussian (blue dotted line), Moffat model (blue solid line) and the fitted outer exponential function (blue dashed line). The left and right lower panels show the cumulative luminosity fraction within a given radius in linear and logarithmic radial scales, respectively. The green line in the lower panels gives the cumulative flux for only the core part of the *PSF* (Gaussian+Moffat).

obtain $h_{g'}$ = 87.38 arcsec and $h_{r'}$ = 74.26 arcsec for the g'- and r'-band scale lengths, respectively, and $I_{0,exp,g'} = 1.556\times10^{-6}$ and $I_{0,exp,r'} = 6.022\times10^{-6}$ for the central intensities in the scaled units (I_0=1). We use these same parameters in all the fields.

To ensure that the scaling between the faint and bright stars works, we plot the profiles of a set of faint stars and the averaged profile in the left panels of Fig. 3.8, the profiles of the bright saturated stars in the middle panels, and finally show the combined stack model and the fitted model in the right panels. For obtaining the combined stack model, we used an average of the bright and faint profile within 6 arcsec $<$ R $<$ 8 arcsec, the faint star average profile within R $<$ 6 arcsec, and in the outer parts the average profile of the saturated stars. The lower right panel shows the profiles of both bright and faint stars around the area where they are combined showing that their profiles agree well in this area.

Sandin (2014) analyzed the outer parts of *PSF*s of several telescopes up to several hundred arcsecs. They found that at the very large radii (R $>$ 300 arcsec) the *PSF* intensity attenuates following $I \propto \mathrm{R}^{-2}$ law. In our data, we can follow

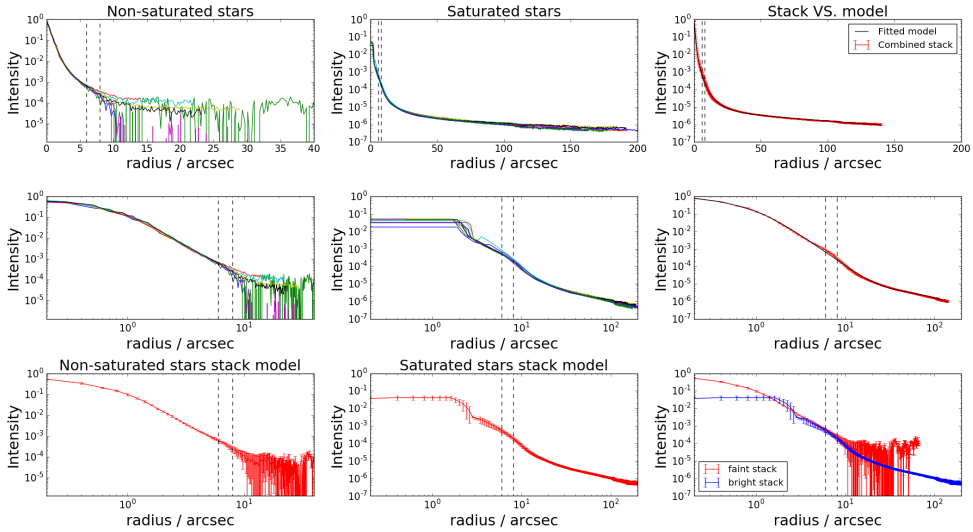

Figure 3.8: Left panels: Scaled luminosity profiles of the non-saturated stars of field 11 as a function of radius, shown in linear (top left) and logarithmic (middle left) scale. The different colors correspond to different stars. In the lowest panel the stack constructed from the stars is shown. The errorbars indicate the scatter between individual stars. Middle panels: Similar graphs for saturated stars of different fields. Top and middle right panels: Comparisons of the full profiles derived from the observed stars (i.e., combined stack of faint and bright stars), and the corresponding fitted model. Bottom right panel: Bright and faint stacks near the transition zone. The transition zone is shown in all panels using the vertical dashed lines.

the *PSF* only up to 200 arcsec. In this region our *PSF*-profile behaves in a similar manner as most of the *PSF*s in Sandin (2014), showing a clear seeing dependent core up to a few tens of arsecs, and an exponential part beyond that. For our purposes it is not necessary to follow the *PSF* further than a few arcminutes.

3.5.2 SUBTRACTION AND MASKING THE FORE-GROUND STARS

Due to the extended *PSF* of OmegaCAM, the bright stars contaminate large areas in the images. SExtractor is not designed to find objects in crowded fields, and therefore these outer halos affect the detection efficiency of SExtractor. In particular, the bright stars have spikes and reflection halos, which appear as false detections in the source lists. To prevent the above mentioned bias in the source lists, we subtract the bright stars ($m_{r'} < 12$ mag) and mask the stars with $m_{r'} < 16$ mag in the images before making the combined detection image. To mask the stars in a systematic manner we use the analytic *PSF* models described above.

In order to decide the masking radius for each star, we need to know their magnitudes. As the bright stars are saturated, we used APASS magnitudes for them. Since APASS includes also galaxies, some of the bright objects in that catalog may be FCC galaxies. To prevent unintentionally masking bright galaxies, we check for FCC galaxies within 5 arcsec around the bright APASS objects before masking or subtracting them. Since we masked only stars that have apparent magnitudes $m_{r'} < 16$ mag, we do not have to be worried about masking galaxies that are not in the FCC. We took the coordinates and magnitudes of the stars and subtract the analytic *PSF* model from all stars brighter than $m_{r'} < 12$ mag, as far as the surface brightness level of 29 mag arcsec^{-2}. The stars with $m_{r'} < 16$ mag are masked up to the radius where the analytical model corresponds to the surface brightness of 25.5 mag arcsec^{-2}. We find that the spikes and reflections are typically well masked using the selected masking limits (see Fig. 3.9 for example masks).

As a result, we obtain images where the bright stars are subtracted and the spikes and reflection haloes are masked. The total fraction of the area that could not be used due to these saturated stars is only ≈ 3 %, which will cause incompleteness of the same order into the dwarf galaxy catalog. Moreover, these excluded regions should not cause any systematic bias to our analysis since the stars are randomly distributed in the survey area. After this preprocessing of the images, they may still include some imaging artifacts, which were manually eliminated afterwards.

3.5.3 CREATING THE FINAL DETECTION IMAGES

To obtain the best image quality for the source detection image, we combine the star-subtracted g', r' and i'-band images of each field as a g'r'i'-composite image. We calculated a weighted average of the frames using the weights 0.4, 0.5 and 0.1 for g', r' and i'-bands, respectively. The weights were selected taking into account the depth of the different bands and the color g'-r' ≈ 0.6 of the early-type dwarf (dE) galaxies (Janz & Lisker 2009).

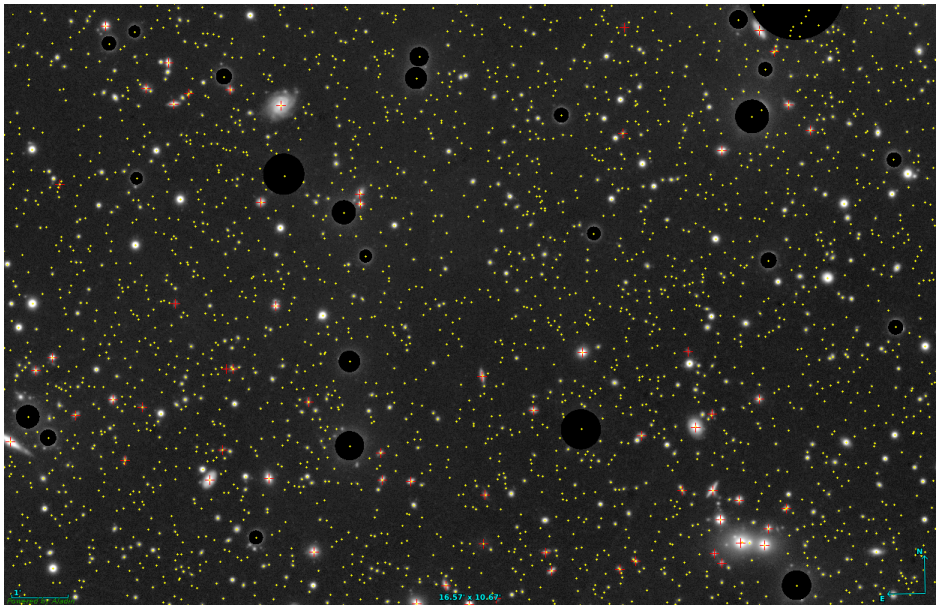

Figure 3.9: Magnification of Field 5 with the detected objects and masks (black circles) overlaid on the image. The yellow points and red symbols correspond to the initial detections of our detection algorithm, and the objects that pass the A_IMAGE > 2 arcsec selection limit, respectively. Aladin (Bonnarel et al. 2000) was used for generating the image. The image is best viewed in color on-screen.

3.6 PRELIMINARY SOURCE LISTS

3.6.1 DETECTION ALGORITHM

In this paper our aim is to detect resolved dwarf galaxies. We used SExtractor for the detection of the objects. An automatic detection method is used instead of a manual one, given the large amount of imaging data. However, SExtractor is not optimal for the detection of low surface brightness galaxies ($\bar{\mu}_{e,r'} \geq 24$ mag arcsec^{-2}), so we test the completeness of our source lists in Section 6.2. An extension dedicated to low surface brightness (LSB) galaxies in the Fornax cluster (Venhola et al. 2017), to be generated with a different detection algorithm, will be added to this catalog in a forthcoming paper (Venhola et al., in prep.). We did not specifically exclude LSB galaxies, but the detection limits in this paper are not very favorable for such galaxies.

SExtractor detects objects by searching for groups of connected pixels that are brighter than a certain detection threshold. In principle the detection can be done with or without subtracting a background model from the detection image. The background model is created by defining a grid of image pixels, and then estimating the background level in each grid box. This is done by iteratively σ-clipping the pixel distribution within the grid box, and then taking a mean. The

Table 3.2: Parameters used in SExtractor in the different lists. The columns in the table correspond to the name of the list (List), detection threshold (Thresh.) in units of background noise standard deviations (1σ corresponds typically to $\mu_{r'} \approx 26$ mag arcsec^{-2}), number of connected pixels above threshold to count as detection (Min. area), and the background model grid size (Back size). In the "LSB" list, an additional 9×9-pixel median filtering was applied to the images before the detection, so the 5σ threshold corresponds to 0.55σ in the non-filtered image.

List	Thresh. (σ_{sky})	Min. area (pix)	Back size (pix)
Small	1	10	100×100
Large	50	10,000	21,000×21,000
LSB	5	25	500×500

grid of means is then interpolated, which makes the background model. In this study the background model is subtracted before detecting the objects.

Some of the bright galaxies are blended with the smaller ones either physically or due to projection. In such cases, we can treat the large galaxies as background and include them into the background model. We can select a background grid size so that it is larger than the sizes of the small galaxies, but smaller than the primary galaxy. While detecting more extended galaxies, both bright and faint, the background grid size should be set to be large enough to prevent introducing false detections, resulting from background maps. For the above reasons, the galaxies have to be detected in several runs aiming for detecting galaxies with different sizes.

We ran SExtractor in three rounds: first for detecting small galaxies, then large galaxies, and finally we tuned the parameters to detect LSB galaxies. For the detection, we used the combined g'r'i'-images (described in Section 5.3) where the bright stars are subtracted and masked. We convolved all the images with a Gaussian kernel with $FWHM$ of ten pixels before the detection, in order to increase the S/N in the images. The SExtractor parameters of the different detection runs are shown in Table 3.2.

SExtractor outputs object lists with several parameters associated with each object. Most of these detections are Milky-Way stars, false detections or unresolved background galaxies that we want to remove from the lists. First the objects located under the masks generated for the bright stars (described in Section 5.2) were removed from all the lists. Also, the faint stars and unresolved galaxies were removed by excluding the objects with the semi major axis smaller than ten pixels (2 arcsec, see Fig. 3.9 and Fig. 3.10) measured by SExtractor (A_IMAGE). This selection based on size excludes also the unresolved Fornax cluster galaxies from our sample (see Section 9.1). However, the 2 arcsec (∼200 pc at the distance of the Fornax cluster) size limit is yet small enough, so that it will not exclude Fornax cluster galaxies similar to the Local Group dSphs that have effective radii between 2 arcsec $<$ R$_e$ $<$ 10 arcsec at the distance of the Fornax cluster (see Fig. 3.17). On average, this size limit excludes 99.5% of the detections per field. The

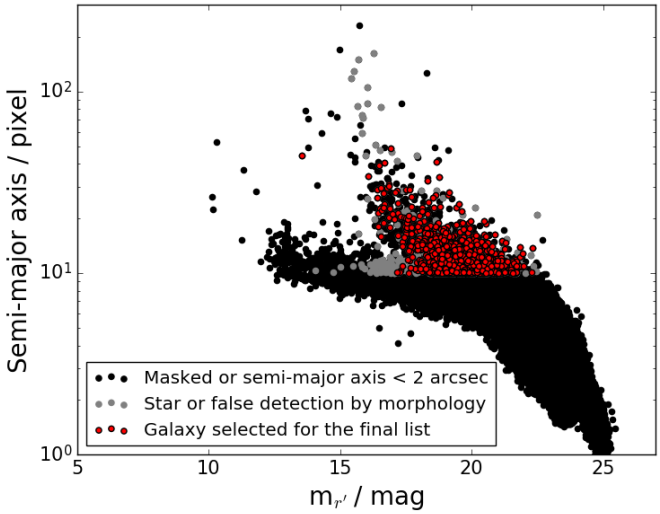

Figure 3.10: Size-magnitude relation of the detected objects in Field 5. Black dots show the objects that have been excluded either for being masked or too small, the gray dots show objects that are morphologically stars or false detections, and the red dots are the galaxies selected for the final catalog.

remaining objects in the three lists were then combined. We searched objects within 3 arcsecs from each other. If the same object appeared in several lists, its parameters and coordinates were taken from the list which had the highest detection threshold (in order 1. "Large", 2."Small", 3."LSB").

As a result, cleaned object lists for all fields were obtained. For each target we used the coordinates, magnitudes and semi-major axis lengths obtained with SExtractor as initial values for the photometric pipeline (Section 7). We did not want to make further filtering based on parameters of targets before running the photometric pipeline, since the photometric parameters, like effective radii or magnitudes, given by SExtractor, are not very robust.

3.6.2 COMPLETENESS OF THE DETECTION

To test the completeness of our detection algorithm, we iteratively embedded 3500 artificial galaxies in sets of 150 galaxies into the Field 10 detection image. As the depth variations in the different fields are only in the order of 0.2 mag (Section 4.1) we assume that the completeness is very similar over the whole survey area. 2D-Sérsic functions were used as artificial galaxies. The mock galaxies were convolved with the *PSF* of OmegaCAM, and the Poisson noise was added into each pixel. The mock galaxies were embedded to the reduced mosaic images with random locations and position angles. We selected a wide range of input parameters to cover the expected parameter space of the dwarf galaxies in the

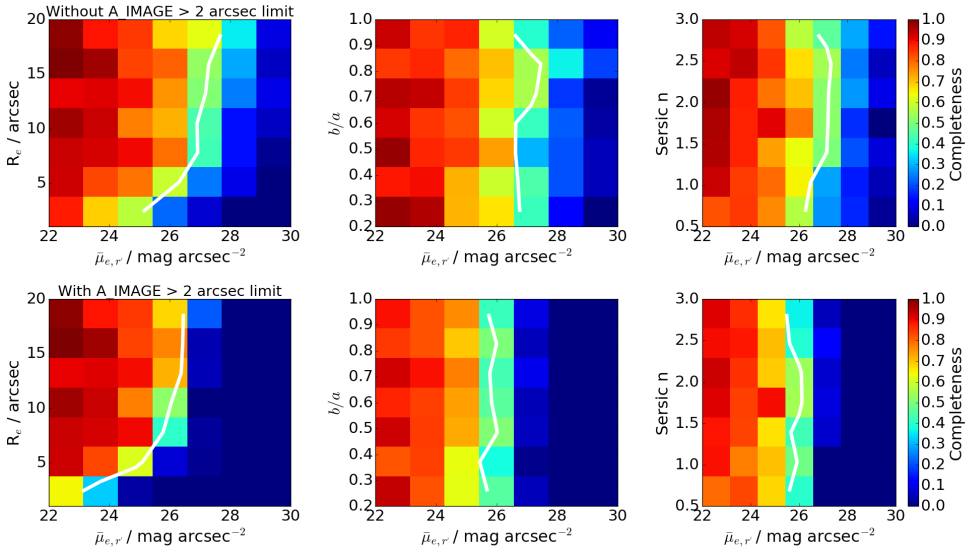

Figure 3.11: Detection efficiency of our detection algorithm is shown color-coded such that red means more efficient and blue less efficient. The detection efficiency is shown for the effective radius (R_e), axis ratio (b/a), and Sersic index (n), as a function of the galaxy mean effective surface brightness ($\bar{\mu}_{e,r}$). The upper row shows the detection efficiency without applying the minimum size limit of A_IMAGE of 2 arcsec, and the lower row shows the detection efficiency after applying the limit. The white line shows the 50% completeness limit.

Fornax cluster ($m_{r'}$=16–25 mag, n=0.5–3, b/a=0.2–1 and R_e=1–20 arcsec). We then ran the detection algorithm to test how many of these galaxies we can detect. By detection we required a detection within 3 arcsec from the central coordinates of the embedded galaxy. To also understand the effect of the minimum size-limit, we finally removed the objects with A_IMAGE $<$ 2 arcsec from the detections.

Figure 3.11 shows the detection efficiency of the galaxies as a function of galaxy magnitude for the different structure parameters with and without using the minimum size limit. We find that the detection efficiency slightly depends on the shape of the galaxy profiles (Sérsic n) so that more extended and more peaked galaxies are more efficiently detected. Applying the minimum size limit lowers the completeness limit from $\bar{\mu}_{e,r'}$ = 27 mag arcsec^{-2} to $\bar{\mu}_{e,r'}$ = 26 mag arcsec^{-2}, and especially it affects the smallest low surface brightness objects. As a result, our detection has the limiting r'-band magnitude with 50% detection efficiency of $m_{r'}$ = 21 mag and the limiting mean effective surface brightness of $\bar{\mu}_{e,r'}$ = 26 mag arcsec^{-2}. In Section 9, we also compare the final detections and completeness with previous galaxy catalogs in the Fornax cluster.

3.7 OBTAINING THE PHOTOMETRIC PARAMETERS

Photometric parameters are derived for classification of the galaxies, with the ultimate goal to identify the galaxies that belong to the Fornax cluster. The parameters are obtained for all non-masked galaxies that have (SExtractor) semi-major axis lengths larger than 2 arcsec ($\approx$ 200 pc at the distance of the Fornax cluster). We fit Sérsic profiles to the 2D flux distributions of the targets using GALFIT (Peng et al. 2002) to obtain the galaxy magnitudes, effective radii and shape properties. We also measured aperture colors, and calculate residual flux fractions (RFF, Hoyos et al. 2011) and concentration (C) for all the objects. A scheme of the photometry measurements is shown in Fig. 3.12, and the steps are described in more detail below. As an input for the photometric pipeline, we use the central coordinates, isophotal magnitudes, and semi-major axis lengths measured with SExtractor.

3.7.1 PREPARING THE IMAGES FOR PHOTOMETRY

First post-stamp images of the galaxies were made in all bands, limiting the semi-width of images to 10 A_IMAGE measured by SExtractor. As these semi-major axis lengths are not always accurate, especially for the low surface brightness objects, some post-stamp images were almost fully covered by the object galaxy. In cases for which too few sky pixels appeared, the image sizes were increased manually. The corresponding sigma-image mosaics were cut in a similar manner.

In the post-stamp images there are also other objects than the primary galaxy like faint stars and other galaxies that need to be masked for not to bias the fitting. We generated initial masks using SExtractor by masking all the sources larger than 100 pixels above the 1σ-threshold. As the primary galaxy was typically also masked, we removed all the masks within two effective radii from the center of the source. In the inner parts, we wanted to mask only point-like sources, so we identified them using SExtractor (CLASS_STAR $>$ 0.3), and then used the analytic *PSF* model to mask the point sources down to 27 mag arcsec^{-2}. These automatically generated masks were then visually inspected and modified (if needed) before fitting.

3.7.2 GALFIT MODELS

3.7.2.1 INITIAL ESTIMATION OF THE PARAMETERS

We estimated the initial input parameters of GALFIT by making an azimuthally averaged radial profile of the galaxy, using circular bins and a bin width of two pixels. We then took the clipped average of each bin and make a cumulative profile up to three semi-major axes lengths (from SExtractor). We then defined the effective radius and magnitude from the growth curve, which parameter values were used as the input for GALFIT.

The centers of the objects are also defined before running GALFIT. For the objects that have a clear center, we fit the central 10 $\times$ 10 pixel area with a 2d-parabola, and take the peak as the center. For the galaxies that have a flat

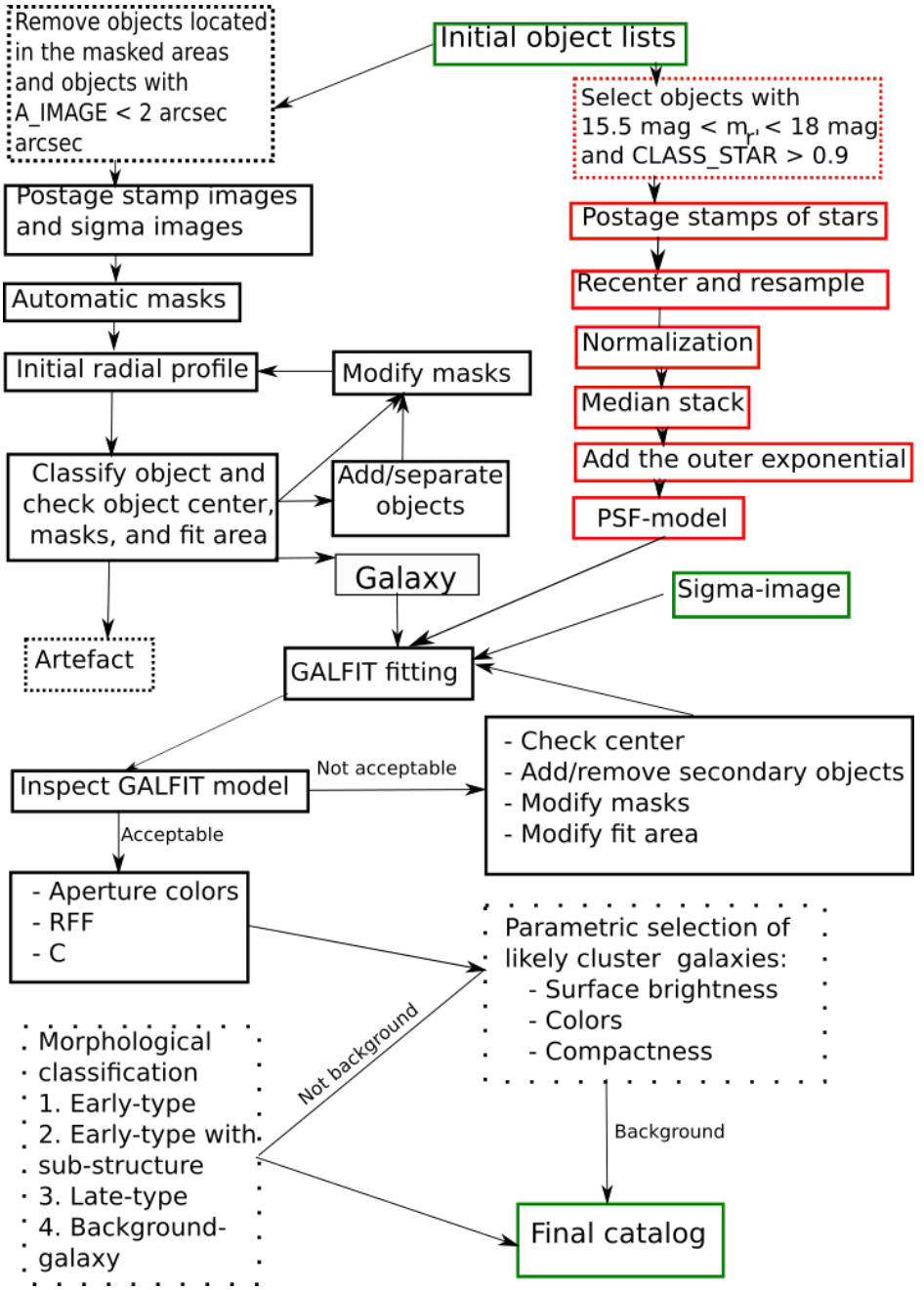

Figure 3.12: Flow chart of the photometric pipeline.

center, we take the SExtractor coordinates as the center and modify them in the cases where they are obviously wrong. This can happen if the object is split into several parts in the deblending done by SExtractor.

3.7.2.2 PARTIALLY OVERLAPPING OBJECTS

In some cases two galaxies are partially overlapping, so that they cannot be measured robustly separately. This problem can be solved by modeling both galaxies simultaneously with GALFIT.

Before running GALFIT, we inspected all the post stamp images for close companions. If the two objects were only identified as single object by SExtractor we separated them and ran the whole pipeline for both of them separately. Initial profiles were then generated for both objects, and an additional Sérsic component was added to the GALFIT model (see next subsection).

3.7.2.3 GALFIT MODELING

We used the idl-interface (Salo et al. 2015) to run GALFIT. The objects are fitted using either a single Sérsic function, or a combination of a Sérsic function and a point source for the nucleus, based on the visual appearance and the radial light profile of the galaxy. In both cases the background is also fitted with a plane of three degrees of freedom (mean intensity, and gradients in x- and y-directions). We left the more complicated multicomponent decompositions for future papers. All the parameters of the Sérsic component and the background are fitted freely. However, for the nucleus, the center is kept fixed, leaving only the magnitude as a free parameter. In case of nucleated dwarfs, we allowed the Sérsic component to have a different center than the nucleus, since it is possible to have off-centered nuclei (see Bender et al. 2005, but also Côté et al. 2006).

We performed the fitting in g' and r' -bands for all galaxies[6]. The fits are inspected, by looking at the residuals, radial profile with the model overlaid, and the original image with the fitted effective radius (R_e) overlaid. For a good fit we required R_e to be within the area that we can see from the galaxy. In the case of a bad fit, (due to imperfect masking or divergence of the model) the masks, center positioning, and the initial radial profile were reiterated.

3.7.3 APERTURE COLORS

We measured colors within the effective radius for all the galaxies using R_e, ellipticity and position angle obtained from the r'-band GALFIT model. For the galaxies within the main cluster, we measure u', g', r', and i' aperture magnitudes. For the galaxies in the Fornax A region, we have only g',r', and i', since that area

[6] u' and i' band were excluded since not all the galaxies have enough signal-to-noise for a robust fit

was not observed in the u'-band. We estimated the uncertainty in the aperture magnitudes as

$$\sigma^2_{\rm aper} = \sigma^2_{ZP} + \left(\frac{2.5}{I_{\rm aper}\ln 10}\right)^2 (\sigma_{\rm I} + \sigma_{\rm sky})^2, \tag{3.7}$$

where $I_{\rm aper}$ is intensity within the aperture, and $\sigma_{\rm I}$, $\sigma_{\rm sky}$ and $\sigma_{\rm ZP}$ are the uncertainties for the surface brightness, the sky, and the photometric zero point, respectively. For the mean intensity we assume Poissonian behavior, so that $\sigma_{\rm I} = \sqrt{I_{\rm aper}/(GAIN \times n)} \times GAIN$, where n is the number of pixels within the aperture. I, $\sigma_{\rm I}$ and $\sigma_{\rm sky}$ are given in flux units, whereas $\sigma_{\rm ZP}$ is in magnitudes.

3.7.4 RESIDUAL FLUX FRACTION (RFF)

The morphological separation of early- and late- type galaxies is done, apart from using the colors, also using the amount of structures in galaxies. Elliptical galaxies are mostly smooth and do not have strongly non-axisymmetric components, S0s have more distinct disk and bulge components, and may have bars, and late-type disk galaxies have star-forming clumps and/or spiral arms. The smoothness parameter is often used to quantify the amount of structures (see Conselice 2014). It is calculated by quantifying the residual after subtracting the smoothed image from the original galaxy image. This approach works well when the galaxies are well resolved and are located at similar distances. However, for distant galaxies with small angular sizes the smoothing flattens the radial profiles, so that the residuals increase systematically. Therefore smoothness does not only measure structure, but is somewhat degenerated with steepness of the slope of the radial profiles.

To overcome the problem related to the smoothness parameter, we decided to use residual flux fraction (RFF) that describes how much a galaxy differs from the used model, which in this case is a Sérsic profile. We measured RFF following Blakeslee et al. (2006):

$$RFF = \frac{\sum_{i=1}^{n_{r<R_P}} (|data_i - model_i| - 0.8\sigma_i)}{F_{r<R_P}}, \tag{3.8}$$

where $n_{r<R_P}$ is the number of pixels within the Petrosian radius (R_P) where the galaxy's surface brightness is 1/5 of the mean surface brightness within that radius. The term $|data_i - model_i|$ corresponds to the absolute value of residual flux at a given point, $F_{r<R_P}$ is the total flux within the R_P, and σ_i is the pixel value of the sigma-image. The factor 0.8σ is the expected mean absolute deviation of the $data_i - model_i$, so that in case of a perfect fit $RFF = 0$. The RFF was measured after masking the small background galaxies and point sources that overlap with the galaxy, and in the cases of large overlapping galaxies the large secondary galaxy was modeled and subtracted before calculation of the RFF. These steps were done in order to prevent secondary sources biasing the RFF measurements.

However, the RFF parameter is not completely redshift-independent, since seeing blurs more the structures in galaxies at higher redshifts. As shown in Fig. 3.27, late-type galaxies are well separated from early-type systems at low redshift, but it becomes difficult to distinguish the various morphological types as one goes to larger redshifts.

3.7.5 CONCENTRATION PARAMETER (C)

Galaxies also differ in their concentration; low mass galaxies have low surface brightnesses and approximately exponential radial profiles, whereas high surface brightness galaxies have central mass concentrations. In Sérsic profiles the parameter n defines the peakedness of the profile, and can be used for morphological classification, in the level that we are interested in this paper. However, we acknowledge that not even for bright elliptical galaxies the Sérsic profile is an accurate model; for ellipticals NUKER-profiles (Lauer et al. 1995) or core-cusp profiles are often used. Therefore, using a non-parametric measure to evaluate the type of profiles is also useful. We used the concentration parameter (C) as given in Conselice (2014)

$$C = 5 * \log\left(\frac{R_{80\%}}{R_{20\%}}\right), \tag{3.9}$$

where $R_{20\%}$ and $R_{80\%}$ are the radii that enclose 20% and 80%, respectively, of the galaxy's total light. The $R_{20\%}$ and $R_{80\%}$ are obtained by first measuring Petrosian magnitude[7] for the galaxy, and defining these radii from the growth curve derived from the radial profile. The lower right panel in Fig.3.27 shows how early-type galaxies of a given luminosity have higher concentration than late-type galaxies. In Fig. 3.13 we show how the non-parametric concentration relates with the Sérsic index n obtained via one-component fit. We also show in Fig. 3.13 how C and n are related for a Sérsic profile (see also (Janz et al. 2014)). Average Sérsic indices of the galaxies follow a similar trend to the pure Sérsic index, but with a large scatter and a small offset so that the real galaxies have higher Sérsic index at a given C. This offset is likely explained by the fact that the effects of the *PSF* are taken into account in the Sérsic n (obtained from the GALFIT models) but not in C.

3.7.6 UNCERTAINTIES OF THE GALFIT MODELS

Our photometric measurements have uncertainties arising from two different sources: at the low surface brightness end of the galaxy distribution we are limited by the signal-to-noise, and at the bright end the galaxies have typically more structure than our simple Sérsic models assume.

We quantify the fit uncertainty in the low surface brightness end using the mock galaxies embedded in the r'-band images (described in Section 6.2). We

[7]Petrosian magnitude is measured using elliptical aperture with size of $1.5\times\rho_P$, where ρ_P is the radius where the local surface brightness is one fifth of the mean surface brightness within the radius.

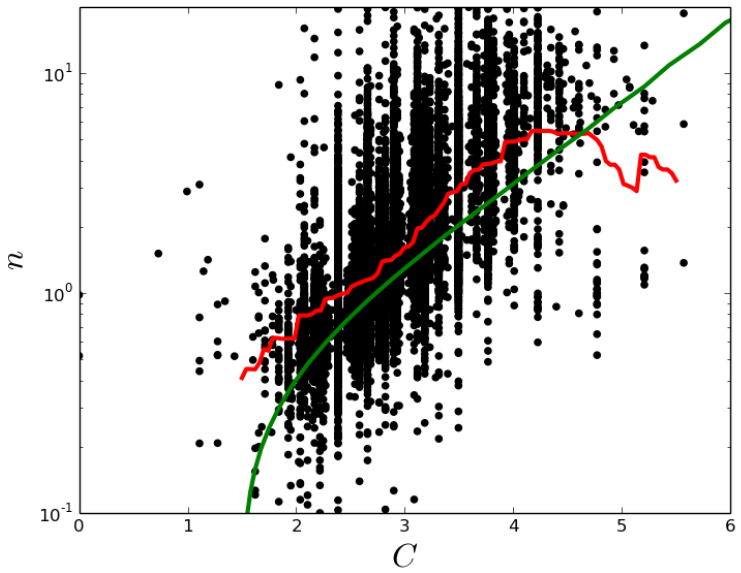

Figure 3.13: Values of the Sérsic index n and the concentration parameter C, measured in r'-band for all the objects in our catalog. The red line shows the running mean of the points ($\log 10(n)$ was used) along the x-axis within intervals of ΔC=0.5, and the green line shows the relation for a pure Sérsic profile.

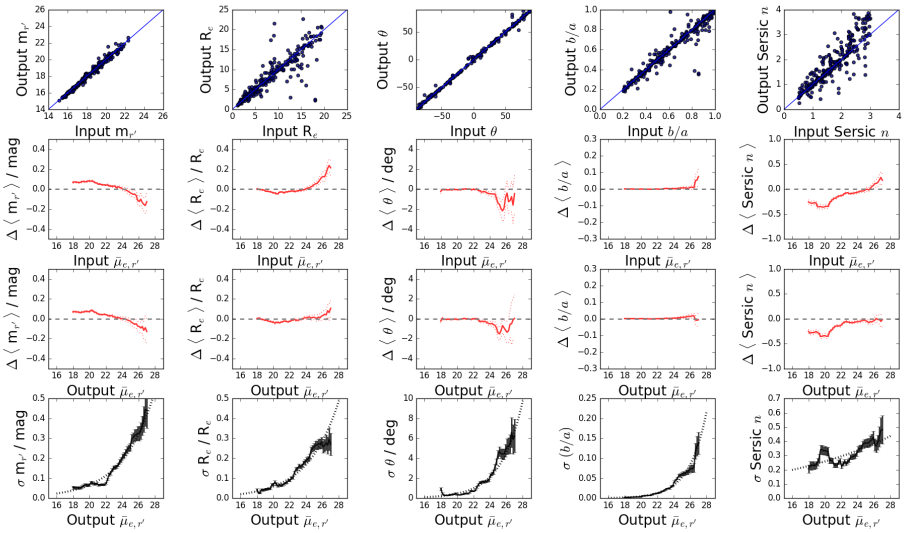

Figure 3.14: Top row panels: Comparison of the input structural parameters of the mock galaxies to the values measured by our photometric pipeline. The shown parameters are apparent magnitude (m$_{r'}$), effective radius in arcsec (R$_e$), position angle (θ), axis ratio (b/a), and Sérsic index (n), and the blue diagonal lines represent the 1:1 ratio. Second and third row panels: Mean differences between the input and output parameters (input - output) as a function of their input and output mean effective r'-band surface brightness, $\bar{\mu}_{e,r'}$, respectively. Bottom row: Standard deviations of the input - output parameter differences as a function of the input mean $\bar{\mu}_{e,r'}$. The dotted lines in the bottom row panels show the fits to the standard deviations as defined in Eq. 3.10.

made photometric measurements for 400 detected mock galaxies having a large range of structural properties. The differences between the input and output values, and the systematic shifts and standard deviations between the input and output values as a function of surface brightness, are shown in Fig. 3.14. As expected, the uncertainties in the parameters increase toward the fainter (lower surface brightness) galaxies. Slight systematic trends also appear in the total magnitudes and Sérsic indices, but are smaller than the uncertainties of those parameters.

Similarly to Hoyos et al. (2011) and Venhola et al. (2017) we fit the standard deviations of the input-output residuals[8] We fit the σ with the function

$$\log_{10}(\sigma) = \alpha \times \bar{\mu}_{e,r'} + \beta, \tag{3.10}$$

[8]By "standard deviation of residual" we mean $\sigma = \sqrt{\Sigma_{j=1}^{N}(input_j - ouput_j)^2/(N-1)}$, where N is the number of mock galaxies in a given $\bar{\mu}_{e,r'}$ bin.

Table 3.3: Fit parameters from the Eq. 3.10. The first column shows the parameter, and second and third columns show the constant (β) and the slope (α) in Eq. 3.10 for the given parameter.

Parameter	α	β
m_r	0.107	-3.309
R_e	0.111	-3.443
θ	0.175	-3.854
b/a	0.211	-6.535
Sérsic n	0.030	-1.194

where α and β are free parameters, and $\bar{\mu}_{e,r'}$ is the measured mean effective surface brightness. The fit results are listed in Table 3.3, and the fits to the standard deviations are shown in Fig. 3.14. We use these functions to estimate the measurement uncertainties for the galaxy parameters given by the photometric pipeline. These uncertainties are given with the galaxy parameters in the catalog. We note that these empirically measured uncertainties are significantly larger than the formal uncertainties given by GALFIT that only take in account the statistical uncertainty due to the pixel noise.

The uncertainty arising from the difference between the intrinsic profile of the galaxy and the fitted model is important for bright galaxies, which typically need several components to adequately fit their light distribution. Also, the models we use cannot fit star-forming clumps of the dwarf irregular galaxies (dIrr), which introduces some additional uncertainty for their fits. The bias introduced by the star-formation areas could be reduced slightly by doing the fits in i'-band, but as the signal-to-noise of the i'-band is significantly lower[9] for the faintest Fornax cluster galaxies than in r'-band, we use r'- and g'-band data for fitting. We used RFF to quantify how well the Sérsic models fit the galaxies. In Fig. 3.15 we show how the RFF is near zero for the early-type galaxies with $m_{r'} > 15$ mag, and then rises for the galaxies brighter than that indicating increasing amount of structure. It is difficult to quantify the uncertainties associated to the model, but in Section 9 we show that even for the most massive dwarfs, our measurements of magnitudes and effective radii agree well with the values from the literature.

3.8 SEPARATION OF THE CLUSTER AND BACKGROUND GALAXIES

Optical photometry alone is not optimal for defining the cluster membership of the objects, since some degeneracy exists in the projected structural and color properties of cluster galaxies and those at higher redshift (see next subsections for details). A reliable separation requires spectroscopic redshifts, but using the known scaling relations between the properties of the galaxies, we can separate

[9]Fornax dwarfs are bluer than r'-i' $\leq$ 0.3, and r'-band is 0.6 mag arcsec^{-2} deeper than i'-band, which makes r'-band at least 0.3 mag deeper than i'-band for those galaxies.

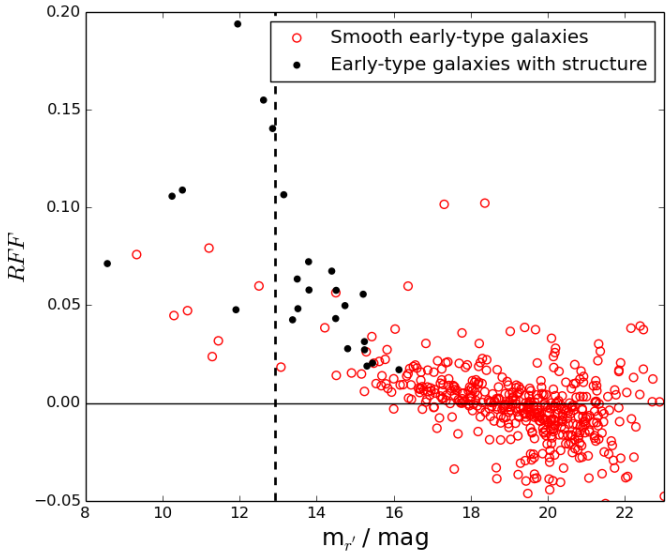

Figure 3.15: RFF shown as a function of the r'-band apparent magnitude for the Fornax cluster early-type galaxies in our catalog. The black points show the galaxies which have clear structure (for example a bar or an inner disk) differing from the single Sérsic model, and the red points are smooth early-type galaxies. The points on the left side of the vertical dashed line are giant galaxies ($M_{r'}$ < -18.5 mag) not included in our final catalog. The horizontal line shows the RFF=0 level. The systematic shift of RFF from zero in the high luminosity end can be understood as galaxies starting to differ from Sérsic profiles, whereas the increasing scatter in the low luminosity end is mostly explained by decreasing signal-to-noise.

the likely cluster members from the background objects. In the following, we calibrate our selection limits using archival spectroscopic data, select the likely cluster members, and finally test the purity of the selections.

The Fornax spectroscopic survey of Drinkwater et al. (2000) and its extension (Maddox et al., in prep.) provide spectra for some galaxies with r'-band magnitudes $m_{r'} < 18$, but is generally limited to relatively high surface brightness objects ($\mu_{0,r'} \lesssim 23$ mag arcsec^{-2}). It has also a smaller spatial extent than the FDS. According to Drinkwater et al. (2001), the mean recession velocity of the Fornax cluster galaxies is $\langle V \rangle = 1493 \pm 36$ km s^{-1} and the standard deviation of the velocity distribution is $\sigma_V = 374 \pm 26$ km s^{-1}. In what follows, we assume that the galaxies belong to the cluster if they have recession velocities within $2\sigma_v$ of the mean corresponding to 745 kms^{-1} < V < 2241 kms^{-1}. As we are interested in identifying galaxies at the distance of the Fornax cluster rather than identifying the galaxies physically bound to the cluster we do not use varying velocity limits at different cluster-centric radii. For the galaxies with no spectroscopic data available, we can use several other criteria to separate them from background galaxies, as explained below. These criteria are tested using the galaxies with spectroscopic data.

3.8.1 EFFECT OF REDSHIFT ON THE MORPHOLOGICAL AND STRUCTURAL PARAMETERS

It is well known that when the distance of a galaxy increases, its angular size decreases, but the surface brightness stays almost constant[10]. This makes intrinsically bright galaxies at large distance to have a low total apparent luminosities but high surface brightness. On the other hand, cluster galaxies follow the magnitude-surface brightness relation (Binggeli et al. 1984), so that the cluster dwarf galaxies with low total luminosity also have low surface brightness. This means that most of the background galaxies should have a brighter surface brightness for a given total magnitude, than the cluster galaxies. Additionally, the intrinsically large background galaxies should have more structure (such as bars or spiral arms) than the low-mass cluster galaxies of a similar apparent size, and also to be more centrally concentrated. However, although we understand well the expected differences between the background and cluster galaxies, it is not trivial how these differences appear in our structural and morphological parameters, once the effects of seeing, S/N, and the use of simple decomposition models are taken into account. In the Appendix 3.12.2 we show quantitatively how the parameters of the galaxies change as they get redshifted. To set the local group dwarf galaxies in the context of Fornax cluster we also show them in Fig. 3.27.

[10]The contribution of the redshift dimming of the surface brightness by factor of $1/(1+z)^4$, is small for the low- to mid-redshift galaxies, with redshift z<0.1 (at z=0.1, there is 50% dimming).

3.8.2 PRELIMINARY SELECTION CUTS

We identified the cluster galaxies using the following criteria: firstly they become bluer with decreasing luminosity (e.g., Roediger et al. 2017), secondly the surface brightness of the cluster galaxies decreases with decreasing total luminosity, and thirdly the faint cluster galaxies are less concentrated than the background galaxies (e.g., Misgeld et al. 2009).

3.8.2.1 COLOR CUT

To calibrate our selection limits, we used the cluster and background galaxies with spectroscopic data. For the color selection we selected the brightest spectroscopically confirmed cluster galaxies[11] and exclude all the galaxies that are at least 0.15 mag redder than that, which corresponds to g'-r' $>$ 0.95 and g'-i' $>$ 1.35 (see the top panel in Fig. 3.16). These limits are $\approx 3\sigma$ of the calibration uncertainties toward red from the color of NGC1399, which means that by this selection limit we are not likely to remove any galaxies with intrinsic colors bluer than that from our sample. This selection excludes more than half (N≈8200) of the detected galaxies. The excluded galaxies include most of the large background ellipticals and spirals, as their intrinsic colors are similar to the largest cluster galaxies, and their apparent colors are even redder due to redshift. However, after this cut our sample still includes a significant amount of low and mid-redshift background field spirals, and possibly also lower redshift moderate mass ellipticals from the background clusters. These galaxies are bluer than the largest ellipticals of the Fornax cluster.

Previous studies have suggested the existence of very red dwarf galaxies in clusters, including both low surface brightness (Conselice et al. 2003) and compact dwarf galaxies (Price et al. 2009). They appear as red outliers from the red sequence. However, no compact elliptical galaxies of Price et al. (2009) would have been excluded with our color cut, since they are still bluer than the most massive ellipticals. Five of the 53 galaxies in the sample by Conselice et al. (2003) would have been excluded from our sample but as Penny & Conselice (2008) showed later using spectroscopic subsample, those red outliers in the sample of Conselice were background galaxies. In principle, the color cut would also remove galaxies that appear red due to their internal dust extinction, but for the evolved nature of the Fornax cluster, it is very unlikely that such galaxies exist in this environment.

3.8.2.2 SURFACE BRIGHTNESS CUT

In order to separate the background galaxies that have higher surface brightness for a given apparent magnitude than the cluster galaxies, we made a linear fit for the cluster galaxies in the magnitude-surface brightness space. For the confirmed cluster galaxies this is shown in Fig. 3.16 (red dots in the middle panel). It appears that the slope of the relation between $m_{r'}$ and $\mu_{e,r'}$ changes at $m_{r'} \approx$

[11] NGC1399 has g'-r' $\approx$ 0.8 and g'-i' $\approx$ 1.2 in the central parts (Iodice et al. 2016).

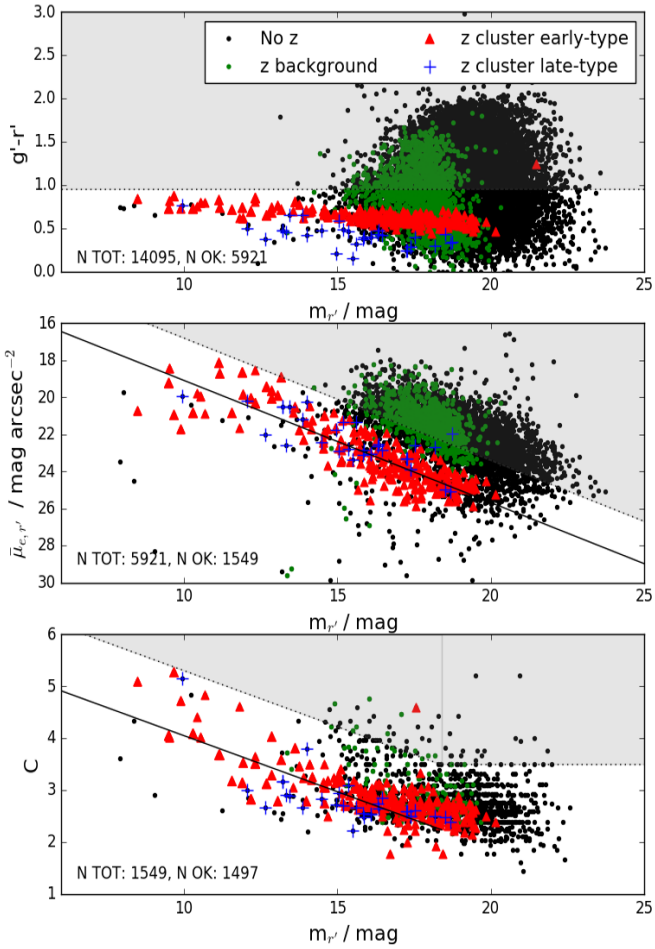

Figure 3.16: Illustration of our main criteria for distinguishing the cluster and background galaxies from each other. The panels from top to bottom show how the g'-r' color (also g'-i' cut was used which looks very similar), the mean effective surface brightness $\bar{\mu}_{e,r'}$, and the concentration parameter C of the spectrally confirmed (Drinkwater et al. 2000) early- (red symbols) and late-type (blue symbols) cluster and background galaxies (green symbols), scale with the r'-band apparent magnitude ($m_{r'}$). The solid lines show the fits to the early-type Fornax cluster galaxies, and the dotted lines show the selection limits. The excluded areas are shaded with gray. The black dots correspond to objects with no spectra available. The numbers in each plot correspond to the total number of galaxies before the cut, and the number of galaxies that remain after the cut. The two lower panels show only the galaxies that have not been excluded in the previous steps.

12 mag so that the galaxies fainter and brighter than that have different slopes (Binggeli et al. 1984, Misgeld & Hilker 2011, Eigenthaler et al. 2018). Since we are interested in dwarf galaxies in this work, we fit the galaxies only in the faint part, that is, with $m_{r'} > 12$ mag, and use this fit for the classification. We then defined the mean deviations of the galaxies around the fit and exclude the galaxies that have brighter surface brightness than three standard deviations from the cluster sequence (gray area in Fig. 3.16 mid panel). This selection aims to exclude massive high surface brightness background galaxies, but as shown in Fig. 3.27, will not exclude many bright galaxies with $z < 0.04$. This selection excludes three quarters of the remaining galaxies leaving only N = 1549 galaxies. We are aware that there exist compact galaxies in the Fornax cluster that might be excluded due to this criterion. We discuss these galaxies in Section 9. However, as shown in Fig. 3.17 this surface brightness cut would not exclude galaxies similar to Local Group dSphs from our sample.

3.8.2.3 CONCENTRATION CUT

Finally, we used the concentration parameter to exclude the remaining background elliptical galaxies, which are otherwise difficult to separate morphologically from the cluster dwarfs. We fit the magnitude-C relation for cluster galaxies with $m_{r'} < 16$ mag, and classify the galaxies that are located more than 2σ above that relation, and have $C > 3.5$, as background galaxies. The latter criterion is adopted to make sure that we did not exclude exponential disks, or galaxies with even flatter luminosity distribution from our sample. By this condition we exclude additional ≈50 galaxies from the cluster sample, leaving 1497 galaxies as likely cluster members (≈10% of the total sample). Even after this cut, there remains some fraction of spectroscopically confirmed background galaxies, which are later removed from the cluster sample according to their visual morphological appearance (see Sect. 8.3).

3.8.3 VISUAL CLASSIFICATION OF THE SELECTED SAMPLE

After selecting the likely cluster member galaxies by their photometric parameters, we make also a first order visual morphological classification of the galaxies. This classification is not meant for the use of any detailed morphological analysis, but rather to further identify the galaxies that belong to the Fornax cluster. To do the classification in practice, we generate color images of all the likely cluster galaxies and inspect the color and residual images (data−model) simultaneously. We separate the galaxies into five groups according to their morphology, with examples shown in Fig. 3.18:

- **Smooth early-type:** Galaxies that have a smooth red appearance, and do not have structures like clearly distinguishable bars or spiral arms. If a dwarf galaxy has an unresolved point-like nucleus, it will be classified into this group as well. This group therefore includes giant early-type galaxies with no clear structure, and nucleated and non-nucleated dwarf ellipticals.

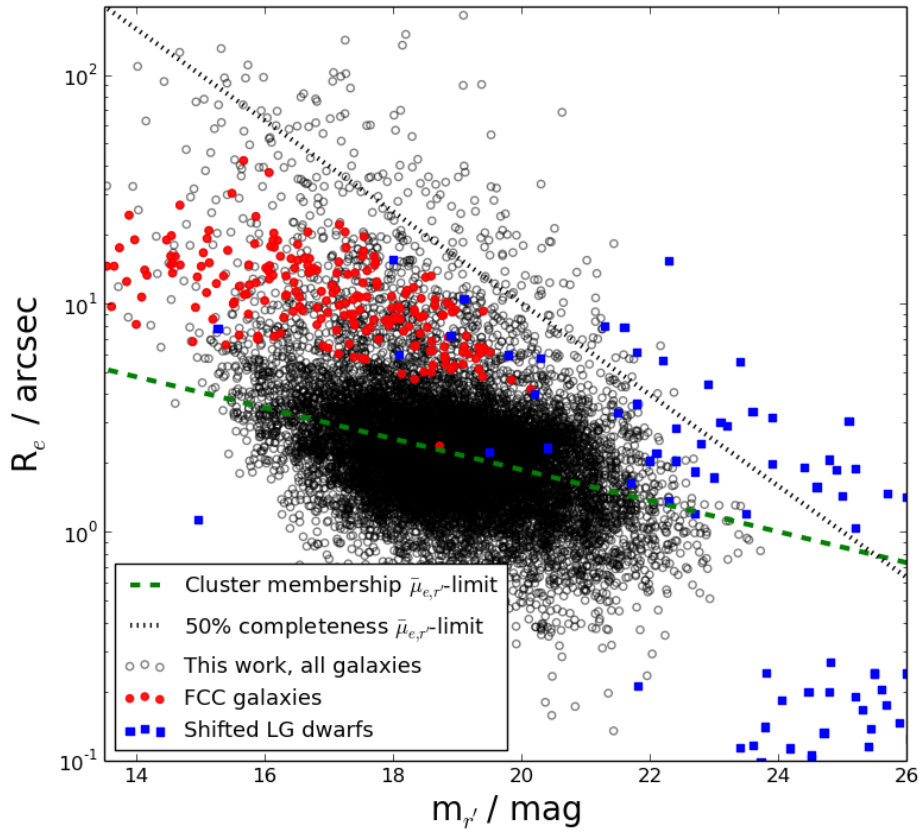

Figure 3.17: Comparison of our surface brightness selection cut (green dashed line) described in Section 8.2.2 with the size-magnitude relation of the galaxies in our sample (black and red symbols), and in the local group galaxies of Brodie et al. (2011) after shifting them to the distance of the Fornax cluster (blue squares). The red points show the galaxies in our sample that are classified as likely cluster members by Ferguson (1989). The gray dotted line shows our 50% surface brightness completeness limit of $\bar{\mu}_e = 26$ mag arcsec^{-2}. As the blue squares are mostly above the surface brightness selection limit, we would not exclude similar galaxies in the Fornax cluster from our sample by applying the selection limit. The blue squares appearing in the bottom right corner are star cluster like objects that would appear as point sources at the distance of the Fornax cluster.

- **Early-type with structure:** Galaxies that are red and have no star-forming clumps, but have structures such as bulge, bar, or spiral arms. They are not well modeled by a single Sérsic function. This group includes S0s and dEs with prominent disk features.
- **Late-type:** Galaxies that are blue, and have star-forming clumps. This group includes spirals, blue compact dwarfs and dwarf irregular galaxies.
- **Background:** Small galaxies that show features like bars or spiral arms. Since such features are not likely to appear in low-mass cluster dwarfs (see Janz et al. 2014), we conclude them to be background galaxies. We are aware that some dwarf galaxies have also spiral structure and bars (Lisker et al. 2006), but those are mostly found in the most massive dwarfs, and even in them, the fraction of light in the disk structures compared to the smooth spherical component of the galaxy is so low, that there is no danger to mix these dwarfs to the background spirals.
- **Unclear:** Galaxies whose morphological type is not clear. For example, galaxies that have low surface brightness, but possess some weak structures resembling a bar or a central bulge.

In summary, of the 1497 identified galaxies there were 577 likely cluster members, of which 453 were classified as smooth early-types, 24 as early-types with structure, and 100 as late-types. Of the parametrically selected galaxies, 897 were classified as background systems and 22 as uncertain cases.

3.8.4 PARAMETRIC CLASSIFICATION OF THE UNCERTAIN OBJECTS

The 22 galaxies, which we were not able to classify morphologically with certainty, may be Fornax cluster galaxies according to their colors, surface brightnesses and concentrations. To give them classifications, we can compare their morphological parameters with those galaxies that we were able to classify morphologically. In Fig. 3.19 we show how the different morphological classes correlate with these parameters, including color, RFF and the C parameters. Such correlations help us to evaluate which of the uncertain cases may still form part of the Fornax cluster. It is clear that in the color-RFF plane a simple color cut is not enough to explain most of the division of galaxies between early-type and late-type systems.

If we concentrate only on the low luminosity galaxies with $m_{r'} > 15$ mag, the separation of early-type and late-type galaxies is simpler (see lower panels in Fig. 3.19). All of them have low concentration parameters and RFF-values, and the g'-r' colors show a straight forward division between early-type and late-type galaxies. Using these properties, we give parametric classifications for the uncertain galaxies. The galaxies with g'-r' < 0.45 and $C < 3.2$ are classified as late-types, the ones with g'-r' > 0.45 and $RFF < 0.05$ and $C < 3.2$ are classified as early-types, and the others are classified as background objects. Applying these criteria, 13 of the 22 galaxies with uncertain classifications appeared to be real cluster members, of which four are late-types and nine early-types. Adding these 13 galaxies into our sample of likely cluster galaxies, our total galaxy number increases to 590 galaxies.

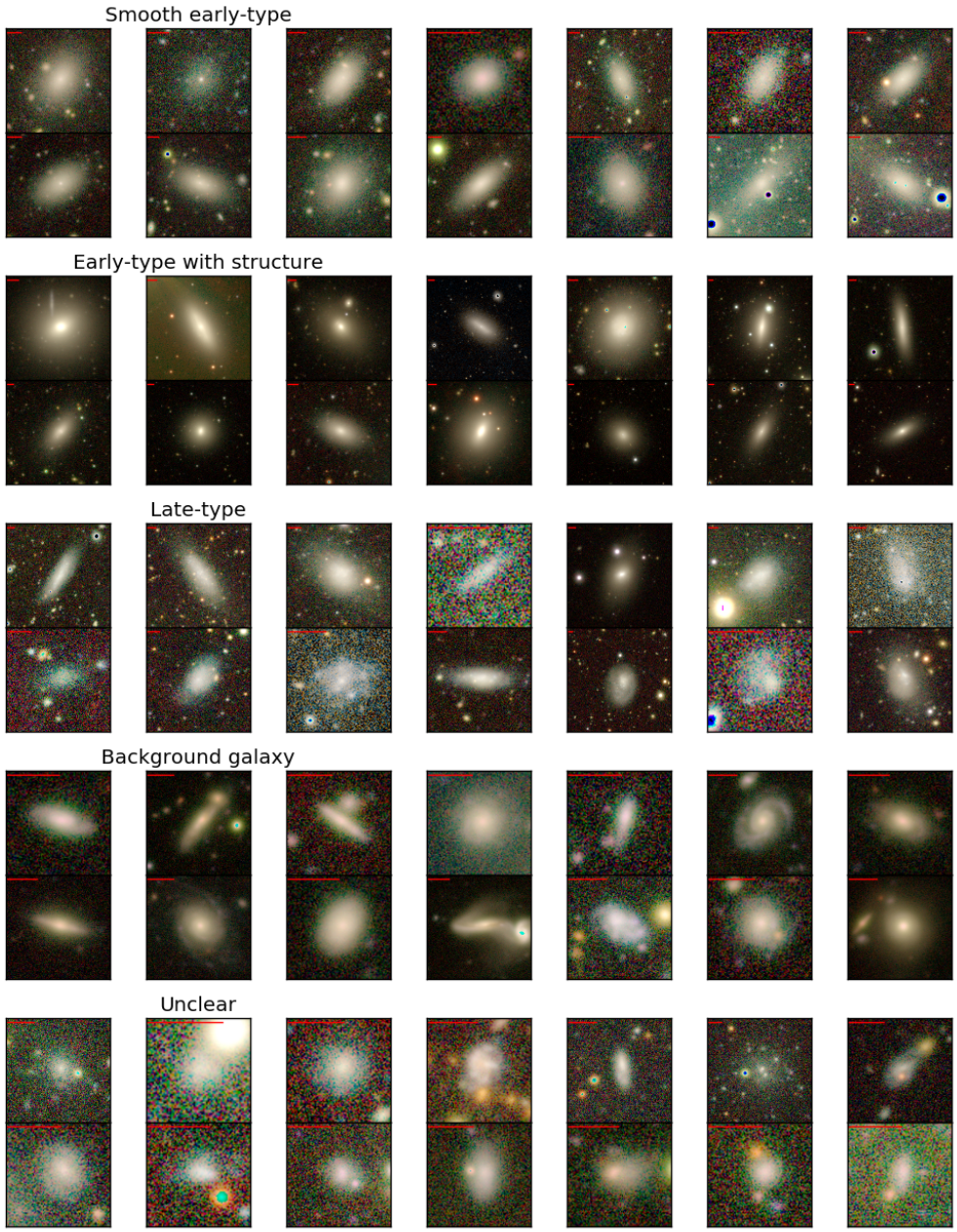

Figure 3.18: Color images of the galaxies with different morphological classifications as defined in Section 8.3. g', r', and i' bands of the FDS data are used as the blue, green, and red channels in the images, respectively. The galaxies have very different sizes on the sky, so that we have added bars with the length of 10 arcsec to each image.

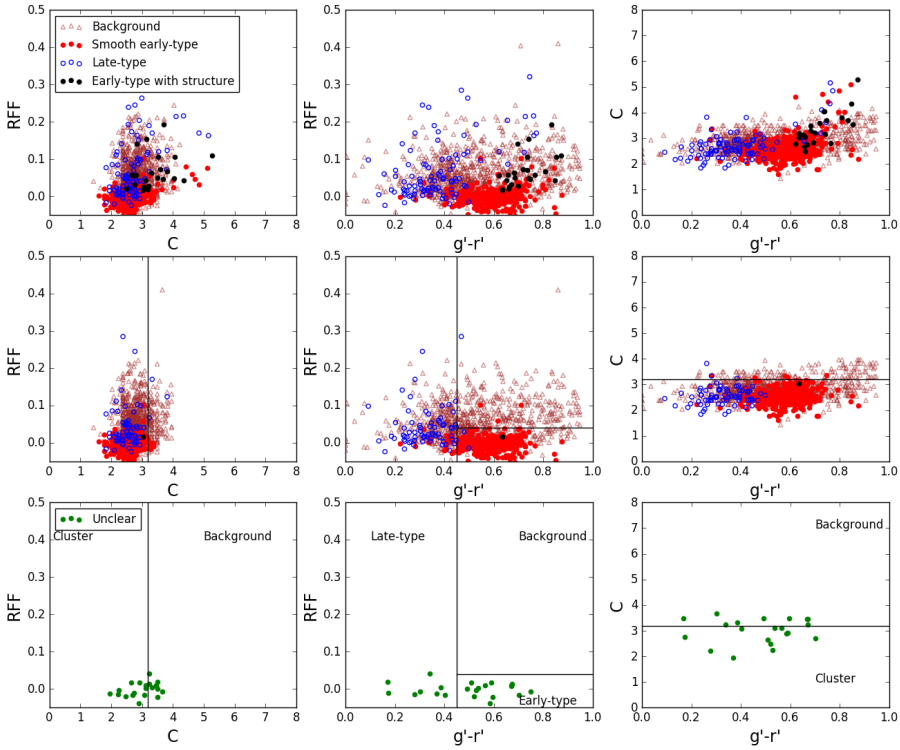

Figure 3.19: Evaluation of the remaining uncertain cluster memberships, after applying the main selection criteria. The top row of panels shows how the g'-r' color, concentration (C), and RFF are related for the galaxies that we selected using the preliminary selection cuts (see Section 8.2) and visual classification (see Section 8.3). The different colors correspond to visual morphological classifications of these galaxies, and the colors are explained in the legend of the upper left panel. The mid row shows the same parameters as the top row but limiting to galaxies with $m_{r'} > 15$ mag. This is the range of the galaxies that we could not classify morphologically with certainty. In the bottom row we show the parameters for these uncertain cases with the green points. The limits that we used for classifying the uncertain cases into early- and late-type cluster, and background galaxies are shown with black lines. Altogether nine of galaxies with uncertain classifications were classified as background, four as cluster late-types, and nine as cluster early-type dwarfs.

3.8.5 FINAL CATALOG

Of the 590 cluster members, 564 are dwarf galaxies ($m_{r'} \geq 12.5$ mag) presented in our Fornax cluster dwarf galaxy catalog. The number of background objects is 13,505. Our catalog has a minimum semi-major axis size limit of 2 arcsec, and it reaches a 50% completeness at limiting surface brightness of $\bar{\mu}_{e,r'} < 26$ mag arcsec^{-2}. Of the cluster dwarf galaxies 470 are early-types, of which 24 have substructure, and the remaining 94 galaxies are classified as late-type systems. The LSB galaxies and the bright galaxies will appear in separate catalogs to be published by Venhola et al. (in prep.) and Iodice et al. (2018), respectively. Producing separate catalogs makes sense because different analysis methods are used to obtain the parameters of the bright galaxies, and in case of the LSBs are also used when identifying the galaxies. For example, with the simple Sérsic fitting used in this study, it is not possible to derive any reliable physical parameters of the bright galaxies (Spavone et al. 2017). However, for completeness in this study we provide also the parameters of all the detected background objects independent of the galaxy magnitude. An extract of the catalog is given in Table 3.4. The full dwarf galaxy catalog with the measured parameters and classifications, and a separate catalog with the background objects, are available as online material at the CDS via anonymous ftp to cdsarc.u-strasbg.fr (130.79.128.5) or via `http://cdsweb.u-strasbg.fr/cgi-bin/gcat?J/A+A/`.

3.9 COMPARISON WITH THE LITERATURE

3.9.1 DETECTIONS

To assess its quality, it is important to compare the completeness of the FDS catalog described in this paper, to the previous most complete Fornax Cluster Catalog by Ferguson (1989). Our galaxy catalog is known to miss some galaxies: those overlapping with the bright stars, galaxies projected on top of the bright galaxies, galaxies that are small, and galaxies which have very low surface brightnesses (such as UDGs). These biases were quantified in Section 6.2 using mock galaxies, which showed that we are able to detect galaxies down to $\bar{\mu}_{e,r} \approx 26$ mag arcsec^{-2} with more than a 50% completeness and miss ≈3% of the galaxies due to overlapping bright objects. Here we make comparisons with the FCC and the LSB galaxy sample of Venhola et al. (2017), latter of which (when extended to the whole cluster) will form part of the complete FDS dwarf galaxy catalog[12]. Additionally, we show a comparison with the visually identified samples of Mieske et al. (2007) and Eigenthaler et al. (2018) that are limited to the central parts of the cluster.

We took the above mentioned catalogs and searched for FDS dwarf galaxies within 5 arcsec from those objects. The black, red, green, and gray lines in the Fig. 3.20 correspond to the detection efficiency while comparing our sample with the FCC galaxies, the LSB galaxies by Venhola et al. (2017), the galaxies in Mieske et al. (2007), and the galaxy sample of Eigenthaler et al. (2018). This comparison

[12]We also miss UCDs and cEs that appear (nearly) unresolved in our data.

Table 3.4: An example page of our dwarf galaxy catalog including likely cluster galaxies. The columns from left to right correspond to: target, right ascension (R.A.) and declination (Dec.) in ICRS coordinates, axis-ratio (b/a), position angle measured from north toward east (θ), apparent r'-band total magnitude ($m_{r'}$), r'-band effective radius in arcseconds (R_e), Sérsic index (n), aperture magnitudes within the effective radius in the u', g', r', and i' filters, the concentration index (C), and the residual flux fraction (RFF). The values after the $\pm$-signs correspond to the 1σ uncertainties in the parameters. The final column gives the morphological type of the galaxy according to our classifications in Section 8.3: 'e' corresponding to smooth early-type, 'e(s)' to early-type with structure, and 'l' to late-type galaxy, and '*' at the end of the morphological classification indicating that the object has a nucleus.

Target	R.A.	Dec.	b/a	θ	$m_{r'}$	R_e	n	u'	g'	r'	i'	C	RFF	Morphology
F12D327	54.3038	-36.2579	0.54 ± 0.08	-84.3 ± 4.6	20.0 ± 0.3	5.9 ± 1.6	0.8 ± 0.4	22.91 ± 0.07	21.58 ± 0.05	21.15 ± 0.04	21.27 ± 0.04	2.0	0.01	e
F12D349	54.2052	-36.2297	0.33 ± 0.05	85.3 ± 3.2	17.3 ± 0.2	13.4 ± 2.8	1.0 ± 0.4	20.44 ± 0.04	19.41 ± 0.03	18.77 ± 0.03	18.39 ± 0.04	2.3	0.00	e
F12D366	55.1832	-36.1853	0.84 ± 0.10	30.9 ± 5.5	17.8 ± 0.3	19.6 ± 5.8	1.0 ± 0.4	20.42 ± 0.06	19.21 ± 0.04	18.62 ± 0.03	18.71 ± 0.04	2.8	-0.02	e
F12D367	54.0536	-36.1665	0.55 ± 0.02	66.7 ± 1.2	15.5 ± 0.1	9.9 ± 1.1	1.5 ± 0.3	18.52 ± 0.04	17.12 ± 0.03	16.49 ± 0.03	16.17 ± 0.04	3.0	0.02	e(s)
F12D396	54.9691	-36.1419	0.56 ± 0.08	85.5 ± 4.4	21.0 ± 0.3	3.4 ± 0.9	0.6 ± 0.4	24.02 ± 0.07	22.93 ± 0.06	22.25 ± 0.05	21.84 ± 0.04	2.1	-0.01	e
F12D399	55.1571	-36.1211	0.67 ± 0.06	-43.0 ± 3.6	18.3 ± 0.2	9.4 ± 2.1	0.7 ± 0.4	20.76 ± 0.04	19.83 ± 0.03	19.24 ± 0.03	18.84 ± 0.04	2.4	-0.01	e
F12D406	54.7741	-36.0989	0.73 ± 0.02	-3.6 ± 1.5	17.0 ± 0.1	6.4 ± 0.8	0.8 ± 0.3	19.78 ± 0.06	18.39 ± 0.03	17.82 ± 0.03	17.56 ± 0.04	2.6	0.01	e*
F12D429	54.5801	-36.0656	0.78 ± 0.04	-15.9 ± 2.6	18.3 ± 0.2	6.5 ± 1.2	0.7 ± 0.3	21.11 ± 0.04	19.80 ± 0.03	19.22 ± 0.03	19.00 ± 0.04	2.4	-0.00	e
F12D433	54.8846	-36.0994	0.90 ± 0.08	79.5 ± 4.3	20.3 ± 0.3	4.7 ± 1.2	0.6 ± 0.4	23.04 ± 0.07	21.81 ± 0.05	21.29 ± 0.04	21.27 ± 0.04	2.3	-0.02	e
F12D436	55.0014	-36.0936	0.59 ± 0.09	-35.2 ± 5.0	20.5 ± 0.3	5.2 ± 1.4	0.8 ± 0.4	23.17 ± 0.10	21.94 ± 0.06	21.43 ± 0.05	21.14 ± 0.04	2.0	-0.01	e
F12D463	54.5262	-36.0501	0.89 ± 0.06	-83.9 ± 3.6	19.9 ± 0.2	4.6 ± 1.0	0.8 ± 0.4	22.33 ± 0.05	21.34 ± 0.04	20.78 ± 0.04	20.57 ± 0.04	2.6	-0.00	e
F12D491	54.4249	-35.9553	0.46 ± 0.11	-13.0 ± 5.8	19.5 ± 0.3	9.4 ± 2.9	0.7 ± 0.4	21.86 ± 0.05	21.16 ± 0.04	20.56 ± 0.04	20.29 ± 0.04	2.2	-0.03	e
F12D492	54.3645	-35.9629	0.90 ± 0.07	10.0 ± 4.1	19.7 ± 0.3	5.9 ± 1.4	1.0 ± 0.4	21.99 ± 0.12	21.03 ± 0.07	20.57 ± 0.05	20.38 ± 0.05	2.4	-0.03	e
F12D608	54.7168	-36.3010	0.89 ± 0.04	56.8 ± 2.5	20.8 ± 0.2	2.0 ± 0.4	1.1 ± 0.3	23.50 ± 0.05	22.39 ± 0.05	21.90 ± 0.04	21.71 ± 0.04	2.2	0.01	e
F13D004	55.0100	-37.9414	0.40 ± 0.08	-38.2 ± 4.6	21.1 ± 0.3	3.5 ± 0.9	0.4 ± 0.4	24.15 ± 0.07	23.54 ± 0.08	23.12 ± 0.07	22.88 ± 0.05	2.1	-0.02	l
F13D042	55.2303	-37.8376	0.62 ± 0.02	36.5 ± 1.4	15.7 ± 0.1	10.9 ± 1.4	1.1 ± 0.3	18.63 ± 0.04	17.25 ± 0.03	16.54 ± 0.03	16.24 ± 0.04	2.8	0.01	e
F13D044	54.4815	-37.8560	0.72 ± 0.05	-45.1 ± 3.0	17.6 ± 0.2	10.6 ± 2.1	1.0 ± 0.4	19.98 ± 0.04	19.20 ± 0.03	18.51 ± 0.03	18.15 ± 0.04	2.9	0.01	e
F13D054	55.1427	-37.8518	0.76 ± 0.04	45.0 ± 2.6	18.5 ± 0.2	6.1 ± 1.1	1.4 ± 0.3	21.18 ± 0.05	19.80 ± 0.03	19.34 ± 0.03	19.09 ± 0.04	3.1	0.01	e
F13D058	55.1262	-37.8280	0.38 ± 0.02	10.0 ± 1.2	16.2 ± 0.1	7.3 ± 0.8	1.4 ± 0.3	18.08 ± 0.04	17.43 ± 0.03	17.11 ± 0.03	16.95 ± 0.04	2.8	0.24	l
F13D074	54.2367	-37.8208	0.64 ± 0.08	-9.4 ± 4.6	18.8 ± 0.3	9.9 ± 2.6	0.7 ± 0.4	23.19 ± 0.11	20.52 ± 0.04	19.86 ± 0.03	19.44 ± 0.04	2.4	-0.00	e
F13D130	54.9101	-37.7097	0.95 ± 0.03	12.7 ± 1.9	19.5 ± 0.2	2.7 ± 0.4	1.3 ± 0.3	22.06 ± 0.05	21.01 ± 0.04	20.51 ± 0.03	20.30 ± 0.04	2.8	0.00	e
F13D162	55.0871	-37.6449	0.57 ± 0.05	88.4 ± 3.1	17.2 ± 0.2	13.8 ± 2.9	0.8 ± 0.4	20.39 ± 0.04	18.91 ± 0.03	18.23 ± 0.03	18.00 ± 0.04	2.5	0.00	e
F13D165	55.0854	-37.6441	0.58 ± 0.05	-88.3 ± 3.0	17.1 ± 0.2	13.6 ± 2.8	0.8 ± 0.4	20.13 ± 0.04	18.76 ± 0.03	18.06 ± 0.03	17.81 ± 0.04	2.5	0.04	e
F13D176	54.0200	-37.6152	0.86 ± 0.07	14.6 ± 4.0	20.3 ± 0.3	4.4 ± 1.1	0.8 ± 0.4	23.84 ± 0.10	21.81 ± 0.05	21.16 ± 0.04	20.97 ± 0.04	2.6	-0.04	e
F13D221	55.1205	-37.5228	0.66 ± 0.02	-53.6 ± 1.5	19.2 ± 0.1	2.3 ± 0.3	1.1 ± 0.3	22.11 ± 0.04	20.98 ± 0.03	20.35 ± 0.03	20.06 ± 0.04	2.6	0.01	e
F13D224	55.2271	-37.5166	0.91 ± 0.07	-63.7 ± 4.3	19.4 ± 0.3	7.1 ± 1.8	0.7 ± 0.4	23.54 ± 2.04	20.70 ± 0.16	20.14 ± 0.10	19.88 ± 0.08	2.4	-0.01	e*
F13D230	55.0774	-37.4994	0.45 ± 0.04	58.0 ± 2.7	17.9 ± 0.2	8.4 ± 1.6	0.9 ± 0.3	21.15 ± 0.04	19.68 ± 0.03	19.00 ± 0.03	18.69 ± 0.04	2.7	0.00	e
F13D258	55.1850	-37.4083	0.76 ± 0.02	-82.1 ± 1.6	16.4 ± 0.2	9.2 ± 1.3	0.8 ± 0.3	19.32 ± 0.04	18.01 ± 0.03	17.29 ± 0.03	17.02 ± 0.04	2.5	0.02	e
F13D284	54.1532	-37.3653	0.52 ± 0.06	-72.3 ± 3.7	19.4 ± 0.2	6.1 ± 1.4	0.8 ± 0.4	22.22 ± 0.04	21.01 ± 0.04	20.42 ± 0.03	20.12 ± 0.04	2.5	-0.00	e
F13D299	54.5557	-37.2899	0.88 ± 0.03	78.1 ± 2.1	14.7 ± 0.2	26.9 ± 4.3	1.3 ± 0.3	17.49 ± 0.04	16.11 ± 0.03	15.45 ± 0.03	14.73 ± 0.04	2.5	0.02	e(s)
...														

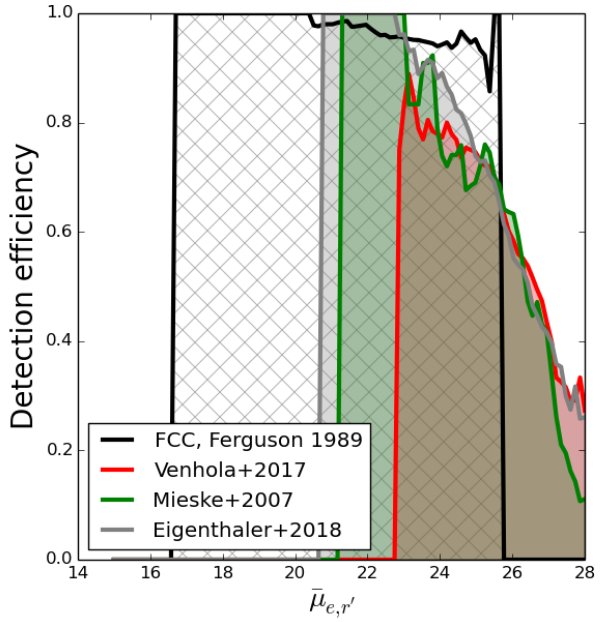

Figure 3.20: Completeness of the cluster galaxies with our detection algorithm compared to the previous Fornax samples. The black, red, green, and gray lines show the detection efficiency of our algorithm when compared with the galaxies from FCC, Venhola et al. (2017), Mieske et al. (2007), and Eigenthaler et al. (2018), respectively.

with other existing catalogs is in good agreement with the mock galaxy tests: at the LSB-end ($\bar{\mu}_{e,r} > 24$ mag arcsec^{-2}) the detection efficiency drops as a function of surface brightness reaching 50% completeness between $\bar{\mu}_{e,r} = 26$-27 mag arcsec^{-2}. Close to 100% completeness is obtained for the non-LSB galaxies.

Ten galaxies are classified as likely Fornax cluster members in the FCC, but not found with our detection method (see Fig. 3.21 for thumbnails): seven of these overlap with saturated stars and are therefore excluded due to the masks, and three were missed due to their low surface brightness. The number of missed galaxies due to the masking is consistent with our estimation in Section 5.2. In the case of FCC162 we could not detect any object in the location indicated in the FCC (see also Eigenthaler et al. 2018). The other two missing galaxies appear morphologically to be cluster members, and they will be included in the LSB extension of this catalog. We have not analyzed here in detail the differences in object detections between our catalog and the catalogs other than FCC, since possible differences are mostly due to our incompleteness at the LSB-end. Our next paper concentrating on the detection of LSB galaxies in the Fornax area

(Venhola et al., in prep.) will include a more detailed comparison with respect to completeness.

Figure 3.22 compares the total dwarf galaxy counts of FCC (Ferguson 1989) and our catalog as a function of the total galaxy magnitude. It is clear that our catalog extends three to four magnitudes deeper than FCC. The numbers of likely cluster members in the magnitude bins match well between the two catalogs, within the magnitude range where the FCC is complete ($m_{r'} \lesssim 18$ mag). FCC has slightly more cluster members in the two brightest bins due to its larger spatial extent.

The spectroscopically confirmed sample of Drinkwater et al. (2000) contains also compact galaxies that are not classified as likely cluster members in the FCC. These compact galaxies are ultra compact dwarf galaxies (UCDs) that have small sizes and high surface brightnesses. To test whether some of these galaxies should be in our catalog according to their size, but were excluded due to their high surface brightness, we cross-matched our initial detection lists with the objects of Drinkwater et al. We find that there are 93 objects in common. We visually checked these objects, and they all appear unresolved in our data, and due to the A_IMAGE > 2 arcsec selection limit are not in our catalog. We show examples of these objects in Fig. 3.23.

3.9.2 MAGNITUDES AND EFFECTIVE RADII

In the FCC, effective radii and magnitudes are defined from IIIa-J-bandbass photometric plates using growth curves, which could lead to a systematical difference compared to our r'-band measurements. However, a comparison with their parameter values can be used as a sanity check for the parameters obtained by us. To match the magnitude system with ours, we use the FCC magnitudes transformed to the B-band[13] as given by Ferguson (1989). To take into account the different photometric filters used in these works we transformed our g'-band magnitudes to the Johnson B-band using the transformation formula defined by Lupton (2005)[14], B = g' + 0.3130×(g'-r') + 0.2271.

The upper panels in Fig. 3.24 show the comparison between our effective radii and magnitudes, and the ones of FCC as a function of mean effective surface brightness for the 215 dwarf galaxies common between the studies. We find that the values agree well with small offsets, $\Delta(R_e(\mathrm{FCC})/R_e(\mathrm{FDS})) = -0.11$ and $\Delta(m_B(\mathrm{FCC})\text{-}m_{B*}(\mathrm{FDS})) = 0.01$ mag, and a relatively small scatter, $\sigma(R_e(\mathrm{FCC})/R_e(\mathrm{FDS})) = 0.18$ and $\sigma(m_B(\mathrm{FCC})\text{-}m_{B*}(\mathrm{FDS})) = 0.25$ mag that increases toward lower surface brightness. For the effective radii the offset likely results from FCC using a bluer filter and a different method when defining R_e, resulting to slightly smaller values as they miss light in the outskirts of the galaxies. As FCC uses magnitudes based on growth curves they miss an increasing fraction of galaxies' light with decreasing surface brightness. This appears as

[13] We also applied the correction that is required to transform the magnitudes measured from photometric plates into CCD magnitudes: B_{CCD}=1.10*B_{photo}-1.37, defined by Ferguson (1989) when the FCC magnitudes were compared to the ones by Caldwell & Bothun (1987).

[14] From the SDSS website `http://www.sdss3.org/dr8/algorithms/sdssUBVRITransform.php`

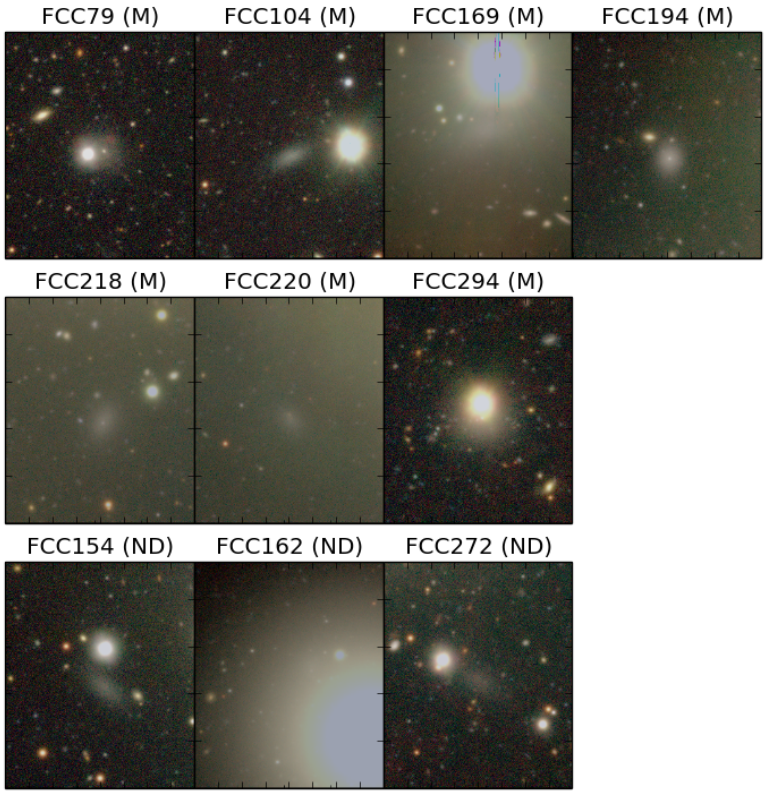

Figure 3.21: i', r', g',- color composite images of the FCC galaxies that are missing from our catalog since they are either located under the masks that were used to exclude objects in the areas contaminated by bright stars, or were not detected. After each object's name we indicate if the object was excluded due to the masks (M) or was not detected (ND).

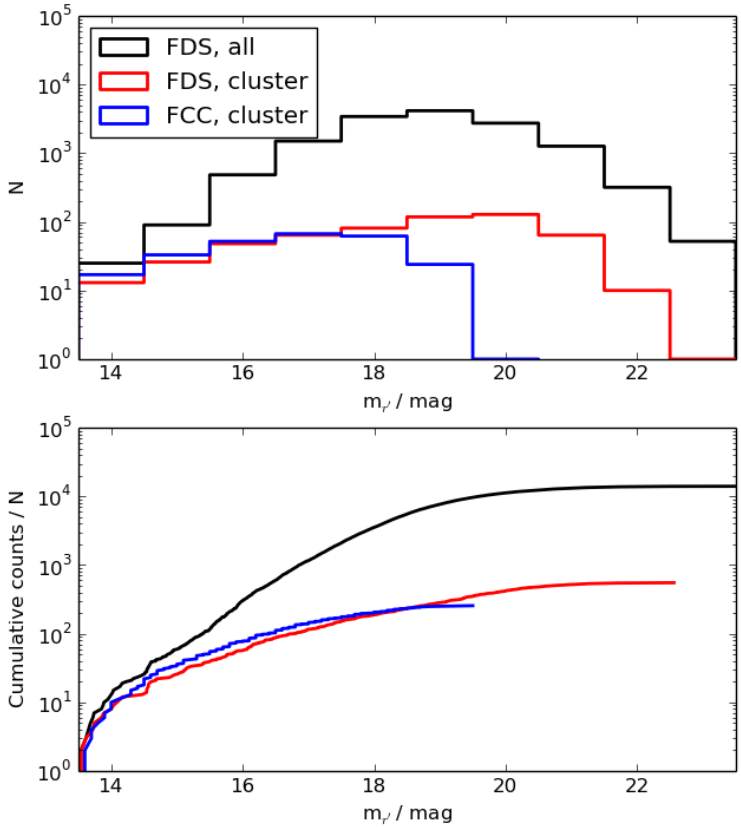

Figure 3.22: Upper panel: Distribution of the apparent r'-band magnitudes of in FCC (the blue histogram), compared to the ones detected in this work. We show the distribution of the galaxies classified as likely cluster dwarfs with the red histogram and the one of the likely background galaxies with the black histogram. Lower panel: Same distributions in a cumulative profile. The FCC magnitudes are transformed from the B-band to r'-band using the mean color difference of $\langle B - r' \rangle = 1$ mag defined comparing our values with the ones of FCC.

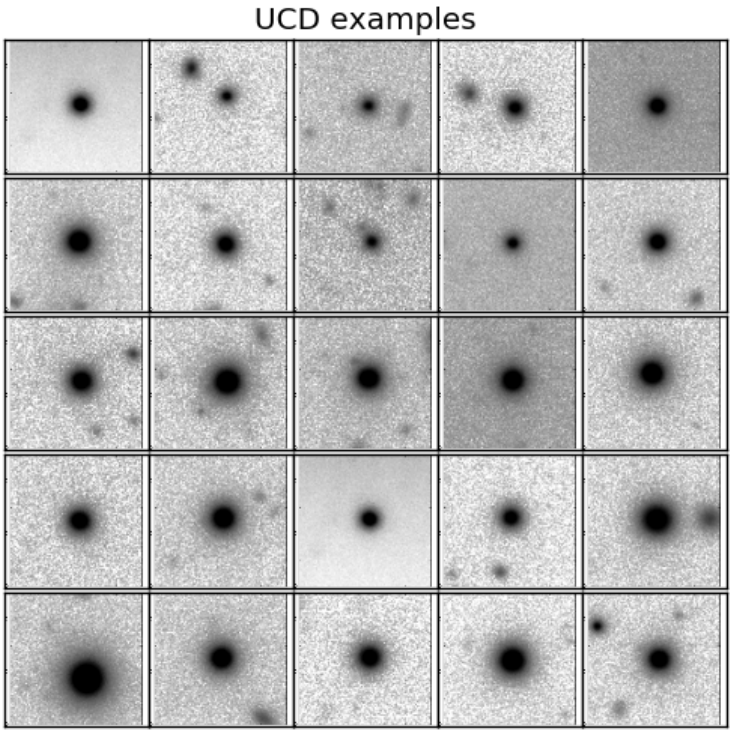

Figure 3.23: r'-band images of UCD galaxies in Fornax, for which the cluster membership has been confirmed with spectroscopic redshifts of Drinkwater et al. (2000), but which do not appear in our catalog due to the selection limit related to size. The size of the postage stamp images is 20 arcsec $\times$ 20 arcsec.

an increasing difference in the apparent magnitude toward the lower luminosity galaxies, between the two studies.

To avoid the caveats included in the filter transformations and methodological differences in the measurements of the magnitudes and effective radii, we also compare our values with the DECAM g'-band magnitudes of Eigenthaler et al. (2018) for the 160 dwarf galaxies common between the works. Eigenthaler et al. use also GALFIT to fit Sérsic profiles to the 2D-light distribution of the galaxies in g'-band, similarly to us. We show the comparisons in the second row panels of Fig. 3.24 for the galaxies common in these studies. This comparison gives the offsets of $\Delta(R_e(\mathrm{NGFS})/R_e(\mathrm{FDS})) = 0.02$ and $\Delta(m_g(\mathrm{NGFS})\text{-}m_g(\mathrm{FDS})) = -0.33$ mag, and scatters of $\sigma(R_e(\mathrm{NGFS})/R_e(\mathrm{FDS})) = 0.12$ and $\sigma(m_g(\mathrm{NGFS})\text{-}m_g)(\mathrm{FDS})) = 0.23$ mag. The observed offset in the magnitudes is surprising given the very good agreement between the effective radii of these two samples. If we neglected the offset, the magnitudes are in good agreement.

To confirm that the observed offset with the NGFS galaxies is not due to a bias in our data we also show a comparison with the magnitudes of Mieske et al. (2007) for the 52 galaxies common in the studies. Their V-band magnitudes, based on the curve of growth analysis, were transformed to g'-band using the transformations given in Appendix 3.12.3. The magnitudes are in agreement but a slight trend is apparent toward low surface brightness end, so that their magnitudes become fainter than ours.

These tests show that our effective radii and magnitudes are in good agreement with the other Fornax galaxy samples in the literature, with the exception of the magnitudes of Eigenthaler et al. which are significantly offset. Since we did not observe such an offset in the photometric quality assessments of our data (Section 4.2), GALFIT model quality assessments (Section 7.2.3), nor in comparison with other samples, we conclude that most probably this offset is due to a bias in the calibration of Eigenthaler et al..

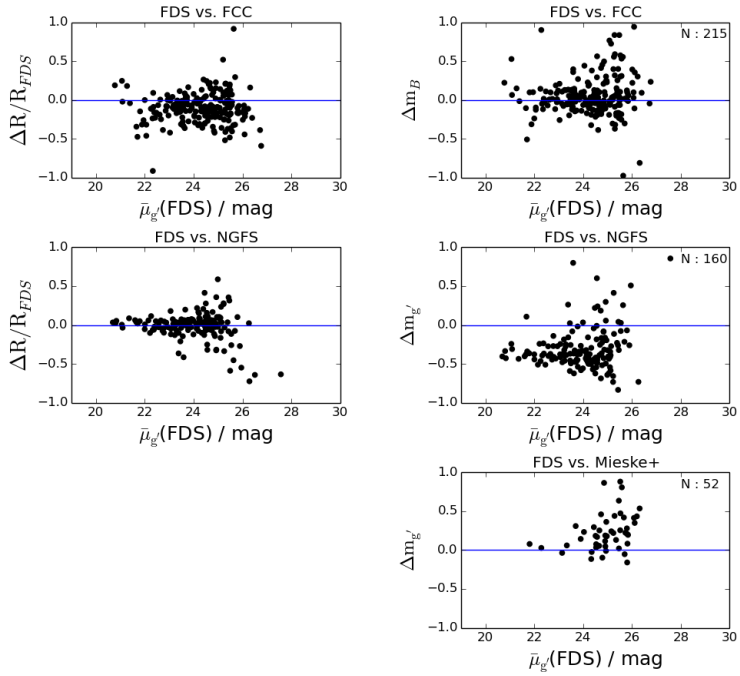

Figure 3.24: Effective radii (R_e, *left panels*) and apparent magnitudes ($m_{B/g'}$, *right panels*) of the galaxies obtained in this work are compared to those given in FCC, NGFS (Eigenthaler et al. 2018), and Mieske et al. (2007), from the top to bottom rows, respectively, using the galaxies common in the studies. The differences are with respect to FDS values, i.e., $\Delta X = X_{FDS} - X_{Ref.}$. The x-axis shows the mean effective surface brightness ($\bar{\mu}_{e,g'}$) of the galaxies, and the blue lines show the zero offsets. Mieske et al. (2007) does not include effective radii for the galaxies, and therefore the comparison is not shown. The number of galaxies in common between the studies are marked into the upper right corners of the right-side panels.

3.9.3 ASSESSMENT OF THE GALAXY COLORS

In Section 4.2, we quantify the uncertainty associated with the photometric calibration of our data. In addition to that, we also test the galaxy colors for possible biases when compared with other samples. The color-magnitude relation of early-type cluster galaxies, in other words the red sequence (RS), shows only minor variations between the different nearby clusters (Hamraz et al. 2018) and a comparison with those relations can be therefore used as a sanity check for the obtained colors. Here we make the comparisons just for the sake of assessing the colors for possible off-sets. A more detailed analysis with a physical interpretation will follow in the upcoming paper (Venhola et al., in prep.).

Due to a lack of other samples in the Fornax cluster, except for the one of the NGFS that has an offset in the g'-band magnitudes with respect to our sample, and Mieske et al. (2007) that uses V-I colors, we also include works for the Virgo cluster into our comparison. Roediger et al. (2017) have measured the colors of the RS in the core parts of the Virgo cluster with MegaCAM in a luminosity range similar to this work. As Roediger et al. use MegaCAM filters that differ from the SDSS filters, we transformed their colors into the SDSS system using the transformations given in Appendix 3.12.3. We also make comparisons with the work of Janz & Lisker (2009) who measure the RS within a larger area in the Virgo cluster using the SDSS filters, but have a smaller luminosity range. To match the sample of Janz et al. with the other samples, we select only their galaxies from the same area as Roediger et al. For the comparison within the Fornax cluster, we use those of Eigenthaler et al. (2018) (see previous subsection for details) and Mieske et al. (2007), of which the latter measure V-I colors that we have transformed to g'-i' colors using the transformation formulas shown in Appendix 3.12.3.

In Fig. 3.25, we show the color-magnitude relation of the early-type galaxies. To match the samples of NGFS and NGVS, we selected only the galaxies located within 1.4 deg (corresponding to two core radii) from the center of the cluster. We find that there are offsets with respect to the sample of Eigenthaler et al. in the u'-r' and u'-g' colors, so that their colors are significantly bluer by 0.3-0.4 mag. When compared with the samples of Mieske et al. or Roediger et al., there are no such offsets. When compared with Janz et al., a small offset appears in the colors of the brightest dwarfs so that their colors are slightly bluer, but since the colors are otherwise very similar this difference is likely explained by the small number of galaxies in that luminosity range.

As a conclusion, our galaxy colors are in good agreement with the previous measurements done in the Virgo and Fornax clusters, except with the sample of Eigenthaler et al. As the galaxy colors are measured similarly in these two samples, using the same filters and there are no significant differences in the measured effective radii, the difference in the colors is likely be due to a calibration bias in the sample of Eigenthaler et al.

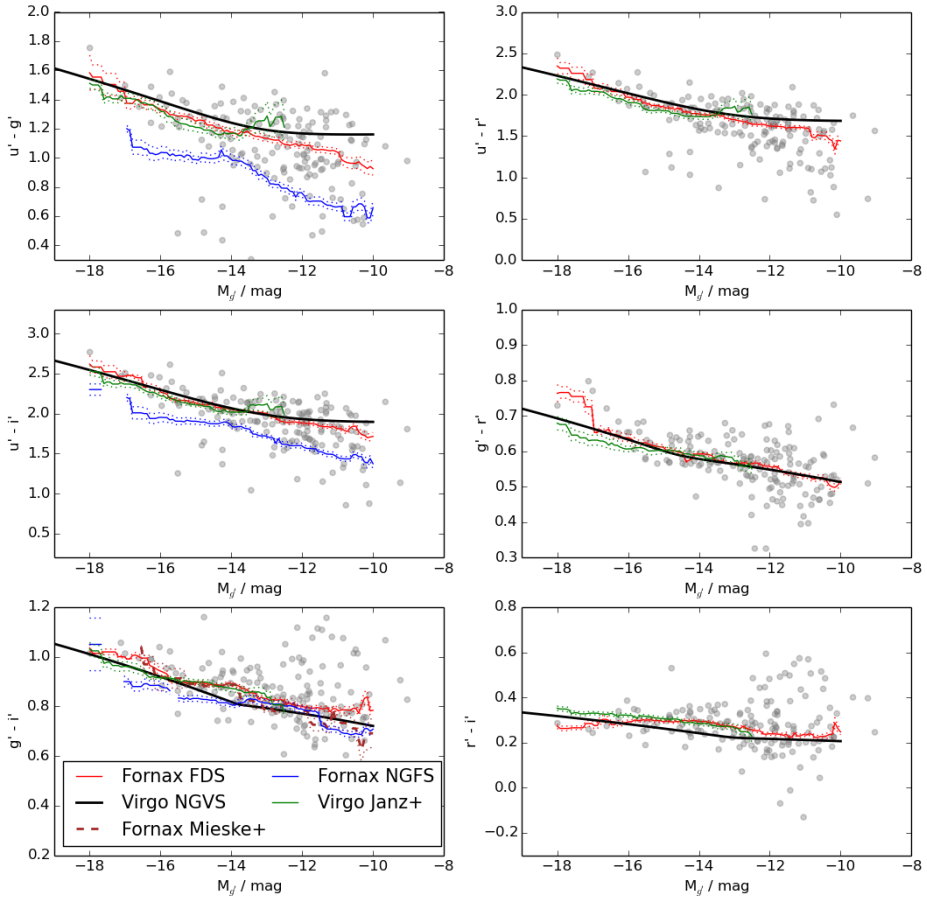

Figure 3.25: Color-magnitude relations of the early-type galaxies in our sample, within two core radii from the cluster center, are shown with the gray dots. The solid red lines show the running means of the colors measured with an interval of $\Delta M_{g'} = 1$ mag, and the red dotted lines show the uncertainty of the mean. The blue solid line, the brown dashed line, and the green solid line show similarly the samples of NGFS (Eigenthaler et al. 2018), Mieske et al. (2007), and Janz & Lisker (2009), respectively. The solid black lines show the color-magnitude relations of the Virgo early-type dwarf galaxies by Roediger et al. (2017).

3.9.4 PARAMETRIC SELECTION ACCURACY AND CONTAMINATION FROM THE BACKGROUND OBJECTS

In Section 8.2 above, we apply the parametric cuts to separate most of the background galaxies from the cluster galaxies. To understand the number of possible background galaxies that remain in the sample after applying the parametric selection cuts, we compared our classifications (cluster member or background galaxy) with the objects that have spectroscopic redshifts in Drinkwater et al. (2000).

In their sample there are 53 cluster galaxies that are not UCDs and 1782 background galaxies, that are also present in our list of detections. We find that only two of the 53 cluster galaxies with known redshifts are excluded from our sample. On the other hand, 194 background galaxies of the original 1782 spectroscopically confirmed background objects remain in our sample after the initial cuts.

After the initial parametric selection of cluster galaxies, we made a visual morphological classification (Section 8.3) to further exclude background galaxies that remained in our sample. We find that all the spectroscopically confirmed cluster galaxies that remained in our sample after the initial cuts, were correctly associated as cluster members according to our morphological classifications. Conversely, of the 194 spectroscopically confirmed background galaxies that remained after applying our cuts, eight were erroneously associated as cluster galaxies by us. We then also removed these eight galaxies from our catalog.

In summary, we find that, using our method (including the initial cuts and morphological classifications of the remaining objects), among the galaxies with spectroscopic redshifts there is a 96.2±2.7% ($\frac{53-2}{53}$) chance for a cluster galaxy to be classified as such. For a background galaxy, we get a 99.6±0.2% ($\frac{1782-8}{1782}$) chance for it to be classified as a background galaxy.

If we assume that the classification accuracy holds also for the galaxies without spectroscopic redshifts, we can estimate the number of possibly erroneously classified background galaxies using our method. However, this estimation probably overestimates the contamination, because in the low-luminosity end the cluster galaxies have low surface brightnesses and they are relatively blue, which makes it easier to separate them from the background objects. We have 14,095 galaxies in our sample, of which 564 galaxies are classified as cluster dwarf galaxies and 13,505 as background galaxies. With our accuracy of 99.6% ± 0.2% that corresponds to ≈ 30–80 false positives corresponding to ≈10% of our final cluster dwarf sample identifications.

3.9.5 CLUSTER MEMBERSHIP CLASSIFICATIONS COMPARED TO EIGENTHALER

Eigenthaler et al. (2018) also use morphological classifications for separating cluster and background galaxies. Since they do not provide a list of background galaxies, here we inspect only the galaxies that have been classified as background galaxies by us and as cluster members by them.

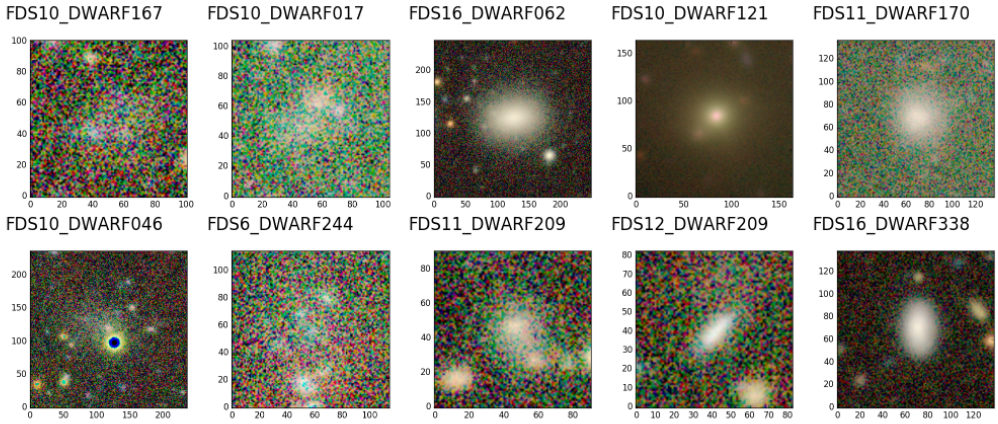

Figure 3.26: Post-stamp images of the galaxies classified as likely cluster members by Eigenthaler et al. (2018) but classified by us as being likely background galaxies.

Two known cluster galaxies were falsely classified as background objects by us when the parametric selection cuts were applied (see Fig. 3.16). These two galaxies are included in the sample of Eigenthaler. Other than that, there are ten galaxies in their sample that we classified as background galaxies according to morphology. These galaxies are shown in Fig. 3.26. As seen from Fig. 3.26 these galaxies are either very small and very faint or show weak central components. From the photometric data alone it is impossible to robustly decide possible cluster membership of these objects. As so few objects of these samples were classified differently, we conclude that the cluster membership classifications of these samples are very similar.

3.9.6 COMPARISON OF OUR MORPHOLOGICAL CLASSIFICATIONS WITH FCC

We also compared the consistency between the morphological classifications of Ferguson (1989) and ours. Ferguson uses the full de Vaucouleurs' classification system instead of our simple division into early and late-type galaxies. In our division, dE's, S0's and E's are early-type galaxies whereas S(B)a/b/c/d's, ImV's, and BCD's are late-type systems. Ferguson has many galaxies that have uncertain classifications, which we have not included in our comparison.

As a result, of the 190 early-type galaxies in FCC we classified 188 as early-types, and two as late-types. The two galaxies with differing classifications (FDS22DWARF244/FCC46 and FDS16DWARF000/FCC148) are both dominated by reddish spheroid component in their outer parts, but have embedded bluish disks. Their colors within the effective radii are also clearly bluer than the ones of the red sequence galaxies. These galaxies clearly have properties of both late-type and early-type galaxies. Since they have signs of recent or ongoing star formation

in their central parts we classify them as late types, consistently with BCDs. We also classified all the 15 late-types in the classification of Ferguson as late-types.

3.10 SUMMARY AND CONCLUSIONS

Optical data covering 26 deg^2 area in the Fornax cluster and the Fornax A subgroup were obtained using the OmegaCAM instrument, attached to the VLT Survey Telescope, located at Cerro Paranal in Chile. A new dwarf galaxy catalog was created, which goes three magnitudes deeper than the previous most complete Fornax cluster catalog (Ferguson 1989). The 26 deg^2 area is fully covered in g', r', and i' -bands, and a 20 deg^2 area of the main cluster was also covered in u'-band. In this paper we present the observations, data reduction, and the quality assessment of the data. We also present a galaxy detection algorithm and photometric pipeline, which were tested and used to create the dwarf galaxy catalog. We first used colors, concentration, and surface brightness to select the likely Fornax cluster galaxies. We classified the selected galaxies into different classes using visual and parametric morphological classifications. Our main results are:

- We generated a new catalog of the resolved galaxies for the 26 deg^2 area in the Fornax cluster. The catalog includes 14,095 galaxies. It reaches 50% completeness limits at major axis length $a > 2$ arcsec, total r'-band apparent magnitude 13 mag $< m_{r'} <$ 21.1 mag (corresponding to -18.5 mag $< M_{r'} <$ -10.5 mag at the distance of the Fornax cluster), and at the mean effective surface brightness $\bar{\mu}_{r'} < 26$ mag arcsec^{-2}.

- We used GALFIT to fit all the galaxies in the catalog using either a single Sérsic function or a Sérsic function with an additional *PSF* component as a nucleus. We used mock galaxies to define the uncertainties in the parameters obtained with these models. The photometric parameters of all 14,095 galaxies are given in electronic form.

- We used cuts in the color-magnitude, luminosity-surface brightness, and luminosity-concentration relations to separate cluster galaxies from the background objects. We then inspected the selected likely cluster galaxies, and classified them according to their visual morphology and morphological parameters. As a result we classify 13,505 galaxies as likely background galaxies and 564 dwarf galaxies as likely cluster members. Of the cluster members 470 galaxies are early-type, and 94 late-type systems. Additionally there are 22 cluster galaxies that are not dwarfs and are not therefore included int our catalogs.

- We compared the galaxies in our catalog with literature, and found that the cluster membership and morphological classifications are consistent with the previous works in the Fornax cluster. 10 galaxies of the FCC within the FDS area are missing from our catalog due to known selection effects, but in general our catalog extends three magnitudes deeper than the FCC.

- Extrapolating from the spectroscopic redshift samples in the bright luminosity regime of our sample, we estimate that we are able to obtain the correct separation between the cluster members and background galaxies with a 0.4% probability of assigning a true background galaxy to the cluster sample and 96.2% for real cluster galaxies. This implies a background galaxy contamination rate of $\approx$ 10% in our final cluster dwarf galaxy sample.

- We compared our photometric parameters with the works of Ferguson (1989), Eigenthaler et al. (2018), and Mieske et al. (2007) and find good agreement for the effective radii and magnitudes, with the exception of comparison with Eigenthaler et al, where we find an offset of 0.3 mag between their and our g'-band magnitudes.

- We assessed the quality of our galaxy colors by comparing them with other samples in the Fornax and Virgo clusters. We showed that our colors are in a good agreement with other previous works. We report and offset between the u'-g' and u'-i' colors of ours and the ones of Eigenthaler et al. (2018).

In summary, together with the catalogs of Iodice et al. (2018) containing massive Fornax cluster galaxies, and Venhola et al. (2017, and in prep.) containing the low surface brightness galaxies, our catalog comprises a complete set of resolved galaxies in the Fornax cluster.

Acknowledgements : A.V. would like to thank the Vilho, Yrjö, and Kalle Väisälä Foundation of the Finnish Academy of Science and Letters for the financial support during the writing of this paper. GvdV acknowledges funding from the European Research Council (ERC) under the European Union's Horizon 2020 research and innovation program under grant agreement No 724857 (Consolidator Grant ArcheoDyn). R.F.P., T.L., E.L., H.S., E.I., and J.J. acknowledge financial support from the European Union's Horizon 2020 research and innovation program under the Marie Skłodowska-Curie grant agreement No. 721463 to the SUNDIAL ITN network. H.S. and E.L. are also supported by the Academy of Finland grant n:o 297738. C.W. is supported by the Deutsche Forschungsgemeinschaft (DFG, German Research Foundation) through project 394551440.

3.11 References

Alam, S., Albareti, F. D., Allende Prieto, C., et al. 2015, ApJS, 219, 12

Bender, R., Kormendy, J., Bower, G., et al. 2005, ApJ, 631, 280

Bertin, E. 2006, in Astronomical Society of the Pacific Conference Series, Vol. 351, Astronomical Data Analysis Software and Systems XV, ed. C. Gabriel, C. Arviset, D. Ponz, & S. Enrique, 112

Bertin, E. 2010, SWarp: Resampling and Co-adding FITS Images Together, Astrophysics Source Code Library

Bertin, E. & Arnouts, S. 1996, A&AS, 117, 393

Bilicki, M., Hoekstra, H., Brown, M. J. I., et al. 2018, A&A, 616, A69

Binggeli, B., Sandage, A., & Tammann, G. A. 1985, AJ, 90, 1681

Binggeli, B., Sandage, A., & Tarenghi, M. 1984, AJ, 89, 64

Blakeslee, J. P., Holden, B. P., Franx, M., et al. 2006, ApJ, 644, 30

Blakeslee, J. P., Jordán, A., Mei, S., et al. 2009, ApJ, 694, 556

Bonnarel, F., Fernique, P., Bienaymé, O., et al. 2000, A&AS, 143, 33

Boylan-Kolchin, M., Springel, V., White, S. D. M., Jenkins, A., & Lemson, G. 2009, MNRAS, 398, 1150

Brodie, J. P., Romanowsky, A. J., Strader, J., & Forbes, D. A. 2011, AJ, 142, 199

Caldwell, N. & Bothun, G. D. 1987, AJ, 94, 1126

Cantiello, M., D'Abrusco, R., Spavone, M., et al. 2018, A&A, 611, A93

Capaccioli, M., Spavone, M., Grado, A., et al. 2015, A&A, 581, A10

Conselice, C. J. 2014, ARA&A, 52, 291

Conselice, C. J., Gallagher, III, J. S., & Wyse, R. F. G. 2003, AJ, 125, 66

Côté, P., Piatek, S., Ferrarese, L., et al. 2006, ApJS, 165, 57

Cutri, R. M., Skrutskie, M. F., van Dyk, S., et al. 2003, VizieR Online Data Catalog, 2246

D'Abrusco, R., Cantiello, M., Paolillo, M., et al. 2016, ApJ, 819, L31

Dressler, A. 1980, ApJ, 236, 351

Dressler, A., Bigelow, B., Hare, T., et al. 2011, PASP, 123, 288

Drinkwater, M. J., Gregg, M. D., & Colless, M. 2001, ApJ, 548, L139

Drinkwater, M. J., Phillipps, S., & Jones, J. B. 1999, in Astronomical Society of the Pacific Conference Series, Vol. 170, The Low Surface Brightness Universe, ed. J. I. Davies, C. Impey, & S. Phillips, 120

Drinkwater, M. J., Phillipps, S., Jones, J. B., et al. 2000, A&A, 355, 900

Eigenthaler, P., Puzia, T. H., Taylor, M. A., et al. 2018, ApJ, 855, 142

Ferguson, H. C. 1989, AJ, 98, 367

Ferrarese, L., Côté, P., Cuillandre, J.-C., et al. 2012, ApJS, 200, 4

Hamraz, E., Peletier, R. F., Khosroshahi, H. G., Valentijn, E. A. amd den Brok, M., & Venhola, A. 2018, MNRAS

Henden, A. A., Levine, S. E., Terrell, D., Smith, T. C., & Welch, D. 2012, Journal of the American Association of Variable Star Observers (JAAVSO), 40, 430

Hilker, M., Mieske, S., & Infante, L. 2003, A&A, 397, L9

Hoyos, C., den Brok, M., Verdoes Kleijn, G., et al. 2011, MNRAS, 411, 2439

Huchra, J. P., Macri, L. M., Masters, K. L., et al. 2012, ApJS, 199, 26

Iodice, E., Capaccioli, M., Grado, A., et al. 2016, ApJ, 820, 42

Iodice, E., Spavone, M., Cantiello, M., et al. 2017a, ApJ, 851, 75

Iodice, E., Spavone, M., Capaccioli, M., et al. 2017b, ApJ, 839, 21

Iodice, E., Spavone, M., Capaccioli, M., et al. 2018, arXiv e-prints [arXiv:1812.01050]

Ivezić, Ž., Lupton, R. H., Schlegel, D., et al. 2004, Astronomische Nachrichten, 325, 583

Jaffé, Y. L., Poggianti, B. M., Moretti, A., et al. 2018, MNRAS, 476, 4753

Janz, J., Laurikainen, E., Lisker, T., et al. 2014, ApJ, 786, 105

Janz, J. & Lisker, T. 2009, ApJ, 696, L102

Jordán, A., Blakeslee, J. P., Côté, P., et al. 2007, ApJS, 169, 213

Jordi, K., Grebel, E. K., & Ammon, K. 2006, A&A, 460, 339

Kron, R. G. 1980, ApJS, 43, 305

Kuijken, K., Bender, R., Cappellaro, E., et al. 2002, The Messenger, 110, 15

Landolt, A. U. 1992, AJ, 104, 340

Lauer, T. R., Ajhar, E. A., Byun, Y.-I., et al. 1995, AJ, 110, 2622

Lisker, T., Glatt, K., Westera, P., & Grebel, E. K. 2006, AJ, 132, 2432

Mieske, S., Hilker, M., Infante, L., & Mendes de Oliveira, C. 2007, A&A, 463, 503

Misgeld, I. & Hilker, M. 2011, MNRAS, 414, 3699

Misgeld, I., Hilker, M., & Mieske, S. 2009, A&A, 496, 683

Moffat, A. F. J. 1969, A&A, 3, 455

Muñoz, R. P., Eigenthaler, P., Puzia, T. H., et al. 2015, ApJ, 813, L15

Nasonova, O. G., de Freitas Pacheco, J. A., & Karachentsev, I. D. 2011, A&A, 532, A104

Ordenes-Briceño, Y., Eigenthaler, P., Taylor, M. A., et al. 2018, ApJ, 859, 52

Paolillo, M., Fabbiano, G., Peres, G., & Kim, D.-W. 2002, ApJ, 565, 883

Peng, C. Y., Ho, L. C., Impey, C. D., & Rix, H.-W. 2002, AJ, 124, 266

Peng, Y.-j., Lilly, S. J., Renzini, A., & Carollo, M. 2012, ApJ, 757, 4

Peng, Y.-j., Lilly, S. J., Renzini, A., & Carollo, M. 2014, ApJ, 790, 95

Penny, S. J. & Conselice, C. J. 2008, MNRAS, 383, 247

Pillepich, A., Springel, V., Nelson, D., et al. 2018, MNRAS, 473, 4077

Pota, V., Napolitano, N. R., Hilker, M., et al. 2018, MNRAS[arXiv:1803.03275]

Price, J., Phillipps, S., Huxor, A., et al. 2009, MNRAS, 397, 1816

Roediger, J. C., Ferrarese, L., Côté, P., et al. 2017, ApJ, 836, 120

Salo, H., Laurikainen, E., Laine, J., et al. 2015, ApJS, 219, 4

Sandin, C. 2014, A&A, 567, A97

Schipani, P., Capaccioli, M., Arcidiacono, C., et al. 2012, in Proc. SPIE, Vol. 8444, Ground-based and Airborne Telescopes IV, 84441C

Schlafly, E. F. & Finkbeiner, D. P. 2011, ApJ, 737, 103

Spavone, M., Capaccioli, M., Napolitano, N. R., et al. 2017, A&A, 603, A38

Spiniello, C., Napolitano, N. R., Arnaboldi, M., et al. 2018, MNRAS, 477, 1880

Sutherland, W., Emerson, J., Dalton, G., et al. 2015, A&A, 575, A25

Trentham, N. & Tully, R. B. 2009, MNRAS, 398, 722

Trujillo, I., Aguerri, J. A. L., Cepa, J., & Gutiérrez, C. M. 2001, MNRAS, 328, 977

Vandame, B. 2001, in Mining the Sky, ed. A. J. Banday, S. Zaroubi, & M. Bartelmann, 595

Table 3.5: Image quality of the FDS fields. The first column gives the name of the field, the four next columns give the mean $FWHM$ and RMS of the $FWHM$ within the field in the different bands, and the four last columns show the surface brightness corresponding to 1σ S/N per pixel for a given field in the different photometric bands.

	$FWHM \pm \sigma_{FWHM}$ / arcsec				depth / mag arcsec^{-2}			
field	u'	g'	r'	i'	u'	g'	r'	i'
Field1	1.17±0.09	1.35±0.09	1.14±0.15	0.69±0.07	25.16	26.76	26.05	25.24
Field2	1.21±0.04	1.11±0.07	0.90±0.07	0.79±0.08	25.14	26.60	26.03	25.00
Field4	1.18±0.11	1.39±0.05	1.19±0.12	0.70±0.07	25.20	26.70	26.01	25.26
Field5	1.33±0.07	1.15±0.10	1.39±0.14	1.08±0.15	25.58	26.79	26.10	25.22
Field6	1.11±0.05	0.84±0.08	1.08±0.08	1.21±0.12	25.68	26.72	25.98	25.07
Field7	1.04±0.05	0.83±0.10	0.95±0.09	1.42±0.11	25.55	26.81	26.06	24.87
Field9	1.38±0.07	1.20±0.08	0.97±0.09	0.84±0.08	25.30	26.83	26.15	25.37
Field10	1.34±0.05	1.15±0.04	1.02±0.12	1.09±0.07	25.66	26.77	26.16	25.24
Field11	1.27±0.05	1.06±0.12	1.09±0.11	1.15±0.06	25.25	26.51	26.02	25.04
Field12	1.15±0.06	0.83±0.10	1.04±0.10	1.17±0.10	25.69	26.74	26.09	25.04
Field13	1.10±0.05	0.91±0.06	1.03±0.06	1.16±0.07	25.39	26.83	26.14	25.44
Field14	1.34±0.06	1.18±0.08	0.96±0.09	0.86±0.07	25.28	26.70	26.00	25.29
Field15	1.30±0.04	1.13±0.05	0.90±0.07	0.97±0.06	25.37	26.60	26.14	25.12
Field16	1.31±0.04	1.26±0.07	0.94±0.08	1.08±0.09	25.52	26.68	26.09	25.21
Field17	1.27±0.04	1.11±0.12	0.87±0.08	1.01±0.08	25.35	26.54	26.21	25.17
Field18	1.11±0.06	0.95±0.08	1.03±0.09	1.12±0.11	25.33	26.79	26.17	25.43
Field19	1.26±0.04	1.14±0.13	0.89±0.07	0.87±0.08	25.25	26.70	26.14	25.23
Field20	1.30±0.06	1.22±0.07	0.95±0.09	1.08±0.07	25.29	26.46	26.06	25.04
Field21	1.22±0.05	1.12±0.06	0.78±0.05	0.88±0.07	25.13	26.51	25.84	25.28
Field22	-±-	1.04±0.07	0.81±0.05	0.85±0.07	-	26.52	25.90	25.16
Field25	-±-	1.11±0.10	0.77±0.06	0.85±0.07	-	26.63	25.84	25.11
Field26	-±-	0.93±0.07	0.81±0.05	0.91±0.07	-	25.89	25.96	25.06
Field27	-±-	1.07±0.10	0.78±0.06	0.89±0.10	-	26.39	25.63	24.88
Field28	-±-	1.08±0.14	0.79±0.09	0.92±0.09	-	26.31	25.57	24.89
Field31	1.33±0.05	1.22±0.13	1.00±0.08	0.86±0.08	25.11	26.58	25.86	24.98
Field33	-±-	1.09±0.07	0.84±0.07	0.83±0.13	-	26.40	25.74	24.80

Venhola, A., Peletier, R., Laurikainen, E., et al. 2017, A&A, 608, A142

Verdoes Kleijn, G. A., Kuijken, K. H., Valentijn, E. A., et al. 2013, Experimental Astronomy, 35, 103

Watson, M. G., Schröder, A. C., Fyfe, D., et al. 2009, A&A, 493, 339

Waugh, M., Drinkwater, M. J., Webster, R. L., et al. 2002, MNRAS, 337, 641

3.12 Appendix

3.12.1 Quality of the FDS fields

We give the quality parameters of all the FDS fields in Table 3.5. The tests made to obtain the parameters are described in Sections 4.1 and 4.3. We also give the parameters of the *PSF* models (Section 5.1) we used for all the fields in Table 3.6.

3.12.2 Quantitative test for the effects of the redshift on the morphological and structural parameters

To test how the increasing redshift changes the measured parameters of the galaxies, we selected a group of spectroscopically confirmed Fornax cluster galaxies with different morphological classes and artificially put them to different distances. We first rebinned the images by a factor of $z/0.005$ (Fornax cluster

is located at the redshift of 0.005) and then convolved the data with the OmegaCAM's *PSF*. Since the convolution reduces the pixel noise in the images, we empirically tested how much the noise is reduced, and added the required amount of noise to match the image quality with the one of the original data.

In Fig. 3.27 we use the photometric parameters (R_e, μ_e, RFF and C) to show how the galaxies move in the magnitude - photometric parameter space, as a function of redshift. As expected, the r'-band apparent magnitude (m_r) and the effective radius (R_e) decrease, and the surface brightness (μ_e) stays almost constant with increasing redshift. The upper right panel in Fig. 3.27 shows that there is not much contamination expected from the background galaxies fainter than $\bar{\mu}_{e,r'} > 23$ mag / arcsec^{-2}. For the galaxies brighter than that, contamination is expected since the parameters of the redshifted galaxies overlap with the cluster galaxies. The two lower panels in the right side show that the RFF and C parameters are also affected by redshift. This can be explained by *PSF* effects, as the relative size of the *PSF* compared to the angular size of the galaxies increases and thus blurs the structures in the galaxies. Regardless of the redshift dependence, the different morphological types can still be clearly separated at the different redshifts using the RFF and C.

3.12.3 FILTER TRANSFORMATIONS

To transform the MegaCAM filters into the SDSS filters we used the following formula provided at the MegaCAM web pages (`http://www1.cadc-ccda.hia-iha.nrc-cnrc.gc.ca/community/CFHTLS-SG/docs/extra/filters.html`):

$$\begin{aligned} u_{Mega} &= u' - 0.241(u' - g') \\ g_{Mega} &= g' - 0.153(g' - r') \\ r_{Mega} &= r' - 0.024(g' - r') \\ i_{Mega} &= i' - 0.085(r' - i'), \end{aligned} \tag{3.11}$$

where x_{Mega} correspond to MegaCAM magnitudes and x' correspond to SDSS magnitudes.

To transform the V-I colors into g'-i' colors, we used the transformations of Jordi et al. (2006)

$$V - I = (0.671 \pm 0.002) * (g' - i') + (0.359 \pm 0.002) \tag{3.12}$$

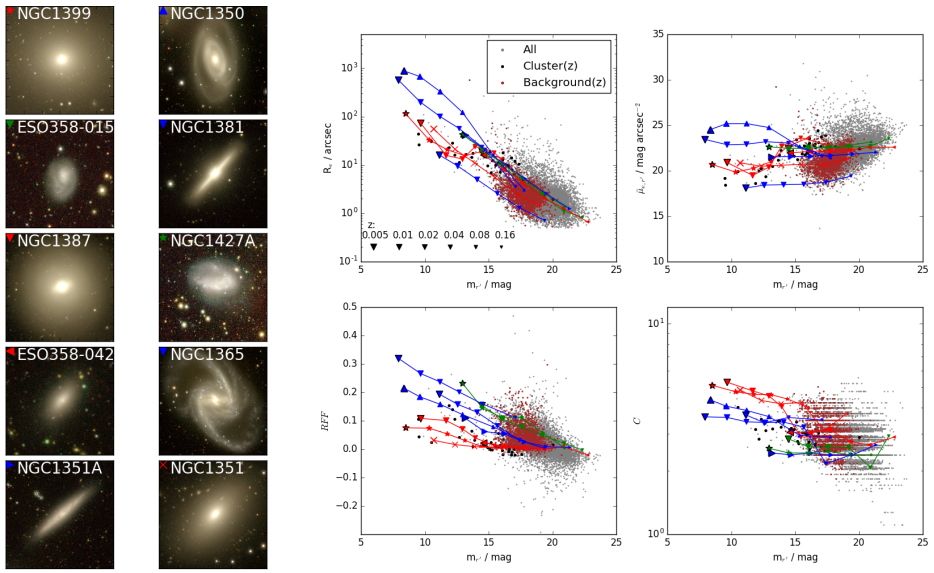

Figure 3.27: Effect of redshift on the photometric parameters of the galaxies. As a function of galaxy magnitude ($m_{r'}$), shown are the effective radius (R_e), the mean effective surface brightness ($\bar{\mu}_{e,r'}$), the Residual Flux Fraction (RFF), and the concentration parameter (C). The galaxies in the images on the left are presented in the right-side panels with the symbols shown in the upper left corner of the images. The different symbol sizes in the panels correspond to the different redshifts, as indicated in the upper left panel. The gray points in the panels correspond to all the galaxies in our sample, with the spectroscopically confirmed cluster and background galaxies indicated with the black and red filled circles, respectively. This figure is best viewed on-screen.

Table 3.6: Parameters of the inner *PSF* fits for each field. The first column gives the number of the field, the next five columns give the parameters of the g'-band fit, and the next five columns for the r'-band fit. The fitted parameters are defined in Eq. 3.5. α and σ are in arcseconds.

	g'					r'				
Field	$I_{0,Gauss}$	σ	$I_{0,Mof}$	α	β	$I_{0,Gauss}$	σ	$I_{0,Mof}$	α	β
Field1	0.181	0.765	0.819	0.763	1.69	0.093	0.638	0.907	0.681	1.67
Field2	0.152	0.574	0.848	0.651	1.72	0.000	0.016	1.000	0.524	1.69
Field4	0.211	0.768	0.789	0.768	1.66	0.103	0.705	0.897	0.692	1.66
Field5	0.139	0.677	0.861	0.692	1.70	0.163	0.903	0.837	0.708	1.50
Field6	0.000	0.000	1.000	0.608	1.90	0.081	0.623	0.919	0.636	1.63
Field7	0.000	0.076	1.000	0.544	1.74	0.070	0.523	0.930	0.558	1.60
Field9	0.165	0.657	0.835	0.718	1.73	0.079	0.521	0.921	0.595	1.67
Field10	0.129	0.651	0.871	0.687	1.72	0.042	0.724	0.957	0.561	1.52
Field11	0.085	0.613	0.915	0.648	1.73	0.061	0.757	0.938	0.635	1.60
Field12	0.000	0.000	1.000	0.532	1.71	0.061	0.597	0.938	0.603	1.61
Field13	0.000	0.000	1.000	0.590	1.76	0.050	0.591	0.950	0.635	1.67
Field14	0.141	0.633	0.859	0.704	1.75	0.088	0.480	0.912	0.576	1.66
Field15	0.128	0.621	0.872	0.664	1.71	0.000	0.118	1.000	0.535	1.67
Field16	0.173	0.693	0.827	0.720	1.70	0.086	0.500	0.914	0.543	1.59
Field17	0.135	0.711	0.865	0.704	1.69	0.000	0.000	1.000	0.565	1.80
Field18	0.065	0.546	0.935	0.593	1.71	0.053	0.560	0.947	0.633	1.68
Field19	0.177	0.573	0.823	0.662	1.72	0.000	0.000	1.000	0.519	1.68
Field20	0.175	0.681	0.825	0.687	1.65	0.053	0.606	0.946	0.544	1.55
Field21	0.114	0.647	0.886	0.683	1.72	0.000	0.000	1.000	0.455	1.66
Field22	0.080	0.592	0.920	0.646	1.75	0.000	0.000	1.000	0.487	1.68
Field25	0.102	0.629	0.898	0.691	1.76	0.000	0.000	1.000	0.487	1.76
Field26	0.000	0.000	1.000	0.655	1.85	0.000	0.000	1.000	0.479	1.68
Field27	0.088	0.607	0.913	0.662	1.75	0.000	0.000	1.000	0.461	1.66
Field28	0.091	0.615	0.909	0.674	1.76	0.000	0.000	1.000	0.459	1.66
Field31	0.185	0.647	0.815	0.729	1.74	0.100	0.491	0.900	0.593	1.68

4. The Fornax Deep Survey (FDS) with the VST. VI Optical properties of the dwarf galaxies in the Fornax cluster

—— A. Venhola, R. Peletier, E. Laurikainen, H. Salo, E. Iodice, S. Mieske , M. Hilker, C. Wittmann, M. Paolillo, M. Cantiello, J. Janz, M. Spavone, R. D'Abrusco, G. van de Ven, N. Napolitano, G. Verdoes Kleijn, M. Capaccioli, A. Grado, E. Valentijn, J. Falcón-Barroso, L. Limatola ——

Accepted to be published in Astronomy & Astrophysics

Abstract

Context: Dwarf galaxies are the most common type of galaxies in galaxy clusters. Due to their low mass, they are more vulnerable to environmental effects than massive galaxies, and are thus optimal for studying the effects of the environment on galaxy evolution. By comparing the properties of dwarf galaxies with different masses, morphological types, and cluster-centric distances we can get information about the physical processes in clusters that play a role in the evolution of these objects and shape their properties. The Fornax Deep Survey Dwarf galaxy Catalog (FDSDC) includes 564 dwarf galaxies in the Fornax cluster and the in-falling Fornax A sub-group. This sample allows us to perform a robust statistical analysis of the structural and stellar population differences in the range of galactic environments within the Fornax cluster.

Aim: By comparing our results with works concerning other clusters and the theoretical knowledge of the environmental processes taking place in galaxy clusters, we aim to understand the main mechanisms transforming galaxies in the Fornax cluster.

Methods: We exploit the FDSDC to study how the number density of galaxies, galaxy colors and structure change as a function of the cluster-centric distance,

used as a proxy for the galactic environment and in-fall time. We use also deprojection methods to transform the observed shape and density distributions of the galaxies into the intrinsic physical values. These measurements are then compared with predictions of simple theoretical models of the effects of harassment and ram pressure stripping on galaxy structure. We use stellar population models to estimate the stellar masses, metallicities and ages of the dwarf galaxies. We compare the properties of the dwarf galaxies in Fornax with those in the other galaxy clusters with different masses.

Results: We present the standard scaling relations for dwarf galaxies, which are the size-luminosity, Sérsic n-magnitude and color-magnitude relations. New in this paper is that we find a different behaviour for the bright dwarfs (-18.5 mag $<$ $M_{r'}$ $<$ -16 mag) as compared to the fainter ones ($M_{r'}$ $>$ -16 mag): While considering galaxies in the same magnitude-bins, we find that, while for fainter dwarfs the g'-r' color is redder for lower surface brightness objects (as expected from fading stellar populations), for brighter dwarfs the color is redder for the higher surface brightness and higher Sérsic n objects. The trend of the bright dwarfs might be explained by those galaxies being affected by harassment and by slower quenching of star formation in their inner parts. As the fraction of early-type dwarfs with respect to late-types increases towards the central parts of the cluster, the color-surface brightness trends are also manifested in the cluster-centric trends, confirming that it is indeed the environment that changes the galaxies. We also estimate the strength of the ram-pressure stripping, tidal disruption, and harassment in the Fornax cluster, and find that our observations are consistent with the theoretically expected ranges of galaxy properties where each of those mechanisms dominate. We furthermore find that the luminosity function, color-magnitude relation, and axis-ratio distribution of the dwarfs in the center of the Fornax cluster are similar to those in the center of the Virgo cluster. This indicates that in spite of the fact that the Virgo is 6 times more massive, their central dwarf galaxy populations appear similar in the relations studied by us.

4.1 INTRODUCTION

The local density of galaxies has been shown to play an important role in galaxy evolution, leading the more quiescent galaxies to appear preferentially in high density regions in the local Universe (Dressler 1980, Peng et al. 2010b). This is the case for high mass galaxies and the tendency is even stronger for low mass galaxies (Binggeli et al. 1990). A range of physical processes has been suggested to be responsible for such environmental variance (Boselli et al. 2008, Serra et al. 2012, Jaffé et al. 2018, Moore et al. 1998,Mastropietro et al. 2005,Ryś et al. 2014, Toloba et al. 2015). However, the properties of galaxies do not only depend on their surroundings, but also on their mass. For example, massive galaxies have been shown to host on average older stellar populations (see e.g. Thomas et al. 2005, Roediger et al. 2017, Schombert 2018), and to have more substructure than the less massive galaxies (Herrera-Endoqui et al. 2015, Janz et al. 2014). In order to isolate the environmental effects from internal processes, we need to study the

galaxies over a range of mass bins and environments. For such a study, dwarf galaxies constitute an important resource. Dwarf elliptical galaxies (dE) are the most abundant galaxies in galaxy clusters. They have low masses and low surface brightnesses, making them relatively easily affected by the environment. Thus, due to their abundance and vulnerability, they can be used to study the effects of environment on galaxy evolution.

Studies concentrating on mid- and high-redshift galaxies have shown an increase in the fraction of massive red quiescent galaxies in clusters since z = 1-2 up to present (Bell et al. 2004, Cassata et al. 2008, Mei et al. 2009). The emergence of these quiescent galaxies is partly explained by their mass: massive galaxies form stars more efficiently (Pearson et al. 2018) and therefore, if no more gas is accreted, run out of their cold gas reservoir faster than less massive galaxies. Additionally, the internal energy of gas and stars in these galaxies increases due to merging of satellite galaxies (Di Matteo et al. 2005), and due to feedback from active galactic nuclei (AGN) and supernovae (Bower et al. 2006, Hopkins et al. 2014), which prevents the gas from cooling and collapsing into new stars. The ensemble of these processes is called mass quenching since they are all related to the mass of the galaxy's dark matter halo, rather than to the environment. If the formation of early-type galaxies would happen only via mass quenching, we should see only very massive early-type galaxies at high redshift, and an increasing number of lower mass early-type galaxies towards lower redshift (Thomas et al. 2005). Indeed, observations have confirmed such evolution among the quiescent galaxies (Bundy et al. 2006) showing that mass-quenching is an important mechanism in galaxy evolution. However, strong correlations are also found with regard to stellar populations and galaxy morphology (Peng et al. 2010b) with the environment, indicating that mass quenching is not the only process contributing to the formation of early-type systems. Additionally, studies analyzing isolated early-type galaxies (Geha et al. 2012, Janz et al. 2017), for which the effects of the external processes can be excluded, have shown that all such quiescent galaxies are more massive than 1×10^9 $M_\odot$, indicating that mass-quenching is only effective in the mass range larger than that.

In dense environments, such as galaxy clusters, galaxies experience environmental processes acting both on their stellar and gas components. Harassment (Moore et al. 1998) is a term used for the high velocity tidal interactions between cluster galaxies, and between a galaxy and the cluster potential, that tend to rip out stellar, gas and dark matter components of the galaxies. Mastropietro et al. (2005) showed that harassment can transform a disk galaxy into a dynamically hot spheroidal system in time scales of a few Gyrs. Additionally, these processes may trigger bursts of star formation that quickly consume the cold gas reservoir, transforming the galaxy into an early-type system (Fujita 1998). Another consequence of harassment is that galaxies should become more compact as their outer parts are removed (Moore et al. 1998). Indeed, Janz et al. (2016a) found that the sizes of field late-type dwarfs are two times larger than those of early and late-type galaxies of the same mass located in the Virgo cluster. However, Smith et al. (2015) showed that harassment is effective in truncating the outer parts of only galaxies that have highly radial orbits with short peri-center distances

with respect to the cluster center. This challenges the idea that harassment alone can explain the difference between the galaxies in different environments.

Another, more drastic consequence of the gravitational interactions is that in the cluster center they are so strong that they may cause complete disruption of dwarf galaxies (McGlynn 1990, Koch et al. 2012). The material of those disrupted galaxies then ends up in the intra-cluster medium, piling up in the central regions of the cluster, and leaving an underdense core in the galaxy number density profile of the cluster. In the Fornax cluster, which is the object of this study, such a core has been observed (Ferguson 1989). Also ultra-compact dwarf galaxies, of which some are likely to be remnant nuclei of stripped dwarf galaxies are detected (Drinkwater et al. 2003, Voggel et al. 2016, Wittmann et al. 2016), which gives further evidence for disruption of the dwarfs. Recently, Iodice et al. (2019) studied massive early-type galaxies (ETGs) in the central region of the Fornax cluster, and showed that in the core of the cluster, the ETGs tend to have twisted and/or asymmetric outskirts, and that patches of intra-cluster light (Iodice et al. 2016, Iodice et al. 2017a) have been also been detected in that region. These findings suggest that in the core of the Fornax cluster, harassment is shaping the massive galaxies. Also D'Abrusco et al. (2016) have identified a population of intra-cluster globular clusters (GCs) that may originate from globular clusters stripped out of the cluster galaxies.

Another process affecting galaxies in clusters, but acting only on their gas component, is ram-pressure stripping (Gunn & Gott 1972). If a gas-rich galaxy moves through a galaxy cluster that contains a significant amount of hot gas, pressure between the gas components can remove the cold gas from the galaxy's potential well. This happens especially on galaxy orbits near the center of the cluster, in which case all the gas of the galaxy might be depleted in a single crossing, corresponding to a time scale of half a Gyr (Lotz et al. 2018). If not all the gas of the galaxy is removed at once, it is likely that the remaining gas is located in its center where the galaxy's anchoring force is strong. This may lead to younger stellar populations in the central part of the dwarf galaxies. Indeed, many dwarf galaxies in clusters have blue centers (Lisker et al. 2006), indicative of their young stellar ages. There is strong observational evidence about the removal of gas from galaxies when they enter the cluster environment: Long H_I tails have been observed trailing behind late-type galaxies falling into clusters (Kenney et al. 2004, Chung et al. 2009). Using Hα- and UV-imaging, ram pressure stripping has been observed in action in infalling galaxies (Poggianti et al. 2017, Jaffé et al. 2018). Also, galaxies in clusters have shown to be mostly gas-poor, and those outside the clusters gas-rich (Solanes et al. 2001, Serra et al. 2012).

As discussed above, both harassment and ram-pressure stripping take place in the cluster environment. The physical theory behind them is well understood. However, what is not known, is the importance of these processes in shaping the dwarf galaxy populations in clusters. Our understanding of this problem is limited on the theoretical side by the resolution of cosmological simulations, which are not able to resolve small galaxies in the cluster environment (Pillepich et al. 2018, Schaye et al. 2015). Observationally, it is due to the lack of systematic studies analysing the properties of dwarf galaxies for a complete galaxy sample, spanning

a range of different galactic environments. Recently, some surveys including the Next Generation Fornax Survey (NGFS, Eigenthaler et al. 2018) and the Fornax Deep Survey (FDS, Iodice et al. 2016) have been set up to address these questions. In this study, we approach this problem from the observational point of view using a size and luminosity limited sample of galaxies in the Fornax cluster. This sample is used to test some first order predictions arising from the current theoretical understanding of the different environmental processes.

The Fornax Deep Survey (FDS) provides a dataset that allows to study the faintest dwarf galaxies over the whole Fornax cluster area. The survey covers a 26 deg^2 area of the cluster up to its virial radius, covering also the non-virialized South-West Fornax A sub-group. The deep u', g', r', i'-data with wide dynamical range allows us to study the galaxy properties and colors down to the absolute r'-band magnitude $M_{r'} \approx$ -10 mag. The Fornax Deep Survey Dwarf galaxy Catalog (FDSDC) by Venhola et. al. (2018) includes 564 dwarf galaxies in the survey area, and reaches 50% completeness at the limiting magnitude of $M_{r'}$ = -10.5 mag, and the limiting mean effective surface brightness of $\bar{\mu}_{e,r'}$ = 26 mag arcsec^{-2}. The minimum semi-major axis size[1] is a = 2 arcsec. Our sample is obtained from data with similar quality to that of the Next Generation Virgo Survey (NGVS, Ferrarese et al. 2012), thus allowing a fair comparison between the faint galaxy populations in these two environments.

In this paper, our aim is to use the FDSDC to study how the galaxy colors, the luminosity function, the fraction of morphological types, and the structure parameters change from the outer parts of the cluster toward the inner parts. If harassment is the main environmental effect acting on galaxies, the galaxies are expected to become more compact (higher Sérsic indices and smaller effective radii) and rounder in the inner parts of the cluster, as their outer parts get stripped and their internal velocity dispersion increases (Moore et al. 1998, Mastropietro et al. 2005). On the other hand, if the main mechanism is ram pressure stripping, the galaxies should not become more compact or rounder towards the cluster center. However, they are expected to become redder and to have lower surface brightnesses after the ram pressure stripping has quenched their star formation. The optical region where the contribution of young stars is significant, is particularly favourable for this kind of studies. We also compare our results with those obtained in the Virgo cluster by NGVS.

In this paper, we first discuss the data and the sample in Section 2. In Sections 3, 4, 5 and 6, we present the distribution, luminosity function, structure, and colors of the dwarf galaxies in the Fornax cluster as a function of their cluster-centric distance and total luminosity, respectively. Finally, in Sections 7 and 8 we discuss the results and summarize the conclusions, respectively. Throughout the paper we use the distance of 20.0 Mpc for the Fornax cluster corresponding to the distance modulus of 31.51 mag (Blakeslee et al. 2009). At the distance of the Fornax cluster, 1 deg corresponds to 0.349 Mpc.

[1]Semi-major axes from SExtractor (Bertin & Arnouts 1996) were used.

4.2 DATA

4.2.1 OBSERVATIONS

We use the FDS, which consists of the combined data of Guaranteed Time Observation Surveys, FOrnax Cluster Ultra-deep Survey (FOCUS, P.I. R. Peletier) and VST Early-type GAlaxy Survey (VEGAS, P.I. E. Iodice), dedicated to the Fornax cluster. Both surveys are performed with the ESO VLT Survey Telescope (VST), which is a 2.6-meter diameter optical survey telescope located at Cerro Paranal, Chile (Schipani et al. 2012). The imaging is done in the u', g', r' and i'-bands using the $1^\circ \times 1^\circ$ field of view OmegaCAM instrument (Kuijken et al. 2002) attached to VST. The observations cover a 26 deg^2 area centered to the Fornax main cluster and the in-falling Fornax A sub-group in which NGC 1316 is the central galaxy (see Fig. 4.1). Full explanations of the observations and the AstroWISE-pipeline (McFarland et al. 2013) reduction steps are given in Peletier et al. (*in prep.*), and Venhola et al. (2018).

The photometric errors related to the zeropoint calibration of the data were defined by Venhola et al. (2018), and they are 0.04, 0.03, 0.03, and 0.04 mag in u', g', r' and i', respectively. The completed fields are covered with homogeneous depth with the 1σ limiting surface brightness over 1 pixel area of 26.6, 26.7, 26.1 and 25.5 mag arcsec^{-2} in u', g', r' and i', respectively. When averaged over a 1 arcsec^2 area, these numbers correspond to 28.3, 28.4, 27.8, 27.2 mag arcsec^{-2} in u', g', r' and i', respectively. The data is calibrated using AB-magnitude system.

The FDS has provided two galaxy catalogs: The catalog containing all dwarf galaxies in the whole FDS area has been presented in Venhola et al. (2018), and the photometry of the ETGs in the central 9 deg^2 area of the cluster by Iodice et al. (2019). This study mostly considers only the dwarf galaxies, but in Section 9,we also use the stellar masses of the ETGs from the catalog of Iodice et al.

4.2.2 GALAXY SAMPLE

We use the FDSDC (Venhola et al., 2018) that is based on the whole data set of the FDS. In Venhola et al. 2018, we ran SExtractor (Bertin & Arnouts 1996) on the stacked g'+r'+i'-images to detect the objects, and then selected those with semi-major axis lengths larger than $a > 2$ arcsec for further analysis. The galaxy catalog contains the Fornax cluster dwarfs with $M_{r'} > -18.5$ mag, and reaches its 50% completeness limit at the r'-band magnitude $M_{r'} = -10.5$ mag and the mean effective surface brightness $\bar{\mu}_{e,r'} = 26$ mag arcsec^{-2}. In Appendix 4.10.1, we show how the minimum size and magnitude limits affect the completeness of the FDSDC in the size-magnitude space.

In Venhola et al. (2018), we produced Sérsic model fits for these galaxies using GALFIT (Peng et al. 2002, 2010a) and the r'-band images of the FDS. For the dwarf galaxies with nuclear star clusters we fit the unresolved central component with an additional PSF component. We also measured aperture colors within the effective radii using elliptical apertures. The effective radius, position angle and ellipticity of the apertures were taken from the r'-band Sérsic fits. For the

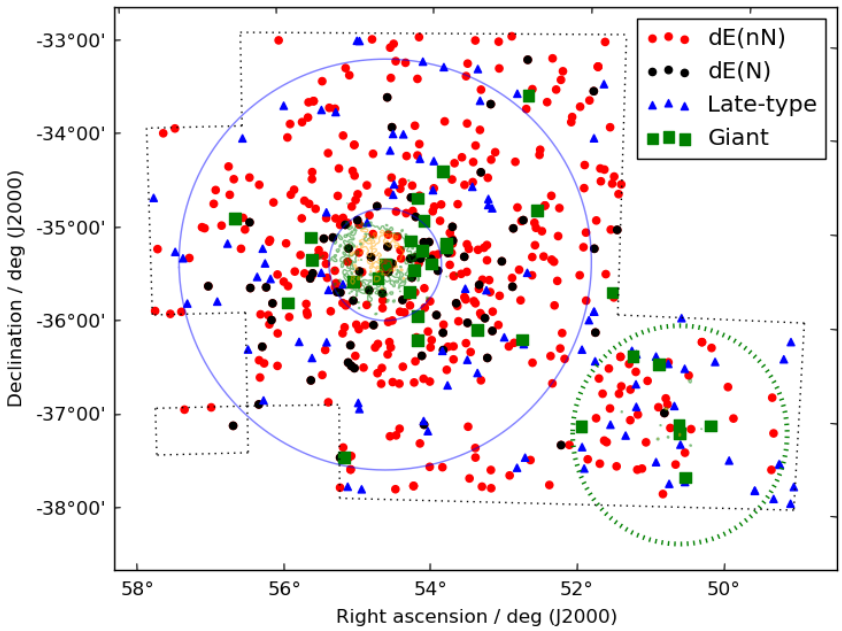

Figure 4.1: Locations of the likely cluster galaxies in the FDSDC (Venhola et al., 2018). The red, black and blue symbols correspond to non-nucleated dwarf ellipticals, dE(nN), nucleated dwarf ellipticals, dE(N) and late-type dwarfs, respectively. The black dotted lines show the extent of the FDS observations. The inner and outer blue circles show the core (Ferguson 1989) and virial radius (Drinkwater et al. 2001) of the Fornax main cluster respectively, and the green dotted circle encloses an area within one degree from the Fornax A sub-group (Drinkwater et al. 2001). The green, yellow, and red contours around the center of the cluster and Fornax A correspond to the 0.96, 1.15, and 1.34 $\times$ 10^{-3} counts arcmin^{-2} sec^{-1} isophotes of the ROSAT X-ray observations, respectively (Kim et al. 1998, Paolillo et al. 2002). In the figure North is up and East is towards left.

total magnitudes and the other structural parameters, we use the values adopted from the same r'-band fits. In the u'-band color analysis, we exclude galaxies that have $\bar{\mu}_{e,r'} > 25$ mag arcsec^{-2}, since their colors are uncertain due to the low signal-to-noise.

We analyze all the galaxies that we classified as likely cluster members in Venhola et al. (2018). We also use the same division of galaxies into late- and early-types as was used in that work. This morphological division was made visually by classifying the red and smooth galaxies as early-types, and the galaxies that have star formation clumps as late-types. For the low mass galaxies for which the visual morphological classification was uncertain, we used a combination of colors, concentration parameter C, and Residual Flux Fraction RFF, to separate them into the different types. Due to a lack of more detailed morphological classifications of the FDSDC galaxies, in this study we refer to the late-type dwarfs as dwarf irregulars, dIrrs, and early-type dwarfs as dwarf ellipticals, dEs. We emphasize that this leads into those classes consisting of several types of objects, e.g. that following the classification system of Kormendy & Bender (2012), spheroidals, dS0s and "true dwarf ellipticals" would all be classified as dEs in this work, and the irregulars would belong to dIrr.

Our total galaxy sample in this work consists of 564 Fornax cluster galaxies. Of these 470 are classified as early-types and 94 as late-types. The early-types are further divided into nucleated, dE(N) (N=81), and non-nucleated, dE(nN) (N=389), dwarf ellipticals. Our sample is at least 95 % complete within the given limits. Since most of the sample galaxies have no spectroscopic confirmations, it is likely that there is some amount of galaxies that are actually background objects. According to the estimation of Venhola et al. (2018), there might be at maximum 10% background contamination in the sample, corresponding to few tens of misclassified background galaxies.

4.2.3 STELLAR MASSES

We estimate the stellar mass of the sample galaxies using the empirical relation observed between the g'-i' color and mass-to-light (M/L) ratio by Taylor et al. (2011):

$$\log_{10}\left(\frac{\mathrm{M}_*}{\mathrm{M}_\odot}\right) = 1.15 + 0.70 \times (g' - i') - 0.4\mathrm{M}_{i'}. \tag{4.1}$$

In the equation, $\mathrm{M}_{i'}$ is the absolute i'-band magnitude. As we have done the Seŕsic model fitting only for the r'-band images, and thus do not have the i'-band total magnitudes for the galaxies, we transform the r'-band total magnitudes into i'-band, by applying the r'-i' color (measured within R_e) correction:

$$\log_{10}\left(\frac{\mathrm{M}_*}{\mathrm{M}_\odot}\right) = 1.15 + 0.70 \times (g' - i') - 0.4\mathrm{M}_{r'} + 0.4 \times (r' - i'). \tag{4.2}$$

The relation between the stellar masses and r'-band magnitudes for the galaxies in our sample are shown with the black symbols in Fig. 4.2. According to Taylor

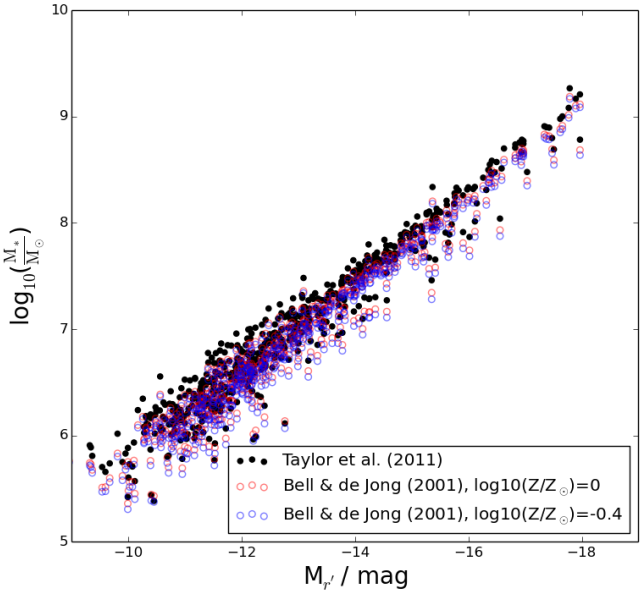

Figure 4.2: Stellar masses of the galaxies as a function of their r'-band absolute magnitude ($M_{r'}$). The black symbols show the transformations when using the relations of Taylor et al. (2011) and the red and blue symbols show the relations when using Bell and de Jong (2001) transformations with the assumed metallicities of 0 and -0.4, respectively.

et al. (2011) the accuracy of the transformed stellar masses is within 0.1 dex. However, their sample does not contain galaxies with $M_* < 10^{7.5}$ $M_\odot$, where we have to use an extrapolation of their relation to obtain the lowest stellar masses. This caveat makes our mass estimations for the lowest mass galaxies uncertain. For quantifying that uncertainty, we estimate the masses also using another method.

To have an independent test for the low mass galaxies and to assess the feasibility of Eq. 4.1 for the galaxies with $M_* < 10^{7.5}$ $M_\odot$, we compare our estimates with those of Bell & de Jong (2001). We adopted the linear fit model of Bell & de Jong that uses the stellar population models of Bruzual & Charlot (2003). In this model, a Salpeter initial mass function was used[2] and metallicities of $\log_{10}(Z/Z_\odot) = 0$ and -0.4. Any lower metallicities are not covered by the Bell & de Jong models and thus we are limited to use these rather high metallicities, although e.g. dwarf galaxy with $M_* = 10^{7.5}$ $M_\odot$ has $\log_{10}(Z/Z_\odot)$ = -1 (see Janz et al. 2016b). Assuming solar metallicity, the equation for the mass to light ratio is

$$\log_{10}\left(\frac{\mathrm{M}}{\mathrm{L_R}}\right) = -0.80 + 1.21 \times (V - I), \tag{4.3}$$

[2]The models of Bell & de Jong (2001) are limited to Salpeter-like initial mass functions, which restricts us from using for example Kroupa initial mass function.

where V and I are magnitudes in the Johnson V and I band filters, and L_R is the luminosity in Johnson R-band. In the case of $\log_{10}(Z/Z_\odot)$ = -0.4, the formula becomes

$$\log_{10}\left(\frac{\mathrm{M}}{\mathrm{L_R}}\right) = -0.87 + 1.27 \times (V - I). \quad (4.4)$$

Using the transformations of Jordi et al. (2006) between the Johnson V,R,I- and the SDSS g',r',i'-filters (see Appendix 4.10.5), and transforming luminosity to magnitudes we can rewrite Eq. 4.3 as follows:

$$\log_{10}\left(\frac{\mathrm{M_*}}{\mathrm{M_\odot}}\right) = 1.04 + 0.817 \times (g' - i') - 0.4 \times M_{r'} + 0.1 \times (r' - i'). \quad (4.5)$$

While comparing Eqs. 4.2 and 4.5 (see Fig. 4.2), we find that the Bell and de Jong calibration is very similar to the one of Taylor et al., differing only by having a lower constant term and a slightly different dependence on the g'-i' and r'-i' colors. The effects of metallicity in the model is negligible (see the red and blue points in Fig. 4.2). Thus, these mass estimates give consistent results within ≈10% accuracy.

Due to the systematic uncertainties in the M/L-ratios for low luminosity galaxies, we do most of the analysis in this work using the r'-band luminosity as a proxy for the stellar mass. However, in crucial parts of the analysis, we also check that the results hold when using the estimated stellar masses instead of luminosities. For the stellar masses we adopt the values from Taylor et al. (2011) (Eq. 4.2). Also the stellar masses for the giant ETGs in Section 8 have been calculated in the same way.

4.3 DWARF GALAXY DISTRIBUTION

4.3.1 LOCATIONS OF THE GALAXIES AND THEIR ENVIRONMENT

In Fig. 4.1 we show the locations of the galaxies in our sample. It is clear that most of the galaxies are strongly concentrated around the center of the Fornax cluster forming a relatively symmetrical and dense main cluster. Another clear but less massive and more loose structure is the Fornax A group South-West from the main cluster, where the galaxies are grouped around the shell galaxy NGC 1316 (Iodice et al. 2017b). The Fornax A galaxy distribution seems to be skewed towards the main cluster. The Fornax cluster is located in a filament of the cosmic web so that the filament crosses the cluster in the North-South axis (see Nasonova et al. 2011 and Venhola et al. 2018). One would expect the infall of galaxies to be enhanced from the direction of the filament, but no clear overdensities towards those directions can be seen in our data.

In order to better see the sub-structures, we convolved the galaxy distribution with a Gaussian kernel with a standard deviation of σ = 15 arcmin. We also used mass weighting for the smoothing. The smoothed distributions with and without mass weighting are shown in Fig. 4.3. As expected, in the smoothed

images the two overdensities in the main cluster and in the Fornax A sub-group are clearly pronounced. From the non-weighted distribution it appears that the galaxy distributions are not perfectly concentrated around NGC 1399 and NGC 1316, but are slightly offset towards the space between those two giant galaxies. The distribution of the galaxies in the center of the cluster has the same two-peaked appearance as the one found by Ordenes-Briceño et al. (2018), who analyzed the distribution of the Fornax dwarfs using the Next Generation Fornax Survey data (NGFS, Muñoz et al. 2015). Also the giant ETGs and GCs in the cluster are concentrated to this same area (Iodice et al. 2019,D'Abrusco et al. 2016).

Due to the relatively symmetric distribution of the galaxies in the Fornax cluster, it is tempting to use the cluster centric distance as a proxy for the galaxy environment and the infall time. We expect the galaxies in the outskirts of the cluster to have spent less time in the cluster environment than the ones in the inner parts. To test how well the cluster-centric distance correlates with the projected galaxy density, we calculate the number of cluster galaxies within 30 arcmin projected radius from each galaxy. We then measure this parameter for all the galaxies and in Fig. 4.4 plot this parameter against the cluster-centric distance. The number of the projected neighbours drops almost monotonically towards the outer parts of the cluster. Only in the Fornax A group deviations from this relation occur. In principle, the projected galaxy density would be a sufficient measure to define the galaxy environment, but since there are some galaxy clumps that may be due to projection effects without any physical meaning, the cluster-centric distance provides a more robust measure. In summary, for our sample, a shorter cluster-centric distance can be interpreted as higher galaxy density environment. Additionally, galaxies located at short cluster-centric distances have on average entered the cluster earlier than those in the outskirts. Thus cluster-centric distance is a more fundamental parameter than the projected galaxy density.

A higher galaxy density is expected to increase the strength of harassment between galaxies, whereas higher relative velocities weaken the strength of individual tidal interactions (Eq. 8.54 of Binney & Tremaine 2008 and Eq. 4.10 of this study). According to Drinkwater et al. (2001) the line of sight velocity dispersion of the main cluster is σ_V = 370 km s^{-1} and in the Fornax A sub-structure σ_V = 377 km s^{-1}. Assuming that both structures are virialized, Drinkwater et al. estimated masses of $5\pm2\times10^{13}$ M$_\odot$ and 6×10^{13} M$_\odot$, for the main cluster and Fornax A, respectively. However, they also stated that, most likely, Fornax A is not virialized and thus the virial mass estimation is only an upper limit. Assuming the same mass-to-light ratios for these two sub-clusters, Drinkwater et al. estimated the mass of the Fornax A to be 2×10^{13} M$_\odot$, being thus $\approx$1/4 of the mass of the main cluster. However, this approximation might still be underestimating the relative masses, since the galaxy population of the Fornax A is dominated by late-type dwarfs, which have on average younger stellar populations and thus lower mass-to-light ratio.

In addition to galaxy density, also hot X-ray emitting gas is an important factor affecting the evolution of the galaxies via ram pressure stripping. Paolillo et al. (2002) and Kim et al. (1998) studied the X-ray gas around NGC 1399 and NGC 1316, respectively, using the RÖntgen SATellite's (ROSAT) X-ray telescope's

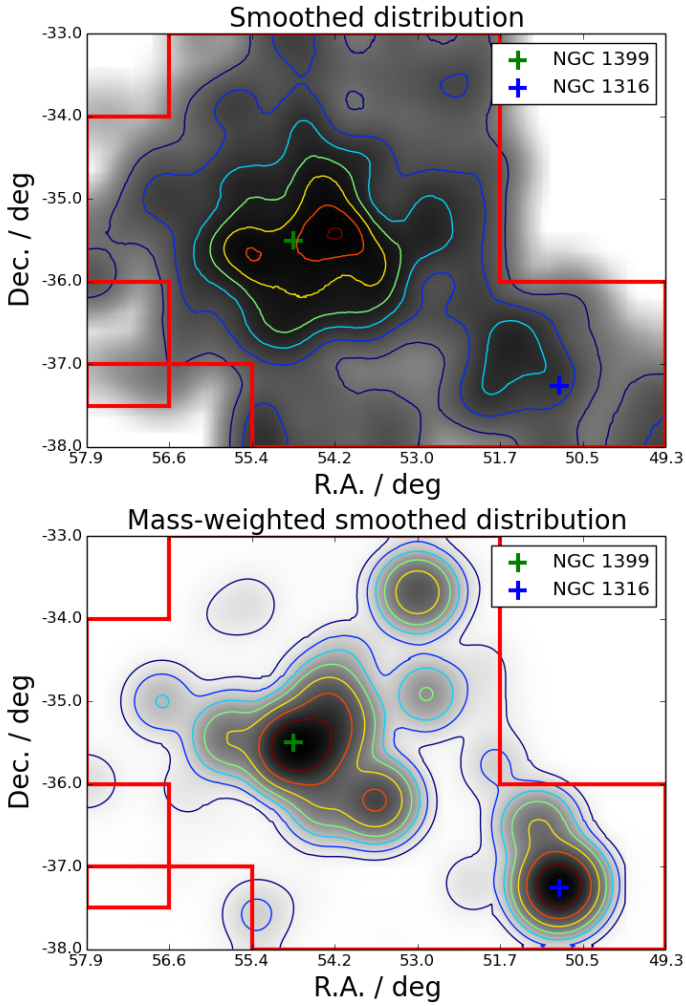

Figure 4.3: Smoothed distributions of the galaxies in the Fornax cluster. The upper panel shows the surface number density distribution of galaxies using a Gaussian convolution kernel with $\sigma = 15$ arcmin. The lower panel shows the smoothed surface mass density distribution using the same kernel. The coloured contours in the upper and lower panels highlight the iso-density curves with linear and logarithmic spacing, respectively. The green and blue crosses show the locations of NGC 1399 and NGC 1316, respectively. The red lines frame the area covered by the FDS. In the figures North is up and East is towards left.

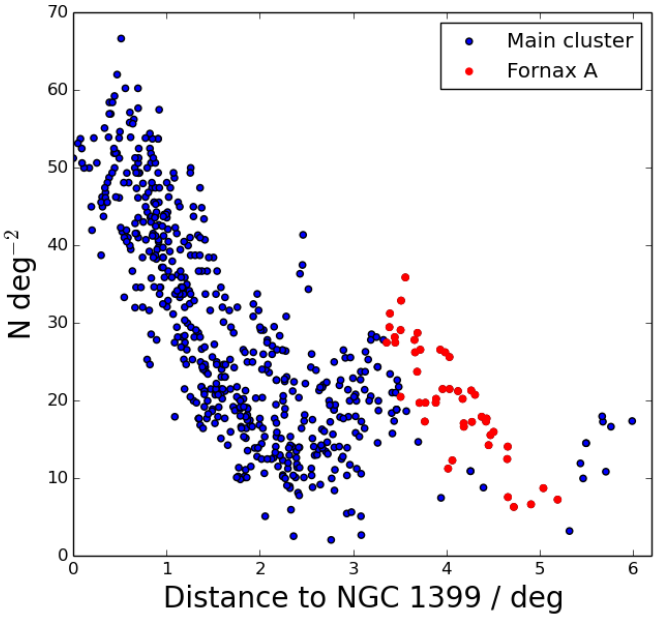

Figure 4.4: Galaxy surface density as a function of the distance from NGC 1399. The red points show the galaxies projected within 1 deg from the NGC1316, which is the central galaxy of Fornax A group. The blue points show the other galaxies.

Position Sensitive Proportional Counters (PSPC) (Pfeffermann et al. 1987) for imaging. In order to compare the distribution of the X-ray gas in the cluster with that of the dwarf galaxies, we took the archival ROSAT data and overlaid intensity contours on Fig. 4.1. The total mass of the X-ray gas within 0.3 deg from the NGC1399 is $M_{gas} \approx 10^{11}$ $M_{\odot}$ (Paolillo et al. 2002), whereas the mass of the X-ray gas associated to Fornax A is only $M_{gas} \approx 10^{9}$ $M_{\odot}$ (Kim et al. 1998). The X-ray gas of the main cluster is detected up to radii of 150 kpc from the center, but due to the small spatial extent of the X-ray observations, in reality it might extend much further. The X-ray emitting gas is also misaligned with respect to NGC 1399. The gas is lopsided towards North-West, which is opposite to the giant ETGs in the center. Based on the X-ray gas distribution, the galaxies travelling through the center of the Fornax cluster are expected to experience much stronger ram-pressure stripping, due to larger gas-density, than the galaxies located in the Fornax A sub-group.

4.3.2 RADIAL DISTRIBUTION OF DWARF GALAXIES

Morphological segregation is known to exist in Virgo (Lisker et al. 2007) and in other clusters (Binggeli et al. 1984), and an analysis of the density-morphology

relation in the Fornax cluster, and in Fornax A, gives an interesting comparison with the previous works. In particular, we expect the different environmental properties in the core and outskirts of the main cluster, and in the Fornax A sub-group, to manifest in the morphology and the physical parameters of the galaxies.

In order to test whether we see different cluster-centric radial distributions among the studied morphological types, we derive radial cluster-centric surface density profiles for the late-types, dE(N)s and dE(nN)s, and compare them with the distribution of giant galaxies ($M_{r'}$ < -18.5 mag) in Fornax. We derive the morphology-density relation also with respect to Fornax A. We use circular bins centered on the central galaxies of the Fornax cluster, NGC 1399, and of the Fornax A, NGC1316. We calculate the number of galaxies in each bin and divide them by the bin area to get the surface density of the galaxies. We assume a simple Poissonian behaviour for the uncertainty in counts in the bins. The partially incomplete coverage of the FDS in the outermost bins is taken into account in the radial profiles. The obtained radial surface density profiles are shown in the upper panels of Fig. 4.5. In the middle panels the radial cluster-centric cumulative fractions are also shown.

We find a clear sequence in the distributions of the different morphological types in the main cluster (upper left panel in Fig. 4.5): from the least centrally concentrated to the most concentrated groups are the late-type dwarfs, dE(nN)s, and dE(N)s. We use a Kolmogorov-Smirnov test to see whether these differences are statistically significant. In Table 4.1 we show the p-values for the assumption that the observed distributions are drawn from the same underlying distribution. In this and later tests in this paper, we require $p < 0.05$ ($>2\sigma$ deviation from the normal distribution) for concluding that two samples differ significantly. We find that the differences are indeed significant between all the samples except between the dE(N)s and giants.

In Fornax A (upper right panel in Fig 4.5) the morphology-density relation is not as clear as in the main cluster. The giants are more centrally concentrated than the dwarfs, but the distributions of the early- and late-type dwarfs do not differ significantly from each other, and are only slightly concentrated towards NGC 1316 in the innermost 0.5 deg area.

To further understand the spatial distribution of the galaxies in the center of the Fornax cluster, we used the onion peeling deprojection method (described in Appendix 4.10.2) for obtaining the galaxy volume densities. The deprojected distributions of the main cluster and the Fornax A sub-group are shown in the bottom row of Fig. 4.5. The deprojected radial distributions reveal that there are no dE(nN)s nor late-type dwarfs within the innermost 0.5 deg from the cluster center. This radius also roughly corresponds to the projected radius, which encloses the area where the giant ETGs are densely concentrated and where their outer parts are disturbed (Iodice et al. 2019). The distribution of the late-type dwarfs shows an even larger de-populated core than for the dE(nN)s, extending to r = 1.5 deg. The large core devoid of galaxies implies that late-type dwarfs cannot exist in the cluster without transforming into something else, and that

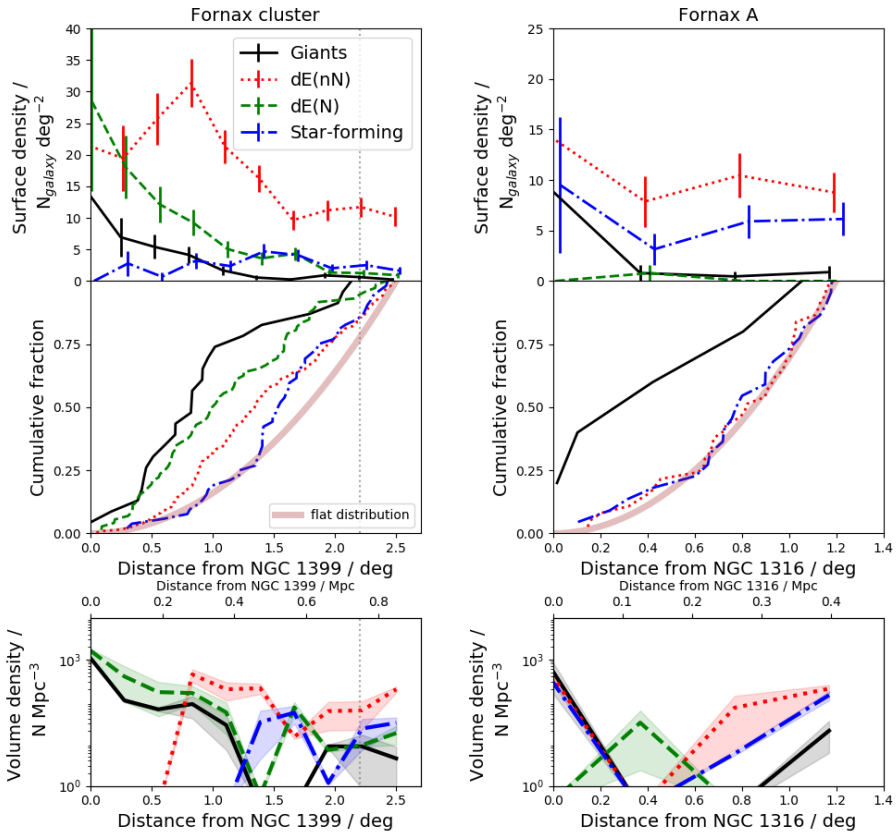

Figure 4.5: Upper panels show the surface number density of the galaxies as a function of the cluster-centric radius (left panels) and the distance from Fornax-A (right panels). The mid panels show the corresponding cumulative number fractions as function of radii. The black solid lines corresponds to the giant galaxies with M'_r < -18.5 mag, the green dashed and red dotted lines correspond to dE(N)s and dE(nN)s, respectively, and the blue dash-dotted lines corresponds to the late-type dwarfs. For a reference, the purple opaque lines show the cumulative profile for a uniform radial surface density distribution without any cluster-centric concentration. In the bottom panels, we show the deprojected volume densities of the galaxies obtained from the radial surface density profiles using the onion peeling technique described in the Appendix 4.10.2. The shaded areas correspond to the uncertainties in the deprojected profiles, estimated with Monte Carlo method. The vertical grey dotted lines in the left panels correspond to the virial radius of the cluster.

Table 4.1: Results of the pairwise Kolmogorov-Smirnov tests used for comparing the radial distributions of the different types of galaxies. The p-values correspond to the hypothesis that a pair of samples is drawn from the same underlying distribution.

	Giants	dE(nN)	dE(N)
dE(nN)	5.5e-04		
dE(N)	3.1e-01	6.5e-04	
dIrr	4.5e-05	5.9e-03	2.0e-05

even dE(nN)s either transform into dE(N) or dissolve in the very central parts of the cluster.

Since our analysis of the radial profiles showed that the cluster core is almost devoid of the dE(nN) and late-types, and yet we observe them with the projected locations near the cluster center, it is useful to quantify how the projected cluster-centric 2D-distance correlates with the 3D-distance. To find the expected 3D-distance for any given 2D-distance, we integrate along the line of sight through the previously obtained volume density distributions, and calculate the density weighted mean 3D-radius of the galaxies. We show the relation between the 2D- and 3D-distances in Fig. 4.6. To quantify the width of the distribution, we also calculate the 25% and 75% quantiles at the given 2D-distance.

We know that in the Virgo cluster the relative abundance of the dE(nN)s, dE(N)s, and the late type dwarfs correlates with the density of the galaxy environment (Lisker et al. 2007). To quantify the behaviour in our data, we plot the early-type galaxy fraction (N_{early}/N_{all}) and the nucleation fraction (N_{nuc}/N_{early}) in the main cluster and Fornax A, as a function of the radius from the central galaxies NGC 1399 and NGC 1316, respectively (see Fig. 4.7). From the upper left panel we see that the early-type fraction declines towards the outskirts of the cluster, being 95% in the center and 80% in the outer parts. Also, the nucleation fraction of the early-types decreases from ≈ 0.5 in the cluster center to 0.1 in the outskirts. Neither the early-type fraction nor the nucleation fraction in the Fornax A increase significantly in the vicinity of NGC1316, and they are clearly lower than in the main cluster, being much closer to the value found in the field, where $\approx$ 50% of the dwarfs are of late type (Binggeli et al. 1990).

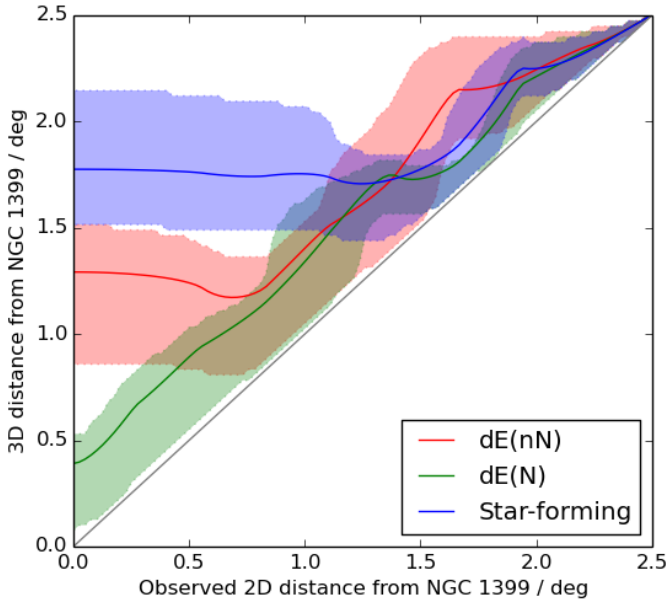

Figure 4.6: Relations between the projected 2D distances and the likely 3D distances for the different morphological types. The green, red, and blue lines correspond to dE(N), dE(nN), and late-type dwarfs. The shaded areas show the range within the 25% and 75% in the probability distributions.

4.4 LUMINOSITY FUNCTION

4.4.1 IN THE WHOLE CLUSTER

In Fig. 4.8 (upper panel) we show the r'-band luminosity functions and the cumulative luminosity functions of the different types of dwarf galaxies. Late-type dwarfs in our sample are slightly more luminous than dE(nN)s (p=0.034), and dE(N)s are on average more luminous than the other two types ($p<10^{-5}$ for both). If we compare the luminosity functions of the early- and late-types, without considering nucleation, the luminosity functions do not differ (p=0.17).

We also show the nucleation and early-type fraction of the Fornax cluster dwarfs as a function of galaxy magnitude (see Fig. 4.9). We find that the nucleation fraction peaks at $M_{r'} \approx$ -16 mag and decreases quickly towards higher and lower luminosity galaxies. This seems to be true independent of the cluster-centric distance. Ordenes-Briceño et al. (2018) analyzed the NGFS galaxy sample in the center of the Fornax cluster (Eigenthaler et al. 2018). They found a nucleation fraction of ≈90% at $M_{r'} \approx$ -16 mag. In the same area, the nucleation fraction obtained by us agrees well with the value of Ordenes-Briceño et al. (2018). For comparison, Côté et al. (2006) who studied the nucleation fraction in the

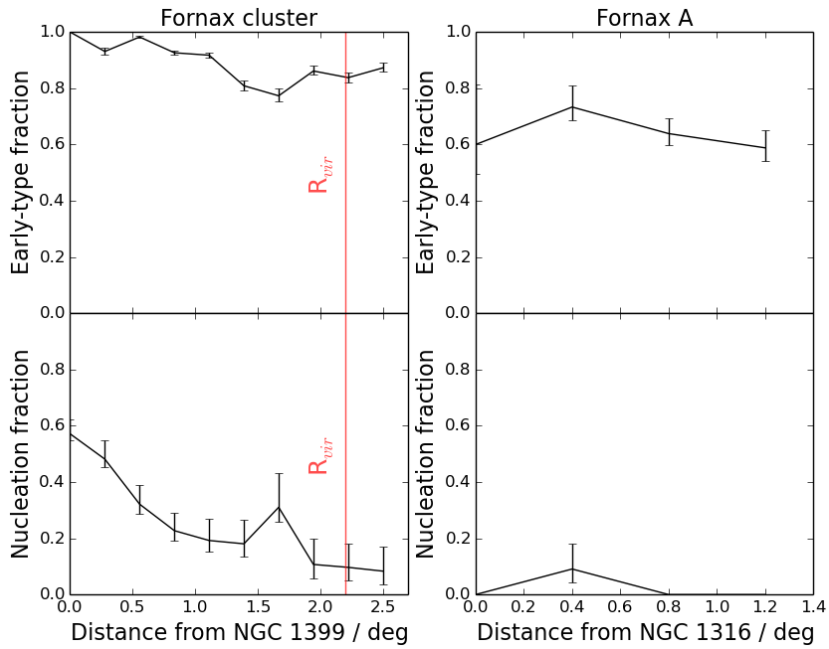

Figure 4.7: Left panels show the early- type fraction (upper left) and the nucleation fraction (lower left) as a function of projected distance from the central galaxy NGC 1399 of the Fornax cluster. Right panels show the same relations as a function of distance from the central galaxy NGC 1316 of the Fornax A sub-group. The red horizontal lines in the left panels show the virial radius of the main cluster.

Virgo cluster using the Hubble Space Telescope (HST) images, found a similar peak of the nucleation fraction as we found, around M_B = -16.5 mag. Near the peak at least 80 % of the galaxies have nuclei, consistent with our study. The result of Côté et al. (2006) for the Virgo dwarfs was later confirmed by Sánchez-Janssen et al. (2018) who identified a similar peak in the nucleation fraction, and using the deep dwarf galaxy sample of the NGVS showed that the nucleation fraction steeply decreases towards the lower luminosities. The early-type fraction (the lower panel of Fig. 4.9) has some dependence of the magnitude as well, so that for galaxies with $M_{r'} <$ -16 mag the early-type fraction is lower than for the less luminous galaxies. The same result holds also in stellar mass bins.

4.4.2 LUMINOSITY FUNCTION IN RADIAL BINS

We calculate the luminosity distributions of the galaxies in four spatial bins: at R $<$ 1.5 deg[3] from NGC 1399 (Bin 1), at 1.5 deg $<$ R $<$ 2.5 deg (Bin 2), at R $>$ 2.5

[3] 1.5 deg corresponds to two core radii (Ferguson 1989) or ∼450 kpc at the distance of the Fornax cluster

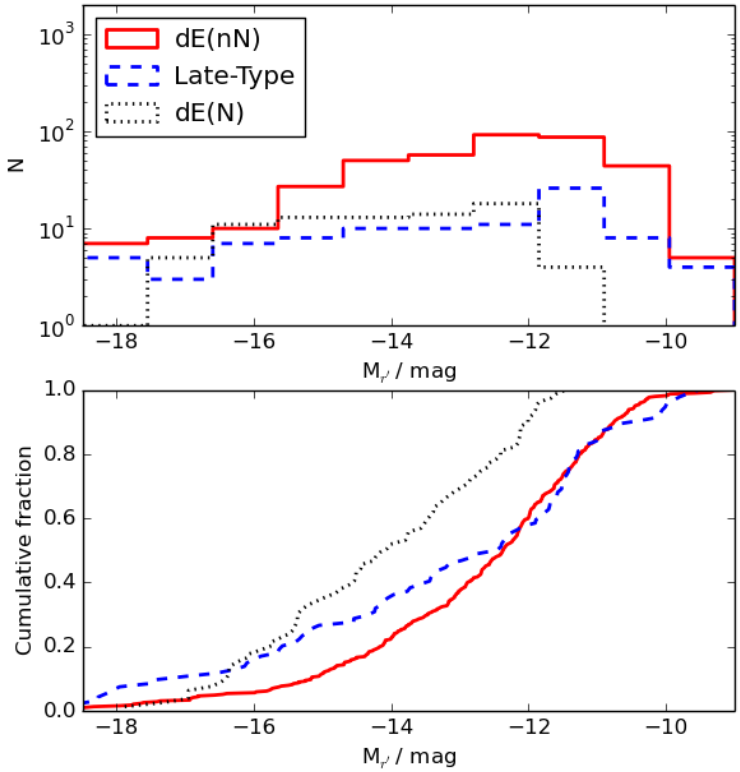

Figure 4.8: Upper panel shows the r'-band luminosity function for the dE(nN) (red solid line), dE(N) (black dotted line) and late-type dwarf galaxies (blue dashed line). The lower panel shows the cumulative luminosity function of the galaxies with the corresponding colors, respectively.

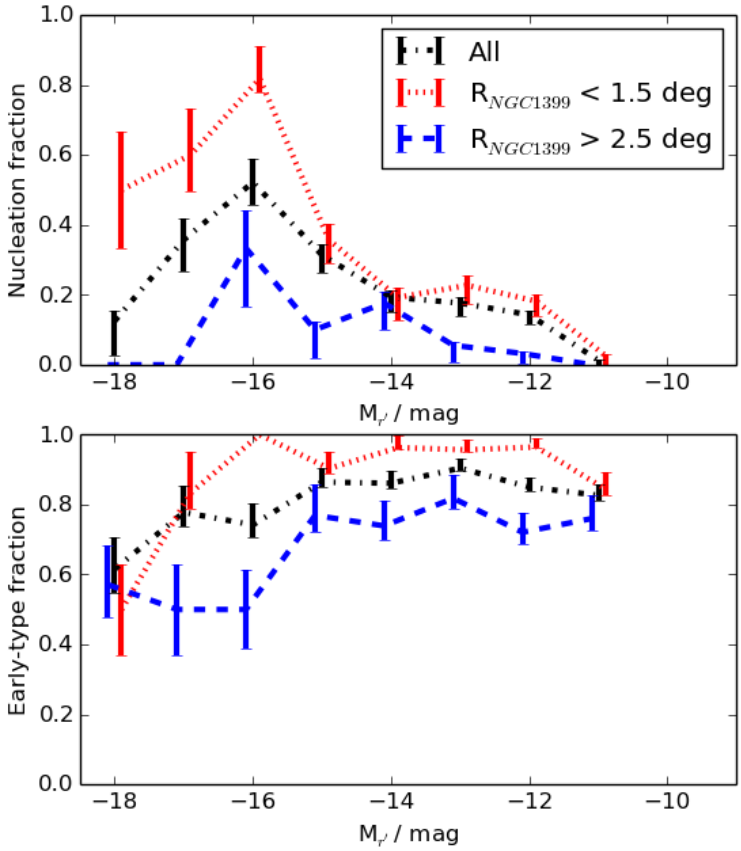

Figure 4.9: Nucleation fractions as a function of absolute r'-band magnitude at different cluster-centric radii. The red dotted, blue dashed, and black dash-dotted lines show the nucleation fraction within 1.5 deg and outside 2.5 deg from the cluster center, and for all galaxies, respectively.

deg (Bin 3), and the galaxies within 1 deg from the Fornax A group (Bin A). In all spatial bins we make a histogram of the galaxy luminosity distribution and fit it with a Schechter function (Schechter 1976):

$$n(M)\mathrm{d}M = 0.4\ln(10)\phi^* \left[10^{0.4(M^*-M)}\right]^{\alpha+1} \exp\left(-10^{0.4(M^*-M)}\right)\mathrm{d}M, \quad (4.6)$$

where ϕ^* is a scaling factor, M^* is the characteristic magnitude where the function turns, and α is the parameter describing the steepness of the low luminosity end of the function. We only fit the galaxies with magnitudes between -18.5 mag $<$ M$_{r'}$ $<$ -10.5 mag, since their parameters can be well trusted and where our sample is at least 50% complete even in the faintest bin.

The completeness of a sample is often defined by finding the surface brightness and size limits where at least 50% of the galaxies having those parameters are

included. This means that, for a given magnitude and surface brightness we have a certain probability of detecting a galaxy, which probability decreases near the completeness limits, and causes a bias to the sample. Another bias may be caused by the selection limits of the galaxy sample. As we show in the Appendix 4.10.1 (Fig. 4.22), around $M_{r'}$ = -12 – -10 mag galaxies with very small or very large R_e start to be excluded due to the detection limits. To correct for the completeness bias, a magnitude dependent completeness correction can be applied to the luminosity function. This correction thus scales up the number of galaxies especially in the lowest luminosity bins where the sample is the most incomplete. However, there is a caveat in this approach: as galaxies with a given magnitude, have a range of surface brightnesses, and the completeness drops towards lower surface brightnesses, the completeness of the galaxies is thus dependent on the galaxies' surface brightness distribution. Venhola et al. used flat R_e and $\bar{\mu}_{e,r'}$ distributions within the ranges of R_e=100 pc – 3 kpc and $\bar{\mu}_{e,r'}$= 22–30 mag arcsec^{-2} for defining the completeness of the FDSDC detections. As there is no way to know the surface brightness distribution of the galaxies that are too faint to be detected, the only way to make the completeness correction is to assume some distribution as Venhola et al. did. Due to these uncertainties in the completeness corrections, we make the luminosity function fits both without any corrections and by correcting the luminosity bins for the completeness according to the completeness tests by Venhola et al. (2018). As Venhola et al. showed, the FDSFC sample misses some known LSB galaxies in the Fornax cluster, and therefore the real slope of the luminosity function is likely to be somewhere between the values found for the completeness corrected and non-corrected luminosity functions.

In Fig. 4.10 (upper panels) we show the luminosity functions and the corresponding Schechter fits in the four spatial bins. Shown separately are also the luminosity functions for the different morphological types (lower panels). From the raw data we obtain the faint end slopes of α = -1.14±0.10, -1.13±0.06, -1.25±0.13 and -1.44±0.13 in the bins from the innermost to the outermost, and with the completeness corrections α = -1.31±0.07, -1.27±0.05, -1.38±0.11 and -1.58±0.16, respectively. The Schechter fits for the dwarf galaxies give similar faint end slopes in the three bins located in the main cluster area. Apparently, Fornax A differs from the other bins, showing a power-law like distribution. The difference can be also clearly seen from the cumulative luminosity functions shown in Fig. 4.11. The peculiar luminosity function of Fornax A can be related to the massive stellar streams around NGC 1316 (see Iodice et al. 2017b), of which some may originate from disrupted dwarf galaxies. However, due to the small number of galaxies we cannot robustly exclude the possibility that the underlying distribution in Bin 4 is similar to the other bins (see Table 4.2), and we do not see the exponential part of the function due to the low number of galaxies. The luminosity functions of different morphological types look qualitatively similar in all four bins, except that the number of dE(N)s decreases towards the outskirts of the cluster.

In the upper left panel of Fig. 4.10, we also show (with the red line) the luminosity function after removing the late-type dwarfs that are likely to appear in the central parts of the cluster only due to the projection effects. This correction

further flattens the faint end slope of the luminosity function, compared to the completeness corrected value.

The faint end slope of the luminosity function in the center of the Fornax cluster have been studied by Hilker et al. (2003) and (Mieske et al. 2007). Both of those studies apply a completeness correction and find a slope of α = -1.1$\pm$0.1, which is consistent with the faint end slope that we find in the center of the cluster when the completeness correction is not applied or when the late-type dwarfs are excluded. Our completeness corrected value of α is slightly steeper than theirs.

For comparison, Ferrarese et al. (2016) who measured the faint end slope in the core of the Virgo cluster using the NGVS galaxy sample, find a completeness corrected α = -1.34$^{+0.017}_{-0.016}$, which is in good agreement with our value (-1.31$\pm$0.07). For the NGVS the luminosity function in the outer parts of the Virgo cluster has not been studied. Other works, including also the outer parts of the Virgo cluster, have shallower observations than ours, and there is no clear consensus about the slope in the outer parts (see the discussion of Ferrarese et al. 2016). In the Coma cluster, which is an order of magnitude more massive than Virgo and Fornax clusters, Bernstein et al. (1995) measure α =-1.42$\pm$0.05, which is consistent within the errors with the values obtained by Ferrarese et al. in the Virgo and by us in the Fornax cluster. Ferrarese et al. (2016) also study the luminosity function in the Local Group using similar sample selection criteria as they used in Virgo, but without applying the completeness correction, and obtain a faint end slope of α = -1.22$\pm$0.04. The obtained value is slightly shallower than in the clusters. An additional study that has a similar depth as the above mentioned ones is by Trentham & Tully (2002), who analyze the mean faint-end slope (-18 mag $<$ M_R $<$ -10 mag) of the luminosity functions in 5 different groups and clusters including Virgo and Coma clusters. Like us, they also made the membership classifications for the faint-end galaxies based on their optical morphology, but did not apply any completeness correction for the luminosity function fitting. They found a mean slope of α = -1.2. Interestingly, the differences between the faint-end slopes of the luminosity functions in these different environments are smaller than the difference between the completeness corrected and non-corrected α-values in the Fornax cluster, which indicate that these differences might emerge artificially from the correction.

The faint end slopes of the early-type galaxy luminosity functions in Hydra I, α = 1.13 $\pm$ 0.04, and Centaurus clusters, α = 1.08 $\pm$ 0.03, were studied by Misgeld et al. (2008) and Misgeld et al. (2009), respectively. In these two works the luminosity functions have been corrected the same way as Hilker et al. (2003) did in the Fornax cluster. The faint-end slopes that they find are similar to the value we found for the early-type dwarfs in the center of the Fornax cluster, α = 1.09 $\pm$ 0.10.

From our data we conclude that the luminosity function does not change significantly in different parts of the Fornax cluster nor between the compared environments. A caveat in our analysis of the Fornax cluster is that our imaging extends only slightly outside the virial radius. To further consolidate the universality of the luminosity function, one should have a control sample further away from the Fornax cluster center.

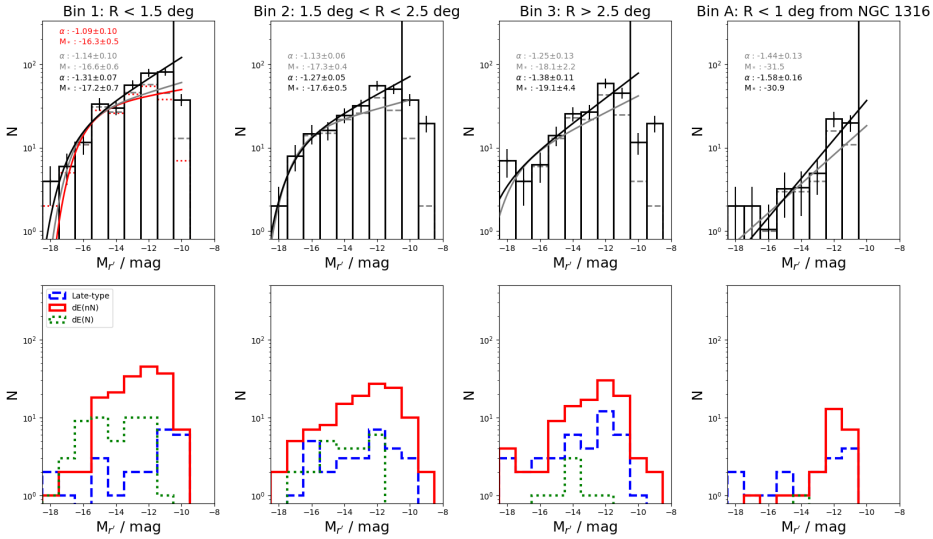

Figure 4.10: Four upper panels show the luminosity function in the different spatial bins around the Fornax main cluster and the Fornax A group. At the distance of the Fornax cluster 1 deg corresponds to 350 kpc. The grey dashed histograms show the observed number of galaxies, and the black histograms show the numbers after correcting for the completeness. The black vertical lines indicate the 50% completeness limit of our catalog. The grey and black curves shows the fitted Schechter function for the observed and completeness corrected luminosity functions, respectively, and the red line in the upper left panel shows the fit for the innermost bin, when the late-type galaxies are excluded from the fit. The fit parameters of each bin are shown in the upper left corner of the panels with the colors corresponding to the colors of the fitted functions. The lower panels show the luminosity distribution for the different types of galaxies in the bins.

Table 4.2: Kolmogorov-Smirnov-test p-values for the hypothesis that given two luminosity distributions are drawn from the same underlying luminosity function. The bins correspond to different cluster-centric distances so that Bin 1 includes galaxies within R $<$ 1.5 deg from NGC 1399, Bin 2: 1.5 deg $<$ R $<$ 2.5 deg, and Bin 3: R $>$ 2.5 deg. Bin 4 includes the galaxies within 1 deg from the NGC 1399.

	Bin 1	Bin 2	Bin 3
Bin 2	0.83		
Bin 3	0.98	0.50	
Bin 4	0.11	0.229	0.31

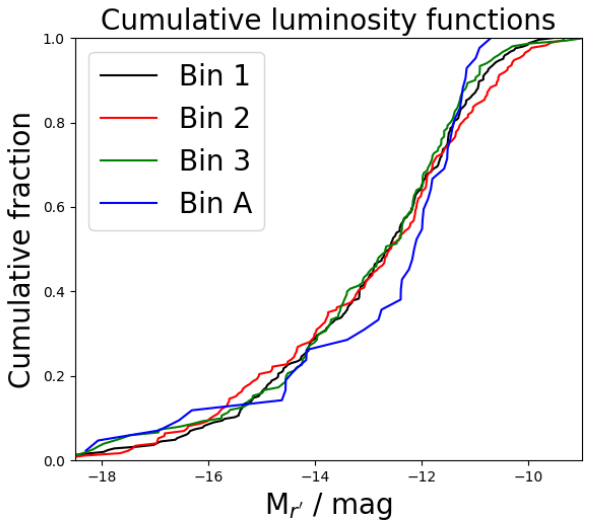

Figure 4.11: Cumulative luminosity functions in the bins defined in the Fig. 4.10.

4.5 DWARF GALAXY STRUCTURE

4.5.1 STRUCTURAL SCALING RELATIONS

In Fig 4.12 we show the measured structural parameters of the galaxies in our sample as a function of their total absolute r'-band magnitude $M_{r'}$. Both for the late- and early-type galaxies the parameters show correlations with $M_{r'}$. In the size-magnitude plane (top panels in Fig. 4.12) the late-type galaxies show almost linear relation between $M_{r'}$ and $\log_{10} R_e$, whereas the early-type galaxies show a knee-like behaviour so that while the galaxies with -18 mag $< M_{r'} <$ -14 mag have nearly constant R_e, the galaxies fainter than that become smaller. One should keep in mind that the largest galaxies among those fainter than $M_{r'}$ = -14 mag might not be detected[4] because of their low $\bar{\mu}_{e,r'}$. Thus the knee might be partially reflecting the completeness limits of our sample. However, the increased number of small dwarfs ($R_e < 0.5$ kpc) among the low luminosity galaxies is not due to any selection effect. We do not find significant differences between the scaling relations of dE(N) and dE(nN). The different relations between $M_{r'}$ and R_e of the early- and late-type galaxies can also be seen in the mean effective surface brightnesses $\bar{\mu}_{e,r'}$. The late-type dwarfs with $M_{r'} >$ -14 mag have brighter $\bar{\mu}_{e,r'}$ than the corresponding early-types, but for the galaxies brighter than that, the order changes.

The bottom panels of the Fig. 4.12 show the Sérsic n parameters of the galaxies as a function of $M_{r'}$. Sérsic n describes the shape of the galaxy's radial intensity profile so that $n = 1$ corresponds to an exponential profile, whereas larger values

[4]We will study those LSB galaxies in more detail, in a future paper (Venhola et al., in preparation), in which we use a new algorithm to detect those galaxies.

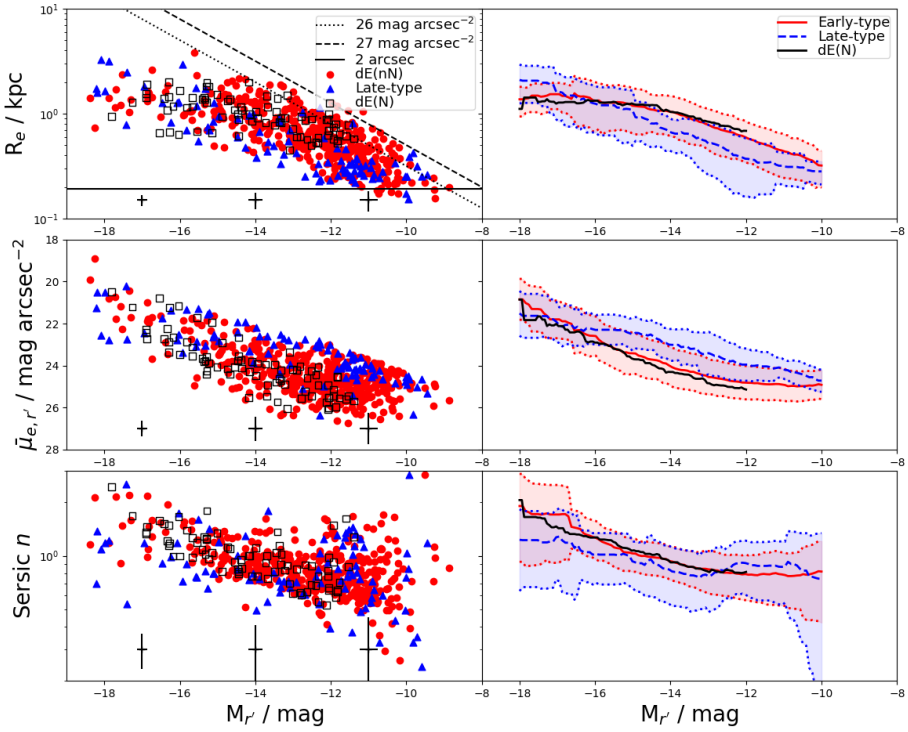

Figure 4.12: From top to bottom, the panel rows show effective radii (R_e), mean effective surface brightness in r'-band ($\bar{\mu}_{e,r'}$), and Sérsic indices (n) for our sample of galaxies as a function of their total r'-band absolute magnitude ($M_{r'}$). The left panels show the individual galaxies, and the right panels show the running means of three different types using a filter size of $\Delta M_{r'} = 0.5$ mag. The blue, red, and black symbols and lines correspond to late-type dwarfs, dE(nN)s, and dE(N)s, respectively. The shaded areas in the right panels correspond to the standard deviations of the points using the same running filter as for the means. For readability, we do not show the standard deviations of the dE(N)s, but they are similar to the ones of dE(nN)s. The black crosses in the left panels show the typical errorbars associated to the values at given magnitudes.

mean increased peakedness of the center. The values less than one correspond to a flatter profile in the center. The Sérsic indices are taken from the GALFIT models, which take into account the PSF convolution, and thus prevent artificial flattening of the galaxy centers for small and peaked galaxies. As mentioned before, the early-type galaxies in the magnitude range between -14 mag $>$ $M_{r'}$ $>$ -18 mag have nearly constant R_e. However, for these morphological types the Sérsic index in this magnitude range grows from $n \approx 1$ to $n \approx 2$, which means that the brighter galaxies become more centrally concentrated. A similar trends between Sérsic index and absolute magnitudes of the early-type dwarfs have also been found in Hydra I (Misgeld et al. 2008) and Centaurus (Misgeld et al. 2009) clusters. The fainter galaxies have nearly constant Sérsic n. For the late-types, the Sérsic n grows slower than for the dEs, from slightly below one to slightly above one with increasing luminosity. As the $M_{r'}$-n relations are different for the two types, the Sérsic n of $M_{r'} <$ -15 mag galaxies are higher for dEs than late-types, whereas for the galaxies fainter than that they are similar.

4.5.2 AXIS-RATIOS

In Fig. 4.13 we show the apparent minor-to-major axis ratio b/a distributions of the different types of dwarf galaxies in our sample. It is clear that the b/a distributions move closer to unity in a sequence from late-types to dE(nN)s and dE(N)s. Qualitatively this can be interpreted as galaxies becoming rounder.

In order to more accurately quantify the shape distributions, we need to take into account the fact that we observe a 2D projection of the intrinsic 3D shape distribution of the galaxies. We use the same deprojection method as Lisker et al. (2007)(described in detail in Appendix 4.10.3) for obtaining the intrinsic minor-to-major axis ($c/a = q$. In order to do the deprojection, we need to assume that the whole galaxy distribution consists of either prolate or oblate spheroids. In the middle panels of Fig. 4.14, we show the q distributions for both prolate and oblate cases.

To judge whether the galaxies are better described by prolate or oblate spheroids, we can study the relation between their b/a and differential surface brightness $\Delta\bar{\mu}_{e,r'}$. By $\Delta\bar{\mu}_{e,r'}$ we mean the difference in the surface brightness with respect to the mean surface brightness of galaxies with the same morphological type and luminosity. For oblate spheroids, $\Delta\bar{\mu}_{e,r'}$ brightens with decreasing b/a, since when b/a=1 we see the system through its shortest axis. For prolate systems there should be an anticorrelation between those quantities since when b/a=1, we look through the longest axis of the system. The relations between b/a and $\Delta\bar{\mu}_{e,r'}$ are shown in the right panels of the Fig. 4.14. We also tested the statistical significance of these correlations using Spearman's rank correlation test that is robust for outliers. We find that for the dEs, the trends behave as expected for oblate spheroids, but for late-types there is no correlation with b/a and $\Delta\bar{\mu}_{e,r'}$. The lack of correlation for the late-types can be explained if they have a significant amount of dust in their disks, which attenuates the light when observed edge-on. We argue that this is likely the case, since late-types, by definition, are gas-rich, star-forming systems, which are typically disks.

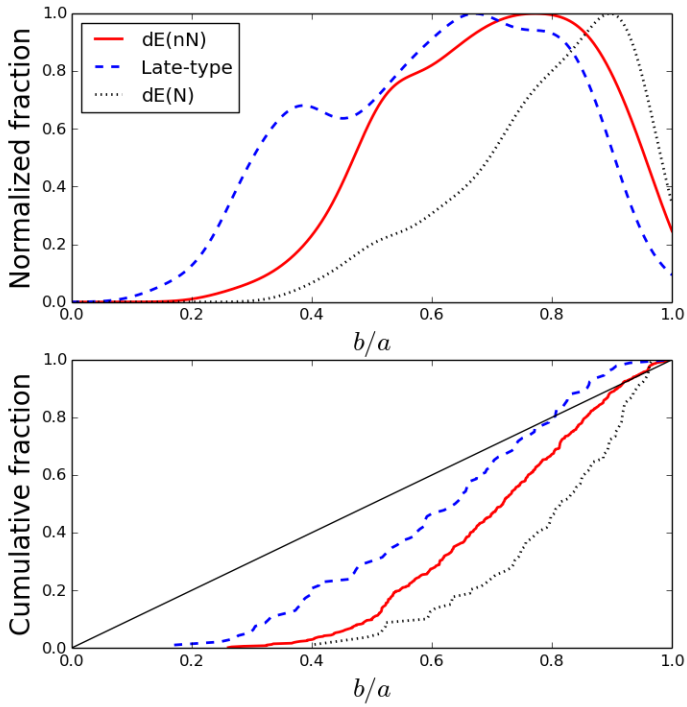

Figure 4.13: Axis ratio distributions of the dE(nN)s, dE(N)s, and late-type dwarfs are shown with the red, black and blue histograms, respectively. The upper panel shows the normalized distributions and the lower panel shows the cumulative ones. The diagonal line in the lower panel represents a flat b/a distribution.

Assuming that all the dwarfs are oblate spheroids, the mode of q grows from 0.3 of the late-types, to 0.5 of dE(nN)s and 0.8 of dE(N)s. This means that the disks of the galaxies become thicker in the same order.Taking into account that the dEs appear deeper in the cluster than the late-types (Section 3.2), the disks of the galaxies become thicker towards the inner parts of the cluster. Since the nucleus and Sérsic components are fitted separately for the dE(N)s, the nucleus does not bias the b/a distribution of those galaxies.

In the Virgo cluster, the b/a-distributions were analyzed by Lisker et al. (2007) and Sánchez-Janssen et al. (2016). Lisker et al. (2007) studied the b/a distributions of the M_B <-13 mag early-type dwarfs. They analyzed dE(N)s and dE(nN)s similarly to us, but they divided their galaxies into bright and faint dEs with the division at M_r=-15.3 mag. Since most of the dE(nN)s in our sample are fainter than that magnitude limit and most dE(N)s are brighter, it makes sense to compare our b/a-distributions with the "dE(N) bright" and "dE(nN) faint" samples of Lisker et al. The distribution of q of dE(N)s in the Fornax cluster shows a similar potentially double-peaked distribution as the one found by Lisker et al.. A small difference between the distributions is that, in the Fornax sample, the galaxies are

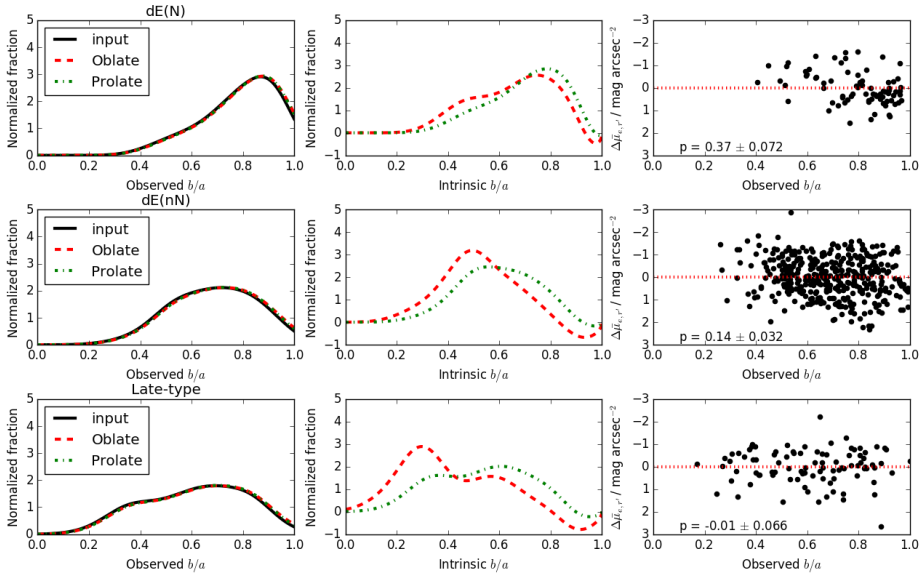

Figure 4.14: Intrinsic shape distributions deduced from the observed b/a distributions. The left panels show the observed b/a distribution with the black lines, and the reprojected b/a distributions obtained from the modelled intrinsic shape distributions with the red dashed and the green dash-dotted lines for an oblate and prolate models, respectively. The middle panels show the intrinsic minor-to-major axis (q) distributions obtained via modelling for the oblate and prolate models. The right panels show the relation of the difference from the magnitude-surface brightness relation with the observed axis ratio. The Spearman's rank correlation coefficient p and its uncertainty are reported in each scatter plot. The rows from top to bottom show the analysis for dE(N), dE(nN) and late-type dwarfs, respectively.

more abundant at the peak located at q=0.8, whereas in Virgo the more dominant peak is at q=0.5. Also the dE(nN) distributions are very similar in the two clusters, both of them showing a clear a peak at q=0.5. Sánchez-Janssen et al. (2016), who also study the b/a distribution of the dwarf galaxies projected in the center of the Virgo cluster, did not divide dEs into different morphological sub-groups. Their sample is complete down to $M_{g'} > -10$ mag. Their b/a distribution is qualitatively very similar to the one of dE(nN)s in our sample. As the dE(nN)s are the most abundant type of galaxies in our sample, we conclude that there are no significant differences between the isophotal shapes of dEs in the Virgo and Fornax clusters.

4.5.3 EFFECTS OF THE ENVIRONMENT ON THE DWARF GALAXY STRUCTURE

If the environment plays an important role in galaxy evolution we should see the galaxies of the same luminosity to have different structures and/or stellar populations depending on their locations in the cluster. In Fig. 4.15, we divide our sample into four magnitude bins, and study how the galaxy properties vary as a function of their cluster-centric distance. We study the radial trends in the same three cluster-centric bins as in Fig. 4.10. According to Section 3.2, the late type galaxies with projected cluster-centric distances R<1.5 deg are likely to have 3D distance larger than 1.5 deg, and the dE(nN)s projected within the inner R<0.8 deg, are likely to have 3D distance larger than 0.8 deg. Thus, we perform the cluster-centric trend analysis also by excluding those galaxies. In Fig. 4.15, we show the radial trends for all galaxies (purple lines) and for the galaxies remaining after excluding the galaxies from the inner parts of the cluster that are likely to appear there only due to the projection effects (the green lines). We also test the significance of all the correlations using the Spearman's rank correlation test, and show the correlation coefficients in the panels of Fig. 4.15. We base our analysis on the values that are obtained by removing the likely projection bias (green lines). All the bin means and the corresponding uncertainties are tabulated in Appendix 4.10.6 in Table 4.3.

In Fig. 4.15, we find that some of the parameters behave similarly with respect to the cluster-centric distance in all the luminosity bins, and some parameters have different trends for the high ($M_{r'}$ <-16.5) and low luminosity ($M_{r'}$ >-16.5) galaxies. For all the mass bins, the mean g'-r' colors of the galaxies become redder and the Residual Flux Fraction (RFF) decreases when going inward, meaning that the galaxies in the center are smoother than the galaxies in the outer parts. For the low luminosity dwarfs, R_e becomes larger, and $\bar{\mu}_{e,r'}$ systematically fainter from the outer parts towards the cluster center. For the bright dwarfs R_e becomes smaller, Sérsic n larger, and $\bar{\mu}_{e,r'}$ stays constant from the outer parts towards the cluster center. An important observation is that these cluster-centric trends are dependent on the galaxy mass.

Janz et al. (2016a) found that the low-mass galaxies outside the clusters are larger than the similar mass galaxies in the Virgo cluster. If we assume that galaxies gradually decrease in size, not only while entering the cluster, but also within the cluster, becoming smaller towards higher density regions, we would

expect to see the same trend in our study. This trend seems to appear among the brightest dwarf galaxies in our sample, but not among the fainter ones that comprise the majority of the galaxies. As the smallest galaxies of Janz et al. have stellar masses of a few times 10^7 $M_\odot$ (similar to our bright dwarfs), our results for the bright dwarfs are consistent with the results of Janz et al. in the mass range they studied.

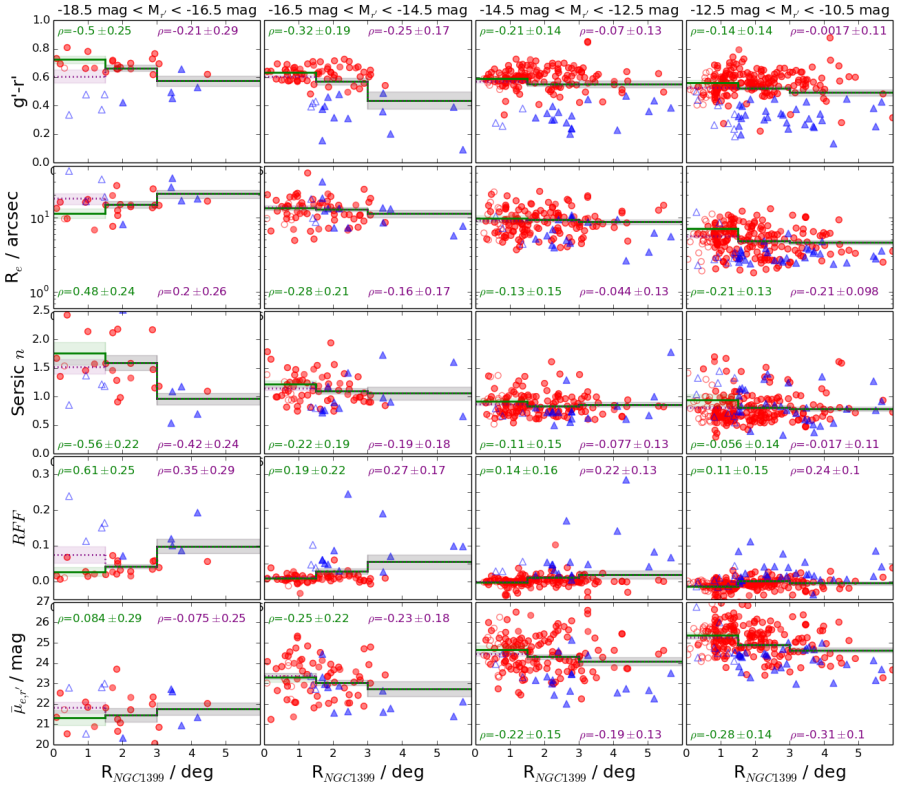

Figure 4.15: Panel rows from top to bottom show the g'-r' color, effective radius (R_e), Sérsic index (n), Residual Flux Fraction (RFF), and the mean effective surface brightness ($\bar{\mu}_{e,r'}$) of the Fornax dwarf galaxies as a function of their cluster-centric distance. The columns correspond to different luminosity bins. The lines and shaded areas show the bin means and uncertainties of the mean for the parameters. The green and purple colors correspond to the values when the projection effects are taken in account (dE(nN)s and late-types excluded from the inner parts as found in Section 3.2), and when raw data is used, respectively. The late-type and early-type dwarfs are shown with the blue and red symbols, respectively. The unfilled symbols correspond to the galaxies excluded from the inner parts in order to minimize the projection bias. The ρ parameter indicates the Spearman's correlation coefficient for the correlation of the parameter with distance, and its uncertainty.

4.6 COLORS OF THE DWARF GALAXIES

4.6.1 COLOR-MAGNITUDE RELATION

In Fig. 4.16 we show the color-magnitude (CM) relations of the galaxies in the Fornax cluster. We show separately dE(nN), dE(N) and late-type galaxies. It is obvious that the morphologically selected late-type galaxies are bluer than early-types in all the CM relations. In addition to their offsets, the relations of the early- and late-type galaxies show also different slopes. The CM relations of the late-type galaxies are rather flat, so that there is not much correlation with the magnitude, whereas the early-type galaxies become bluer with decreasing total luminosity in all colors. Since the early-type galaxies become bluer towards lower luminosity, the late- and early-type galaxies have almost similar colors in the low luminosity end. This phenomenon is particulary visible in the colors including the u'-band. The dE(N)s seem to follow the same CM relation as the dE(nN)s.

4.6.2 DEPENDENCE ON THE ENVIRONMENT

We have already shown that the early-type galaxies are redder than the late-type systems, and that their fraction increases towards the inner parts of the cluster. This makes the average color of the galaxies in the center of the cluster to be redder than in the outer parts. Here we concentrate on the early-type galaxies in order to see if we see possible environmental dependency also on their colors separately (see Fig. 4.17).

To test this, we divided our early-type galaxy sample into three spatial bins and measured their CM relations using a running mean in each bin. We measured separately the galaxies within two core radii, within the virial radius, and outside that. The CM relations in the different spatial bins, and the CM relations in the core of the Virgo cluster (Roediger et al. 2017) for comparison, are shown in Fig. 4.17. We transformed the MegaCAM magnitudes used by Roediger et al. into the SDSS ones by using the formulas provided at the MegaCAM web pages (`http://www1.cadc-ccda.hia-iha.nrc-cnrc.gc.ca/community/CFHTLS-SG/docs/extra/filters.html`). We find that when compared with Roediger et al. (2017), the CM relation in the inner bin of the Fornax cluster is in good agreement with the galaxy colors in Virgo in all the colors except in g'-i, where there is an offset of $\approx$0.1 mag, between -14 mag $< M_{g'} <$ -10 mag. As there is some uncertainty related to the filter transformations, we do not want to over-interpret the physical meaning of the offset. Within the accuracy of our measurements, we find that the CM relations of the early-type galaxies are similar in the cores of the Virgo and the Fornax clusters.

When comparing the CM relations within the Fornax cluster, we find that for a given magnitude the u'-g', u'-r', and u'-i' colors become redder towards the inner parts of the cluster, whereas for g'-r' no significant differences are seen. Since the u'-band covers a wavelength range on the blue side of the Balmer jump at 4000 Å, it is very sensitive to ongoing or recent star formation. It seems that, regardless of the fact whether the low-mass galaxies in the outer parts of the cluster are

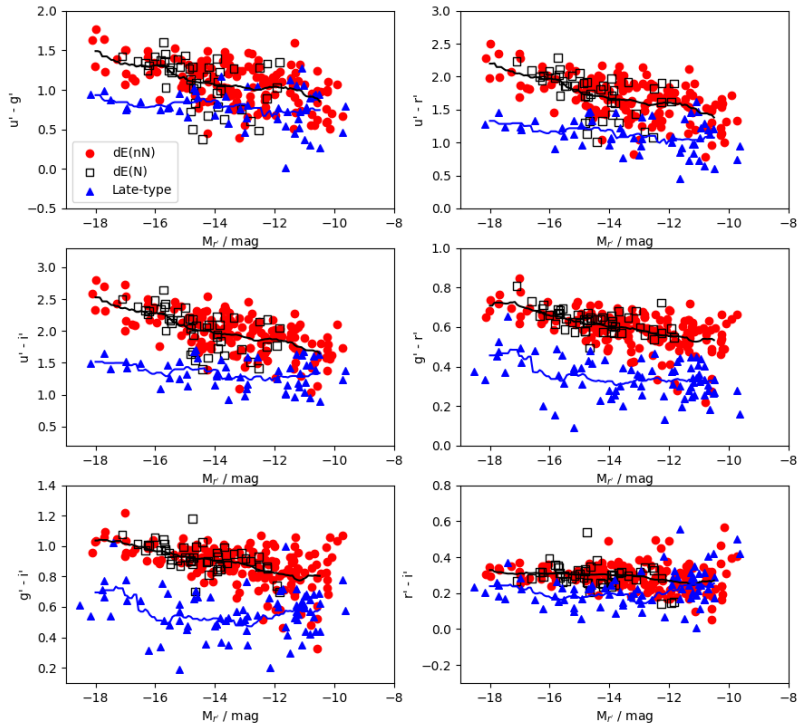

Figure 4.16: Color-magnitude relations of the galaxies in the Fornax cluster. The blue and red symbols correspond to the late-type galaxies and dE(nN)s, respectively, and the black squares correspond to the dE(N)s. The black and blue lines show the 2σ-clipped running means for late-types and dEs, respectively, with a kernel width of 1.6 mag.

classified as dEs or not, they are on average younger than the dEs in the inner parts of the cluster. Furthermore, this color difference might be intrinsically even more significant than we observe, since as shown in Section 3, we see the galaxies in projection, which causes some of the galaxies apparently located in the cluster center to actually in the outskirts of the cluster.

Radial color trends in the Fornax cluster were also found for the giant ETGs by Iodice et al. (2019). They showed that the giant ETGs that are located within projected distance of $\approx$ 1 deg from the cluster center are systematically redder than the galaxies outside that radius. This trend is thus similar as the dwarfs have, but the color difference of the giant ETGs is also clear in the g'-r' and g'-i' colors, which is not the case for the dwarfs.

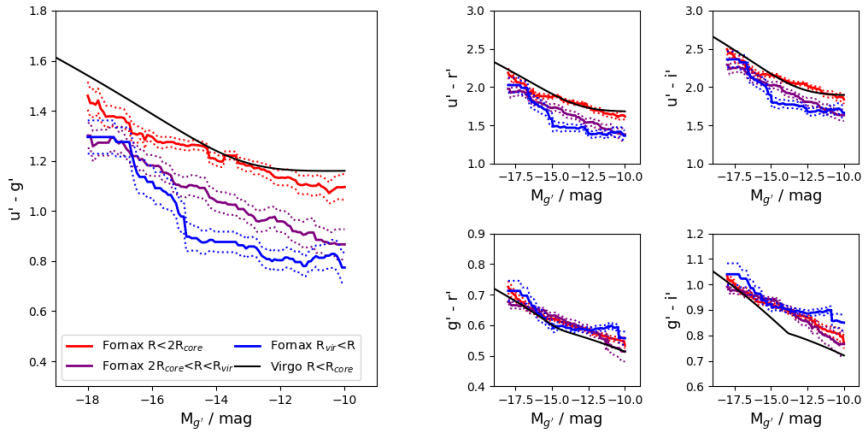

Figure 4.17: The panels show the running means of the color-magnitude relations in different colors for the dEs. The red, purple and blue lines corresponds to inner, middle and outer bins in the Fornax cluster, respectively. The black lines show the Roediger et al. (2017) color-magnitude relation in the core of the Virgo cluster. We use the g'-band absolute magnitudes on the x-axis instead of r'-band, since the analysis for the Virgo was done using g'-band.

4.7 DISCUSSION

In the previous sections we have extensively studied the structures, colors, and distributions of dwarf galaxies in the Fornax cluster. When similar observations are available in the literature, we have also compared our measurements with those. In the following sub-sections we discuss how these observations can be understood in the context of galaxy evolution.

4.7.1 HOW DO THE PROPERTIES OF THE DWARF GALAXIES CHANGE FROM THE OUTSKIRTS TO THE CORE OF THE FORNAX CLUSTER?

We studied how the properties of the dwarf galaxies in the Fornax cluster change as a function of the cluster-centric distance, and found the following changes in their structure and colors:

- For all the galaxies, their colors become redder (Sections 5.3 and 6.2, Fig. 4.15 and Fig. 4.17) and RFF decreases when moving inward, i.e. they become more regular.
- For the low-luminosity dwarf galaxies ($M_{r'}$ > -16 mag), R_e grows, and $\bar{\mu}_{e,r'}$ fades towards the inner parts of the cluster (Fig. 4.15).
- For the brightest dwarfs, their $\bar{\mu}_{e,r'}$ stays constant, Sérsic n increases and R_e decreases towards the inner parts of the cluster Fig. 4.15).

- The shape of the galaxies become rounder (Section 5.2) in a sequence from late-types, to dE(nN)s to dE(N)s. As the galaxies are also mostly located at different cluster-centric radii in that same order, the mean cluster-centric distance decreasing from late types to dE(N)s (Section 3.2), we can conclude that the shapes of the galaxies become rounder towards the inner parts of the cluster.

We found that the luminosity function remains constant in the different parts of the cluster (Section 4.2), but the fractions of the relative contributions of the morphological groups change. The least centrally concentrated are late-type dwarfs, then dE(nN), and dE(N) (Section 3.2). When taking into account the projection effects, we found that there are probably no late-type galaxies within 1.5 deg from the cluster center, and no non-nucleated dEs within the innermost 0.8 deg of the cluster. This innermost area of the cluster is densely populated by giant ETGs (Iodice et al. 2019) and intra-cluster X-ray gas (Paolillo et al. 2002), and in this area also asymmetric outer parts have been detected in the giant ETGs (Iodice et al. 2019), indicating strong tidal forces in that area. The ETGs in the center of the cluster are also systematically redder than the giant ETGs outside that dense core, indicating that their star formation was quenched early on (Iodice et al. 2019). These observations, combined with the structural trends strongly suggest that the cluster environment is transforming the dwarf galaxies both structurally and morphologically, and that these transformations are not independent of the galaxy mass.

4.7.2 WHAT CAUSES THE CLUSTER-CENTRIC RELATIONS?

Unfortunately the current large-scale hydrodynamical simulations, like Illustris-TNG, cannot accurately model the galaxies with stellar masses of $M < 10^8$ $M_\odot$ due to resolution issues. However, we can still try to understand the mechanisms that are taking place in the Fornax cluster. If we make a simple assumption that the transformation of galaxies from star forming late-types to the quiescent early-types happens only through harassment or gas-stripping, what would we expect to see in the dwarf galaxy populations?

In the case of harassment, the high velocity encounters strip off material from the galaxies, but it is relatively inefficient in removing a significant number of stars (Smith et al. 2015). However, even if the harassment is not very important, it is known to slowly increase the Sérsic n of the galaxies, increase their surface brightness in the center, and make them redder, as the star formation stops (Moore et al. 1998, Mastropietro et al. 2005). The observational consequences of this process would then be that at a given mass, the galaxies become redder with brighter $\bar{\mu}_{e,r'}$, and increasing C. Harassment also heats the stars in a galaxy, resulting in thickening of its disk.

In the case of ram-pressure stripping, the stars are not affected, and thus their evolution after the gas-removal happens via fading of their stellar populations. A direct observational consequence of this would be that a galaxy with a given mass should become redder with fading $\bar{\mu}_{e,r'}$, while for C no correlation with color is expected.

A caveat in distinguishing these two scenarios from each other is that in a case where ram-pressure stripping is unable to remove all the gas from a galaxy, it will start working from outside in. This means that the gas is first stripped from the outer parts of the galaxy, and the star formation may still continue in the center. This process is able to accumulate more stellar mass into the galaxy center after its outer parts are quenched, and thus lead to higher surface brightness and increased peakedness of the luminosity profile. The stellar populations will be also younger in the galaxy center with respect to the outskirts. Some dwarf galaxies in the clusters indeed have negative color gradients and young centers (Urich et al. 2017), which may indicate this process being important as well. As these two processes, harassment and partial ram-pressure stripping, leave similar imprints to the galaxies and both work most effectively in the center of the cluster, it is not possible to distinguish between them from our observational data, but we can still distinguish between complete ram pressure stripping and the other scenarios.

Using our sample, we can test these theoretical predictions in a straightforward manner. In Fig. 4.18, we divide the galaxies in four luminosity bins to reduce the degeneracy caused by the luminosity correlations of the parameters, and, using these bins, compare the galaxy colors with their C and $\bar{\mu}_{e,r'}$. We test the significance of the correlations between those parameters also using Spearman's rank correlation test, and show the correlation coefficients of each bin in the corresponding panels. We find that the galaxies in the highest luminosity bin ($M_{r'}$ $<$ -16.5 mag) become redder with increasing surface brightness, whereas in the case of the less luminous galaxies, their $\bar{\mu}_{e,r'}$ fades while they get redder. The increase in C and surface brightness in the high-luminosity bin with increasing g'-r' is consistent with the harassment and imperfect ram-pressure stripping scenarios, whereas the low-luminosity galaxies are in agreement with the complete ram-pressure stripping showing no clear correlation between C and colors.

To confirm that the trend between the surface brightness and color for faint dwarfs is consistent with fading of the stellar populations, we show in Fig. 4.18 the evolutionary models of a single stellar population using the models of Vazdekis et al. (2010). We use a Kroupa initial mass function (IMF), and show the models for stellar populations with metallicities $\log_{10}(Z/Z\odot)$=0.0, -1.0 and -1.8 dex. The initial surface brightness of the stellar population models is set manually, but the colors are predicted purely by the model. We find that the relation between colors and $\bar{\mu}_{e,r'}$ of the $M_{r'} >$ -16.5 mag galaxies is roughly similar to the stellar population isochrones.

Since the use of luminosity bins may involve some bias caused by some red and blue galaxies moving from one bin to another, we also repeat the analysis in stellar mass bins. In Fig. 4.19 and Fig. 4.20, we show that the same trends between $\bar{\mu}_{e,r'}$, g'-r', and C as seen in the luminosity bins, are visible also when using mass bins.

As a summary, we find that the colors, C and $\bar{\mu}_{e,r'}$ of our galaxies are consistent with the scenario in which the most luminous dwarf galaxies ($M_{r'} <$ -16 mag) get quenched via harassment and/or by impartial gas stripping, since they become redder and their C increases with increasing surface brightness. The quenching of the low-mass galaxies is rather consistent with complete gas-stripping and

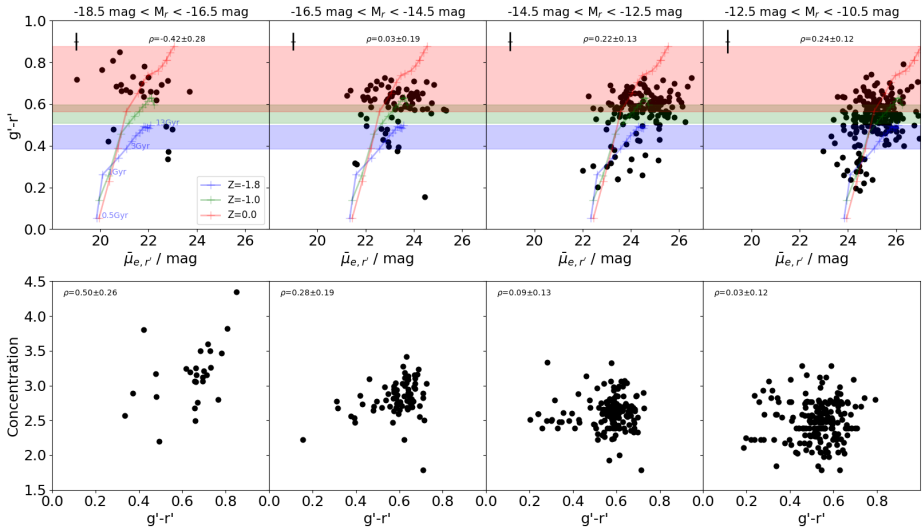

Figure 4.18: Upper and lower panels show the g'-r' color and the concentration parameter C of the galaxies as a function of their mean efffective surface brightness in the r'-band ($\bar{\mu}_{e,r'}$), respectively. The different columns show the relations for different luminosity ranges. The lines show the evolutionary track of single stellar population for a Kroupa-like IMF with metallicities of $\log_{10}$(Z/Z$\odot$)=0.0, -1.0 and -1.8 from 0.5 Gyr to 13 Gyr (the coloured dots on the lines correspond to 0.5, 1, 2, 3, 4,...,13 Gyrs). We have also shaded the color ranges corresponding the stellar population ages between 3 to 13 Gyrs with the colors matching the corresponding evolutionary tracks. The ρ-values reported in the upper part of the panels correspond to the Spearman's correlation coefficient and it's uncertainty calculated for the point in the corresponding panel.

subsequent fading. These two different mechanisms taking place in the different luminosity-ranges, can explain also why at the low-mass end (M$_{r'}$ > -14 mag) the late-type galaxies are smaller than the early-type galaxies, while in the low-luminosity end the opposite is true (see Fig. 4.12).

4.7.3 EFFECTS OF THE ENVIRONMENTAL PROCESSES

The properties of dwarf galaxies in our sample are consistent with a scenario in which the massive dwarfs are transformed by harassment and imperfect ram-pressure stripping, and the less massive by complete ram-pressure stripping. In order to confirm that this is indeed a physically feasible scenario, we next estimate the physical strengths of the different environmental processes using analytic formulae.

In the following calculations we assume the cluster to be a static entity whose potential and galaxy density does not change. This is clearly not true in time scales

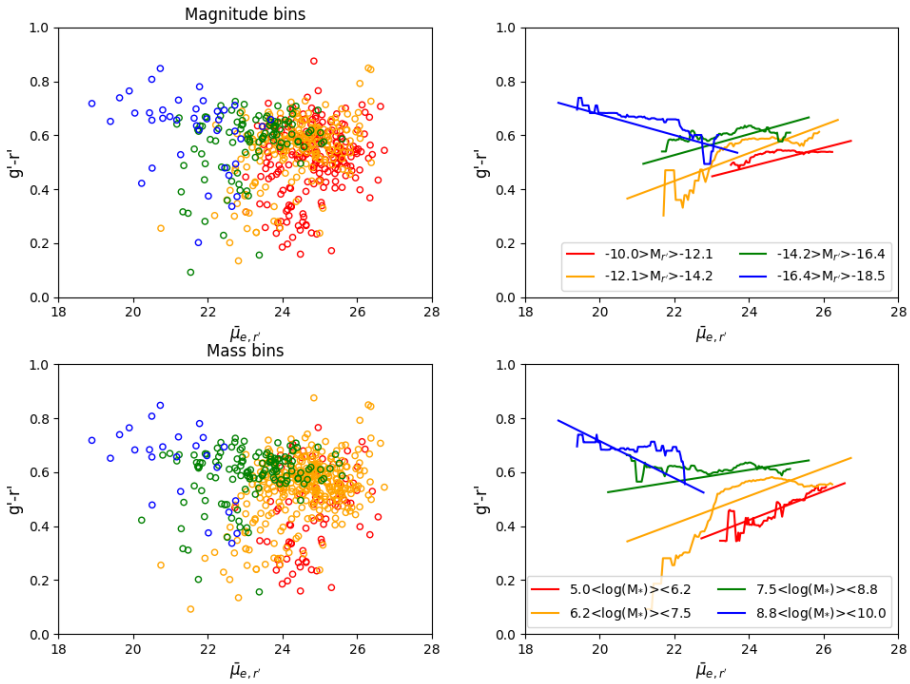

Figure 4.19: The left panels show the $\bar{\mu}_{e,r'}$ versus g'-r' relation for the individual galaxies, and the right panels show the running medians and linear fits for the different bins. In the upper panels luminosity bins are used, and in the lower panels mass bins are used.

of several Gyrs. However, the assumption of static cluster is necessary, since we lack information about the past evolution of the Fornax cluster and the analytical calculations would become difficult without such assumption. Thus, our following calculations are more accurate for processes that are effective in short time scales, and the results regarding longer time scales should be interpreted with caution.

4.7.3.1 RAM-PRESSURE STRIPPING

For estimating the strength of ram-pressure stripping, we follow the approach of Jaffé et al. (2018). The pressure between the hot intra-cluster gas and cold gas of an infalling galaxy, can be calculated using the relative speed of the galaxy with respect to the cluster Δv_{cl} and the density of the intra-cluster gas ρ_{ICM} (Gunn & Gott 1972)

$$P_{ram} = \rho_{ICM}(\Delta v_{cl})^2. \tag{4.7}$$

We estimate the radial gas density profile using the integrated gas mass profile from Paolillo et al. (2002) (Fig.17 of Paolillo et al.), which we approximate within

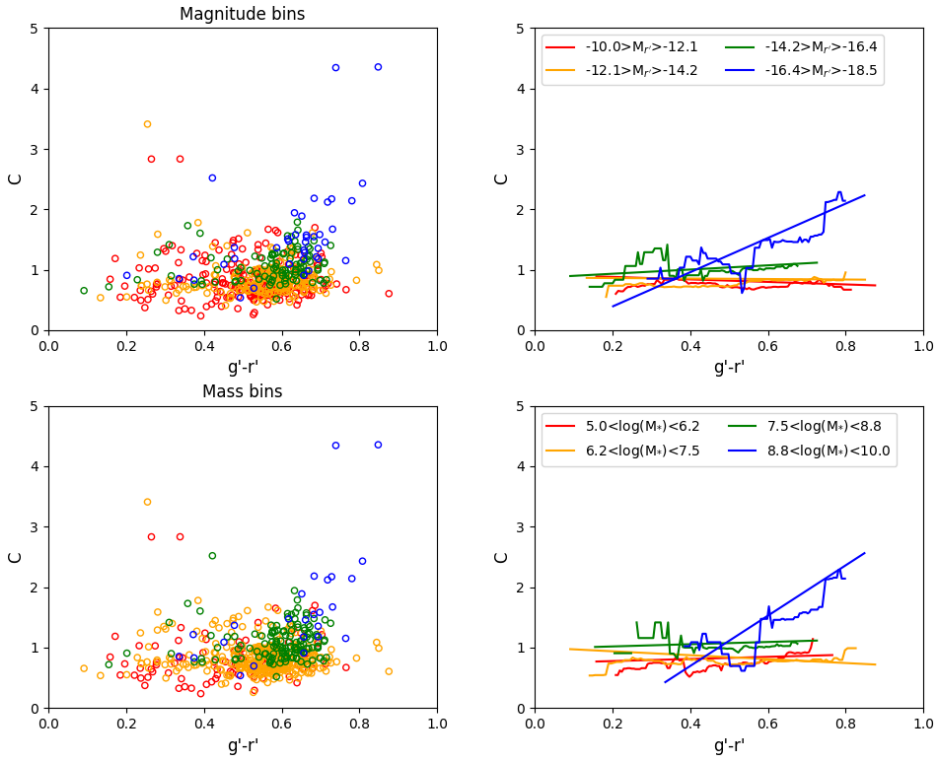

Figure 4.20: Same as Fig. 4.19, but shows C versus g'-r'.

1 deg from the cluster center with a power law $M(< R) = 5 \times 10^5 R^{1.5}$ M$_\odot$, where R is in arcsec.

In order to calculate how much gas of the galaxy gets stripped, we need to calculate the anchoring force per unit area of the gas in a galaxy, Π_{gal}. The upper limit of the anchoring force at the galacto-centric distance r' can be estimated by (Gunn & Gott 1972)

$$\Pi_{gal}(r') \; = \; 2\pi G \Sigma_s(r') \Sigma_g(r'), \tag{4.8}$$

where Σ_g and Σ_s are the surface density profiles of the gas and stars of the galaxy, respectively. We acknowledge that this analytical form gives only an upper limit for the anchoring force and it may thus lead to overestimating the radius where the gas can be bound within the galaxy. However, for our purpose it is not important to find the exact maximum radius where the gas can be bound, but to find the mass range where the galaxies can retain gas bound at least in their central parts. For simplicity, we estimate both the gas and stellar profiles of the galaxies with an exponential disk[5]

$$\Sigma_{s/g}(r') \; = \; \Sigma_{s/g,0} \exp\left(-r'/R_d\right), \tag{4.9}$$

[5]Exponential disk corresponds to a Sérsic profile with n=1.

where R_d is the disk scale length (corresponding to 1.678R$_e$), and $\Sigma_0 = M_d/(2\pi R_d^2)$, where M_d is the mass of the disk. For the stellar disk $M_{d,s}$ we use the masses from Section 2.2.1 and take R$_{e,s}$ from the r'-band Sérsic profiles. For the gas component we use the values from Popping et al. (2014), who found that the H$_I$ and H$_{II}$ masses for log(M$_*$/M$_\odot$) $\approx$ 7 galaxies are both on the order of 150% of the stellar mass. We realize that the relative fractions of the H$_I$ and H$_{II}$ masses and their total mass both depend on the stellar-mass of the galaxy (Catinella et al. 2018, Popping et al. 2014), but as we aim to make an order of magnitude estimate, we do not take these factors into account in our model. The gas extent is approximated to be $R_{d,g} = 1.7 \times R_{d,s}$, as found by Cayatte et al. (1994) for the Virgo gas-rich spirals. This results into $\Sigma_{g,0} = 0.3 \times \Sigma_{s,0}$.

Using the ρ_{ICM} and Π_{gal} profiles, we calculate the galacto-centric stripping radii R$_s$ (where $\Pi_{gal} = P_{ram}$), at the cluster-centric distances 0.3 deg and 1 deg for galaxies travelling with velocities of Δv_{cl} = 370 kms^{-1} and 550 kms^{-1}. As Π_{gal} depends on R_d, we use the mean R_d of a given galaxy mass for calculating R$_s$. The R$_s$ as a function of the galaxy mass are shown in the left panel of Fig. 4.21. We find that ram-pressure strips all the gas from galaxies with M$_* < 10^{7.5-8}$ M$_\odot$ that enter the sphere within the inner 1 deg ($\approx$0.5 R$_{vir}$) of the cluster. Ram-pressure is also capable of stripping the gas of more massive galaxies at galacto-centric distances larger than r=2-3 kpc, but a remarkable finding is that ram pressure-stripping cannot strip the gas of the M$_* >10^8$ M$_\odot$ galaxies from their inner $\approx$2 kpc areas. Thus, in order to get rid of the remaining cold gas of these massive dwarfs, either star-formation has to consume the gas, or tidal interaction play an important part in removing it.

There are some caveats in the analytic ram-pressure model adopted by us (see the discussion of Jaffé et al. 2018). The model assumes a disk-like galaxy that is falling into the cluster face-on, and does not take into account the dark matter potential. As we showed in the Section 4.2, the late-type dwarfs have rather low intrinsic q ratios, which supports the disk assumption. Roediger & Brüggen (2006) showed that the inclination angle of the infalling galaxy does not play a major role in the significance of the gas mass-loss in the ram-pressure stripping. Finally, the mass of the dark matter halo is not as flattened as the stellar disk, and Díaz-García et al. (2016) showed that only 4 % of the total mass of the dark matter halo is within the optical part of the disk. This means that DM does not significantly alter our estimation of the anchoring force in the disk plane. However, a larger DM halo clearly makes the potential well of the galaxy deeper, and thus makes it harder for the gas to escape from the halo. We argue that even if the gas does not escape from the halo, but is pushed significantly outside the stellar disk, it is likely to be stripped due to the tidal forces in the cluster that are effective outside a few effective radii (see the next sub-sections). Thus, we can likely rely on these ram-pressure stripping approximations at least as order of magnitude estimations of the removal of cold gas from the disk plane.

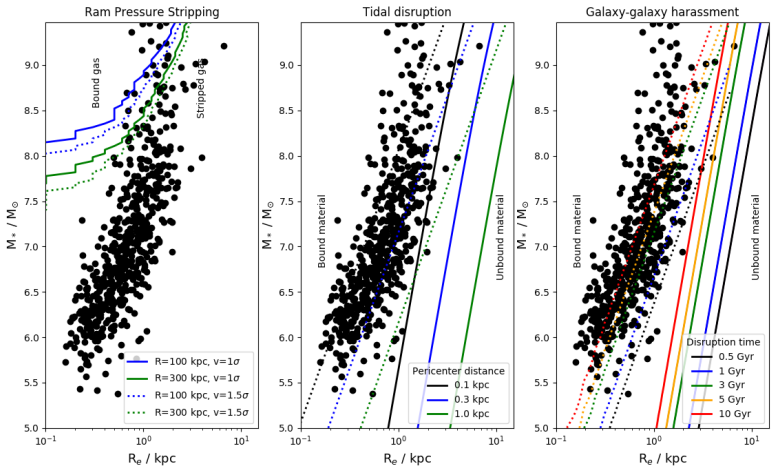

Figure 4.21: Effectiveness of the different environmental processes in the galaxy stellar mass-effective radius plane. The black points correspond to the FDSDC galaxies. The lines in the **left panel** shows the stripping radius as a function of galaxy's stellar mass. For the areas at the right side of the lines $\Pi_{gal} < P_{ram}$, and thus all the gas gets stripped. The blue and green lines show the stripping radii at the cluster-centric distances of 100 and 300 kpc ($\approx$ 0.3 deg and 1 deg), respectively, and the solid and dotted lines correspond to galaxy velocities of 370 kms^{-1} and 550 kms^{-1}, respectively. The lines in the **middle panel** shows the the relation between the tidal radius and galaxy mass for three orbits with different peri-center radii. The solid and dotted lines show the tidal radii for the galaxies when assuming DM-halo and without DM-halo, respectively. The solid and dotted lines in the **right panel** show the disruption times against harassment for the given mass and effective radius galaxies, when assuming a dark matter halo and when using only the stellar mass for the calculation, respectively.

4.7.3.2 TIDAL DISRUPTION FROM THE CLUSTER'S TIDAL FIELD

The effects of the tidal interactions on galaxy structure are difficult to quantify without using full galaxy simulations. However, we can calculate for a given orbit and galaxy mass what is the maximum galacto-centric radius where it can keep material gravitationally bound.

The tidal radius R_{tidal} is the maximum galacto-centric radius, where material can still be gravitationally bound to a galaxy. For an orbit with a cluster pericenter distance R_{peri} and eccentricity e, the tidal radius can be calculated as follows (King 1962, Wittmann et al. 2016):

$$R_{tidal} = R_{peri} \left(\frac{M_{obj}}{M_{cl}(< R_{peri})(3+e)} \right)^{\frac{1}{3}}, \tag{4.10}$$

where M_{obj} is the mass of the galaxy and $M_{cl}(< R_{peri})$ is the cluster's mass within the pericenter distance of the orbit from the cluster center. For the eccentricity of the orbit, e, we adopt a value of 0.5[6]. The R_{tidal} as a function of galaxy stellar mass are shown with the dotted lines in the middle panel of Fig. 4.21 for three orbits with different R_{peri}. It is evident that, if we only take into account the stellar mass of the galaxies, many galaxies should be tidally disrupted even on orbits with large pericenter distances. However, it is generally believed that dwarf galaxies are typically dark matter dominated, which has to be taken into account in the calculation. We adopt the stellar-to-halo mass relation of Moster et al. (2010) (see Appendix 4.10.4 for details) to estimate the halo masses of the sample galaxies. Since the DM-halo is more extended than the stellar component of the galaxies, we only take into account the DM-halo mass within 2R$_e$. Díaz-García et al. (2016) found that by multiplying the halo-to-stellar mass relation of Moster et al. by a factor of 0.04, the relation becomes consistent with the dark matter masses within the optical radii of the S^{4}G (Sheth et al. 2010) galaxies, estimated using the H$_I$ rotation amplitudes and stellar gravity fields calculated from 3.6 μm images. We thus use the Moster et al. DM masses multiplied by the factor of 0.04 in our calculations. We acknowledge that the harassment in the cluster affects also the DM halo, by stripping material out from it (Ryś et al. 2014, Smith et al. 2015). Therefore our estimations for the radii where the material can be gravitationally bound to the galaxies should be considered as upper limits. We show R_{tidal} where the dark matter contribution has been taken into account shown with the solid lines in Fig. 4.21. In this case, the material is bound to the galaxies up to the radius of r=2-3 R$_e$'s even on the orbit with the smallest pericenter distance. Analogously, this same test could be done to probe whether the dwarfs could survive in the cluster when Modified Newtonian Dynamics is applied. However, this is out of scope of this paper.

4.7.3.3 GALAXY-GALAXY HARASSMENT

Another process that disrupts galaxies in the cluster environment is harassment. Since the relative speeds of the galaxies are large ($\sqrt{2} \times 370$kms^{-1} ≈500 kms^{-1}) in the cluster, we can use the high-velocity impulse approximation. If the relative velocities are high enough, the potentials of the galaxies do not change during the interactions, and the internal kinetic energy of a galaxy can be assumed to change instantaneously. Binney & Tremaine (2008) approximate that in a galaxy cluster with the velocity dispersion of σ and galaxy number density of n_p of M_p mass galaxies, the disruption time for galacto-centric radius a, can be calculated as (see their Eq. 8.54)

$$t_d = \frac{0.043}{W} \frac{\sqrt{2}\sigma M_s r_h^2}{G M_p^2 n_p a^3}, \tag{4.11}$$

[6]This value is not based on any observational evidence of the typical orbits in the Fornax cluster, but is rather adopted to represent an orbit between a radial and circular orbit. The results are not very sensitive for this parameter, since its variation between 0 and 1 only results into a 15% difference between the estimated tidal radii.

where M_s is the mass of the subject galaxy, r_h is the perturbers' half mass radius, and W is a parameter related to the shape of the perturbing galaxy's mass distribution (we assume $W = 1$). We obtain n_p=25 N Mpc^{-3} by calculating the number density of the giant galaxies ($M_{r'}$ < -18.5 mag) within the virial radius of the cluster. We take the masses and effective radii for those galaxies from Iodice et al. (2019) whenever available, and for those with no measurements by Iodice et al., we use the magnitudes and effective radii from the FCC. From the magnitudes we estimate the stellar masses of those galaxies, and use them for obtaining the halo masses using the stellar-to-halo mass relation of Moster et al. For M_p, we take the median of those galaxy masses $M_p = 10^{11.6}$ M$_\odot$. Since we cannot measure r_h from the data, we need to obtain the relation between r_h and R$_e$ from the simulations. We select a cluster with a similar mass as the Fornax cluster has from the Illustris simulation (Pillepich et al. 2018), and take the median r_h/R$_e$ of the giant galaxies in that cluster. More precisely, we selected the giant galaxies of the Illustris group 11 (M_{vir}=7.9×10^{13} M$_\odot$), and found the median r_h/R$_e$ = 3.6. For r_h we thus multiply the median R$_e$ of the Fornax giant galaxies, and obtain a value of r_h ≈14 kpc.

In the right panel of Fig. 4.21, we show the disruption times for the given mass and R$_e$ of the galaxies. We show again the disruption times with and without the dark matter halo contributions, indicated with the solid and dotted lines, respectively. We find that a large fraction of galaxies would be short lived without any dark matter halos. While taking into account the dark matter contribution, we find that most of the galaxies can keep the stars bound within their R$_e$ for more than 10 Gyr. Especially the low-mass dwarfs are all very resistant against the harassment due to their high M/L-ratios.

4.7.3.4 ARE THE THEORY AND OBSERVATIONS CONSISTENT?

In Sections 5.3 and 7.2, we discussed that the properties of the galaxies with M$_*$ > 10^8 M$_\odot$ are consistent with them being affected by harassment and outer disk gas stripping in the cluster environment, whereas the galaxies smaller than that are consistent with being mostly quenched by ram-pressure stripping. By calculating the strengths of the different environmental processes, we found that ram-pressure stripping is indeed efficient in removing all the gas from M$_*$ < 10^8 M$_\odot$ galaxies, but can not remove the gas in the innermost ≈1 kpc of the galaxies more massive than that. As ram-pressure stripping quenches the galaxy more rapidly than the other processes, our finding that the early-type fraction in the high-luminosity end of the luminosity function is lower than in the low-mass end (Fig. 4.9), seems to be compatible with the scenario that the high-mass galaxies will remain longer as late-type than the low-mass galaxies. We found that tidal disruption of galaxies due to the cluster potential is very rare, but over time the galaxy-galaxy interactions cause the outskirts of the most extended galaxies to disrupt. Indications of such interactions have also been observed for the giant ETGs in the center of the cluster (Iodice et al. 2019).

The physical processes that we suggest to explain our observations in the Fornax are also consistent with the conclusions of the kinematic studies of dwarf

galaxies in the Virgo cluster (Ryś et al. 2014, Toloba et al. 2015). Toloba et al. (2015) found that the the specific stellar angular momentum dwarf galaxies in the Virgo cluster decreases towards the inner parts of the cluster and that the dEs which rotate fast have often disc structures like spiral arms. Ryś et al. (2014) also found that dwarfs in the central parts of the Virgo have lower M/L-ratios than those in the outskirts. Those observations can be explained with the scenario where ram-pressure stripping quickly quenches majority of the galaxies, and harassment then slowly rips off DM from the outer parts of their halos and heats up the stellar disks of the galaxies. In the Fornax cluster similar studies have not yet been made.

For the low-mass galaxies the observed properties are well in agreement with the ram pressure-stripping scenario. All the low-mass dwarfs will lose their gas when they enter the inner 1 deg of the cluster, and their star formation will thus stop and stellar populations start fading. Harassment seems to be less important for these galaxies since they reside in massive DM haloes. However, in 10 Gyrs, these galaxies start to lose their material outside the galacto-centric radii of 2 kpc, which corresponds to several effective radii. For an exponential profile the stellar mass outside that radius is small.

The gas of the $M_* > 10^8$ $M_\odot$ galaxies is also removed from their outer parts by ram-pressure stripping, but they can not be fully quenched just by that process. Thus to fully deplete the gas of a massive dwarf galaxy it must experience harassment or transform the remaining cold gas in the center into stars. This is also consistent with our observations. We acknowledge that also internal processes like feedback from active galactic nuclei and supernovae (Silk 2017, Dashyan et al. 2018) can play a role in the quenching of dwarfs in the different mass ranges, but as those processes are yet poorly constrained we focus our discussion to the external processes only. As the gas depletion time scales by ram-pressure stripping are longer then the crossing time scales, it is likely that there are some galaxies with central star formation also in the cluster center. However, according to the galaxy density profiles in Fig. 4.5 such galaxies seem to be rare. The disruption time scales also show that the outer $R > 5$ kpc parts of the massive dwarf galaxies will be tidally disrupted in about 5 Gyr, which also explains why we do not see many galaxies with such large R_e in the Fornax cluster. To differentiate the effects between the ram-pressure stripping and harassment in massive dwarfs, it would require to study the radial chemical abundances of the stellar populations and look at the radial surface brightness profiles in detail for truncations. This is out of reach of this study, and should be studied in future.

A point that should be considered also in the case of these massive dwarfs, is that their progenitors have likely had slightly different size than the present day late-types in the Fornax cluster. van der Wel et al. (2014) show that the median R_e of galaxies with stellar mass 10^9 $M_\odot < M_* < 10^{9.5}$ $M_\odot$ has grown by $\sim 30\%$ since $z=1$. This indicates that the environmental effects are only partially responsible for the contraction of R_es of massive dwarfs from the outer to inner parts of the cluster, and it is partly also resulting from the fact that the progenitors of the innermost dEs were smaller than the late-types that we observe now falling into the cluster.

In Section 4.2, we did not find significant changes in the luminosity function in different parts of the Fornax cluster. This finding is consistent with the theoretical expectation that not many galaxies should be disrupted due to the cluster potential, and that the disruption time scales are mostly long even within the inner parts of the Fornax cluster.

To conclude, our observations and the theoretical predictions of the efficiency of the different environmental processes are in agreement. Qualitatively, these environmental processes can explain the cluster-centric distribution of different types of dwarfs (Section 3), shapes of the parameter scaling relations and the cluster-centric trends (Section 5), as well as the changes in the galaxy colors (Section 6). Clearly, it is necessary to test these results with more elaborated simulations and follow-up observations.

4.7.4 ARE THE DWARF GALAXIES IN THE VIRGO AND FORNAX CLUSTERS DIFFERENT?

The most complete dwarf galaxy sample in terms of luminosity in the Virgo cluster is the one of the NGVS (Ferrarese et al. 2012). The multi-filter observations of the NGVS have similar depth and resolution as ours. What makes the comparison difficult is that, up to now, the NGVS collaboration has only published the results for the core part of the cluster.

In the previous sections, we have shown that the color-magnitude relations of the early-type galaxies are similar in the cores of the Fornax and Virgo clusters, the axis-ratio distributions are similar, and that the faint end of the luminosity functions have similar shapes in these clusters. Additionally, the segregation in the spatial distributions of the galaxies with different morphological types has also been observed in both clusters. Thus, there is no observational evidence that the dwarf galaxies in these two clusters are different.

As the Virgo and Fornax clusters have different total masses and Virgo seems to contain more sub-structure than Fornax, it is surprising that we did not find differences in their dwarf populations. The galaxy number density in the center of the Fornax is two times higher than in the Virgo cluster (Jordán et al. 2007), and the velocity dispersion in the Virgo cluster is two times higher $\approx$ 700 km s^{-1} (Binggeli et al. 1993) than in Fornax, making the harassment time scales in the Virgo cluster four times longer with respect to the Fornax cluster. The mass concentration around M87 (Fabricant et al. 1980) in the center of the Virgo cluster is only slightly higher than the one around NGC 1399, which makes the tidal disruption of the dwarfs similar around these two galaxies. On the other hand, the density of the X-ray gas in the center of Virgo (Fabricant et al. 1980) is roughly five times higher than in the Fornax cluster (Paolillo et al. 2002) which, combined with the two times higher velocities of the Virgo dwarfs, makes ram-pressure in the Virgo cluster $\approx$20 times more efficient than in the Fornax cluster. By converting the gas-density and galaxy velocity dispersion of the Virgo cluster into the ram-pressure stripping model of Section 7.3.1, we find that in Virgo, ram-pressure stripping should be able to deplete all the gas from three times more massive galaxies than in the Fornax cluster.

Since the low mass dwarf galaxies ($\log_{10}(M_*/M_\odot)<7.5$) seem not to be effected by harassment even in the Fornax cluster due to their massive DM haloes, and they are likely quenched by ram-pressure stripping in both clusters, there should be no difference in their properties due to the environmental effects discussed here. Since ram-pressure stripping is effective for more massive galaxies in the Virgo cluster, we should see there more dEs with larger effective radii ($R_e > 2$kpc) than in the Fornax cluster with masses $7.5<\log(M_*/M_\odot)<8.5$. These galaxies that fall into the category of Ultra Diffuse Galaxies (UDG), have been detected both in the Fornax (Bothun et al. 1991, Muñoz et al. 2015,(Venhola et al. 2017)) and Virgo clusters (Sandage & Binggeli 1984, Mihos et al. 2015), but systematic studies of the abundance of UDGs in both clusters are still lacking. In order to perform a more quantitative and less speculative comparison between these clusters we need to wait for the publication of the full sample of the NGVS.

4.8 SUMMARY AND CONCLUSIONS

In this paper, we have analyzed the photometric properties of the dwarfs in the FDSDC. The used sample consists of 564 dwarf galaxies within the stellar mass range of 2×10^5 $M_\odot < M_* < 2\times10^9$ $M_\odot$ corresponding to r'-band absolute magnitude range of -9 mag $>$ $M_{r'}$ $>$ -18.5 mag. Using the photometric measurements and morphological classifications of Venhola et al. (2018), and the statistical analysis in this work, we wanted to understand how the properties of the dwarf galaxies are affected by the cluster environment, and what are the most important processes transforming the galaxies.

We showed that the cluster environment changes the morphology of the galaxies from late-type to early-type, manifested as an increasing early-type fraction and a drop of late-types towards the inner parts of the cluster. We also showed evidence that the environmental transformation happens via different mechanisms depending on the mass of the galaxy. The most massive dwarf galaxies ($M_{r'} <$ -16 mag) became more concentrated and redder towards the center of the cluster, which is consistent with the effects of harassment and outer disk gas stripping. The less luminous galaxies are redder in the cluster center but they have systematically lower surface brightnesses than the population in the outer parts of the cluster. These trends are consistent with the scenario in which star formation is shut down via complete gas-stripping. The further evolution is explained by a passive fading of the stellar populations. We also showed that the theoretical predictions of the effects of harassment and ram-pressure stripping in the Fornax cluster, are consistent with our observations, thus giving further support for the theory.

Our main conclusions are:

- We find that morphology and spatial distribution of the dwarf galaxies in the Fornax cluster are strongly correlated, so that the most concentrated are dE(N)s, then dE(nN)s, and least concentrated are the late-type dwarfs (Fig. 4.5). By deprojecting the radial galaxy surface number density profiles into

3D number density profiles, we have shown that the cluster-center is devoid of late-type dwarfs and dE(nN)s.

- The early-type fraction and nucleation fraction increase towards the center of the main cluster (Fig. 4.7). In Fornax A, the nucleation- and early-type-fractions are lower than in the main cluster and they do not show clear correlation with the group-centric distance.

- The late-type dwarfs and early-type dwarfs have similar luminosity functions, but only if both dE(N)s and dE(nN)s are considered into the early-type population (Fig. 4.8). The nucleation fraction is a strong function of magnitude and it reaches its peak around $M_{r'}$ = -16 mag, and then quickly declines towards the low luminosity end (Fig. 4.9).

- The luminosity function of the dwarf galaxies does not significantly change in the different parts of the cluster (Fig. 4.10). We also showed that this is not in contradiction with the theoretical predictions, since the cluster tidal field in the center of the Fornax cluster can only disrupt galaxies on orbits with small cluster-centric pericenters. The luminosity function in the Fornax cluster is also identical to those in the Virgo and Coma clusters, but has steeper low mass end than the luminosity function in the Local Group, if the completeness correction is applied.

- We find that the size (R_e), colors, peakedness (Sérsic n), and surface brightness ($\bar{\mu}_{e,r'}$) of the early- and late-type galaxies in the Fornax cluster follow different relations with respect to the absolute magnitude of the galaxies (Fig. 4.12). Their shape distribution differs as well (Fig. 4.14). However, dE(N)s have identical colors and sizes as the dE(nN)s of a given mass.

- We show that the color-magnitude relation of the dEs in our sample does not show statistically significant variations with respect to the cluster-centric distance in the colors that do not include u'-band (Fig. 4.17). When considering the colors including the u'-band, we find that the dEs become significantly redder towards the inner parts of the cluster, indicating that the galaxies in the outer parts were quenched more recently that those in the inner parts.

- We find that in luminosity bins the low-luminosity galaxies ($M_{r'} > $ -16 mag) become redder, more extended and have lower surface brightnesses towards the center of the cluster (Fig. 4.15). The most luminous dwarf galaxies ($M_{r'} <$ -16 mag) become more peaked and redder towards the inner parts of the cluster. The result that the low-luminosity dwarf galaxies become redder with decreasing surface brightness seems to be consistent with an evolution where the gas reservoirs of these galaxies are fully removed by gas stripping,

and they then simply fade to red and old systems. The galaxies with $M_{r'}$ $<$ -16 mag become redder with increasing surface brightness, which is consistent with both harassment and imperfect ram-pressure stripping, in which their inner parts continue to form stars longer than their outskirts. It is likely that both of these processes take place. These observations are in good agreement with our calculations in Section 6.2, which showed that the ram-pressure stripping can not remove all the gas from the most massive dwarfs and thus they need to be quenched some other way, possibly by tidal interactions or by feedback from active galactic nuclei.

Acknowledgements: We would like to thank Thorsten Lisker for the valuable help and discussions during the FDS. A.V. would like to thank the Vilho, Yrjö, and Kalle Väisälä Foundation of the Finnish Academy of Science and Letters for the financial support during the writing of this paper. GvdV acknowledges funding from the European Research Council (ERC) under the European Union's Horizon 2020 research and innovation programme under grant agreement No 724857 (Consolidator Grant ArcheoDyn). R.F.P., T.L., E.L., H.S., E.I., and J.J. acknowledge financial support from the European Union's Horizon 2020 research and innovation programme under the Marie Skłodowska-Curie grant agreement No. 721463 to the SUNDIAL ITN network. H.S., E.L., and A.V. are also supported by the Academy of Finland grant n:o 297738. C.W. is supported by the Deutsche Forschungsgemeinschaft (DFG, German Research Foundation) through project 394551440. J.F-B acknowledges support from grant AYA2016-77237-C3-1-P from the Spanish Ministry of Economy and Competitiveness (MINECO).

4.9 References

Bell, E. F. & de Jong, R. S. 2001, ApJ, 550, 212

Bell, E. F., Wolf, C., Meisenheimer, K., et al. 2004, ApJ, 608, 752

Bernstein, G. M., Nichol, R. C., Tyson, J. A., Ulmer, M. P., & Wittman, D. 1995, AJ, 110, 1507

Bertin, E. & Arnouts, S. 1996, A&AS, 117, 393

Binggeli, B., Popescu, C. C., & Tammann, G. A. 1993, A&AS, 98, 275

Binggeli, B., Sandage, A., & Tarenghi, M. 1984, AJ, 89, 64

Binggeli, B., Tarenghi, M., & Sandage, A. 1990, A&A, 228, 42

Binney, J. & Tremaine, S. 2008, Galactic Dynamics: Second Edition (Princeton University Press)

Blakeslee, J. P., Jordán, A., Mei, S., et al. 2009, ApJ, 694, 556

Boselli, A., Boissier, S., Cortese, L., & Gavazzi, G. 2008, ApJ, 674, 742

Bothun, G. D., Impey, C. D., & Malin, D. F. 1991, ApJ, 376, 404

Bower, R. G., Benson, A. J., Malbon, R., et al. 2006, MNRAS, 370, 645

Bruzual, G. & Charlot, S. 2003, MNRAS, 344, 1000

Bundy, K., Ellis, R. S., Conselice, C. J., et al. 2006, ApJ, 651, 120

Cassata, P., Cimatti, A., Kurk, J., et al. 2008, A&A, 483, L39

Catinella, B., Saintonge, A., Janowiecki, S., et al. 2018, MNRAS, 476, 875

Cayatte, V., Kotanyi, C., Balkowski, C., & van Gorkom, J. H. 1994, AJ, 107, 1003

Chung, A., van Gorkom, J. H., Kenney, J. D. P., Crowl, H., & Vollmer, B. 2009, AJ, 138, 1741

Côté, P., Piatek, S., Ferrarese, L., et al. 2006, ApJS, 165, 57

D'Abrusco, R., Cantiello, M., Paolillo, M., et al. 2016, ApJ, 819, L31

Dashyan, G., Silk, J., Mamon, G. A., Dubois, Y., & Hartwig, T. 2018, MNRAS, 473, 5698

Dejonghe, H. 1987, MNRAS, 224, 13

Di Matteo, T., Springel, V., & Hernquist, L. 2005, Nature, 433, 604

Díaz-García, S., Salo, H., Laurikainen, E., & Herrera-Endoqui, M. 2016, A&A, 587, A160

Dressler, A. 1980, ApJ, 236, 351

Drinkwater, M. J., Gregg, M. D., & Colless, M. 2001, ApJ, 548, L139

Drinkwater, M. J., Gregg, M. D., Hilker, M., et al. 2003, Nature, 423, 519

Eigenthaler, P., Puzia, T. H., Taylor, M. A., et al. 2018, ApJ, 855, 142

Fabian, A. C., Hu, E. M., Cowie, L. L., & Grindlay, J. 1981, ApJ, 248, 47

Fabricant, D., Lecar, M., & Gorenstein, P. 1980, ApJ, 241, 552

Fall, S. M. & Frenk, C. S. 1983, AJ, 88, 1626

Ferguson, H. C. 1989, AJ, 98, 367

Ferguson, H. C. & Sandage, A. 1988, AJ, 96, 1520

Ferrarese, L., Côté, P., Cuillandre, J.-C., et al. 2012, ApJS, 200, 4

Ferrarese, L., Côté, P., Sánchez-Janssen, R., et al. 2016, ApJ, 824, 10

Fujita, Y. 1998, ApJ, 509, 587

Geha, M., Blanton, M. R., Yan, R., & Tinker, J. L. 2012, ApJ, 757, 85

Gunn, J. E. & Gott, III, J. R. 1972, ApJ, 176, 1

Herrera-Endoqui, M., Díaz-García, S., Laurikainen, E., & Salo, H. 2015, A&A, 582, A86

Hilker, M., Mieske, S., & Infante, L. 2003, A&A, 397, L9

Hopkins, P. F., Kereš, D., Oñorbe, J., et al. 2014, MNRAS, 445, 581

Iodice, E., Capaccioli, M., Grado, A., et al. 2016, ApJ, 820, 42

Iodice, E., Spavone, M., Cantiello, M., et al. 2017a, ApJ, 851, 75

Iodice, E., Spavone, M., Capaccioli, M., et al. 2017b, ApJ, 839, 21

Iodice, E., Spavone, M., Capaccioli, M., et al. 2019, A&A, 623, A1

Jaffé, Y. L., Poggianti, B. M., Moretti, A., et al. 2018, MNRAS, 476, 4753

Janz, J., Laurikainen, E., Laine, J., Salo, H., & Lisker, T. 2016a, MNRAS, 461, L82

Janz, J., Laurikainen, E., Lisker, T., et al. 2014, ApJ, 786, 105

Janz, J., Norris, M. A., Forbes, D. A., et al. 2016b, MNRAS, 456, 617

Janz, J., Penny, S. J., Graham, A. W., Forbes, D. A., & Davies, R. L. 2017, MNRAS, 468, 2850

Jordán, A., Blakeslee, J. P., Côté, P., et al. 2007, ApJS, 169, 213

Jordi, K., Grebel, E. K., & Ammon, K. 2006, A&A, 460, 339

Kenney, J. D. P., van Gorkom, J. H., & Vollmer, B. 2004, AJ, 127, 3361

Kim, D. W., Fabbiano, G., & Mackie, G. 1998, ApJ, 497, 699

King, I. 1962, AJ, 67, 471

Koch, A., Burkert, A., Rich, R. M., et al. 2012, ApJ, 755, L13

Kormendy, J. & Bender, R. 2012, ApJS, 198, 2

Kriss, G. A., Cioffi, D. F., & Canizares, C. R. 1983, ApJ, 272, 439

Kuijken, K., Bender, R., Cappellaro, E., et al. 2002, The Messenger, 110, 15

Lisker, T., Glatt, K., Westera, P., & Grebel, E. K. 2006, AJ, 132, 2432

Lisker, T., Grebel, E. K., Binggeli, B., & Glatt, K. 2007, ApJ, 660, 1186

Lotz, M., Remus, R.-S., Dolag, K., Biviano, A., & Burkert, A. 2018, ArXiv e-prints [arXiv:1810.02382]

Mastropietro, C., Moore, B., Mayer, L., et al. 2005, MNRAS, 364, 607

McFarland, J. P., Verdoes-Kleijn, G., Sikkema, G., et al. 2013, Experimental Astronomy, 35, 45

McGlynn, T. A. 1990, ApJ, 348, 515

Mei, S., Holden, B. P., Blakeslee, J. P., et al. 2009, ApJ, 690, 42

Mieske, S., Hilker, M., Infante, L., & Mendes de Oliveira, C. 2007, A&A, 463, 503

Mihos, J. C., Durrell, P. R., Ferrarese, L., et al. 2015, ApJ, 809, L21

Misgeld, I., Hilker, M., & Mieske, S. 2009, A&A, 496, 683

Misgeld, I., Mieske, S., & Hilker, M. 2008, A&A, 486, 697

Moore, B., Lake, G., & Katz, N. 1998, ApJ, 495, 139

Moster, B. P., Somerville, R. S., Maulbetsch, C., et al. 2010, ApJ, 710, 903

Muñoz, R. P., Eigenthaler, P., Puzia, T. H., et al. 2015, ApJ, 813, L15

Nasonova, O. G., de Freitas Pacheco, J. A., & Karachentsev, I. D. 2011, A&A, 532, A104

Ordenes-Briceño, Y., Eigenthaler, P., Taylor, M. A., et al. 2018, ApJ, 859, 52

Paolillo, M., Fabbiano, G., Peres, G., & Kim, D.-W. 2002, ApJ, 565, 883

Pearson, W. J., Wang, L., Hurley, P. D., et al. 2018, A&A, 615, A146

Peng, C. Y., Ho, L. C., Impey, C. D., & Rix, H.-W. 2002, AJ, 124, 266

Peng, C. Y., Ho, L. C., Impey, C. D., & Rix, H.-W. 2010a, AJ, 139, 2097

Peng, Y.-j., Lilly, S. J., Kovač, K., et al. 2010b, ApJ, 721, 193

Pfeffermann, E., Briel, U. G., Hippmann, H., et al. 1987, in Proc. SPIE, Vol. 733, Soft X-ray optics and technology, 519

Pillepich, A., Springel, V., Nelson, D., et al. 2018, MNRAS, 473, 4077

Plummer, H. C. 1911, MNRAS, 71, 460

Poggianti, B. M., Moretti, A., Gullieuszik, M., et al. 2017, ApJ, 844, 48

Popping, G., Somerville, R. S., & Trager, S. C. 2014, MNRAS, 442, 2398

Roediger, E. & Brüggen, M. 2006, MNRAS, 369, 567

Roediger, J. C., Ferrarese, L., Côté, P., et al. 2017, ApJ, 836, 120

Ryś, A., van de Ven, G., & Falcón-Barroso, J. 2014, MNRAS, 439, 284

Sánchez-Janssen, R., Côté, P., Ferrarese, L., et al. 2018, arXiv e-prints [arXiv:1812.01019]

Sánchez-Janssen, R., Ferrarese, L., MacArthur, L. A., et al. 2016, ApJ, 820, 69

Sandage, A. & Binggeli, B. 1984, AJ, 89, 919

Schaye, J., Crain, R. A., Bower, R. G., et al. 2015, MNRAS, 446, 521

Schechter, P. 1976, ApJ, 203, 297

Schipani, P., Capaccioli, M., Arcidiacono, C., et al. 2012, in Proc. SPIE, Vol. 8444, Ground-based and Airborne Telescopes IV, 84441C

Schombert, J. M. 2018, AJ, 155, 69

Serra, P., Oosterloo, T., Morganti, R., et al. 2012, MNRAS, 422, 1835

Sheth, K., Regan, M., Hinz, J. L., et al. 2010, PASP, 122, 1397

Silk, J. 2017, ApJ, 839, L13

Smith, R., Sánchez-Janssen, R., Beasley, M. A., et al. 2015, MNRAS, 454, 2502

Solanes, J. M., Manrique, A., García-Gómez, C., et al. 2001, ApJ, 548, 97

Taylor, E. N., Hopkins, A. M., Baldry, I. K., et al. 2011, MNRAS, 418, 1587

Thomas, D., Maraston, C., Bender, R., & Mendes de Oliveira, C. 2005, ApJ, 621, 673

Toloba, E., Guhathakurta, P., Boselli, A., et al. 2015, ApJ, 799, 172

Trentham, N. & Tully, R. B. 2002, MNRAS, 335, 712

Urich, L., Lisker, T., Janz, J., et al. 2017, A&A, 606, A135

van der Wel, A., Franx, M., van Dokkum, P. G., et al. 2014, ApJ, 788, 28

Vazdekis, A., Sánchez-Blázquez, P., Falcón-Barroso, J., et al. 2010, MNRAS, 404, 1639

Venhola, A., Peletier, R., Laurikainen, E., et al. 2018, A&A, 620, A165

Venhola, A., Peletier, R., Laurikainen, E., et al. 2017, A&A, 608, A142

Voggel, K., Hilker, M., & Richtler, T. 2016, A&A, 586, A102

Wittmann, C., Lisker, T., Pasquali, A., Hilker, M., & Grebel, E. K. 2016, MNRAS, 459, 4450

4.10 APPENDIX

4.10.1 COMPLETENESS OF THE FDSDC

Since the FDSDC is a size and magnitude limited galaxy sample we show in Fig. 4.22 how these selection limits restrict our analysis to a certain area in the size-luminosity parameter space. The galaxies are detected using SExtractor, which uses minimum isophotal size threshold for detecting objects. Ferguson & Sandage (1988) showed that if a sample is limited by a minimum diameter d_{lim} at isophote μ_{lim}, a galaxy with an exponential light profile and effective radius R_e should have a total apparent magnitude

$$m_{tot} < \mu_{lim} - \frac{r_{lim}}{0.5487 R_e} - 2.5 \log_{10} \left[2\pi \left(0.5958 R_e \right)^2 \right], \tag{4.12}$$

in order to be selected into the sample. For the FDSDC d_{lim} = 4 arcsec and μ_{lim} $\approx$ 26.5 mag arcsec^{-2}. In Fig. 4.22 we show this relation with the solid line.

4.10.2 ONION PEELING DEPROJECTION METHOD

In order to analyze 3D radial distributions of galaxy number densities instead of projected distributions, we derived deprojected distributions from the observed ones, by using the "onion peeling" method (Fabian et al. 1981; Kriss et al. 1983). In order to perform this transform, we need to do two assumptions:

- **Spherical symmetry :** We assume that the galaxies are distributed with spherical symmetry around the cluster.
- **No blending bias :** We assume that we see all the galaxies within our selection limits, so that we do not need to estimate how many galaxies are hiding behind large galaxies.

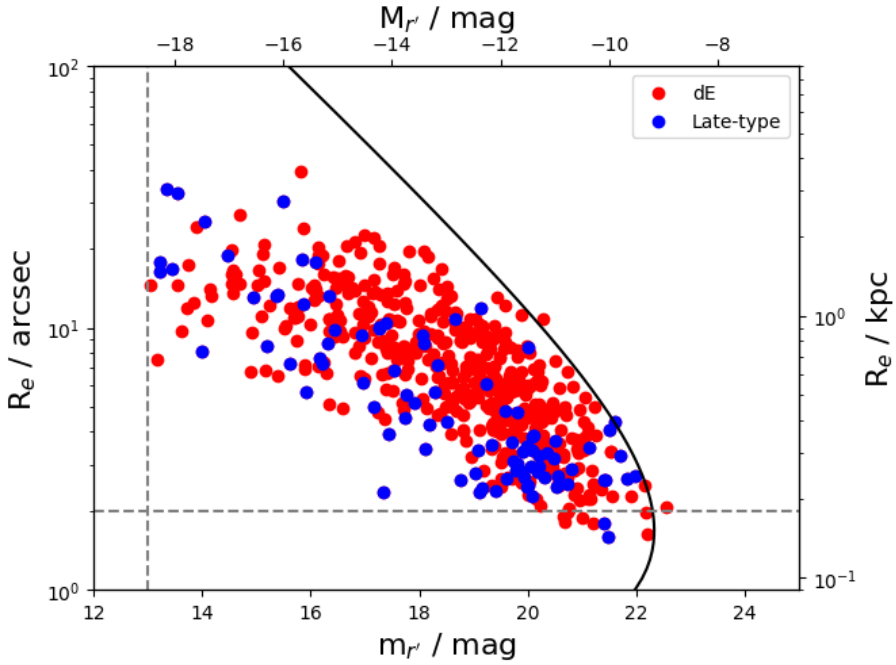

Figure 4.22: Total r'-band apparent magnitudes ($m_{r'}$) and effective radii (R_e) are shown for the late-type (blue symbols) and early-type (red symbols) galaxies of the FDSDC. The vertical and horizontal dashed lines show the minimum magnitude ($M_{r'} > -19$ mag) and minimum size limits ($a > 2$ arcsec) of the sample, respectively. The solid line shows the selection curve resulting from the SExtractor detection. An object can be detected is it has diameter larger than 4 arcsec at the 26.5 mag arcsec^{-2} isophote. The upper x-axis and the right y-axis show the absolute magnitudes and effective radii of the galaxies at the distance of the Fornax cluster.

Both of the above mentioned assumptions can be argued against, but they are necessary to do in order to perform the deprojection. However, since Fornax (especially within the virial radius) is fairly compact and relaxed system the assumption of spherical symmetry is not completely unrealistic. Also, since the galaxy density in the central parts is ≈ 50 galaxies deg^{-2} and a typical size for a galaxy is R$_e \approx 10$ arcsec that corresponds to area of 2.5×10^{-5} deg^2, blending seems to not be a severe problem in our case.

We first assume that the cluster can be described as a set of concentric spherical layers with constant densities ρ_i. We can only observe the projected densities θ_i at the different cluster-centric radii, but using the spherical geometry of our cluster model we can deduce the intrinsic structure. If our bins have radial width of h, we can write the projected density of a bin k as:

$$\theta_k = \frac{\Sigma_{i,i\geq k}\, V_i^k\, \rho_i}{\pi\left[(r_k+\frac{h}{2})^2-(r_k-\frac{h}{2})^2\right]}, \tag{4.13}$$

where r_k is the radius of the bin k, and V_i^k is the volume of the intersection of a sphere with radius r_i and a co-centric hollow cylinder with edge thickness of h and outer radius of $r_k + h/2$. The density of the outermost bin i=o can be straightforwardly obtained from the observations as:

$$\theta_o = \frac{V_o^o\,\rho_o}{\pi\left[(r_o+\frac{h}{2})^2-(r_o-\frac{h}{2})^2\right]} \;\rightarrow\; \rho_o = \frac{\theta_k \pi\left[(r_o+\frac{h}{2})^2-(r_o-\frac{h}{2})^2\right]}{V_o^o} \tag{4.14}$$

and it can be used to solve the other densities iteratively from outwards-in.

For estimating the uncertainty, we did 100 Monte Carlo simulations of the observed radial distribution, and in each realization we varied the number of galaxies in the bin assuming a Poisson uncertainty. We ran the onion peeling deprojection methods for each Monte Carlo realization, and estimated the uncertainty by taking the standard deviation of the results.

To confirm that the method works, we tested it with a Plummer sphere (Plummer 1911), for which the volume density is related to radius r as follows (we used $M = a = 1$):

$$\rho(r) \;=\; \left(\frac{3M}{4\pi a^3}\right)\left(1+\frac{r^2}{a^2}\right)^{-\frac{5}{2}}, \tag{4.15}$$

and the projected surface density can be solved (Dejonghe 1987):

$$\rho_p(r_p) \;=\; \frac{M}{\pi a^2(1+\frac{r_p^2}{a^2})^2}. \tag{4.16}$$

We applied the onion peeling method for the analytical surface density profile, and solved the corresponding volume density. The results are shown in Fig. 4.23. It is clear that the method is capable of solving the volume density very accurately, only differing slightly in the very outer parts. This small deviation is expected, since the analytical model extends to infinity, whereas the onion peeling method has to be started from some finite radius.

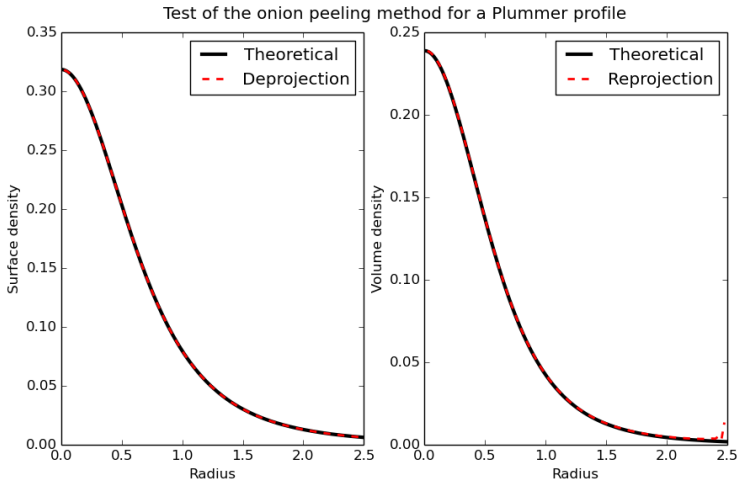

Figure 4.23: Test of the onion peeling method for a Plummer sphere. The black line in the left panel shows the analytically calculated surface density for a Plummer sphere as a function of radius. The black line in the right panel show the corresponding analytical volume density. The red dashed lines in the right and left panels show the deprojected volume and surface density, respectively, obtained from the analytical surface density profile using the onion peeling method.

4.10.3 METHOD FOR OBTAINING INTRINSIC AXIS RATIO DISTRIBUTIONS

In Section 4, we analyze the observed axis-ratio (b/a) distribution, and use it to obtain the intrinsic axis ratios. We used the analytic approach of Fall & Frenk (1983) (see also Lisker et al. 2007) to obtain the intrinsic distributions. In order to use the analytic formulae, we need to assume that all the galaxies have either oblate or prolate spheroidal shape. Assuming oblate galaxies with observed b/a-distribution function $\phi(p)$, where p is the observed b/a, we can obtain the intrinsic axis ratio distribution function as follows:

$$\psi(q) = \frac{2}{\pi\sqrt{1-q^2}}\frac{\mathrm{d}}{\mathrm{d}q}\int_0^q \mathrm{d}p \frac{\phi(p)}{\sqrt{p^2-q^2}}, \tag{4.17}$$

where q is the intrinsic axis ratio. When prolate intrinsic shapes are assumed, the intrinsic distribution can be obtained as

$$\psi(q) = \frac{2}{\pi q^2\sqrt{1-q^2}}\frac{\mathrm{d}}{\mathrm{d}q}\int_0^q \mathrm{d}p \frac{p^3\phi(p)}{\sqrt{p^2-q^2}}. \tag{4.18}$$

In order to avoid the singularity in the formulae, we apply a variable change $x = p/q$. This variable change allows us to write the integral in form $\int \mathrm{d}x f(x)(1-x^2)^{-1/2}$. Using Gauss-Chebyshev quadrature for the integral, we can write in the

form:

$$\int_0^1 \mathrm{dx} \frac{f(x)}{\sqrt{1^2 - x^2}} = \Sigma_{i \in A} w_i f(x_i), \text{ where } A = \{i | x_i > 0\}\,, \tag{4.19}$$

with

$$x_i = \cos\left(\frac{2i-1}{2n}\pi\right), \tag{4.20}$$

and

$$w_i = \frac{\pi}{n} \tag{4.21}$$

We used $n = 100$, for calculating the integrals. When deriving $\phi(p)$, from the observed b/a distribution, we smooth the distribution using convolution. In the convolution we use a Gaussian filter with σ=0.075.

4.10.4 HALO-TO-STELLAR MASS RELATION

In Section 7, we use the stellar-to-halo mass relation from Moster et al. (2010). The used relation between the stellar mass of a galaxy M_* and its dark matter halo mass M_{halo} is

$$\frac{M_*(M_{halo})}{M_{halo}} = 2\left(\frac{M_*}{M_{halo}}\right)_0 \left[\left(\frac{M_{halo}}{M_I}\right)^{-\beta} + \left(\frac{M_{halo}}{M_I}\right)^{\gamma}\right]^{-1}, \tag{4.22}$$

where $\frac{M_*}{M_{halo}}_0$ is a normalization factor, M_I is a characteristic mass, and β and γ are the slopes in the low and high mass ends, respectively. The constants in the relation were obtained by Moster et al. by applying abundance matching between the theoretical halo-mass function and observed galaxy-mass function and then fitting the stellar-to-halo mass function. The obtained constants were $\log_{10} M_I$=11.884, $\left(\frac{M_*}{M_{halo}}\right)_0 = 0.02820$, $\beta = 1.057$, and $\gamma = 0.556$. In Fig 4.24, we show the halo-to-stellar mass relation used in this work.

4.10.5 TRANSFORMATIONS BETWEEN PHOTOMETRIC FILTERS

In Section 2.3 we transformed the Johnson R-band magnitudes and V-I filter colors into the SDSS g', r', and i' bands using the transformations from Jordi et al. (2006). The used transformation between the R-band magnitude, M_R, and r'-band magnitude, $M_{r'}$, is:

$$M_R - M_{r'} = -0.153 \times (r' - i') - 0.117, \tag{4.23}$$

where $r' - i'$ corresponds to the SDSS color. The V-I color, $V - I$, was transformed to $g' - i'$ as follows:

$$V - I = 0.675 \times (g' - i') + 0.364, . \tag{4.24}$$

4.10.6 TABLE OF VALUES IN FIG. 4.15

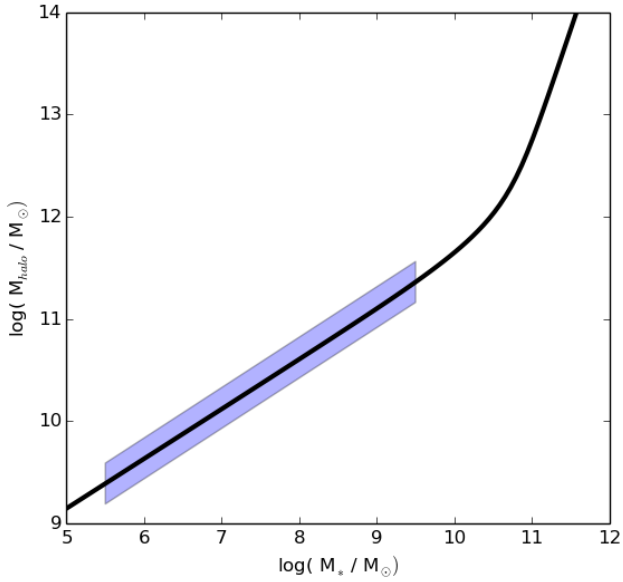

Figure 4.24: Relation between the stellar mass of a galaxy and its dark matter halo mass. The black line shows the Eq. 1.22 (Moster et al. 2010), and the blue shaded area indicates the mass range of the FDSDC galaxies.

Table 4.3: Mean values of the bins in Fig. 4.15 and the corresponding uncertainties. The rows of the table show the means of g'-r' colors, effective radii (R_e), Sérsic indices (n), residual flux fractions (RFF), and mean effective surface brightnesses ($\bar{\mu}_{em.r'}$) in the magnitude and spatial bins. The mean values are followed by their uncertainties. We show the bin means calculated from the raw data (R), and from the sample of galaxies remaining after the projection bias (see Section 5.1) is taken in account (B). The columns separated with vertical lines correspond to the magnitude bins, and the sub-columns referred as 'in', 'mid', and 'out', correspond to the spatial bins defined in the Section 5.1.

	-18.5 mag $< M_{r'} <$ -16.5 mag			-16.5 mag $< M_{r'} <$ -14.5 mag			-14.5 mag $< M_{r'} <$ -12.5 mag			-12.5 mag $< M_{r'} <$ -10.5 mag		
	in	mid	out	in	mid	out	in	mid	out	in	mid	out
g'-r' (B)	0.72 ± 0.03	0.66 ± 0.02	0.57 ± 0.04	0.63 ± 0.009	0.57 ± 0.02	0.44 ± 0.06	0.59 ± 0.009	0.55 ± 0.02	0.55 ± 0.02	0.56 ± 0.02	0.52 ± 0.01	0.49 ± 0.02
g'-r' (R)	0.61 ± 0.05	0.66 ± 0.02	0.57 ± 0.04	0.6 ± 0.01	0.57 ± 0.02	0.44 ± 0.06	0.57 ± 0.01	0.55 ± 0.02	0.55 ± 0.02	0.53 ± 0.01	0.52 ± 0.01	0.49 ± 0.02
R_e (B)	11.5 ± 1.8	15.1 ± 1.5	20.9 ± 2.8	13.5 ± 0.9	12.9 ± 0.9	11.3 ± 1.3	9.8 ± 0.9	9.3 ± 0.5	8.7 ± 0.7	7.0 ± 0.4	4.8 ± 0.3	4.7 ± 0.3
R_e (R)	18.1 ± 3.0	15.1 ± 1.5	20.9 ± 2.8	13.6 ± 0.9	12.9 ± 0.9	11.3 ± 1.3	9.1 ± 0.5	9.3 ± 0.5	8.7 ± 0.7	5.6 ± 0.2	4.8 ± 0.3	4.7 ± 0.3
n (B)	1.8 ± 0.2	1.6 ± 0.1	0.96 ± 0.1	1.2 ± 0.06	1.1 ± 0.05	1.1 ± 0.1	0.92 ± 0.05	0.84 ± 0.02	0.86 ± 0.04	0.94 ± 0.1	0.82 ± 0.03	0.79 ± 0.04
n (R)	1.5 ± 0.1	1.6 ± 0.1	0.96 ± 0.1	1.1 ± 0.04	1.1 ± 0.05	1.1 ± 0.1	0.88 ± 0.02	0.84 ± 0.02	0.86 ± 0.04	0.81 ± 0.03	0.82 ± 0.03	0.79 ± 0.04
RFF (B)	0.027 ± 0.01	0.041 ± 0.005	0.099 ± 0.02	0.0085 ± 0.003	0.028 ± 0.007	0.055 ± 0.02	-0.0027 ± 0.003	0.012 ± 0.003	0.019 ± 0.01	-0.014 ± 0.003	0.00098 ± 0.003	-0.0047 ± 0.005
RFF (R)	0.075 ± 0.02	0.041 ± 0.005	0.099 ± 0.02	0.011 ± 0.003	0.028 ± 0.007	0.055 ± 0.02	-0.00033 ± 0.002	0.012 ± 0.003	0.019 ± 0.01	-0.013 ± 0.002	0.00098 ± 0.003	-0.0047 ± 0.005
$\bar{\mu}_{e,r'}$ (B)	21.3 ± 0.4	21.5 ± 0.3	21.7 ± 0.3	23.3 ± 0.2	23.0 ± 0.1	22.7 ± 0.4	24.7 ± 0.2	24.3 ± 0.1	24.1 ± 0.2	25.4 ± 0.2	24.9 ± 0.1	24.6 ± 0.1
$\bar{\mu}_{e,r'}$ (R)	21.8 ± 0.3	21.5 ± 0.3	21.7 ± 0.3	23.4 ± 0.2	23.0 ± 0.1	22.7 ± 0.4	24.5 ± 0.1	24.3 ± 0.1	24.1 ± 0.2	25.3 ± 0.1	24.9 ± 0.1	24.6 ± 0.1

5. The Fornax Deep Survey: Identification of low surface brightness galaxy candidates with Max-Tree Objects (MTO)

—— *A. Venhola, R. Peletier, E. Laurikainen, H. Salo, C. Haigh, M.H.F. Wilkinson, D. Prole*

Manuscript to be published in Astronomy & Astrophysics.

Abstract

Context: Low Surface Brightness (LSB) dwarf galaxies that exist in the cluster environment are an interesting group of objects, as their contribution to the galaxy luminosity function and their connection with the other types of dwarfs are not yet clear. A key point in obtaining knowledge about these galaxies is the production of deep homogeneous LSB galaxy catalogs. Efforts for producing such catalogs from the existing deep datasets available nowadays have been made, but are mostly generated using outdated detection algorithms. In this work we apply a state of art detection algorithm for identifying low surface brightness galaxies from the Fornax Deep Survey (FDS) data and demonstrate how it improves the detection completeness compared to SExtractor, the program that has been mostly used up to now.

Aims: We test the detection completeness and parameter extraction accuracy of a max-tree based image segmentation method, Max-Tree Objects (MTO), and apply it to the FDS to identify LSB candidates. These candidate lists will be analyzed in detail in a future work where we will identify the cluster member LSB galaxies from the background galaxies and artefacts, and perform a full analysis of these galaxies.

Methods: We use simulated images with known ground truth and real images where the objects have been visually identified. We compare the detection completeness and the object parameters extracted using MTO with those obtained using SExtractor. We then use MTO to detect all the LSB sources in the FDS images and visually classify a subset of the detected objects.

Results: We show that MTO obtains much better completeness than SExtractor in detecting LSBs and extracts more accurate object magnitudes and sizes in the whole parameter range. These improvements reduce the biases in the spatial and surface brightness completeness of the final sample. Using MTO we identify 7270 LSB galaxy candidates from the FDS data, of which 4975 are new identifications that are not present in the previous FDS catalogs. According to our preliminary analysis of the detections obtained with MTO, approximately 25% of these objects appear to be LSB galaxies, the rest being detections of imaging artefacts and diffuse light in background galaxy groups.

5.1 INTRODUCTION

In recent years, there has been an increasing interest in Low Surface Brightness (LSB) galaxies[1] as several deep surveys like the Next Generation Virgo Survey (NGVS, Ferrarese et al. 2012), the Kilo Degree Survey (KiDS, de Jong et al. 2015) and the Fornax Deep Survey (FDS, Iodice et al. 2016, Peletier et al., *in prep.*) have gathered large amounts of deep data that reveal previously unseen LSB galaxies in clusters (Muñoz et al. 2015, Koda et al. 2015, Müller et al. 2015). The contribution of these LSB galaxies to the galaxy luminosity function, and their properties in general are not yet well known. Also a subgroup of LSB galaxies called Ultra Diffuse Galaxies (van Dokkum et al. 2015), that are defined by having large effective radii ($R_e > 1.5$ kpc), has been studied in several environments in order to understand whether they form in a way similar to other dwarfs (Di Cintio et al. 2017, Conselice 2018), or whether they have some other formation mechanism, as suggested by the abnormally low and high dark matter halo masses claimed to been found in some UDGs (van Dokkum et al. 2016, van Dokkum et al. 2018).

In order to study this poorly known LSB galaxy population, we need to identify and quantify them in a robust manner. Many galaxy catalogs compiled from the data of new surveys are produced by identifying the galaxies either visually, or automatically using SExtractor (Bertin & Arnouts 1996). The problems related to those methods are well known and pointed out for example in Chapter 2 of this thesis and by Akhlaghi & Ichikawa (2015). At present, many better methods have become available, such as Max-Tree Objects (MTO) (Teeninga et al. 2016), NoiseChisel (Akhlaghi & Ichikawa 2015) and ProFound (Robotham et al. 2018). However, these improved algorithms have not yet been widely used, and for example the statistical studies of UDGs (Yagi et al. 2016, van der Burg et al. 2016, Mancera Piña et al. 2018) are all based on catalogs obtained with now outdated methods. With the new detection algorithms we can reduce the systematic biases in the LSB samples and moreover obtain more complete catalogs from the currently available data sets.

In this study, we apply MTO for detecting LSB galaxies in the Fornax cluster. A few studies have mapped the LSB galaxy population in the Fornax cluster

[1]We define LSB galaxy as galaxy with the r'-band mean effective surface brightness $\bar{\mu}_{e,r'} \gtrsim 23$ mag arcsec^{-2}

before: Bothun et al. (1991) studied the properties of the LSB galaxies from deep photographic plate images. They identified LSBs in two separate fields covering ≈ 2 deg^2 area in the Fornax cluster. Muñoz et al. (2015) analyzed deep images taken with the Dark Energy Camera (DECam) instrument, and searched for new faint galaxies in the central parts of the Fornax cluster. Their observations in g'-band reached point sources down to 26.6 mag with signal-to-noise[2] $S/N > 5$, and revealed more than hundred previously non-detected dwarf (r'-band magnitude $M_{r'} >$-19 mag) LSB galaxies. In Chapter 2 of this thesis, Venhola et al. studied the LSB galaxy population in the 4 deg^2 area around the center of the cluster. The faintest objects in our catalog reach $\bar{\mu}_{e,r'} \approx 28$ mag arcsec^{-2} and have sizes up to $R_e \approx 10$ kpc, making it the most complete compilation in that area of the Fornax cluster. However, all of these works concentrate on relatively small areas in the central parts of the Fornax cluster, and thus there is a need for a LSB catalog that covers the whole cluster.

In this chapter, we apply MTO for detecting LSB galaxies in the full FDS dataset. The resulting LSB candidate list will later be analyzed further in a forthcoming paper, in which we separate the real cluster members from the background objects and analyze the cluster member LSBs. In Section 5.2, we briefly summarize the FDS dataset and the available catalogs, in Section 5.3, we shortly review a few common algorithms used for detecting LSB objects and introduce MTO. In Sections 5.4 and 5.5, we assess the accuracy of the MTO objects detection and parameter extraction, and describe the production process of the LSB candidate lists, respectively. Finally, in Section 5.6, we summarize and discuss the results.

5.2 FDS DATA AND CATALOGS

We use the FDS as dataset in this work. Since the survey and its observations have been described in detail in the previous chapters of this thesis, we only recap the most important characteristics here.

The ESO VLT Survey Telescope (VST) observations of the FDS cover a 21 deg^2 area centered to the Fornax main cluster in u', g', r' and i'-bands, and an additional 5 deg^2 area centered to the in-falling Fornax A sub-group, observed in g', r' and i'-bands. The reduction and calibration steps of the data are descried in the Chapters 2 and 3 of this thesis.

The photometric uncertainties of the data were defined by Venhola et al. (2018) the photometric zeropoint calibration uncertainties being 0.04, 0.03, 0.03, and 0.04 mag in u', g', r' and i', respectively. Fields are covered with a homogeneous depth with the 1σ limiting surface brightness over 1 pixel (0.2 arcsec × 0.2 arcsec) of 26.6, 26.7, 26.1 and 25.5 mag arcsec^{-2} in u', g', r' and i', respectively., which when averaged over 1 arcsec^2 corresponds to limiting surface brightnesses of 28.3, 28.4, 27.8, 27.2 mag arcsec^{-2} in u', g', r', and i', respectively.

The FDS has provided three galaxy catalogs. The FDS Dwarf Catalog (FDSDC) containing all the dwarf galaxies with semi-major axis $a > 2$ arcsec in the whole

[2]Signal-to-noise in a background subtracted image with a Gaussian background noise with variance of σ^2, is defined as $S/N = f/\left(\sqrt{N}\sigma\right)$, where f is the sum of the object flux in N pixels.

FDS has been presented in Chapter 3, and the photometry of the giant early type galaxies in the central 9 deg^2 area of the cluster by Iodice et al. (2018). In Chapter 2 of this thesis, we presented an LSB galxy catalog that was made by visually identifying LSB galaxies from the 4 deg^2 in the center of the cluster. That catalog is complete within the depth limits of the data, as it was made by inspecting the images manually and selecting all LSB objects. In this work, we utilize the LSB catalog and FDSDC for testing the detection completeness obtained using MTO.

5.3 LSB OBJECT IDENTIFICATION

In order to discuss the problem of object identification in detail, we first divide the process into smaller pieces. The process of finding a desired kind of objects from an image consists of the following steps:

1. **Background determination** The background level and its variance are determined.
2. **Source detection:** The pixels in the image that contain signal in addition to the background noise are detected.
3. **Image segmentation:** The image pixels that contain signal are labelled so that the pixels containing signal from a certain object have the corresponding labels associated to them.
4. **Parameter extraction:** For each object, a set of parameters is calculated from the pixel data. These parameters are then used to select the objects of interest.

During this process, inaccuracies in performing each step are accumulated to the proceeding steps, e.g. if the detection method fails to detect the outer parts of a LSB galaxy, it will also fail to quantify the galaxy size accurately. Thus, in order to detect all the objects in an image, each of these steps have to be done as accurately as possible.

5.3.1 COMMON DETECTION METHODS

Often used methods for faint object detection have been visual inspection of images and using SExtractor (Bertin & Arnouts 1996). In visual inspection, the three first steps of the object detection are done by a human investigator: one first recognizes the background, then identifies the objects, and finally stores the positions of the objects of interest. The objects of interest are then quantified by some method of choice. Visual inspection appears to be the most accurate and complete way of doing the identifications since for example the extremely large UDGs with $R_e \approx 10$ kpc have only been detected visually (Mihos et al. 2015, Venhola et al. 2017). Visual checking is also very effective in separating artefacts from real objects, and it is thus often combined with automatic methods, so that automatically generated initial detection lists are visually checked in order to remove artefacts (e.g. van der Burg et al. 2016). However, visual inspection is not applicable for large data sets and suffers from fuzzy selection limits as the selection of objects cannot be accurately quantified.

The most common automated method, SExtractor, uses thresholding for source detection, i.e. it detects groups of connected pixels above a certain intensity threshold. Before applying the threshold to an image, SExtractor estimates the image background by analyzing pixel value distributions in a user-defined grid that covers the image. It calculates a background value in each grid panel, then generates a background model by interpolating the values in the grid, and finally subtracts the background model from the image. Then it applies the desired detection threshold and checks for each group of pixels that exceeds the threshold, and decides whether the group contains several nested objects. This is done by defining a logarithmically increasing set of intensity levels between the detection threshold and the maximum intensity of the object, and checking at each intensity level whether the object divides into multiple peaks. The peaks are fit using bivariate Gaussians, and the object pixels are then labelled so that each pixel gets the same label as the peak whose Gaussian function has the highest intensity in that pixel. This results in a segmentation image, which is then used, in combination with the input image, to do the parameter extraction for detected objects.

SExtractor can be easily applied to large datasets, but when applied to LSB detection it suffers from fragmentation of objects that have surface brightness similar to the detection threshold (Teeninga et al. 2016). It also mixes some faint objects into brighter ones, which caveat makes it non-ideal for detecting LSB galaxies (Teeninga et al. 2016). The detection efficiency of SExtractor has been improved in some studies by applying some pre-processing of the images, like smoothing (see for example van der Burg et al. 2016), cross-matching filters (Sabatini et al. 2003), and using wavelet filters (Zaritsky et al. 2019). These methods can indeed improve the automatic detection significantly (Sabatini et al. 2003, Zaritsky et al. 2019). However, even when combined with filtering, SExtractor still suffers from weaknesses at the algorithmic level, e.g. the output parameters of SExtractor are not accurate due to incomplete detection of objects in their outskirts where the surface brightness is lower than the detection threshold (e.g. Akhlaghi & Ichikawa 2015). This bias then makes the selection of objects inaccurate if it is based on the parameters measured by SExtractor.

Improvements for the faint object detection have been obtained using different approaches on the algorithm level like in NoiseChisel (Akhlaghi & Ichikawa 2015), ProFound (Robotham et al. 2018), and DBSCAN (Prole et al. 2018). They have also been successfully applied in some recent studies (e.g. Prole et al. 2018, Borlaff et al. 2018, Davies et al. 2018) but have not yet stabilized their position as standard tools of the field. All these new methods improve two basic steps of SExtractor that are the background estimation and the object segmentation. The background estimation is improved by accurately masking the objects before measuring the background. They typically use only a single background value for the whole image, which prevents subtraction of any diffuse components in the image as a background. Object segmentation is improved by applying different morphological image processing operations (for a review see Salembier & Wilkinson 2009) like dilations, erosions and openings to the initial detection maps obtained by thresholding. Those processes aim to filter out false

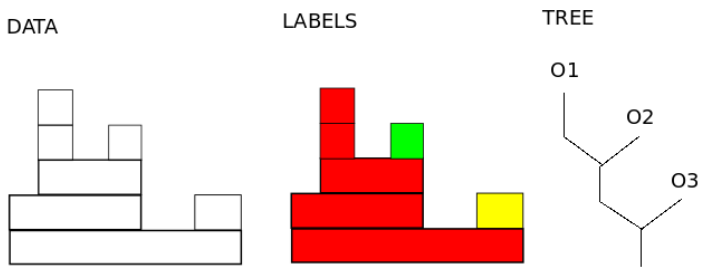

Figure 5.1: An example of a max-tree built for a one dimensional signal. The left panel shows the signal so that the x-axis corresponds to location and y-axis to intensity (both in arbitrary units). The middle panel shows the signal with object labelling done similarly as in MTO. The different colors correspond to parts of the signal associated to different objects. The right panel shows a tree representation of the signal, where the three objects are shown with labels O1, O2, and O3.

detections and connect fragmented objects. The object separation is also improved by using watershed segmentation instead of deblending. In addition to those improvements, for example NoiseChisel calculates signal-to-noise S/N ratios for the initial detections and uses that measure for making the decision whether a detection is real, which further improves the purity of the sample.

In this work, we apply MTO that uses a different approach from the above mentioned ones and is based on a tree structure. This method is adopted specifically keeping in mind that many galaxies in the clusters appear partially or fully overlapping on the sky. This sets a requirement for the detection algorithm to be able to effectively identify the objects in the image and to keep track of the hierarchy of the structures, i.e. if a small galaxy appears in the outskirts of a larger object, it is necessary to detect both and to obtain realistic parameters for them.

5.3.2 MAX-TREE OBJECTS

Tree structures have been long used in mathematical morphology for a compact representation of the structures in images (Salembier et al. 1998, Souza et al. 2016). The idea of a max-tree is to find the maximum connected structures at any given threshold level and represent the hierarchy of those as a tree. The branches of the tree represent the connected structures above the given threshold and the nodes represent bifurcations of the structures when the threshold changes. To demonstrate this, we show in Fig. 5.1 an example of a simple max-tree representing a 1D signal.

The algorithm of MTO has been described in detail by Teeninga et al. (2016). MTO assumes that an image, with a gain of g, consists of three different components: Gaussian background noise with variance $g^{-1}B$, a Poisson distributed signal $g^{-1}O$, and other noise sources R, resulting from sources such as read noise, dark current and quantisation. The background is assumed to be flat over the whole image, thus being well approximated by the mean of the pixel values of the pixels devoid of object signal. The main steps of the algorithm are the following:

1. **Background estimation:** The image is divided into 64×64 pixel tiles. In each tile statistical tests are made to test the Gaussianity and flatness of the tiles. The Gaussianity test is done using the D'Agostino-Pearson K2-statistic. Then the tiles are tested for absence of gradients by comparing the different quadrants of the tiles with each other. The tiles passing these two tests are then selected, and the mean value of those tiles is subtracted from the image. Background variance $g^{-1}B$ is also measured from the selected tiles. The background becomes the first node of the tree.
2. **Identification of significant branches:** The image is thresholded with increasing threshold levels, and at each level the maximum connected structures are identified. The significance of each structure is tested by calculating its power[3], and it is considered as a significant branch if its power exceeds the limit α. We used the default value for α that rejects the detections that are below the 5σ S/N level. The hierarchical structure of the branches is then stored into a tree.
3. **Labelling of the branches:** The branches in the tree are labelled so that the branches that belong to the same object obtain the same label. In case of nodes, i.e. several branches sharing the same parent, the branch with the most power obtains the same label as its parent, and all the other branches obtain new labels.
4. **Generation of the segmentation map:** Finally, a segmentation map is produced by projecting the tree into a plane with similar dimensions as the input image has. The labels for the segmentation map are taken from the highest level branch that is present in the given pixel.
5. **Parameter extraction:** Structural parameters for each object are measured from the input image. These parameters are calculated using the pixels that have the corresponding label in the segmentation image. For nested objects, the intensity level of the parent node is subtracted from the object's pixel values before calculating the parameters. This works as a local background estimation and thus prevents the measured surface brightness of the nested objects being biased by their parent objects. Parameters that we use in this work are the object center coordinates that are calculated from the flux weighted mean positions of the pixels. Total magnitudes are calculated as a sum of the flux in those pixels. For the measure of size, we use semi-minor and semi-major axes, which are calculated from the pixel value distribution moments (see Appendix 5.8.1).

[3]The power of a branch consisting of the pixel set P is defined as $Power(P) = \Sigma_{x \in P} \left(f(x) - A\right)^2$, where $f(x)$ returns the flux in pixel x and A is the intensity level of the parent node.

For a given input image, MTO outputs a segmentation map, and an object list including the locations of the detected objects and their parameters. SExtractor gives also similar outputs and the same parameters, which makes the comparison of these two methods straightforward.

5.4 QUALITY ASSESSMENT OF MTO

In this section, we assess the detection completeness and parameter extraction accuracy of MTO and compare those with the ones obtained using SExtractor. We acknowledge that a comparison of MTO and the other new LSB detection methods like NoiseChisel would be useful in order to see which one of them preforms best. However, such comparison is out of scope of this study and will be presented in a separate work (Haigh et al., *in prep.*). In any case, performing the comparison with respect to SExtractor is most urgent, since it is the most commonly used program in object detection, and any possible improvements in detection completeness would demonstrate that the previous LSB studies done with SExtractor could be improved by applying MTO.

SExtractor has a lot of configuration parameters that need to be adjusted in the right way in order to obtain an optimal detection performance. For the background estimation one needs to set up the background grid size, which should be larger than the objects of interest, to guarantee that they are not subtracted with the background. For the object detection one needs to set up the detection threshold and the minimum number of pixels above the detection threshold that is considered as an object. We optimized these parameters of SExtractor by finding a set of parameters, which gives the best completeness and purity[4] for the mock images described in the next subsection. The details about how we found the optimal parameters and the used parameters are described in Appendix 5.8.2. In order to improve the detection of LSB objects with SExtractor, a convolution with a Gaussian kernel with σ=3 pixels was also applied to images while running the detection.

In order to quantify the detection efficiency and accuracy of parameter extraction of a detection algorithm, it should be tested with data that is similar to the data for which one aims to apply the detection algorithm, and moreover for which one has a known ground truth, i.e. for which the embedded structures and locations of the objects in it are known. It is possible to generate artificial data with known ground truth, but there is always a level of uncertainty whether it will work as an accurate test, since in the real data there are always features that are difficult to model, e.g. reflections or residual patterns from the background subtraction. In the next subsections, we test MTO and SExtractor with artificially made mock images that have made to resemble the FDS data. In order to test the algorithm also with real OmegaCAM data, we test both algorithms for the areas of the FDS where the visually made LSB catalog is available.

[4]The purity, $P = T/A$, is defined as the ratio of the number of true detections, T, and the total number of detections, A.

5.4.1 TESTS WITH MOCK GALAXIES

For generating the mock images, we used the background noise and PSF model of the r'-band FDS field 11 described in Chapter 3. The artificial observations were produced by first generating a blank image with a size of 10,000 $\times$ 10,000 pixels. We then injected 1500 point sources representing stars to the image, using an apparent luminosity distribution drawn from an empirical power law distribution $\propto m_{r'}^{3}$ between object magnitudes of 10 mag $< m_{r'} <$ 23 mag. This distribution and the number density of the stars was selected to be similar to that found from the FDS images. The objects were injected into a 9,000 $\times$ 9,000 pixels area in the image, leaving an empty control area near the edges of the image to control the false positive rate. We then embedded Sérsic models to the image, which we consider as mock galaxies, representing both the cluster and background galaxies. The number of background and cluster galaxies were 4000 and 50, respectively, per image. The structural parameter ranges of the mock galaxies were matched with the values found for the cluster and background galaxies in Chapter 3 of this thesis[5], but so that their surface brightness distribution was extended down to $\bar{\mu}_{e,r'}$ = 31 mag arcsec^{-2}. After embedding all the objects in units of electron counts, the image was convolved with the OmegaCAM r'-band PSF, and the Poisson noise was applied. Finally, Gaussian background noise was added to the pixels and the pixel values were divided by the gain factor. We generated 30 such mock images. An example of a mock image is shown in the left panel of Fig. 5.2.

We then ran MTO and SExtractor for the 30 simulated images, and compared their detections with the known ground truths. An example of the detections can be seen in the two right panels of Fig. 5.2. In the detection distribution of SExtractor, some artificial features can be seen: there are empty areas with no detections around some of the objects. These areas are located around the bright and extended objects, indicating that SExtractor works ineffectively near them. These features are not seen in the distribution of the objects detected with MTO.

Completeness of the detections is defined to be the fraction of detected objects within a certain parameter range from the total number of objects in that parameter range. Good detection method should thus obtain completeness as close to unity as possible in the parameter range of interest. For calculating the number of detections, we defined an object to be detected if there is an object in the output catalog of the given method that has semi-major axis $a >$ 10 pix (2 arcsec) and that is located within half R_e from the center of the embedded mock galaxy. We adopted the $a >$ 10 pix selection limit as we will use it later with the real data as well. Completeness of both methods as a function of the input r'-band mean effective surface brightness ($\bar{\mu}_{e,r}$) and effective radius (R_e) are shown in Fig. 5.3. MTO obtains approximately 1 mag arcsec^{-2} deeper 50% completeness limits for $\bar{\mu}_{e,r}$, and increases the completeness for galaxies with large and small

[5]For the mock background galaxies, we used flat distributions of mean effective surface brightnesses between 21 mag arcsec^{-2} $< \bar{\mu}_{e,r'} <$ 31 mag arcsec^{-2}, effective radii between 0.5 arcsec $< R_e <$ 3.5 arcsec, and Sérsic indices between $2 < n < 4$. For the cluster galaxies the corresponding ranges were 21 mag arcsec^{-2} $< \bar{\mu}_{e,r'} <$ 31 mag arcsec^{-2}, effective radii between 2.5 arcsec $< R_e <$ 40 arcsec, and Sérsic indices between $0.5 < n < 2$. The used axis ratio were between $0.3 < b/a < 1$.

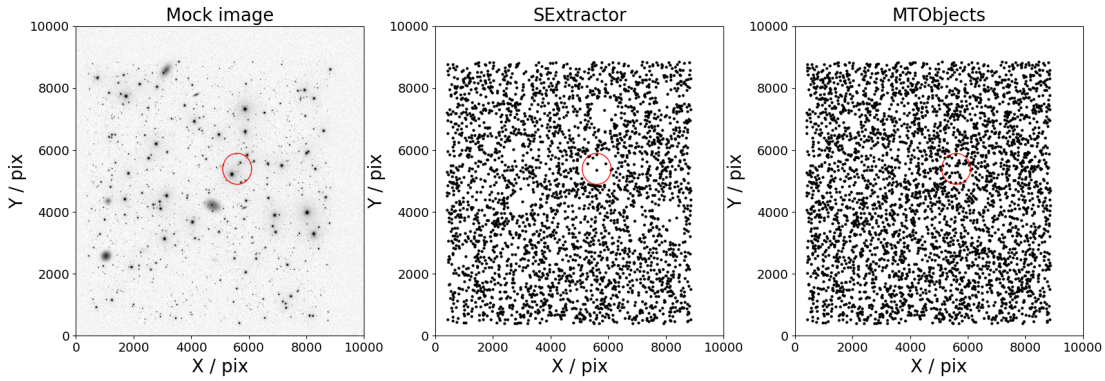

Figure 5.2: An example of a simulated mock image (the left panel), and the locations of the identified objects using SExtractor (the middle panel) and MTO (the right panel). The area in the right of the mock image is devoid of mock galaxies in order to control the amount of false positives. The red circles in the images indicate an area in the image where the detection efficiency of SExtractor is affected by bright objects.

R_e. The most significant improvement is obtained in the 75 % completeness limit, which is approximately 2–3 mag arcsec^{-2} deeper for MTO than SExtractor.

As we know the input effective radii and magnitudes of the mock galaxies, we can compare those with the parameters extracted by MTO and SExtractor. With MTO and SExtractor we did not measure the effective radii but rather the semi major-axes based on second order moments of the pixel value distribution of the objects. This means that we need to compare those two different measures of size in order to study how well the extents of the objects are measured. In Fig. 5.4, we show the comparison of the input versus output values of both methods as a function of the input surface brightness of the objects. The trends for the two methods are qualitatively similar showing a decreasing trends in the extracted objects sizes and apparent magnitudes towards lower surface brightnesses. Both of these methods underestimate the sizes and measure too faint apparent magnitudes for the lowest surface brightness objects, but SExtractor underestimates the values more severely. It is also important to take into account the fact that MTO detects approximately 1/3 more objects than SExtractor, which means that its trends get affected by objects that SExtractor fails to detect. To take this into account, in Fig. 5.5 we show the comparison of the parameters obtained by SExtractor and MTO for the objects that both programs have detected. Clear trends are visible both in object sizes and apparent magnitudes, so that SExtractor measures fainter magnitudes and smaller sizes for the objects than MTO. Those differences become especially significant for the objects fainter than $\mu > 24$ mag arcsec^{-2} since there is $\approx$ 30% systematic difference in the sizes and 0.5 mag difference in the apparent magnitudes.

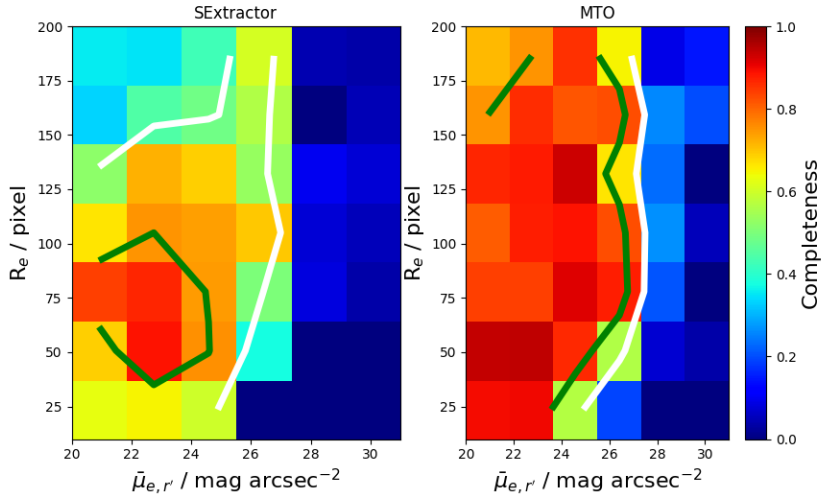

Figure 5.3: Detection completeness of SExtractor (left panel) and MTO (right panel), obtained using the mock galaxies, as a function of the input r'-band mean effective surface brightness ($\bar{\mu}_{e,r}$) and effective radius (R_e). The colors in the panels correspond to the completeness indicated by the color bar. The green and white lines show the 75 % and 50 % completeness limits, respectively. One pixel corresponds to 0.2 arcsec or to 20 pc at the distance of the Fornax cluster.

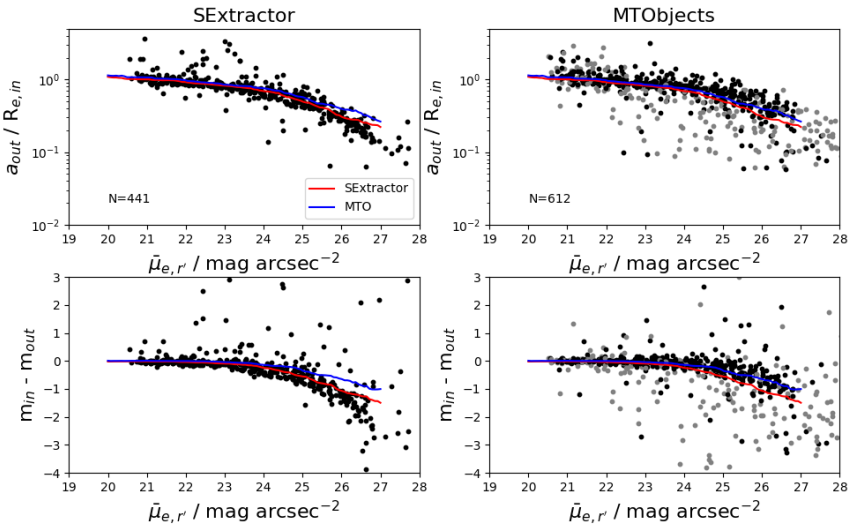

Figure 5.4: The upper panels show the ratio between the measured semi-major axis length and the input effective radii ($a_{out}/R_{e,in}$) for the mock galaxies as a function of their mean effective surface brightness in r'-band ($\bar{\mu}_{e,r'}$). The lower panels show the difference between the input magnitudes (m_{in}) and the measured magnitudes (m_{out}). The left and right panels show the comparisons when using SExtractor and MTO, respectively. The blue (MTO) an red (SExtractor) lines correspond to the running means of the measurements with a filter size of $\Delta\bar{\mu}_{e,r'}$ = 1 mag arcsec^{-2}. The grey and black symbols in the right panels correspond to the objects which are only detected using MTO and to the objects detected using both methods, respectively.

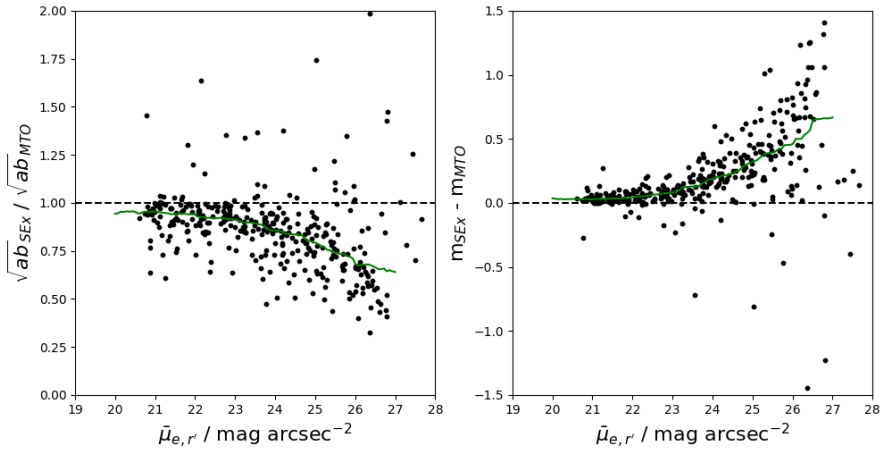

Figure 5.5: Comparison of the parameters extracted by SExtractor and MTO for the mock galaxies detected by both methods. The left panel shows the ratio between the circularized radii of the objects obtained by SExtractor ($\sqrt{ab}_{SEx}$) and by MTO ($\sqrt{ab}_{MTO}$) as a function of the input r'-band mean effective surface brightness ($\bar{\mu}_{e,r'}$). The right panel show the difference between the apparent magnitudes obtained with SExtractor (m_{SEx}) and MTO (m_{MTO}). The black lines show the running medians of the measurements with a filter size of $\Delta\bar{\mu}_{e,r'} = 1$ mag arcsec^{-2}.

In summary, we found that MTO detects galaxies more homogeneously and has deeper completeness limits than SExtractor. Additionally, it measures the size and luminosity parameters of the galaxies more accurately than SExtractor. In spite of the fact that MTO improves the accuracy of extracted magnitudes with respect to SExtractor, it still measures 1-2 mag too faint magnitudes for many objects (lower right panel of Fig. 5.4). At least two factors contribute to that bias: the outer parts of the objects that are nested with brighter objects will be associated with the brighter ones as no models are assumed for the objects. Additionally, the outer parts of the faintest objects are lost into the noise. These biases can be improved by modelling the objects with GALFIT, which we will do in the upcoming paper.

5.4.2 QUALITY ASSESSMENT USING THE LSBS OF VENHOLA ET AL., 2017

In order to test the detection completeness with the real data, we use the visually identified LSB sample of Venhola et al. (2017, Chapter 2 of this thesis). This sample is assumed to reach the depth limits of the data, as it contains all the LSB galaxies that can be seen in the images by visual inspection.

In order to perform a quantitative test, we run MTO and SExtractor for the 4 deg^2 area in the center of the Fornax cluster that is covered by the LSB catalog. We then compare the object lists produced by each of the methods with the LSB catalog. We consider a LSB galaxy detected, if there is a source with A $>$ 2 arcsec in the object list within half R_e from the object location indicated in the LSB catalog. In Fig. 5.6, we show the R_e and $\bar{\mu}_{e,r'}$ distribution of the LSB galaxies, and indicate the objects detected by each of the methods in the two different panels.

MTO and SExtractor detected 154 and 121 objects, respectively, of the 205 LSB galaxies. We found that MTO was able to increase the completeness limit of the detections towards lower surface brightnesses, and both towards larger and smaller effective radii. The increase in the completeness at the small R_e is likely due to the less severe underestimation of sizes of the objects while using MTO with respect to SExtractor. The increased completeness in the low surface brightness-end and at the large R_e is due to the MTO's ability to detect the maximum connected structures in the images and its more accurate background estimation. In the case of SExtractor, parts of those objects are detected but they are fragmented into smaller pieces that do not fulfil our selection criteria.

As our criterion for the detection of an object allows quite a large offset between the locations of the detection and the center of the known LSB galaxy, we inspected the segmentation maps of all the UDGs (LSB galaxy with $R_e > 1.5$ kpc), for which the allowed offset is largest. We found that the two largest LSB galaxies (highlighted in Fig. 5.6) are not visible in the segmentation maps of MTO, and the detections are caused by smaller galaxies overlapping with them. This reduces the number of detections obtained with MTO to 152 galaxies.

In summary, our analysis in this and in the previous subsections showed that using MTO, we can detect the LSB dwarfs with more than 50 % completeness down to $\bar{\mu}_{e,r'} \approx 27.5$ mag arcsec^{-2} in the FDS data, which is approximately one magnitude deeper than with SExtractor.

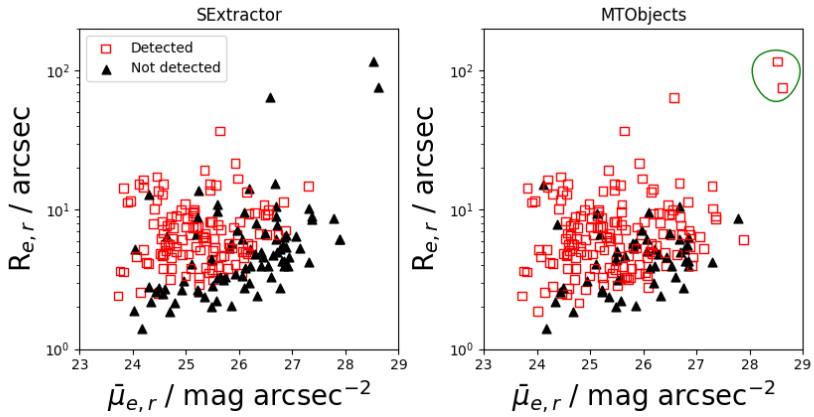

Figure 5.6: Comparison of the detection completeness of SExtractor with the detection completeness obtained with MTO for the LSB galaxy sample described in Chapter 2 of this thesis. The left panel shows the objects detected using SExtractor and the right panel shows those detected by MTO. The two extended LSB galaxies, which appear as detections due to the smaller LSB galaxies on top of them are circled with green.

5.5 INITIAL CANDIDATE CATALOG FOR LSBS IN THE FDS

In order to detect LSB galaxies from the full FDS dataset, we ran MTO for all the 26 FDS fields using specific detection images and masks. We used the same stacked g'+r'+i' band mosaics that were described in Chapter 3 of this thesis. As a result we obtained the locations, magnitudes, and the minor- and major-axis radii of the objects. We then used the masks generated in Chapter 3, which were used to mask the bright stars from the data, and removed all the detections that were within the masked areas.

We then selected the objects with $a > 2$ arcsec and which had median surface brightness of the detected pixels fainter than 23 mag arcsec^{-2}. These selected objects comprise the Initial Candidate Catalog (ICC). These selection limits were adopted for the following reasons: the 2 arcsec minimum limit was selected due to the resolution of the FDS observations that have typical PSF full width half-max (FWHM) of 1 arcsec. This selection criterion thus excludes stars and unresolved background galaxies. The surface brightness limit is motivated by the definition of LSBs. We acknowledge the fact that when using this relatively high surface brightness limit, the ICC is likely contain also some too high surface brightness galaxies to be considered as a LSB galaxy. However, this is not a problem since we will later apply more selection criteria for the parameters obtained later using GALFIT, in order to select the objects for the final LSB galaxy catalog. As a result we obtain a sample of 7,270 LSB galaxies. The locations of those galaxies are

shown in Fig. 5.7. In order to check whether there is clustering within the larger candidates we show also the distributions with size cuts also in Fig. 5.7. It appears that some clustering of larger galaxies appears around the main cluster and Fornax A, but without more careful analysis of these objects it is not possible to know whether it is due to the large candidates being mostly cluster members or some other effect.

In the top panel of Fig. 5.7, some variations in the number of detected objects are apparent. These variations may be partly explained by the varying seeing across the FDS fields, which makes small background galaxies to appear larger and thus our selection based on object sizes picks them up. Another contributing factor is the small variations in the depth of the data in the different fields. Additionally, the halos of the bright stars contribute to the detections. These significance of these issues will be studied in detail in the forthcoming paper.

As Venhola et al. (2017) pointed out, the contamination caused by cirrus is low in the Fornax cluster (Chapter 2). Thus, the objects in the ICC that are not artefacts or background objects are most likely members of the Fornax cluster.

We compared the locations of the ICC galaxies with the galaxies in the FDSDC and the background galaxy catalog of Chapter 3, in order to find out how many new candidates appear in the ICC. We considered a galaxy to be previously found if the ICC object was located within the effective radius of an object in the previous catalogs. We find that that 2,475 galaxies in our sample were detected in the above mentioned catalogs. This means that our ICC contains 4,795 new LSB candidates.

5.5.1 MORPHOLOGY OF THE ICC OBJECTS

We will perform a detailed photometric analysis and morphological classification of all the objects in the future paper. However, in order to obtain a qualitative idea of the content of the ICC, we classified some galaxies from the ICC that visually resemble LSB dwarfs, as LSB galaxy candidates and other objects as likely artefacts. We show some typical examples of the identified objects with different ranges of semi major axis lengths in Figs. 5.8, 5.9 and 5.10. We did the initial morphological classifications for 500 randomly selected galaxies with 2 arcsec $< a <$ 10 arcsec, and for all the larger objects. According to these classifications, the fraction of cluster LSB candidates of the total detections are 25%, 62%, and 18% for the bins with 2 arcsec $< a <$ 10 arcsec (N=500), 10 arcsec $< a <$ 15 arcsec (N=69), and $a >$ 15 arcsec (N=57), respectively.

In Fig. 5.8 we show the LSB galaxy candidates and the likely artefacts with effective radii within 2 arcsec $< a <$ 10 arcsec. The LSB candidates of this range are mostly blueish, relatively round and symmetrical objects, whereas most artefacts are closely clustered groups of reddish compact objects that are most likely background galaxy groups and clusters. Those background galaxy groups get identified as LSBs as they are connected at the low intensity level. When MTO builds a tree for such clustered objects, the connected low luminosity envelope has to be associated with some of the objects. The object which gets associated

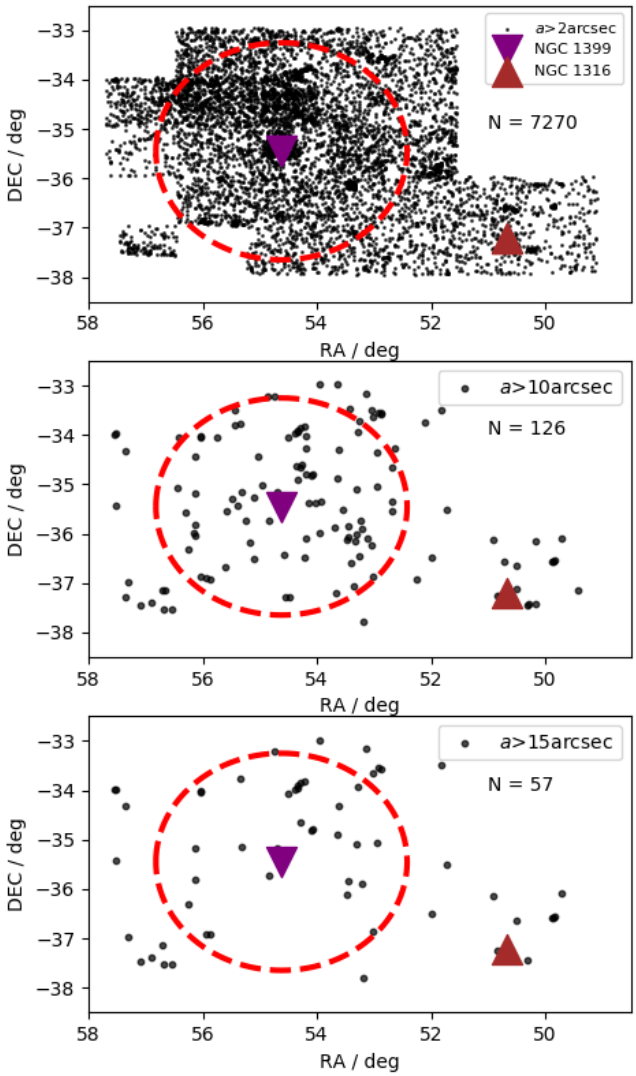

Figure 5.7: Locations of the objects in the initial candidate list (ICC). The panels from the top to bottom show the objects with $a > 2$ arcsec, $a > 10$ arcsec, and $a > 15$ arcsec. The axes show the right ascension (RA) and declination (DEC) of the objects in the International Celestial Reference System (ICRS) coordinates. The red circle shows the virial radius of the Fornax cluster (Drinkwater et al. 2001), and NGC 1399 and NGC 1316 are marked with the purple and brown triangles, respectively.

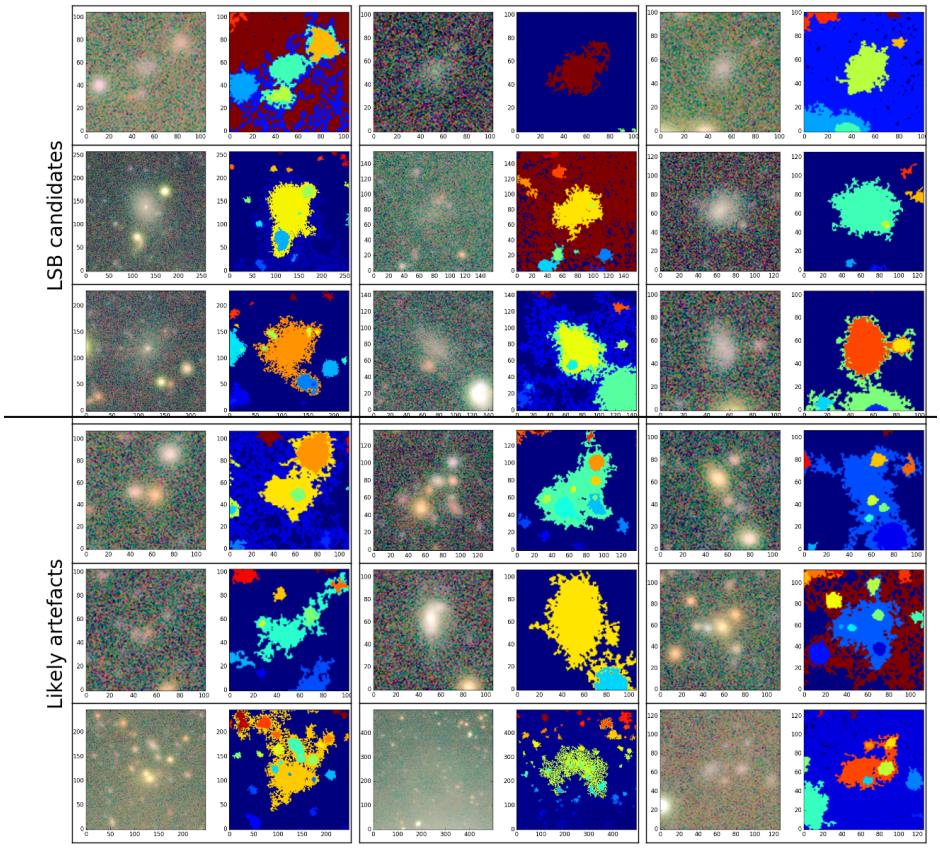

Figure 5.8: Examples of the ICC objects with 2 arcsec $< a <$ 10 arcsec. For each object we show a color image combined from the i', r', and g'-band FDS observations. The panels on the right side of the color images show the segmentation maps produced by MTO in which the pixels with different object labels are indicated with different colors. The panels above and below the horizontal line show examples of likely LSB galaxies and likely artefacts, respectively.

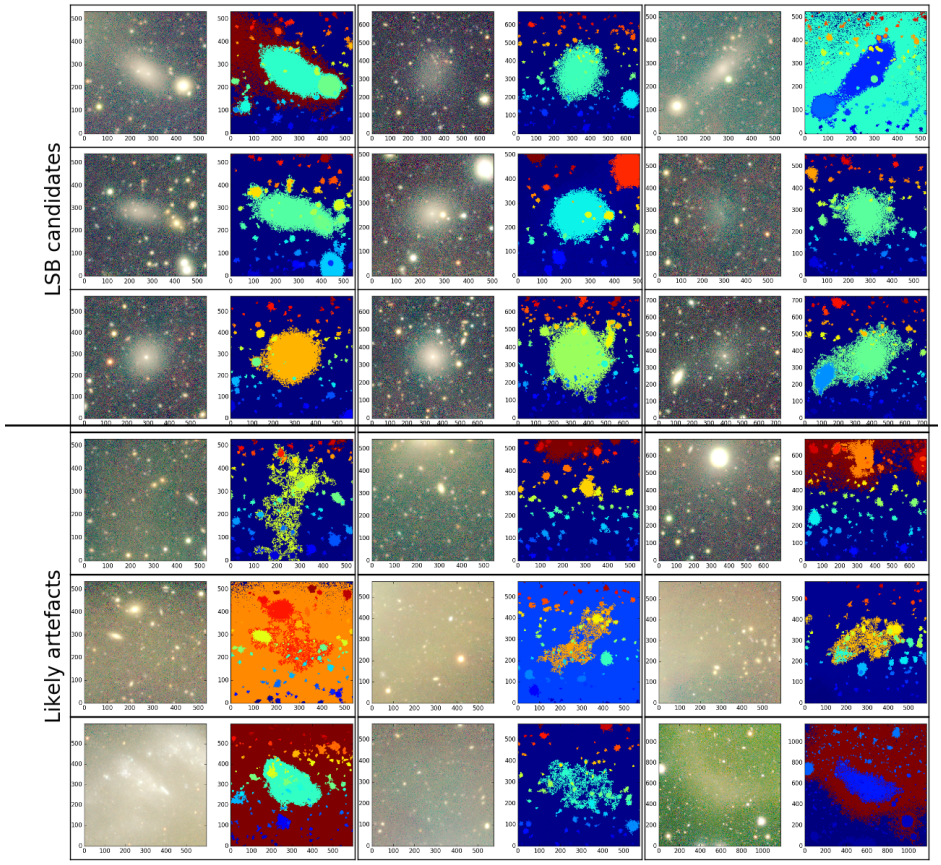

Figure 5.9: Examples of the ICC objects with 10 arcsec $< a <$ 15 arcsec. Contents of the panels are explained in Fig. 5.8.

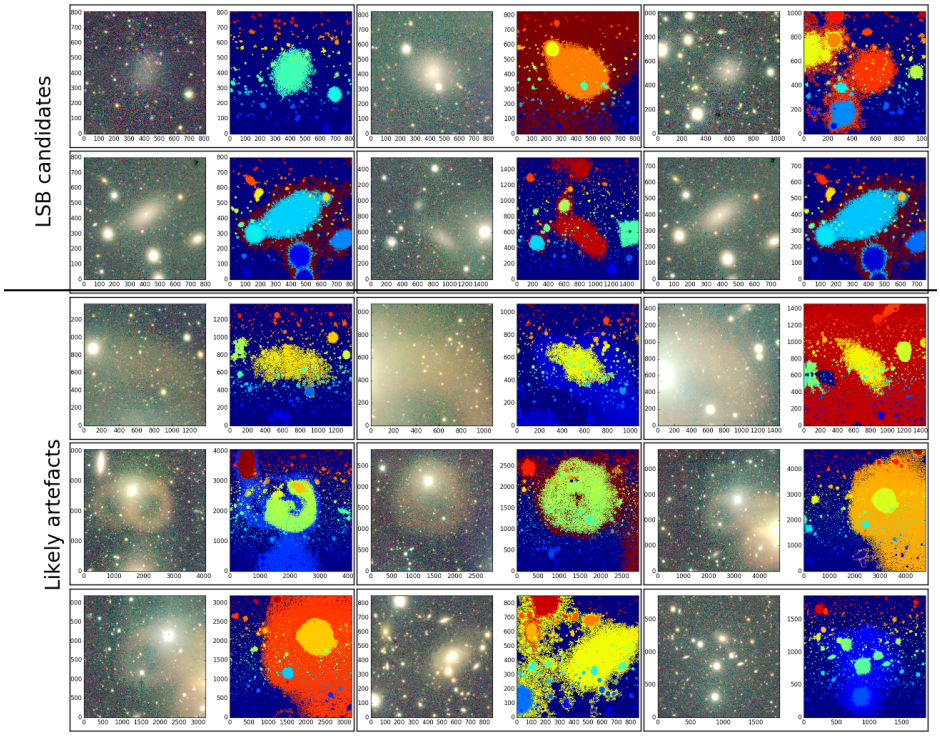

Figure 5.10: Examples of the ICC objects with $a > 15$ arcsec. Contents of the panels are explained in Fig. 5.8.

with the LSB envelope then appears in the output catalog as an extended object with low surface brightness.

In Figs. 5.9 and 5.10, we show examples of the more extended LSB candidates and artefacts. In this category the false positives are typically associated to the PSF reflection rings of the OmegaCAM, which were discussed in Chapter 2 of this thesis. The large LSB candidates have typical sizes and appearances of UDGs, which suggests that MTO is indeed useful in automatically detecting such galaxies.

These tests demonstrate well that MTO is effective in detecting LSB galaxies from the images. However, inspection of the detected objects showed that when the selection of objects is only based on surface brightness and radii of the objects, it also picks up many objects from the images that are not LSB galaxies. Thus, in order to obtain a clean sample of LSB galaxies, we need to apply more structural selection criteria or perform visual classifications for the detections. A major source of contamination are the groups of galaxies that are connected on low luminosity levels. The essential problem with these types of objects is not the ability of MTO to detect the different galaxies from the images, but to divide the low surface brightness envelopes around the galaxies between the objects. However, this is not possible to do with MTO, since deblending of the outer envelope requires assumptions of the galaxy light profiles, which are not made within MTO. A potential way to solve this problem is to combine GALFIT modelling with MTO, so that MTO measures initial object parameters for GALFIT, which then fits a set of Sérsic models to the galaxy groups. The final object selection can then be made using the structural parameters obtained from GALFIT.

5.6 SUMMARY AND CONCLUSIONS

In this chapter, we have summarized the first results of the ongoing efforts to produce a LSB extension to the FDSDC. First, we introduced the MTO-algorithm and described how it differs from the other methods used for detection of the LSBs. We demonstrated how MTO is superior to SExtractor in detecting objects homogeneously across the images and obtaining better completeness for the detections. As MTO detects the outskirts of the galaxies more accurately than SExtractor, it is also capable of measuring the galaxy structural parameters more accurately. We then applied MTO to the FDS data. As a result, we obtained an initial LSB candidate catalog in the area of the FDS that includes 4,795 new LSB candidates that are not present in the previous Fornax cluster galaxy catalogs.

In the forthcoming paper we plan to combine GALFIT with MTO, in order to obtain accurate structural parameters for the LSB galaxies in the ICC. The resulting catalog will be the most complete spatially extended LSB galaxy catalog of the Fornax cluster.

5.7 References

Akhlaghi, M. & Ichikawa, T. 2015, ApJS, 220, 1

Bertin, E. & Arnouts, S. 1996, A&AS, 117, 393

Borlaff, A., Trujillo, I., Román, J., et al. 2018, arXiv e-prints [arXiv:1810.00002]

Bothun, G. D., Impey, C. D., & Malin, D. F. 1991, ApJ, 376, 404

Conselice, C. J. 2018, Research Notes of the American Astronomical Society, 2, 43

Davies, L. J. M., Robotham, A. S. G., Driver, S. P., et al. 2018, MNRAS, 480, 768

de Jong, J. T. A., Verdoes Kleijn, G. A., Boxhoorn, D. R., et al. 2015, A&A, 582, A62

Di Cintio, A., Brook, C. B., Dutton, A. A., et al. 2017, MNRAS, 466, L1

Drinkwater, M. J., Gregg, M. D., & Colless, M. 2001, ApJ, 548, L139

Ferrarese, L., Côté, P., Cuillandre, J.-C., et al. 2012, ApJS, 200, 4

Iodice, E., Capaccioli, M., Grado, A., et al. 2016, ApJ, 820, 42

Iodice, E., Spavone, M., Capaccioli, M., et al. 2018, A&A, submitted

Koda, J., Yagi, M., Yamanoi, H., & Komiyama, Y. 2015, ApJ, 807, L2

Mancera Piña, P. E., Peletier, R. F., Aguerri, J. A. L., et al. 2018, MNRAS, 481, 4381

Mihos, J. C., Durrell, P. R., Ferrarese, L., et al. 2015, ApJ, 809, L21

Muñoz, R. P., Eigenthaler, P., Puzia, T. H., et al. 2015, ApJ, 813, L15

Müller, O., Jerjen, H., & Binggeli, B. 2015, A&A, 583, A79

Prole, D. J., Davies, J. I., Keenan, O. C., & Davies, L. J. M. 2018, MNRAS, 478, 667

Robotham, A. S. G., Davies, L. J. M., Driver, S. P., et al. 2018, MNRAS, 476, 3137

Sabatini, S., Davies, J., Scaramella, R., et al. 2003, MNRAS, 341, 981

Salembier, P., Oliveras, A., & Garrido, L. 1998, IEEE Trans. Image Proc., 7, 555

Salembier, P. & Wilkinson, M. H. F. 2009, IEEE Signal Processing Magazine, 26, 136

Souza, R., Tavares, L., Rittner, L., & Lotufo, R. 2016, in 2016 29th SIBGRAPI Conference on Graphics, Patterns and Images Tutorials (SIBGRAPI-T), IEEE, 15–23

Teeninga, P., Moschini, U., C. Trager, S., & Wilkinson, M. 2016, Mathematical Morphology - Theory and Applications, 1

van der Burg, R. F. J., Muzzin, A., & Hoekstra, H. 2016, A&A, 590, A20

van Dokkum, P., Abraham, R., Brodie, J., et al. 2016, ApJ, 828, L6

van Dokkum, P., Danieli, S., Cohen, Y., et al. 2018, Nature, 555, 629

van Dokkum, P. G., Abraham, R., Merritt, A., et al. 2015, ApJ, 798, L45

Venhola, A., Peletier, R., Laurikainen, E., et al. 2017, A&A, 608, A142

Yagi, M., Koda, J., Komiyama, Y., & Yamanoi, H. 2016, ApJS, 225, 11

Zaritsky, D., Donnerstein, R., Dey, A., et al. 2019, ApJS, 240, 1

5.8 Appendix

5.8.1 Pixel value distribution moments

MTO and SExtractor both measure semi-major and -minor axis lengths for the objects. For calculating these parameters, second order pixel value distribution moments are used. If we mark x- and y-coordinates and intensity of a pixel i as x_i, y_i and I_i,respectively, we can calculate the second order moments as follows

$$\begin{aligned} \overline{x^2} &= \frac{\sum_i I_i x_i^2}{\sum_i I_i} - \overline{x}^2, \\ \overline{y^2} &= \frac{\sum_i I_i y_i^2}{\sum_i I_i} - \overline{y}^2, \\ \overline{xy} &= \frac{\sum_i I_i x_i y_i}{\sum_i I_i} - \overline{x}\,\overline{y}. \end{aligned} \tag{5.1}$$

The second order moments measure the spread along the x- and y-axes, and they are transformed to semi-minor axis b and semi-major axis a as

$$\begin{aligned} a^2 &= \frac{\overline{x^2}+\overline{y^2}}{2} + \sqrt{\left(\frac{\overline{x^2}-\overline{y^2}}{2}\right)^2 + \overline{xy}^2}, \\ b^2 &= \frac{\overline{x^2}+\overline{y^2}}{2} - \sqrt{\left(\frac{\overline{x^2}-\overline{y^2}}{2}\right)^2 + \overline{xy}^2}, \end{aligned} \tag{5.2}$$

and the position angle θ

$$\tan(2\theta) = 2\frac{\overline{xy}}{\overline{x^2} - \overline{y^2}}. \tag{5.3}$$

5.8.2 SExtractor configuration parameters

Configuration parameters of SExtractor are described in detail in the SExtractor guide that is available at `https://www.astromatic.net/pubsvn/software/sextractor/trunk/doc/sextractor.pdf`. The most important parameters for the object detection are the size of the background grid, detection threshold and the minimum area of the detections. In order to decide which parameter values we should adopt for the detection tests we ran a test for a set of parameters. We selected a few of reasonable values for each parameter and ran SExtractor using all combination of those parameters for one of the mock images described in Section 1.5.2. We used values of 500, 1000, 10000 pixels for the background grid size, 0.5 and 1σ for the detection threshold, and 10, 50, 100 pixels for the minimum detection area. We then selected the set of parameters that provided the best combination of completeness and purity of the detections. The optimal performance was obtained using background size of 500 pixels, detection threshold of 1σ, and minimum detection area of 10 pixels. We then used the following set of configuration parameters when running SExtractor:

```
DETECT_MINAREA   10,          # minimum number of pixels above threshold
DETECT_THRESH    1,           # <sigmas> or <threshold>,<ZP> in mag.arcsec-2
ANALYSIS_THRESH  1,           # <sigmas> or <threshold>,<ZP> in mag.arcsec-2
FILTER           Y,           # apply filter for detection (Y or N)?
DEBLEND_NTHRESH  64,          # Number of deblending sub-thresholds
DEBLEND_MINCONT  0.005,       # Minimum contrast parameter for deblending
CLEAN            Y,           # Clean spurious detections? (Y or N)?
CLEAN_PARAM      1.0 ,        # Cleaning efficiency
MASK_TYPE        CORRECT,     # type of detection MASKing can be one of
                              # NONE, BLANK or CORRECT
MAG_ZEROPOINT    0.0,         # magnitude zero-point
PIXEL_SCALE      0.2,         # size of pixel in arcsec (0=use FITS WCS info)
SEEING_FWHM      1.2,         # stellar FWHM in arcsec
STARNNW_NAME     default.nnw, # Neural-Network_Weight table filename
BACK_SIZE        500,         # Background mesh <size> or <width>,<height>
BACK_FILTERSIZE  3,           # Background filter <size> or <width>,<height>
BACKPHOTO_TYPE   GLOBAL,      # can be GLOBAL or LOCAL
MEMORY_OBJSTACK  3000,        # number of objects in stack
MEMORY_PIXSTACK  3000000,     # number of pixels in stack
MEMORY_BUFSIZE   1024,        # number of lines in buffer
```

6. SUMMARY OF THIS THESIS AND FUTURE PROSPECTS

6.1 SUMMARY OF THIS THESIS

In this thesis, I have presented the new Fornax Deep Survey Dwarf Catalog (FDSDC, Chapter 2) and the low surface brightness galaxy catalog for the central parts of the Fornax cluster (FDS LSB-catalog, Chapter 1), using the data of the Fornax Deep Survey (FDS). Together these catalogs comprise the most excessive galaxy catalog in the area of the Fornax cluster, reaching approximately 3 magnitudes deeper than the previous most complete catalog of that area, the Fornax Cluster Catalog (FCC) by Ferguson (1989). Using the measured properties of the galaxies in the catalogs, I have studied how the cluster environment shapes the galaxies. This work has provided a detailed view of the dwarf galaxy populations in the Fornax cluster and using statistical analysis we have shown that evolution of the low and high-mass galaxies are largely driven by different mechanisms. Namely, ram-pressure stripping efficiently strips all the gas from the dwarf galaxies with $M_* < 10^8 M_\odot$, but it cannot strip all the gas from the most massive dwarfs. The early-type dwarf galaxies with $M_* > 10^8 M_\odot$, will retain some of the gas in their centers, which allows them to form stars longer than in their outskirts. This process leaves a blue dense core into the centers of these massive dwarfs. The star formation will only stop if all the gas in the center is used, or if it is heated by the tidal interactions.

The main results of this thesis chapter by chapter are:

- **Chapter 2:** We showed that number of UDGs in the central parts of the Fornax cluster is typical for its mass. In general the LSB dwarfs seem to form a continuous distribution of structural parameters with no signs of UDGs being a separate group of objects. We compared the size distribution of the LSB dwarfs in the Fornax cluster with the one of the LSB dwarfs in the Coma, and found that they are similar. The UDGs can be seen as the most extended end of the R_e distribution of the normal dwarfs that drops exponentially towards larger R_e. The LSB dwarfs including UDGs have a wide range of colors, but most of them are early-types. There seems to be no significant difference between the properties of the LSB dwarfs in the center of the Fornax and in the Centaurus group environment, although in Centaurus there are more late-type LSBs.
- **Chapter 3:** We presented the new Fornax Deep Survey Dwarf Catalog (FDSDC). The catalog contains 564 likely Fornax cluster dwarfs in the area of the main cluster and in the Fornax A sub-group. We assessed the quality of the catalog by comparing it with the previous works in the Fornax cluster, and estimated that the contamination due to the misclassified background galaxies is less than 10 % in the final catalog.
- **Chapter 4:** We analysed the dwarf galaxies in the FDSDC in order to understand their distribution within the cluster, their luminosity function, colors and structures, and to see how these properties change with respect to the cluster-centric distance. We found that the galaxies become redder and smoother towards the center of the cluster, and that their disk thickness grows, and morphology changes from late-types to early-types towards the center of the cluster. We found that the early- and late-type galaxies follow different trends between their total r'-band absolute magnitude ($M_{r'}$), effective radii (R_e) and Sérsic index (n). These differences are also manifested in the cluster-centric trends, so that in the mass range $M_* < 10^8 M_\odot$ the galaxies' R_e grows and $\bar{\mu}_{e,r'}$ decreases towards the center of the cluster, whereas for the more massive galaxies these parameters behave the opposite way. These results suggest that the gas in the outer parts of massive dwarfs is stripped by the ram-pressure, and that their central star-formation only stops after the gas is finished or it gets heated by the tidal interactions. The less massive dwarfs are likely to get fully quenched by ram-pressure stripping. We also showed that the theoretical predictions for those physical processes in the Fornax cluster are consistent with our findings. We also showed that although harassment is efficient in the Fornax cluster, frequent disruption of dwarf galaxies is not expected in the central parts. This was confirmed by our observation that the luminosity function does not change with respect to the cluster-centric radius. We compared our observations in the Fornax cluster with the results of the Next Generation Virgo Cluster survey, and found that within the accuracy of the observations, there are no differences in the dwarf populations in the centers of these two clusters.
- **Chapter 5:** I introduced and assessed the quality of a max-tree based image segmentation method called Max-Tree Objects (MTO), and applied

it for identifying a low surface brightness candidates in the FDS data. I discussed some advantages and disadvantages of MTO with respect to SExtractor and other segmentation programs, and show that the accurate Max-Tree presentation of the image does not only make it possible to detect very diffuse galaxies from images, but also improves the automated mask production and model selection for further fitting.

6.2 FUTURE PROSPECTS

In this thesis we have extensively studied the optical properties of the dwarf galaxies in the Fornax cluster, but there are still gaps in our view of this cluster. In order to say that we have obtained a comprehensive understanding of the state of the galaxies in the cluster, we must also cover the other wavelengths like the infrared and UV. Additionally, we need to study the neutral, ionized and molecular gas, in and outside of the Fornax cluster. Additionally, we need to get the redshift and kinematic information for a statistically significant sample of galaxies and compare that information with our findings in this thesis. To be fair, the building of the full picture of the state of the Fornax cluster has only taken some first steps within this thesis.

Filling many of the above mentioned gaps have already been started in forms of follow-up surveys of the Fornax cluster. The SAMI Fornax cluster survey has obtained integral field unit data for more than 60 dwarf galaxies in the cluster. The Atacama Large Millimeter/submillimeter Array (ALMA) has been used to observe CO and H_{II} in the large galaxies of the cluster (Zabel et al. 2018). The MeerKAT Fornax Survey has started observing the neutral hydrogen H_I in the Fornax cluster. Infrared and near and far ultraviolet studies of the cluster have been started using Vircam, attached to Vista and Astrosat, respectively. Also H_α observations have been performed using OmegaCAM. These ongoing surveys will clearly provide a very comprehensive view on the Fornax cluster during the upcoming years.

Studying the galaxies in a single cluster comprehensively is of course important, but to understand the environmental processes in a wider scales, we need also to compare the galaxies in totally different environments. Similar efforts as in the Fornax cluster has been started also in other nearby galaxy clusters. For example in the Virgo cluster, the NGVS have studied extensively the dwarf galaxy populations, although analysis so far has been limited to the central parts, and the analysis of the whole cluster is yet to be done. In the Perseus cluster, Wittman et al. are currently preparing a catalog of the central population of dwarf galaxies. With these cluster studies, combined with studies done for galaxy groups like those obtained by Müller et al. (2015), we can start building a picture how the mass and dynamical state of the large scale environment affects the evolution of dwarfs.

6.3 References

Ferguson, H. C. 1989, AJ, 98, 367

Müller, O., Jerjen, H., & Binggeli, B. 2015, A&A, 583, A79

Zabel, N., Davis, T. A., Smith, M. W. L., et al. 2018, MNRAS

7. Nederlandse samenvatting

De evolutie van dwergsterrenstelsels in het Fornax cluster

Sterrenstelsels zijn gravitationeel gebonden systemen van donkere materie, sterren en interstellaire materie. Het zijn de bouwstenen van het universum die leven in verschillende omgevingen, van sterk geïsoleerde sterrenstelsels tot clusters van duizenden sterrenstelsels. Sterrenstelsels transformeren gas in sterren en co-evolueren door de kosmische tijd heen met de grotere structuren van het universum, in wisselwerking met hun omgeving. Dit proces, dat de evolutie van sterrenstelsels wordt genoemd, heeft geleid tot een verbazingwekkende diversiteit aan sterrenstelsels met verschillende groottes en vormen die we waarnemen in het lokale universum. Het verkrijgen van een gedetailleerd inzicht in dit proces van de evolutie van sterrenstelsels was één van de belangrijkste doelen van astronomisch onderzoek gedurende de vorige eeuw.

In dit proefschrift concentreer ik me op de evolutie van lage massa sterrenstelsels met een stellaire massa variërend van 10^5 tot 10^9 $M_\odot$. Ongeacht hun lage massa vormen ze een belangrijk deel van het lichtgevende universum doordat ze het meest voorkomende type sterrenstelsel zijn. Vanwege hun grote aantallen bieden ze een krachtig hulpmiddel om de evolutie van sterrenstelsels te bestuderen. Vooral omdat hun lage massa ze kwetsbaar maakt voor interacties met hun omgeving, kunnen ze ons informatie geven over hoe de omgeving van sterrenstelsels hun eigenschappen beïnvloedt. Omdat de oppervlaktehelderheid van dwergsterrenstelsels overeenkomt met hun massa,

maakt de lage oppervlaktehelderheid van de dwergsterrenstelsels het echter moeilijk om ze waar te nemen.

Studies die zich concentreren op de heldere populatie van dwergsterrenstelsels in clusters hebben aangetoond dat die sterrenstelsels compacter en roder zijn dan de sterrenstelsels met een vergelijkbare massa buiten de clusters. Er is ook aangetoond dat de interne bewegingen van dwergsterrenstelsels veranderen als een functie van de lokale dichtheid van sterrenstelsels, namelijk dat de sterrenstelsels in de centra van clusters meestal systemen zonder veel stellaire rotatie, die echter toeneemt hoe meer je richting de buitendelen gaat. Deze tendensen kan men verklaren als gevolg van "galaxy harassment", een term die we gebruiken voor de snelle getijdenwisselwerkingen tussen de sterrenstelsels in het cluster. Een andere eigenschap van dwergsterrenstelsels waarvan is vastgesteld dat die gecorreleerd is met diens omgeving, is de hoeveelheid koud gas in hun schijven. Wanneer sterrenstelsels door de zwaartekracht ingevangen worden door een cluster, kan het koude gas, dat het bevat, weggeblazen worden uit het stelsel door het hete gas dat zich in de cluster bevindt. Dit proces, genaamd ram-pressure stripping, zorgt ervoor dat de sterrenstelsels in het cluster hun koude gas verliezen.

Tegenwoordig kunnen nieuwe grote instrumenten, zoals OmegaCAM op de 2.6 m VST op Cerro Paranal en DeCAM op de Blanco 4 m telescoop op Cerro Tololo Inter-American Observatory, optische multi-band beelden van grote delen van de hemel verkrijgen die veel dieper zijn dan de beelden van de Sloan Digital Sky Survey (SDSS) en andere grote projecten in het verleden. Dit stelt ons in staat om dwergsterrenstelsels in allerlei omgevingen met ongekende nauwkeurigheid te bestuderen. Deze nieuwe observaties hebben honderden nieuwe dwergsterrenstelsels onthuld in de Virgo-, Fornax- en Coma-clusters, die zo een nieuwe kijk bieden op de populaties van deze clusters en ons in staat stellen om voor de eerste keer te zien hoe deze omgevingen de eigenschappen van deze zwakke sterrenstelsels beïnvloeden. Tegelijkertijd zorgen de nieuwe gegevens ook voor een nieuwe vraag naar algoritmen die deze zwakke sterrenstelsels éénduidig kunnen identificeren aan de hand van de beelden. Met standaardalgorithmen kunnen lang niet alle structuren die in de nieuwe kaarten te zien zijn goed worden verwerkt.

In dit proefschrift analyseer ik de optische gegevens van de Fornax Deep Survey (FDS), een diep optisch onderzoek van het Fornax-cluster, gemaakt met OmegaCAM door een Nederlands-Italiaanse samenwerking. De gegevens hebben betrekking op een 26 $\deg^2$ gebied in het midden van het Fornax-cluster en in de Fornax A-subgroep. Met behulp van deze gegevens analyseer ik de dwergsterrenstelsels in deze cluster en onderzoek ik hoe hun eigenschappen als functie van afstand tot het centrum van het cluster veranderen. Mijn doel is om te begrijpen hoe het cluster de structuur en sterrenpopulaties van sterrenstelsels beïnvloedt wanneer ze het cluster binnengaan en daar evolueren.

RESULTATEN VAN DIT PROEFSCHRIFT

Dit proefschrift bestaat uit een wetenschappelijke inleiding (hoofdstuk 1), drie wetenschappelijke hoofdstukken die gebaseerd zijn op onderzoeken gepubliceerd in wetenschappelijke tijdschriften (hoofdstuk 2-4) en het vierde wetenschappelijke hoofdstuk dat is gebaseerd op een manuscript dat later zal worden gepubliceerd. (Hoofdstuk 5). In deze hoofdstukken heb ik de volgende resultaten verkregen:

In hoofdstuk 2 heb ik visueel gezocht naar LSB-sterrenstelsels met een lage oppervlaktehelderheid (Low Surface Brightness) in een gebied van 4 vierkante graad in het midden van het Fornax-cluster. Dit leverde een catalogus van 204 LSB-selsels op. Ik heb hun structuur gemeten door 2D Sérsic-functies aan hun lichtprofielen te fitten en hun kleuren te meten voor de gebieden waarbinnen de helft van hun totale licht wordt uitgezonden. We hebben ontdekt dat de locaties van de LSB-sterrenstelsels minder centraal geclusterd zijn in het cluster dan de dwergsterrenstelsels met een hoge oppervlaktehelderheid. We hebben ontdekt dat de kleuren en andere eigenschappen van de LSB dwergsterrenstelsels vergelijkbaar zijn met de meer heldere dwergsterrenstelsels van een bepaalde massa. We hebben gevonden dat de meeste van de grootste LSB-sterrenstelsels asymmetrisch lijken te zijn, wat erop wijst dat hun groottes tijdelijk kunnen worden verhoogd vanwege getijde-interacties. De structuur van de LSB-dwergsterrenstelsels in het midden van het Fornax-cluster lijkt niet te verschillen van die van LSB-dwergsterrenstelsels in een veel minder geconcentreerde omgeving van de Centaurus-groep. In de Centaurus-groep zijn er echter meer blauwe LSB-dwergsterrenstelsels. Gezien de massa van het Fornax-cluster lijkt het een typische hoeveelheid -grote- LSB-dwergsterrenstelsels te hebben, Ultra Diffuse Galaxies (UDG's) genaamd.

In Hoofdstuk 3 gebruik ik SExtractor om sterrenstelsels in de hele FDS-dataset te detecteren. Vervolgens heb ik de 2D-lichtverdeling van de sterrenstelsels met Sérsisc-functies beschreven met behulp van GALFIT en meet ik hun kleuren, concentratie en de resterende flux. Met behulp van een subsample met spectriscopisch bevestigde afstanden heb ik selectie-methoden gedefinieerd, die worden gebruikt om clusterstelsels van achtergrondobjecten te onderscheiden. Als resultaat heb ik een sample verkregen van 564 dwergsterrenstelsels in het Fornax-cluster. Ik heb de volledigheid van deze gegenereerde catalogus vergeleken met andere catalogi van het Fornax-cluster en heb geconcludeerd dat het de meest complete compilatie van dwergsterrenstelsels in de cluster is. Ik heb ook afgeschat dat de fractie van ongewenste achtergrondsterrenstelsels maximaal 10% bedraagt.

In hoofdstuk 4 heb ik de verdeling, kleuren, structuur en aantallen van de dwergsterrenstelsels in het Fornax-cluster geanalyseerd met behulp van de catalogus die is beschreven in hoofdstuk 3. Ik laat zien dat de sterrenstelsels van verschillende morfologische typen zich gemiddeld op verschillende afstanden van het centrum bevinden. Omdat de helderheid van de sterrenstelsels op deze verschillende afstanden echter niet significant verandert, is het waarschijnlijk dat de transformaties van de sterrenstelsels van het ene morfologische type naar het andere op een dusdanige manier plaatsvinden dat de sterrenstelsels tijdens dit proces geen aanzienlijke hoeveelheden massa verliezen. We hebben ontdekt dat de dwergsterrenstelsels van alle massa's roder worden en hun optische uiterlijk

egaler wordt richting de binnenste delen van het cluster. We vinden echter verschillen tussen sterrenstelsels met $M_* > 10^8$ $M_\odot$ en sterrenstelsels met minder massa: de karakteristieke afmetingen van zware dwergsterrenstelsels hebben de neiging af te nemen en hun oppervlaktehelderheid neemt toe richting het midden van het cluster, en hun oppervlaktehelderheid neemt ook toe als ze roder worden. De minder zware dwergsterrenstelsels gedragen zich op een tegenovergestelde manier, d.w.z. hun oppervlaktehelderheid neemt af richting het midden van het cluster terwijl ze roder worden. Deze observaties komen overeen met een geremde stervorming in de dwergsterrenstelsels met lage massa, veroorzaakt door "ram-pressure stripping"tijdens het invallen in de cluster en dat hun daaropvolgende evolutie meestal wordt bepaald door het uitdoven en het roder worden als gevolg van veroudering van hun gemiddelde sterpopulaties. Dit scenario bleek ook haalbaar toen we de efficiëntie van ram-pressure stripping berekenden met behulp van een eenvoudig analytisch model. In het geval van de zware dwergsterrenstelsels kan ram-pressure stripping volgens onze berekeningen niet al het gas uit hun centrale delen verwijderen en dus kunnen er sterren gevormd blijven worden, zelfs in de clusteromgeving. Die sterrenstelsels verhogen dus hun centrale dichtheid als gevolg van uitgebreide stervorming in hun centrum en/of als gevolg van galaxy harassment.

In hoofdstuk 5 heb ik een op max-tree gebaseerd algoritme, genaamd Max-Tree Objects (MTO), voor de identificatie van sterrenstelsels getest en de resultaten die met MTO zijn verkregen vergeleken met de resultaten die zijn verkregen met de standaard methode in het vakgebied, SExtractor. Onze tests, uitgevoerd met gesimuleerde en echte FDS-afbeeldingen, hebben aangetoond dat MTO volledi ger is bij het detecteren van sterrenstelsels dan SExtractor, en dat het ook de buitendelen van de sterrenstelsels beter identificeert, wat leidt tot nauwkeuriger metingen van helderheid en grootte. Vervolgens hebben we MTO toegepast op de hele FDS-gegevensset om nieuwe, zwakke dwergsterrenstelsels te identificeren. We zullen een volledige analyse van de nieuw geïdentificeerde objecten uitvoeren in een volgende artikel.

CONCLUSIES VAN HET PROEFSCHRIFT

In dit proefschrift heb ik dwergsterrenstelsels geanalyseerd in het Fornax-cluster met behulp van de optische gegevens van de Fornax Deep Survey. Met behulp van die dataset heb ik nieuwe lichtzwakke dwergsterrenstelsels van het Fornax-cluster geïdentificeerd en zo een completer inzicht gekregen in de populatie van de sterrenstelsels in het cluster.

Ik heb ook nieuw observationeel bewijs verkregen dat onze huidige theorieën over de evolutie van sterrenstelsels ondersteunt in een omgeving met een hoge dichtheid. Onze metingen ondersteunen het idee dat de buitenste delen van het gas van de meest zware dwergsterrenstelsels worden verwijderd door ram-pressure stripping tijdens het passeren van het cluster, en dat verdere evolutie in het cluster plaatsvindt via centrale stervorming en het strippen en verwarmen van hun stellaire component door galaxy harassment. Nieuw in deze studie

was om te laten zien dat de eigenschappen van de laagste massa sterrenstelsels eenvoudigweg kunnen worden verklaard door een snelle verwijdering van gas via ram-pressure stripping en daaropvolgende uitdoving als gevolg van veroudering van de sterpopulaties.

Deze studie heeft ons begrip van sterrenstelsels en hun evolutie in dit nabije cluster vergroot. De catalogi en de beeldgegevens die in dit werk worden gepresenteerd dienen ook als basis voor toekomstige vervolgstudies die de gasinhoud, sterpopulaties en bewegingen van de dwergsterrenstelsels in de Fornax-cluster zullen analyseren.

8. Acknowledgements

8.1 Acknowledgements

First of all, I would like to to thank my supervisors Reynier, Heikki and Eija for giving me the chance to work in this exciting project and for supporting me throughout it. I have been in a privileged situation where I have had the chance to work with three different persons, who all have a common goal of producing high quality science. In particular, I would like to thank Reynier for teaching me how important it is to gather a strong scientific network around you and how to work within large scientific collaborations. Heikki for teaching me that understanding even the smallest details of the analysis is important, since eventually they make the difference between a good and a bad study. Eija for teaching me how important the clarity of the concepts and clear structuring of the text is, for making my research understandable for others (and also to myself).

I acknowledge the financial support I have received from Vilho, Yrjö, and Kalle Väisälä foundation and from the University of Oulu. This thesis has benefited from interactions within the SUNDIAL ITN network, a EU Horizon 2020 research and innovation program under the Marie Skłodowska-Curie grant agreement No 721463. I also acknowledge the Finnish centre for Astronomy with ESO (FINCA) for the mobility grants I received during this thesis.

I would also like to thank all the collaborators within the FDS team, for the support and comments during writing of the papers and having a good spirit within the collaboration during these years. I thank Michael Wilkinson and

Caroline Haigh for introducing me with the max-tree methods and for the exciting collaboration with their applications to astronomical data.

I would not have been able to deal with the FDS data without the help of the AstroWISE team in Groningen. I would especially like to thank Gijs, Danny, and Ewout for teaching me the secrets of AstroWISE and for giving help and technical support whenever needed. I would also like to thank the computer group in Groningen for the technical support with the machines and for the kind and helpful atmosphere they always have when problems appear.

I would like to thank Lucia and Anthony for dealing with all the bureaucracy related to my double degree between the University of Oulu and University of Groningen. I know it was a great effort, but at least I have been enjoying the outcome quite a lot.

I would like to thank Jorrit for helping me with the Dutch summary of my thesis.

I would like to thank all the nice people at the astronomy research unit of Oulu and at the Kapteyn institute. It has been a fun and invaluable experience to learn to know people from different countries and cultures. Both institutes have always been pleasant places to work and being allowed to work around so talented and smart people has been a privilege.

I would like to thank all my friends who have been around since my childhood and those whom I have met during this PhD project. You are too many to be all listed here, but I assure that I have not forgot any of you in my thoughts. You all are a reason why it is so easy to be happy in this life. I would not have managed to succeed in this project nor much else without you. Especially, I would like to thank the boys of Kastelli. I am convinced that as long as you are around, my life will never become boring (nor safe). I would also especially like to thank Enrico and Katya for always being so nice and friendly, and for the great times we have had together in the Netherlands.

I would like to thank my family and relatives for being nice and supporting me in this quite peculiar endeavour of making a PhD thesis abut the evolution of galaxies. Especially, I would like to thank my parents for letting me to pursue those things in my life which I found interesting.

Finally, I would like to thank Sonja for understanding and supporting me when I needed to work for whole nights, and for reminding me that the previous is not usually a good idea. Thanks for reminding me everyday that there are more important things in the Universe than astronomy.